Novel Leading Edge Film Cooling Experiments and Geometries



Nicholas Edwin Holgate

Trinity College

University of Oxford

A thesis submitted for the degree of

Doctor of Philosophy

Hilary 2019

Acknowledgements

Thank you to Professor Peter Ireland for accepting me as his student; it is thanks to him perhaps above any other that I have been able to have this tremendous learning experience in Cambridge and Oxford these past four years. His knowledge and unlimited research ideas have always been a wonderful source of encouragement and inspiration. Beyond academics, he has also supplied me with extraordinary teaching, travel, and career-building opportunities, all of which have been greatly appreciated. Thank you also to the many other academic and technical staff of the Whittle Lab and the Oxford Thermofluids Institute for the great breadth of advice and support with which you have constantly provided me.

Thank you to my financial sponsors the Engineering and Physical Sciences Research Council and Rolls-Royce plc, and especially to the engineers at Rolls-Royce who have provided me with a wide range of industrially relevant research directions at the same time as suitable academic freedom. Thank you also to the staff of Darwin College and Trinity College for maintaining these supportive and enjoyable co-curricular structures which help to make the Oxbridge experiences so special.

Thank you to my friends and colleagues in the OTI, especially Alex Murray, Alex Bucknell, Marios, and Femi from my cohort of the Centre for Doctoral Training. The academic and social camaraderie between we five and the ten others in our cohort helped to make the CDT's master's and DPhil both exceptional experiences for me. Thank you to my other good friends in Cambridge and Oxford who are too many to name, but especially Chris, John, and Fan, for involving me in so many interesting opportunities and experiences. Thank you also to my close friends back home for your support both remotely and while visiting the UK, especially Rowan, Ollie, and Jack. Most importantly, thank you to my family and to Shan for your ongoing love, support, and encouragement.

Pour Gael, qui réalisa ses rêves
Que la route monte à ta rencontre,
Que le vent soit toujours dans ton dos.

Abstract

The continuing rapid growth of civil aviation and the associated greenhouse gas emissions necessitate further reduction of gas turbine engine specific fuel consumption. Since the use of high pressure compressor bleed air to cool combustor and turbine components is parasitic to engine efficiency, one of the key drivers of this progress is the ongoing improvement of the efficiency with which the coolant air is used. Because it is exposed to the undiluted and highly turbulent combustor outlet gases, the leading edge of the nozzle guide vane requires a sizeable proportion of the overall turbine coolant. Moreover, the low mainstream flow momentum in the leading edge stagnation region means that film coolant jets are highly prone to lift off of the surface, so are often poorly utilised. This study investigates the performance of this film coolant both experimentally and computationally, and proposes a novel film cooling geometry in which jets initially travel against the mainstream flow before crossing the geometric stagnation line. This is shown to achieve vastly more effective film coolant usage near the stagnation line than can conventional designs, without compromising performance farther downstream on the vane surface. Additionally, the importance of combustor dilution port flows in determining the performance of conventional leading edge film cooling designs is quantified, as is the importance of infrared calibrations which take into account temperature inhomogeneities which can occur in advanced aerothermal experimental apparatuses. A novel infrared thermography technique has been developed for determining both of the ubiquitous film cooling performance parameters in a single experiment, where usually two are required. Also proposed is a leading edge coolant supply passage geometric modification which reduces the risk of destructive ingestion of hot combustion gases into film cooling holes. This innovation is also conducive to the improvement of gas turbine engine efficiency, primarily through its potential to facilitate reduced parasitic combustor pressure losses.

Contents

Acknowledgements i

Abstract ii

Contents iii

List of Figures vi

List of Tables xiii

Nomenclature xv

1 Introduction 1

1.1 The Need for Cooling in Modern Jet Engines . . . 1

1.1.1 The Growth of Commercial Air Travel . . . 1

1.1.2 Theoretical Basis for Increasing Turbine Entry Temperatures . . . 2

1.2 The Role of Film Cooling . . . 6

1.3 Achievements and Publications of the Present Work . . . 8

2 Literature Review 11

2.1 Fundamentals of Film Cooling . . . 11

2.2 Film Cooling Dimensionless Parameters . . . 13

2.3 Comparisons of Film Cooling on Static and Rotating Aerofoils . . . 15

2.4 Coolant Jet Lift-off . . . 15

2.5 Hole Geometry . . . 19

2.5.1 Hole Position, Spacing, and Angling . . . 19

2.5.2 Hole Shape . . . 20

2.6 Leading Edge Film Cooling . . . 21

2.7 Mainstream and Surface Effects . . . 24

2.7.1 Combustor-Turbine Interactions . . . 25

2.8 Computational Modelling of Film Cooling . . . 26

2.8.1 Reynolds-Averaged Navier-Stokes Studies . . . 26
2.8.2 Large Eddy Simulation Studies . . . 27
2.8.3 Hybrid and Direct Numerical Simulation Studies . . . 28
2.8.4 CFD Strategy of the Present Work . . . 30
2.9 Conclusions from Existing Literature and Contributions of the Present Work . . . 31

3 Oxford Combustor-Turbine Interactions Rig 33
3.1 Introduction to Combustor-Turbine Rigs . . . 33
3.1.1 Examples of Previous Combustor-Turbine Rigs . . . 34
3.2 Overview of the Oxford Combustor-Turbine Interactions Rig . . . 37
3.2.1 Pressure Leading Edge Test Pieces . . . 39
3.2.2 Film Effectiveness Leading Edge Test Pieces . . . 41
3.2.3 Rig Modifications by the Author . . . 42
3.3 Effect of Dilution Port Mass Flow Rates on Cascade Aerodynamics . . . 43
3.4 Technique for Controlling Two Coolant Feeds with a Single Plenum . . . 44
3.5 Predicting the Nondimensional Parameters for Heated Flow . . . 48
3.6 Mass Flow Rate Uncertainty Analysis . . . 49
3.7 Window Analysis . . . 51
3.8 Film Effectiveness Conductivity Correction . . . 54
3.8.1 Analytical and Computational Studies of Film Effectiveness Conduction Error . . . 57
3.8.2 Experimental Correction with Conduction Images . . . 61
3.9 Conclusions . . . 65

4 Infrared Thermography 67
4.1 Introduction to Full-surface Temperature Measurement . . . 68
4.2 Two Types of Infrared Cameras . . . 71
4.3 Thermal Radiation Theory . . . 72
4.3.1 Interactions Between Infrared Radiation and Matter . . . 72
4.3.2 Planck's Law and the Stefan-Boltzmann Law . . . 74
4.3.3 Grey-body Analysis in the CTI Rig . . . 75
4.4 Black-body Calibration . . . 79
4.5 Grey-body Calibration . . . 81
4.5.1 Dependence of Emissivity on Observation Angle . . . 82
4.5.2 Dependence of Window Transmissivity on Temperature . . . 84
4.5.3 Surrounding Radiance Test Piece . . . 86

4.6 Accuracy Advantage of a Spatial Infrared Calibration in the CTI Rig . . . 90
4.7 An Experimental-Numerical Method for Transient Infrared Measurement of Film Effectiveness and Heat Transfer Coefficient in a Single Test . . . 92
4.7.1 Previous Techniques . . . 94
4.7.2 Outline of the Novel Technique . . . 96
4.7.3 Advantages of the Novel Technique . . . 99
4.8 Conclusions . . . 102

5 Radial Showerhead Film Cooling Measurements Downstream of Combustor Dilution Ports 104
5.1 Introduction . . . 105
5.1.1 Radial Film Cooling Geometries . . . 106
5.2 Upstream Temperature Profile Correction . . . 109
5.3 Film Cooling Uncertainty Analysis . . . 114
5.3.1 Film Effectiveness . . . 114
5.3.2 Heat Transfer Coefficients . . . 115
5.4 Data Averaging Methodology . . . 116
5.5 Results . . . 118
5.5.1 Dilution Port Temperature Profiles . . . 118
5.5.2 CFD Simulation of Dilution Port Momentum Flux Ratios . . . 119
5.5.3 Dilution-Film Interaction Effectiveness . . . 123
5.5.4 Heat Transfer Coefficients . . . 131
5.5.5 Net Heat Flux Reduction . . . 134
5.6 Conclusions . . . 135

6 Reverse-Blowing Films Crossing Over the Aerofoil Stagnation Line 139
6.1 Introduction and Motivation . . . 140
6.2 Cooling Hole Geometries . . . 142
6.3 CFD Study of Radial and Cross-Over Film Cooling Geometries . . . 146
6.3.1 Mesh, Model, and Boundary Condition Studies . . . 146
6.4 Results . . . 148
6.4.1 Detailed Effectiveness - Reverse-Blowing Geometries . . . 148
6.4.2 Detailed Effectiveness - Radial Geometries . . . 150
6.4.3 Stagnation Line Performance . . . 155
6.4.4 Lateral and Area Averages . . . 158
6.5 Coolant-Mainstream Mixing Analyses . . . 162
6.5.1 Known Coolant Mass Flow Rate . . . 165
6.5.2 Known Mainstream Mass Flow Rate . . . 166
6.6 Conclusions . . . 169

7 Pressure Margin Enhancement with a Coolant Passage Insert 171
7.1 Introduction and Motivation . . . 171
7.2 Pressure Margin Insert Theory and Preliminary Design . . . 175
7.2.1 Experimental Approach . . . 175
7.2.2 External Pressure Distribution . . . 176
7.2.3 Inviscid Analysis for Insert Cross Section Design . . . 178
7.3 Internal Pressure and Pressure Margin Results . . . 181
7.3.1 Internal Pressures with Overly Broad or Narrow Inserts . . . 181
7.3.2 Internal Pressures with Successfully Designed Inserts . . . 184
7.3.3 Pressure Margins . . . 184
7.3.4 Uncertainty Analysis . . . 187
7.4 Viscous Modelling for Prediction of Coolant Pressure Margin . . . 188
7.5 Conclusions . . . 191

8 Conclusions and Recommendations 192
8.1 A Spatially Resolved Infrared Camera Calibration in the Presence of NGV Endwall Film Cooling (Section 4.6) . . 192
8.2 A Novel Method for Measuring Film Cooling Effectiveness and Heat Transfer Coefficients in a Single Test (Section 4.7) . 193
8.3 A Novel Method for Measuring NGV Leading Edge Film Effectiveness in the Presence of Non-uniform Temperature Profiles (Section 5.2) . . . 194
8.4 Quantification of the Enhancement by Dilution Port Turbulence of the Film Effectiveness Produced by Lifted-off Leading Edge Coolant Jets (Section 5.5) . . . 195
8.5 Quantification of the Film Effectiveness Advantages of Leading Edge Films Which Blow Across the Geometric Stagnation Line in Criss-cross Patterns (Section 6.4) . . . 196
8.6 Quantification of the Improvements to Minimum Hole Pressure Margin Due to a Novel Geometric Modification to Leading Edge Coolant Supply Passages (Section 7.3) . . . 197
8.7 Scope for Further Research . . . 197

A Operating Procedures for the Oxford Combustor-Turbine Interactions Rig 199
A.1 Setup . . . 199
A.2 Experiment . . . 200

B Heat Transfer Coefficient Uncertainty Contributions 201

References 205

List of Figures

1.1 Temperature-entropy diagram of three ideal Brayton cycles: baseline, increased compressor pressure ratio, and increased combustor heat addition. 3

1.2 Brayton cycle thermal efficiency and specific power curves for $\eta_{comp} = \eta_{turb} = 0.9$. The fine red lines indicate the positions of the curves' respective maxima. 7

2.1 RANS CFD results showing absolute flow velocity contours and directional arrows for a single, streamwise-blowing film cooling hole at three blowing ratios. The planes interrogated in Figures 2.2 and 2.3 are indicated. 16

2.2 RANS CFD results showing growth of vortices within a streamwise-blowing film cooling hole at three blowing ratios. x is the distance along the hole centreline from the hole inlet, and L is the hole length. 17

2.3 RANS CFD results showing development of counter-rotating kidney vortices downstream of a single, streamwise-blowing film cooling hole at three different blowing ratios. d is the distance downstream from the hole exit's downstream edge and D is the hole diameter. 18

2.4 Results of a RANS CFD leading edge film cooling simulation performed by the present author. Owing to the significant lift-off of the modelled stagnation region coolant jets, the local and downstream NGV surface temperatures are well above the coolant feed temperature. 22

3.1 Oxford Combustor-Turbine Interactions Rig with main features indicated. . 37

3.2 (a) Rohacell film effectiveness (left, before painting) and 3D-printed resin pressure (right) leading edge test pieces. (b) View looking downstream at the NGV cascade with a pressure test piece inserted. 40

3.3 The 'inlet' (left) and 'main' (right) pieces of the pressure model containing internal tappings at $s = 0.15$ and $s = 0.30$ within the 'inlet' piece. In order to exit the rig, the pressure tapping hoses must pass through spanwise cavities in the 'main' piece. 41

3.4 Predicted strain in a Rohacell test piece under typical rig differential pressure conditions. 43

3.5 The effects of dilution on NGV pressure ratio and capacity ($J_E = M = 0$). 45

3.6 (a) Determining flow rate-dependent supply chamber and baffle plate total pressure losses by exhausting to atmosphere. (b) Blocking RIDN holes to measure flow rate-dependent leading edge discharge coefficients. (c) Using known total pressure losses and discharge coefficients to determine flow split. 47
3.7 Experimentally observed variations between cold and hot dimensionless mass flow rate parameters, which fit well with the semi-empirical proportional relationships for M and J but not Re_{throat}. 50
3.8 Germanium windows (blue) as assembled within a window block (green) with two gaskets and an aluminium window frame. 52
3.9 Inlet fluid temperature profile boundary condition (left), mesh and temperature result cross section (middle) and outlet fluid temperature result (right) for the reduced domain, conjugate CFD simulation of the window frame during heated rig operation. Dilution port coolant $T_{p,D}$ and combustor simulator inlet T_{inlet} reference temperatures. 55
3.10 Close-up of the mesh region indicated in Figure 3.9, showing (a) perspex (b) window frame (c) Germanium window (d) fluid, and the high mesh density gaskets. 56
3.11 Two adjustable height windows facilitating downstream suction side observations on the central NGV. 56
3.12 One-dimensional thermal resistances model for steady-state analysis of a solid with convective heat transfer on both sides. h_e and h_i are the external (hot gas) and internal (coolant) heat transfer coefficients, respectively. L is the solid wall thickness. 58
3.13 Contours of the nondimensionalised discrepancy between test piece driving gas temperature and surface temperature, for two values of film effectiveness and various material thicknesses and conductivities. CTI rig Rohacell test piece performance indicated on each plot. 61
3.14 Curves representing the data in Figure 3.13. 61
3.15 An example of the experimental test piece thermal conductivity correction used ($J_D = 9$, $J_E = 0$, $M = 3.5$). 63

4.1 Graphical illustration of Planck's law, showing that an ideal black-body in thermal equilibrium and near room temperature emits thermal radiation mainly in the infrared spectrum. Spectrum boundaries from [1]. 75
4.2 Three sources of infrared radiation incident upon an IR camera's individual microbolometer from a small surface area on a test surface. The test surface emissions (P_s) are attenuated by the window. The test surface reflections (P_R) are attenuated first by their reflection from the surface and then by the window. 77

4.3 3D-printed cavity black-body used to calibrate the black-body temperature corresponding to IR camera raw count outputs. 80
4.4 Linear black-body calibration relationships for cameras A and B used for CTI rig surface temperature measurements (each with two different lenses) and a third camera C illustrating viewing distance dependence. 81
4.5 (a) Black paint emissivity as a function of viewing angle, as measured on a flat aluminium plate at a constant temperature and (b) Combined transmissivity-emissivity factor as a function of plate temperature, plate viewed through the rig IR-transparent windows at a constant viewing angle. 83
4.6 The distribution of observation angles with the test piece surface normals around a cross section of the central NGV leading edge for the two camera positions in the CTI rig. 84
4.7 IR calibration leading edge test piece (a) before painting and (b) after painting. 87
4.8 MATLAB-generated interface for manually selecting regions around surface thermocouples at which to average pixels to determine corresponding T_{bb} data (pressure side camera). The average for each thermocouple is the mean of all the pixels bounded between its pair of roughly concentric rectangles. Since at this stage of analysis surface temperatures are not known, the colour contouring is by camera raw count (scale omitted). 88
4.9 Normalised surrounding radiance distributions for outer endwall film cooling momentum flux ratios $J_E = 0$, 4, 7, 10. Pressure and suction side views with spanwise positions indicated (left), and full-field IR camera black-body temperatures from suction side view (right) to indicate endwall coolant's effect on vane. For these cases, $J_D = M = 0$. 91
4.10 Contours of suction side film effectiveness discrepancy for $J_D = 9$, $J_E = 7$, $M = 1.5$ when calculated with a spatial calibration compared to calculation with (a) mean surrounding radiance (b) minimum surrounding radiance. . 93
4.11 Iterative progress of the HTC-finding algorithm, showing convergence of FD-predicted surface temperature histories towards the measured surface temperature history for a single pixel. 100

5.1 Hole row cross sections illustrating the three possible types of arrangement of radial cooling holes, and showing the definition of the hole surface angle. 106
5.2 Three removable NGV leading edge test pieces showing their varying spanwise distributions of surface angles (α) of the PS2-SS2 radial holes (compound angles $\beta = 90°$). 108
5.3 Hole angles in a cross-sectional plane, consistent for all three radial models. 109

5.4 Film effectiveness for two dilution port flow rates, including the influence of the two vane inlet temperature profiles. $J_E = 0$, $M = 3.5$. (a) $J_D = 0$ and (b) $J_D = 9$. 110
5.5 Conceptualisation of the additive film effectiveness as the additional temperature reduction when films are turned on with pre-existing upstream dilution. 111
5.6 An example of the film effectiveness data processing used. Note the different colour scale employed for DFI images. Positive/negative DFI effectiveness indicates that dilution port turbulence enhances/diminishes local film effectiveness, the mechanisms for which are discussed in section 5.5. 113
5.7 Percentage HTC uncertainties on the PS and SS on one of the film-cooled leading edge models investigated ($M = 3.5$, $J_D = 9$). Geometric stagnation line indicated. 116
5.8 The two regions of interest (green lines), stagnation region (red dashed lines), and hole row locators (blue lines) used in producing averages of thermographic measurements. 116
5.9 Contours of absolute change in pressure side film effectiveness due to a change of Reynolds number from 8.5×10^5 to 1.0×10^6. $J_D = J_E = 0$, $M = 1.5$. 119
5.10 Nondimensionalised vane adiabatic wall temperature profiles due to dilution ports. $J_D = 4,\ 9,\ 15$, $J_E = 0$, $M = 0$. $\eta_D(\mathbf{x}) = \frac{T_{inlet,D} - T_{aw,D}(\mathbf{x})}{T_{inlet,D} - T_{p,D}}$ (Equation 5.3). 120
5.11 12.3 million element CFD mesh used to predict temperature profiles on the CTI rig's central NGV leading edge due to dilution ports. 122
5.12 CFD-predicted nondimensionalised vane adiabatic wall temperature profiles due to dilution ports. Isotherms show the increasing penetration of dilution jets into the mainstream with increasing momentum flux ratio. $J_D = 4,\ 9,\ 15$, $J_E = 0$, $M = 0$. $\eta_D(\mathbf{x}) = \frac{T_{inlet,D} - T_{aw,D}(\mathbf{x})}{T_{inlet,D} - T_{p,D}}$ (Equation 5.3). . . . 122
5.13 Contours of CFD-predicted turbulent kinetic energy (TKE) in the combustor simulator in planes orthogonal to the NGV spanwise direction. $s = \frac{1}{4}$, $\frac{1}{2}$, $\frac{3}{4}$ and $J_D = 4,\ 9,\ 15$. 123
5.14 DFI effectiveness for model RAD-A at $M = 1.5$ and 2.5, and three dilution momentum flux ratios, $J_D = 4,\ 9,\ 15$. The DFI effectiveness represents the gain in effectiveness of the leading edge film due to the dilution port turbulence. 125
5.15 DFI effectiveness for model RAD-A at $M = 3.5$ and three dilution momentum flux ratios, $J_D = 4,\ 9,\ 15$. 126
5.16 DFI effectiveness for model RAD-B at $M = 1.5$ and 2.5, and three dilution momentum flux ratios, $J_D = 4,\ 9,\ 15$. 127

5.17 DFI effectiveness for model RAD-B at $M = 3.5$ and three dilution momentum flux ratios, $J_D = 4$, 9, 15. 128
5.18 DFI effectiveness for model RAD-C at $M = 1.5$ and 2.5, and three dilution momentum flux ratios, $J_D = 4$, 9, 15. 129
5.19 DFI effectiveness for model RAD-C at $M = 3.5$ and three dilution momentum flux ratios, $J_D = 4$, 9, 15. 130
5.20 (a) Film effectiveness (b) Frossling number, and (c) estimated net heat flux reduction on the pressure side of model RAD-C. $M = 3.5$, $J_D = 9$, $J_E = 0$. 133
5.21 (a) Film effectiveness (b) Frossling number, and (c) estimated net heat flux reduction on the suction side of model RAD-C. $M = 3.5$, $J_D = 9$, $J_E = 0$. . 134
5.22 Laterally averaged Frossling number for all three radial showerhead leading edge models. $M = 1.5$, 2.5, 3.5, $J_D = 0$, 4. 136
5.23 Laterally averaged Frossling number for all three radial showerhead leading edge models. $M = 1.5$, 2.5, 3.5, $J_D = 9$, 15. 137

6.1 An example of a conventional, radially film cooled leading edge, illustrating how the PS1 and SS1 coolant is swept downstream away from the stagnation line. 140
6.2 Three leading edge test pieces with reverse-blowing PS1 and SS1 hole rows blowing in various criss-cross patterns over the stagnation line. The PS2 and SS2 rows blow radially. Hole colouration indicates the nature of the inter-row hole intersections. 144
6.3 Hole angles in a cross-sectional plane, with some slight variations between the three reverse-blowing models (listed in order REV-A,B,C). 145
6.4 Model RAD-B CFD reduced domain geometry with walls and boundary condition locations indicated. The coolant pressure outlet is on the hidden end of the coolant passage. 147
6.5 Film effectiveness for models REV-A,B,C at $M = 1.5$ and 2.5, $J_D = 9$. . . 151
6.6 Film effectiveness for models REV-A,B,C at $M = 3.5$, $J_D = 9$. 152
6.7 Streamlines of coolant from the PS1 and SS1 reverse-blowing holes of models REV-A1/A2,B1/B2,C1/C2, at three blowing ratios, according to steady RANS CFD simulations. The mainstream flow velocity magnitude is shown as a grey-scale contour. 153
6.8 Detailed near-midspan stagnation region film effectiveness predictions for models REV-A,B,C, $M = 3.5$, according to steady RANS CFD simulations. 154
6.9 Film effectiveness for models RAD-A,B,C at $M = 1.5$ and 2.5. $J_D = 9$. . . 155
6.10 Film effectiveness for models RAD-A,B,C at $M = 3.5$. $J_D = 9$. 156

6.11 Streamlines of coolant from the radial holes of models RAD-A,B,C, at three blowing ratios M = 1.5, 2.5, 3.5, according to steady RANS CFD simulations. The mainstream flow velocity magnitude is shown as a grey-scale contour. 157
6.12 Film effectiveness along the geometric stagnation line of models RAD-A,B,C and REV-A,B,C at three blowing ratios $M = 1.5$, 2.5, 3.5. $J_D = 9$. . 157
6.13 Laterally averaged film effectiveness for models RAD-A,B,C and REV-A,B,C at three blowing ratios $M = 1.5$, 2.5, 3.5. $J_D = 9$. 159
6.14 RANS CFD predictions of velocity in a plane through the PS1 hole row of leading edge model RAD-B, showing the increased flow separations and reduced mass flow rates in holes inclined against the coolant passage bulk flow. $M = 3.5$. 160
6.15 Area-averaged film effectiveness for models RAD-A,B,C and REV-A,B,C at three blowing ratios $M = 1.5$, 2.5, 3.5. $J_D = 9$. 162
6.16 A thin streamtube beginning upstream of the NGV pressure side stagnation region (red) interacting with coolant from reverse-blowing model REV-A and a streamtube of equal initial width which passes through the cascade at a distance from the NGVs (green). 164
6.17 Normalised, estimated streamtube width of mainstream gas participating in coolant mixing at various positions downstream of the geometric stagnation line. All six leading edge models. $M = 1.5$, 2.5, 3.5. $J_D = 9$. 167
6.18 Estimated fraction of PS1 and SS1 hole row coolant effectively cooling between these two rows. All six leading edge models. M = 1.5, 2.5, 3.5. $J_D = 9$. 168

7.1 Illustration of the placement of the pressure margin inserts studied herein, all of which cover the PS3 to SS4 hole rows, inclusive. 173
7.2 NGV leading edge (a) without and (b) with a half-span insert, with internal pressure contours from RANS CFD ($\%m_{NGV}$ = 9.9). A rise of static pressure inside the insert is evident. Pressures relative to the indicated stagnation line ($P_i = 0$). 174
7.3 Experimental pressures on NGV exterior, with no insert present. Filled/empty circles are normalised by $(\frac{1}{2}\rho v^2)_{throat}$ including/excluding the NGV coolant mass flow rate. 177
7.4 Experimentally measured static pressures inside the NGV coolant passage for seven pressure margin inserts. $\frac{x}{C_x} < 0$ and $\frac{x}{C_x} > 0$ are the coolant passage wall regions internal to the NGV pressure and suction sides, respectively. Note the vertical axis scale variations. 183

7.5 Pressure margins across film cooling hole rows for seven pressure margin inserts. Note the change of vertical axis scale for $s = 0.30$ results. Covered hole rows are shaded. 186
7.6 Measured SS1 hole row pressure margins for $\%\dot{m}_{NGV} = 7.1$, all seven tested inserts. 187
7.7 Viscous model hole pressure margin predictions for inserts F and G. $\%\dot{m}_{NGV} = 4.7$. 190

B.1 Suction side HTC uncertainty contributions of the material thermal diffusivity (α), the time error (Δt), and the film effectiveness (η). 201
B.2 Suction side HTC uncertainty contributions of the surface temperature (T_s), the coolant temperature (T_c), and the mass-averaged mainstream temperature (T_∞). 202
B.3 Pressure side HTC uncertainty contributions of the material thermal diffusivity (α), the time error (Δt), and the film effectiveness (η). 203
B.4 Pressure side HTC uncertainty contributions of the surface temperature (T_s), the coolant temperature (T_c), and the mass-averaged mainstream temperature (T_∞). 204

List of Tables

4.1 The key advantages and disadvantages of various full-surface temperature measurement techniques with respect to film cooling experiments. 70

5.1 Hole pitch, surface distance of exit centre from stagnation line, and hole length by row, normalised by hole diameter, for all three radial cooling models. 107
5.2 Uncertainties for dilution-only, dilution-and-films, additive, and dilution-film-interaction effectiveness results. The uncertainties vary slightly both between cases and within individual images, resulting in the reported overall maxima and minima. 115

6.1 Characteristics of reverse-blowing cooling hole rows (PS1 and SS1) on the three reverse-blowing models designed for experiments. Hole stagger and spacing are expressed in terms of the hole diameter D. 143
6.2 Hole pitch P, surface distance of hole exit centre from stagnation line S, and hole length L by row, normalised by hole diameter D, for radial and reverse-blowing models. 145

7.1 Lengths and inlet areas of the seven tested inserts. 181
7.2 Estimated maximum uncertainties for the derived insert performance flow quantities. 188

Nomenclature

Greek

α	Absorptivity
β	Film cooling hole compound angle
γ	Ratio of specific heats, experimental conduction correction factor
Γ	NGV capacity
$\Delta p_{0,loss}$	Total pressure loss through feed plenum
ϵ	Emissivity
$\eta_{correction}$	Film effectiveness correction constant
η	Film cooling effectiveness
η_t	Ideal cycle thermal efficiency
η_{comp}	Compressor isentropic efficiency
$\eta_{t,real}$	Real cycle thermal efficiency
η_{turb}	Turbine isentropic efficiency
$\theta = \frac{T_3}{T_1}$	Temperature ratio
λ	Wavelength
ξ	Fraction of radiant flux directed towards a pixel (view factor)
ϱ	Reflectivity
ρ_c	Coolant density
ρ_∞	Mainstream density
σ	Stefan-Boltzmann constant
τ	Transmissivity
ϕ	Nondimensional metal temperature
$\chi = \frac{\gamma-1}{\gamma}$	Isentropic relationship exponent

Lower-case

$c_{1,2}$	Black-body calibration constants
c_p	Specific heat at constant pressure
c	Speed of light
c_V	Specific heat at constant volume
d	Observation distance
f	Darcy friction factor
h_0	Heat transfer coefficient, uncooled surface
h	Planck constant, heat transfer coefficient
j_{bb}	Radiosity of a black-body
j_{gb}	Radiosity of a grey-body
k_B	Boltzmann constant
k	Thermal conductivity
k_f	Fluid thermal conductivity
$\dot{m}_a$	Engine air mass flow rate
$\dot{m}_c$	Film coolant net mass flow rate
$\dot{m}_{c,L}$	Mass flow rate of locally mixing coolant
$\dot{m}_{c,row}$	Mass flow rate of coolant from an individual row

$\dot{m}_f$	Engine fuel mass flow rate
$\dot{m}_1$	Mass flow rate at cascade inlet
$\dot{m}_T$	Coolant passage inlet mass flow rate
$\%\dot{m}_{NGV}$	Leading edge film coolant as percentage of overall throat flow
m_{ST}	Streamtube mass flow rate
p_{0c}	Coolant total pressure
$p_{sc,passage}$	Coolant static pressure
$p_{s,e}$	Hole exit static pressure
$p_{s,i}$	Hole inlet static pressure
p_n	Pressure at thermodynamic cycle stage n
$p_{se,max}$	Maximum external aerofoil static pressure
p_s	Static pressure
$p_{s,atm}$	Atmospheric static pressure
p_{01}	Total pressure at cascade inlet
p_{01}	Static pressure at cascade exit
q''	Surface heat flux per unit area
q''_0	Surface heat flux per unit area, uncooled
q_{in}	Specific combustion heat added to cycle
q_{out}	Specific heat lost from cycle to atmosphere
q^*	Normalised surrounding radiance
r	Pressure ratio
s	Fractional spanwise distance
v_e	Propulsive jet velocity
v_c	Coolant jet velocity, coolant passage bulk velocity
v_∞	Mainstream bulk velocity upstream of NGV
$v_{\infty,hole}$	Mainstream velocity at hole exit
v_θ	Mainstream whirl velocity
w	Specific useful mechanical work per cycle, NGV leading edge axial width
$\boldsymbol{x}$	Pixel coordinate
x	Streamwise distance from stagnation line

Upper-case

$A(s)$	Coolant channel cross-sectional area with span
A_T	Coolant passage constant cross-sectional area
A_h	Film cooling hole combined area of minimum cross sections
$A_{min}(s)$	Minimum cross-sectional area with span of converging coolant channel, to achieve a given pressure margin
A_s	Area of an element of the test surface visible to a pixel
Bi	Biot number
B_λ	Spectral radiance (Planck's law)
C_d	Discharge coefficient
C_x	NGV axial chord length
D_h	Hydraulic diameter
D	Cylindrical hole cross-sectional diameter/fan hole cross-sectional slot width
DR	Density ratio
$F(s)$	Darcy-Weisbach equation
Fr	Frossling number
H	Insert length as fraction of span

J_D	Dilution port momentum flux ratio
J_E	Outer endwall momentum flux ratio
K_L	Diffuser pressure loss coefficient
L	Film cooling hole length, thickness of conductive solid
M	Average blowing ratio
M_{hole}	Local blowing ratio
P_i	Normalised coolant pressure
PM	Hole row pressure margin
PM_{design}	Design pressure margin
P_{NGV}	NGV pitch
P_{opt}	Pixel-incident radiative power due to optical pathway emissions
P	Film cooling hole row pitch
P_e	Radiative power emitted by a small test piece surface region
P_R	Pixel-incident radiative power due to test surface reflections
PR	NGV pressure ratio
P_s	Pixel-incident radiative power due to test surface emissions
P_{total}	Pixel-incident total radiative power
$Q(s)$	Ratio of static-to-total pressures
$Re_{throat/w}$	Reynolds number (NGV throat and chord length/NGV inlet and leading edge axial width)
R	Specific gas constant for air
T_{air}	Temperature of air in the combustor simulator
T_{amb}	Ambient temperature
T_{aw}	Adiabatic wall temperature
$T_{aw/c,cond}$	Uniform mainstream temperature and coolant temperature for experimental conduction correction tests
T_c	Coolant reference temperature
T_{ci}	Coolant temperature at feed passage entry
T	Temperature
T_{bb}	Black-body temperature
T_s	Temperature of a test surface
T_0	Total temperature
$T_{0,rel}$	Total temperature in rotating frame
T^*	Film effectiveness uncorrected for conduction
T_∞	Mainstream (hot gas) reference temperature
T_n	Temperature at thermodynamic cycle stage n
T_{ref}	Reference hot gas driving temperature
T_R	Effective reflected temperature
T_{01}	Total temperature at cascade inlet
T_w	Surface thermocouple temperature
T_{window}	Temperature of an infrared window
U	Turbine rotor velocity
W_{ST}	Streamtube width

Abbreviations

CAD/CAM	Computer-Aided Design/Manufacturing
CFD	Computational Fluid Dynamics
CTI	Combustor-Turbine Interactions

DES	Detached Eddy Simulation
DNS	Direct Numerical Simulation
FPA	Focal Plane Array
FSN	Fuel Spray Nozzle
HPT	High Pressure Turbine
IR	Infrared
LDA	Laser Doppler Anemometry
LES	Large Eddy Simulation
NGV	Nozzle Guide Vane
PIV	Particle Image Velocimetry
PS	Pressure Side
PSP	Pressure-Sensitive Paint
$(U)RANS$	(Unsteady) Reynolds-Averaged Navier–Stokes
ROI	Region of Interest
$RIDN$	Radial Inner Discharge Nozzle
$RODN$	Radial Outer Discharge Nozzle
RQL	Rich-burn, Quick-mix, Lean-burn
SAS	Scale-Adaptive Simulation
SFC	Specific Fuel Consumption
SP	Specific Power
ST	Specific Thrust
SS	Suction Side
TBC	Thermal Barrier Coating
TET	Turbine Entry Temperature
TKE	Turbulent Kinetic Energy

Chapter 1

Introduction

In this chapter, the need for improvements in film cooling technology is illustrated through an exploration of the ongoing growth of the civil aviation industry and the need to further increase turbine entry temperatures to slow the associated growth of greenhouse emissions. This includes remarks on the efficacy of film cooling relative to its companion cooling technologies (thermal barrier coatings and internal cooling). Finally, the key results of the present work's research into film cooling are summarised.

1.1 The Need for Cooling in Modern Jet Engines

1.1.1 The Growth of Commercial Air Travel

Aircraft jet engines provide a fast and increasingly cost-effective medium of transportation; expressed in 2017 United States dollars, the average cost of a return trip between Boston and Los Angeles decreased from $4,695 in the year 1941 to $775 in the year 2000, continuing to $473 in 2017 [2]. This progress has facilitated the enormous increase in civil air traffic leading to over 1.6 billion journeys worldwide in 2000 and over 3.5 billion in 2017 [3]. Air transportation 'broadens people's leisure and cultural experiences' and at present supports an estimated 36 million tourism jobs [4]. These cost reductions and the benefits they confer are driven largely by the ongoing reductions in fuel consumption per passenger-kilometre. For regional flights, this decreased from around 3.6 litres per 100 km per passenger in the late 1990s (e.g. Boeing 737-600) to around 2.0 litres per 100 km in the mid 2010s (e.g. Bombardier CS300) [5, 6]. These values depend upon the routes

flown and the load factors achieved (proportion of passenger seats occupied), as well as technological factors. The contribution of technological improvements towards fuel efficiency has been approximately evenly split between airframe and engine improvements [7].

Despite these advances, the rapid growth of the industry has significantly outpaced reductions of per-passenger-kilometer greenhouse gas emissions. This is exacerbated by the lack of effective emissions regulations for airliners, whose profits can frequently be maximised by extending the operational lifetimes of older, less fuel efficient aircraft [8]. In a 1999 report, the Intergovernmental Panel on Climate Change estimated that aviation generates 3.5% of anthropogenic climate change [7]. This proportion is expected to continue to grow, since decarbonisation of air transport is not technologically feasible in the foreseeable future, whereas conversion of land transportation, electricity production, and space heating to renewable energy sources is proving to be less challenging [9]. The growth of aircraft emissions will likely be partially offset by as yet unproven concepts for aircraft fuel efficiency, such as blended wing-body airframes and counter-rotating, open-rotor engines. Regardless of the progress of these novel concepts, incremental efficiency improvements will continue to be attained by increasing turbine entry temperatures (TETs) and reducing the cooling air necessary to prevent turbine failures due to those temperatures. These technological improvements will also contribute towards the reduction of emissions from gas turbines used for power generation. Even after majority-renewable, centralised electricity generation has been achieved around the world, these will still be needed in certain remote areas and in areas where renewable peak demand strategies such as variable solar thermal and hydroelectric are not viable.

1.1.2 Theoretical Basis for Increasing Turbine Entry Temperatures

The fundamental enabling phenomena of aircraft jet propulsion and turbine work are the conversions of fuel chemical energy first into increased mean kinetic energy of gas particles (by combustion) and second into unidirectional bulk kinetic energy of those particles (by expansion in moving from high to low pressure). For a given pressure drop, the acceler-

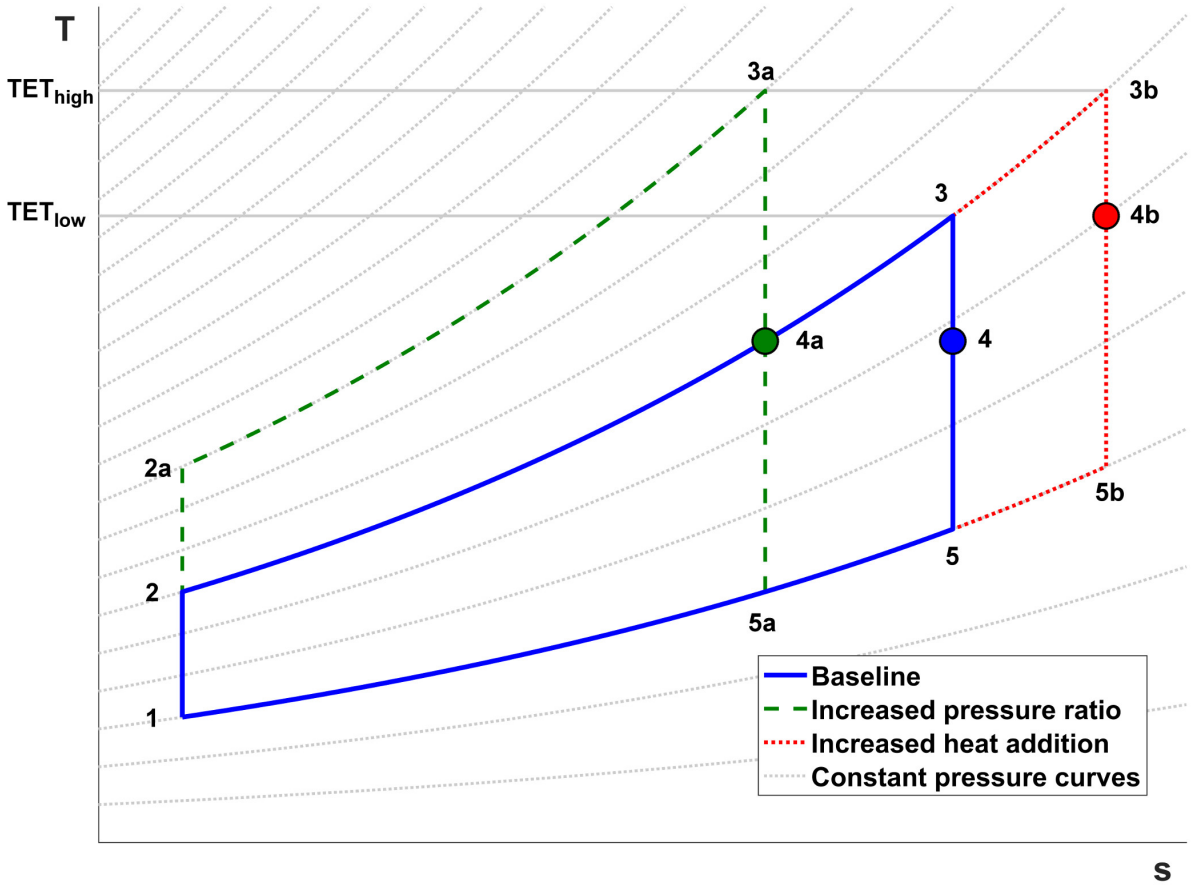


Figure 1.1: Temperature-entropy diagram of three ideal Brayton cycles: baseline, increased compressor pressure ratio, and increased combustor heat addition.

ation on an expanding packet of gas increases with the temperature of the gas, due to the increased net force provided by the more energetic gas particles colliding with their neighbours downstream. For a turbine, which must supply a particular amount of torque to a matched compressor or other load, this implies that as the TET increases, the turbine pressure drop can be decreased, leaving a greater amount of spare pressure for doing useful expansion in later turbine stages or a jet nozzle.

In addition to the above physical understanding, the beneficial effects of increasing the TET are apparent from consideration of the ideal Brayton cycle which governs gas turbine engines. As illustrated in Figure 1.1, this consists of isentropic compression ($1 \rightarrow 2$), isobaric heat addition ($2 \rightarrow 3$), compressor-matched, isentropic turbine expansion ($3 \rightarrow 4$), and load turbine or jet nozzle isentropic expansion ($4 \rightarrow 5$). The TET (T_3) can be increased in two ways:

1. Increasing the pressure ratio of the compressor $r = \frac{p_2}{p_1}$ $(1 \rightarrow 2a)$ or

2. Increasing the heat added at a constant high pressure $(2 \rightarrow 3b)$

The cycle improvements which each of these yield can be understood quantitatively with metrics such as the thermal efficiency, the specific power, the specific fuel consumption, and the specific thrust. The thermal efficiency, η_t, is the fraction of the chemical heat energy, q_{in}, which is turned into useful mechanical work, w. According to the first law of thermodynamics, the work out is equal to the sum of the heat additions q_{in} (positive) and q_{out} (negative, heat rejected to atmosphere during $5 \rightarrow 1$):

$$\eta_t = \frac{w}{q_{in}} = \frac{q_{in} + q_{out}}{q_{in}} = 1 + \frac{q_{out}}{q_{in}} \tag{1.1}$$

For a calorically perfect gas undergoing constant pressure heat exchange these heat flows are equal to the constant specific heat, c_p, multiplied by the temperature change through each process:

$$\eta_t = 1 + \frac{c_p(T_1 - T_5)}{c_p(T_3 - T_2)} = 1 - \frac{T_1(\frac{T_5}{T_1} - 1)}{T_2(\frac{T_3}{T_2} - 1)} \tag{1.2}$$

For an ideal Brayton cycle, $p_2 = p_3$, $p_5 = p_1$, and the compression and expansion processes are idealised as isentropic:

$$\frac{p_5}{p_3} = \frac{p_1}{p_2} \implies \frac{T_5}{T_3} = \frac{T_1}{T_2} \implies \frac{T_5}{T_1} = \frac{T_3}{T_2} \tag{1.3}$$

Equation 1.3 simplifies Equation 1.2 to either of the forms in Equation 1.4, where use is also made of the isentropic pressure change relation for an ideal gas:

$$\eta_t = 1 - \frac{T_1}{T_2} = 1 - r^{\frac{1-\gamma}{\gamma}} \tag{1.4}$$

where $r = \frac{p_2}{p_1}$ is the compressor pressure ratio. Similarly, the specific power is given by:

$$SP = \frac{w}{c_p T_1} = \frac{c_p(T_3 - T_2) + c_p(T_1 - T_5)}{c_p T_1} = (1 - r^{\frac{\gamma-1}{\gamma}})\Big(1 - \frac{T_3}{T_2}\Big) \tag{1.5}$$

and can also be expressed as only a function of the thermal efficiency, the pressure ratio, and the temperature ratio, $\theta = \frac{T_3}{T_1}$:

$$SP = \eta_t(\theta - r^{\frac{\gamma-1}{\gamma}}) \tag{1.6}$$

The specific fuel consumption SFC (mass of fuel used per unit thrust force) is given by:

$$SFC = \frac{\dot{m}_f}{(\dot{m}_a + \dot{m}_f)v_e} \tag{1.7}$$

while the specific thrust (thrust per unit engine air mass flow rate) is given by:

$$ST = \frac{(\dot{m}_a + \dot{m}_f)v_e}{\dot{m}_a} \tag{1.8}$$

where $\dot{m}_f$ and $\dot{m}_a$ are the fuel and air mass flow rates, respectively, and v_e is the exit velocity of the engine's propulsive jet.

Increasing the TET by increasing the pressure ratio but maintaining the heat added at constant pressure results in an alternative cycle 'a' also shown in Figure 1.1. In this scenario, the increase in the TET (T_3) equals the increase in the compressor exit temperature (T_2). From Equation 1.4, the thermal efficiency rises with the pressure ratio (though with diminishing returns, especially since more compressor stages add more complexity and weight to the engine). This means that more of the energy of combustion q_{in} produces useful work and the jet velocity v_e will be increased. Assuming that the mass flow rates remain fixed, this would increase the thrust without changing the fuel consumption (Equations 1.7 and 1.8). However, it is clear from Figure 1.1 that the fraction of the available thermal energy which goes towards producing thrust ($4 \rightarrow 5$) rather than compression ($3 \rightarrow 4$) is reduced. Although the absolute thrust-producing work is increased, in practice the additional losses in non-ideal compressors and turbines place upper limits on the pressure ratio for optimal thermal efficiency.

Increasing the TET by increasing the heat addition results in another alternative cycle 'b' also shown in Figure 1.1. Due to the unchanged compression work and the divergence of the constant pressure curves, the specific thrust will again increase, though insufficiently to prevent the specific fuel consumption from increasing slightly due to the increased fuel requirement [10]. For an ideal cycle, since the pressure ratio is unchanged, neither is the thermal efficiency. However, for real compressors and turbines with overall compression and expansion isentropic efficiencies of η_{comp} and η_{turb}, the true thermal efficiency of the Brayton cycle is given by [11]:

$$\eta_{t,real} = \frac{\frac{1-r^{\chi}}{\eta_{comp}} + \theta(1 - r^{-\chi})\eta_{turb}}{\theta - 1 + \frac{1-r^{\chi}}{\eta_{comp}}} \tag{1.9}$$

where $r = \frac{p_2}{p_1}$, $\theta = \frac{T_3}{T_1}$, and $\chi = \frac{\gamma-1}{\gamma}$. When $\eta_{comp} = \eta_{turb} = 1$, Equation 1.9 reduces to Equation 1.4. The numerator of Equation 1.9 is the specific power output. For thermal efficiency, optimal compressor pressure ratios exist for each given temperature ratio because the losses in real compressors and turbines increase under heavier loads. Specific power optima exist even for ideal turbomachinery, because some compression is needed to achieve sufficient expansion of the heated gases through the turbines and nozzle, but too much reduces the fraction of the available heat energy extracted in the jet nozzle rather than the turbine. Both of these performance metrics can be improved by increasing the TET, as shown by the curves of $\theta = \frac{T_3}{T_1}$ in Figure 1.2. At any given temperature ratio, the thermal efficiency is always maximised at a higher pressure ratio than the specific power. This is a major reason for the higher pressure ratios in the engines of civil aircraft which favour thermal efficiency (and fuel efficiency) over the high specific power (and speed) of military aircraft.

1.2 The Role of Film Cooling

TETs in modern jet engines exceed 1700 °C [12], in stark contrast with those of both German and British WWII-era operational turbojets of approximately 780 °C [13, 14]. Modern superalloys' high melting points of around 1000 °C [12] have played one part in

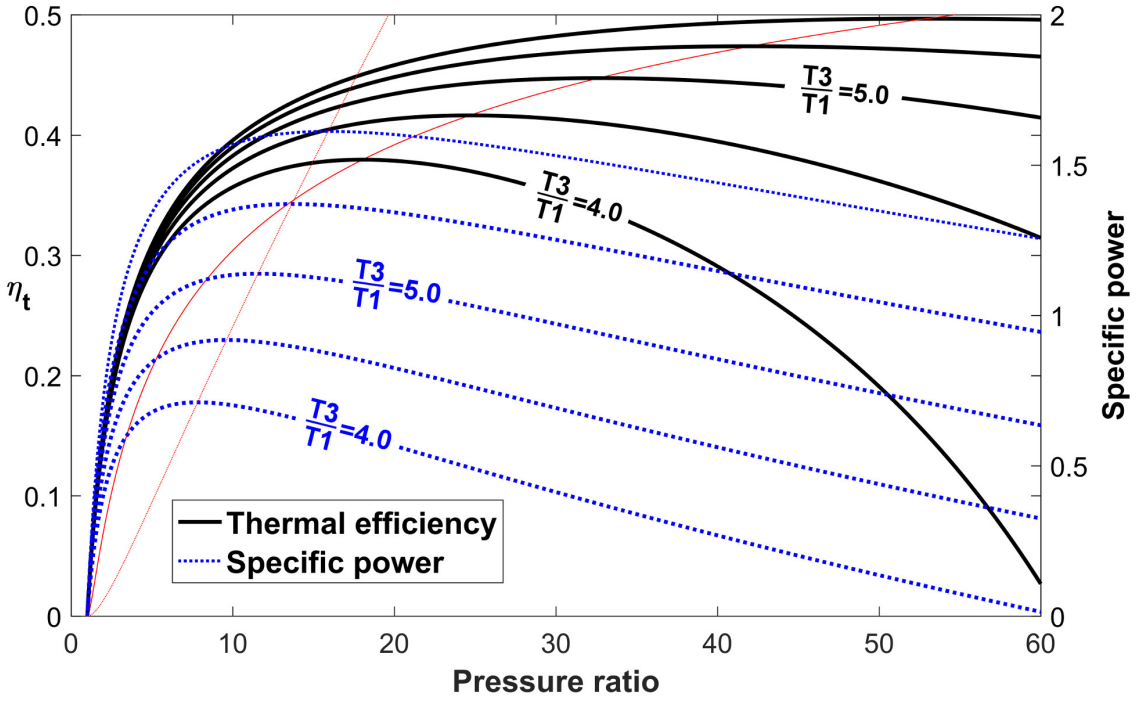


Figure 1.2: Brayton cycle thermal efficiency and specific power curves for $\eta_{comp} = \eta_{turb} = 0.9$. The fine red lines indicate the positions of the curves' respective maxima.

allowing these remarkable temperatures, though high pressure turbine aerofoils can only withstand the remaining 700 °C thanks to the implementation of internal air cooling in the 1960s, film cooling in the 1970s, and ceramic thermal barrier coatings (TBCs) in the 1980s [15, 16]. Depending on their thicknesses, TBCs typically reduce the metal-ceramic interface temperature of an air-cooled, high pressure turbine nozzle guide vane (NGV) by 200-300 °C [16]. In addition to high temperatures, turbine aerofoils must also withstand intense aerodynamic loading and, in the case of rotating blades, centrifugal forces. Failure of a single turbine component would usually involve debris causing further damage to downstream components, resulting in catastrophic failure of the entire engine. When rotating parts fail, they can be ejected at high speed through the engine nacelle, potentially also penetrating the wing[1] or even the fuselage[2]. However, thanks to extensive engineering and stringent inspection of components in the path of combustion gases, in-service failures are rare [17]. When they do occur, they are usually caused by malfunctioning auxiliary engine systems, such as an erroneously manufactured, leaking oil pipe which caused an engine fire aboard Qantas Flight 32 in August of 2010 [18].

[1] e.g. Qantas Flight 32, November 2010
[2] e.g. Southwest Airlines Flight 3472, August 2016 and Flight 1380, April 2018

Since TETs should continue to rise in order to continue to improve the fuel efficiency and specific power of gas turbine engines, cooling technology must improve commensurately so as to maintain the high levels of reliability which have come to be expected. Even without increased TETs, improved cooling technology can reduce the amount of coolant flow needed, reducing the amount of turbine work used to compress coolant. Internal turbine work is ultimately parasitic to the operation of a gas turbine, the purpose of which is to produce either thrust or external rotational work. The present studies are concerned primarily with the optimisation of aerofoil leading edge film cooling. By reducing heat flux into the TBC, films reduce the rate of TBC degradation as well as the thermal stresses in the underlying superalloy, enhancing the expected aerofoil lifetimes at a given TET. Relative to what can be achieved with internal cooling systems alone, film cooling typically reduces the aerofoil bulk temperature by approximately an additional 20% of the mainstream-coolant temperature difference [19].

1.3 Achievements and Publications of the Present Work

Film cooling of NGV leading edges is subject to particular difficulties discussed in detail in the following chapter. In brief, these are the strong propensity for coolant jets to lift off of the surface, the strong turbulence of the flow exiting the combustor, and the risk of ingestion of hot gas into the film cooling holes. The six principal achievements of the work contained herein fall into two broad categories:

1. Achievements in experimental techniques which will continue to aid turbine cooling researchers in the future:

   (a) **A spatially resolved infrared camera calibration in the presence of NGV endwall film cooling (section 4.6).** Errors in measured leading edge film effectiveness of up to 0.05 were observed when the reduced thermal emissions of a film-cooled endwall were not correctly accounted for.

(b) **A novel method for measuring film cooling effectiveness and heat transfer coefficients in a single test (section 4.7).** Unlike conventional methods, this permits the use of thin-walled test pieces with unequal initial temperatures on the film-cooled and internal surfaces.

(c) **A novel method for measuring NGV leading edge film effectiveness in the presence of non-uniform temperature profiles (section 5.2).** This permits the true contribution of experimental film cooling geometries to be determined under engine-representative conditions.

2. Achievements in directly addressing the difficulties of film cooling NGV leading edges through geometric manipulations of the cooling system:

(a) **Quantification of the enhancement by dilution port turbulence of the film effectiveness produced by lifted-off leading edge coolant jets (section 5.5.3).** High surface angle stagnation region jets can produce up to 0.2 additional effectiveness due to the turbulence produced by upstream dilution ports. Well-attached jets suffer a slight decrease in effectiveness due to the accelerated removal of coolant into the mainstream.

(b) **Quantification of the film effectiveness benefits of leading edge films which blow across the geometric stagnation line in criss-cross patterns (section 6.4).** Compared to conventional designs, the best of these arrangements can triple or quadruple the film effectiveness achieved between the two film cooling hole rows straddling the NGV's geometric stagnation line.

(c) **Quantification of the improvements to minimum hole pressure margin due to a novel geometric modification to leading edge coolant supply passages (section 7.3.3).** The modification takes the form of an insert to be attached inside existing NGVs or other cooled components. The tested inserts greatly enhanced the pressure margins of hole rows at risk of ingestion by reducing the excessive margins of other rows. Reliable predictions of insert performance were obtained with an analytical model.

These achievements have resulted in five original academic papers, as detailed below:

1. N. E. Holgate, P. T. Ireland, E. Romero. Coolant Jets Blowing Across the Airfoil Stagnation Line to Enhance Film Effectiveness. *Submitted to the Journal of Turbomachinery, paper TURBO-19-1083*, 2019.

2. N. E. Holgate, P. T. Ireland, E. Romero. An Experimental-numerical Method for Transient Infrared Measurement of Film Cooling Effectiveness and Heat Transfer Coefficient in a Single Test. *Submitted to the International Society of Air-breathing Engines (ISABE) Conference 2019, paper ISABE-2019-24211, and accepted by The Aeronautical Journal, manuscript AeroJ-2015-5186*, 2019.

3. N. E. Holgate, P. T. Ireland, E. Romero. The Effects of Combustor Cooling Features on Nozzle Guide Vane Film Cooling Experiments. *ASME TurboExpo 2018 (received a Best Paper Award in the Heat Transfer category), paper GT2018-75249, and Journal of Turbomachinery, paper TURBO-18-1217*, 2018.

4. N. E. Holgate, P. T. Ireland, K. Self. Nozzle Guide Vane Film Cooling Effectiveness for Radial Showerheads with Restricted Cooling Hole Surface Angles. *ASME TurboExpo 2017, paper GT2017-64645*, 2017.

5. N. E. Holgate, I. Cresci, P. T. Ireland, A. Rawlinson. Prediction and Augmentation of Nozzle Guide Vane Film Cooling Hole Pressure Margin. *12th European Conference on Turbomachinery, Fluid Dynamics and Thermodynamics (ETC), paper ETC2017-128*, 2017.

Chapter 2

Literature Review

In this chapter, a summary is given of the most important past academic findings on nozzle guide vane film cooling, with a special focus on the leading edge. This further establishes the context of the research by outlining the fundamental challenges facing designers of film cooling systems. Information regarding previous work on more specific issues considered within the scope of the present work is given towards the start of the relevant chapters.

2.1 Fundamentals of Film Cooling

Although operational turbine metal temperatures depend upon the combined effects of external film cooling and internal cooling, in the first instance turbine cooling researchers and designers usually separately assess the benefits of each. The basic principle underlying the success of film cooling is that lower gas temperature adjacent to a surface reduces the temperature difference between the surface and the surrounding hot gas, hence reducing the driving potential for heat transfer into that surface. This is achieved by injecting relatively low temperature air (typically sourced from the exit of the final compressor stage) from holes in the surface to be cooled. This produces regions of air near the surface with some mixing-dependent distribution of temperatures intermediate to the hot gas and coolant temperatures. Heat is transferred from air to metal predominantly by conduction, but this is nevertheless modelled with a convective heat transfer coefficient,

h, which is inversely related to the thermal boundary layer thickness:

$$h = \frac{q''}{T_{ref} - T_s} \tag{2.1}$$

where q'' is the local surface heat flux per unit area and T_s is the surface temperature. T_{ref} is a reference hot gas driving temperature which varies over the surface, mainly due to its mixing with the film coolant. By convention, the reference temperature distribution used is the adiabatic wall temperature, T_{aw}. This is a theoretical temperature distribution which would occur if the cooled surface were perfectly adiabatic i.e. zero conductivity. It can be measured as the surface temperature distribution on a film-cooled test piece with very low thermal conductivity. This convention standardises experimental film cooling results which would not be comparable across test pieces with varying thermal conductivities. To account for the variations in driving temperatures between different experiments and engine conditions, the adiabatic wall temperature is nondimensionalised as the film cooling effectiveness:

$$\eta = \frac{T_\infty - T_{aw}}{T_\infty - T_c} \tag{2.2}$$

where T_∞ and T_c are the mainstream and film coolant reference temperatures, respectively. Ideally, no mixing with the mainstream would occur and metal-adjacent fluid of temperature $T_{aw} = T_c$ would reduce the thermal potential across the entire surface by as much as is possible with the given air source temperatures ($\eta = 1$). Since mixing is inevitable and complex, a surface distribution of η is sought, whose values can vary between unity and zero (for regions entirely unaffected by the film cooling, with $T_{aw} = T_\infty$). The effectiveness is sensitive to many flow variables including jet-to-mainstream mass and momentum flux ratios and mainstream flow pressure gradients and turbulence, as well as surface geometry parameters like curvature, roughness, hole shape and ejection angle. While the thermal potential ($T_{aw} - T_s$) is decreased by film cooling, the heat transfer coefficient increases because of increased turbulence caused by wakes behind jets, interactions between jets, and shear layers with the mainstream flow. Hence, a film cooling configuration must ultimately be evaluated in terms of a distribution of net surface heat

flux reduction, defined as:

$$\Delta q_r = 1 - \frac{q''}{q''_0} = 1 - \frac{h(T_{aw} - T_w)}{h_0(T_\infty - T_w)} \approx 1 - \frac{h}{h_0}\left(1 - \frac{\eta}{\phi}\right) \tag{2.3}$$

where q''_0 and h_0 are respectively the surface heat flux per unit area and the heat transfer coefficient for the same geometry but with no film cooling. The final result is a close approximation (as shown by Sen et al. [20]) in which ϕ is the nondimensionalised metal surface temperature, which depends also upon any internal cooling and TBC which may be present:

$$\phi = \frac{T_\infty - T_s}{T_\infty - T_{ci}} \tag{2.4}$$

Since the metal temperature is the fundamental engineering concern in turbine cooling, it is also known as the overall effectiveness. The temperature of coolant entering the internal cooling passages, T_{ci}, is lower than that of the exiting film coolant, T_c, because of heat transfer from metal to coolant due to internal cooling mechanisms. Because film cooling experiments are usually conducted without any internal cooling, this parameter is not measured, and is instead often estimated as the typical operational, film cooled turbine aerofoil value of $\phi = 0.6$ [20, 21].

2.2 Film Cooling Dimensionless Parameters

To permit comparison of results between different experimental setups and to apply them to real engine conditions, the film cooling literature almost ubiquitously expresses coolant jet flow conditions with two particular dimensionless parameters: the coolant-to-mainstream mass flux ratio, commonly known as the 'blowing ratio':

$$M_{hole} = \frac{\rho_c v_c}{\rho_\infty v_{\infty,hole}} \tag{2.5}$$

and the density ratio:

$$DR = \frac{\rho_c}{\rho_\infty} \tag{2.6}$$

The blowing ratio determines the coolant mass flow rate relative to that of the mainstream, and is hence dominant in determining the distance that coolant jets penetrate into the mainstream. v_c and $v_{\infty,hole}$ are the coolant and mainstream flow velocities, respectively, at the exit of a given film cooling hole. This makes the blowing ratio on an aerofoil a strong function of the streamwise position of the hole in question, since the mainstream velocity varies radically, especially on the suction side. An average blowing ratio is often used to nondimensionalise the coolant mass flow rate to the entire cooled aerofoil (or leading edge):

$$M = \frac{\dot{m}_c}{\rho_\infty v_\infty A_h} \tag{2.7}$$

where $\dot{m}_c$ is the overall mass flow rate of film coolant, A_h is the combined area of all the minimum cross sections of holes in the test piece, and v_∞ is the mainstream bulk velocity approaching the cooled component. Thole and Bogard [22] showed that the momentum flux ratio:

$$J = \frac{\rho_c v_c^2}{\rho_\infty v_\infty^2} \tag{2.8}$$

is in fact superior for predicting the attached/detached state of film cooling jets with an arbitrary density ratio. On a flat plate with a single row of cylindrical, 35° surface angle, streamwise-blowing holes, for $J < 0.4$ the jets remain attached, for $0.4 < J < 0.8$ the jets detach then reattach downstream, and for $J > 0.8$ the jets remain detached. Nevertheless, this parameter has remained less widely used than the blowing ratio in film cooling literature.

The density ratio has a second-order but non-negligible effect on the behaviour of the films. Drost and Bölcs [23] found that higher density ratio coolant reduces its momentum at a given mass flow rate, reducing lift-off. Similarly, Pietrzyk et al. [24] found that for a given blowing ratio, higher density coolant tends to penetrate less far, and entrains less hot mainstream gas. Due to the prohibitive costs of experiments with engine-realistic air temperature ratios, experimentalists seeking to approximate correct density ratios typically employ a heavier-than-air coolant gas (frequently carbon dioxide).

2.3 Comparisons of Film Cooling on Static and Rotating Aerofoils

The challenges of film cooling static components such as high pressure turbine NGVs differ slightly from those of cooling rotors. NGVs are subject to both radial and circumferential variations in their inlet hot gas temperature profile, whereas rotors spin much too quickly to respond to the circumferential variations. NGVs also experience hotter gas temperatures owing to their location immediately downstream of the combustor; considerations of typical NGV coolant mass flow rates suggest a reduction to the mass-averaged rotor hot gas temperatures on the order of 100 K. Furthermore, since the rotor velocity, U, is in the same direction as the whirl velocity of the incident flow, v_θ, the stagnation temperature in the rotor frame of reference is reduced by approximately 10% according to:

$$T_{0,rel} = T_0 - \frac{U^2}{2c_p}\left(\frac{2v_\theta}{U} - 1\right) \tag{2.9}$$

However, unlike blades, NGVs are not subject to the interference of centrifugal forces in the behaviour of film coolant. Takeishi et al. [25] measured significant reduction in film cooling effectiveness on the pressure side of a turbine blade undergoing rotation, but little change on the suction side. Ahn et al. [26] showed experimentally that a significant factor in determining leading edge film cooling performance for rotating blades is the rotational speed, due to its influence on the mainstream flow incidence and hence the stagnation line position, which significantly alters the proportions of leading edge coolant travelling to each side of the blade.

2.4 Coolant Jet Lift-off

Higher blowing ratios have the potential to enhance area-averaged cooling effectiveness because of the greater amount of coolant relative to mainstream flow. However, beyond a point, higher blowing ratios tend to reduce cooling effectiveness (despite the increased coolant mass flow rate) because the jets lift off of the cooled surface and entrain mainstream fluid below themselves. The primary mechanism for these phenomena is the pres-

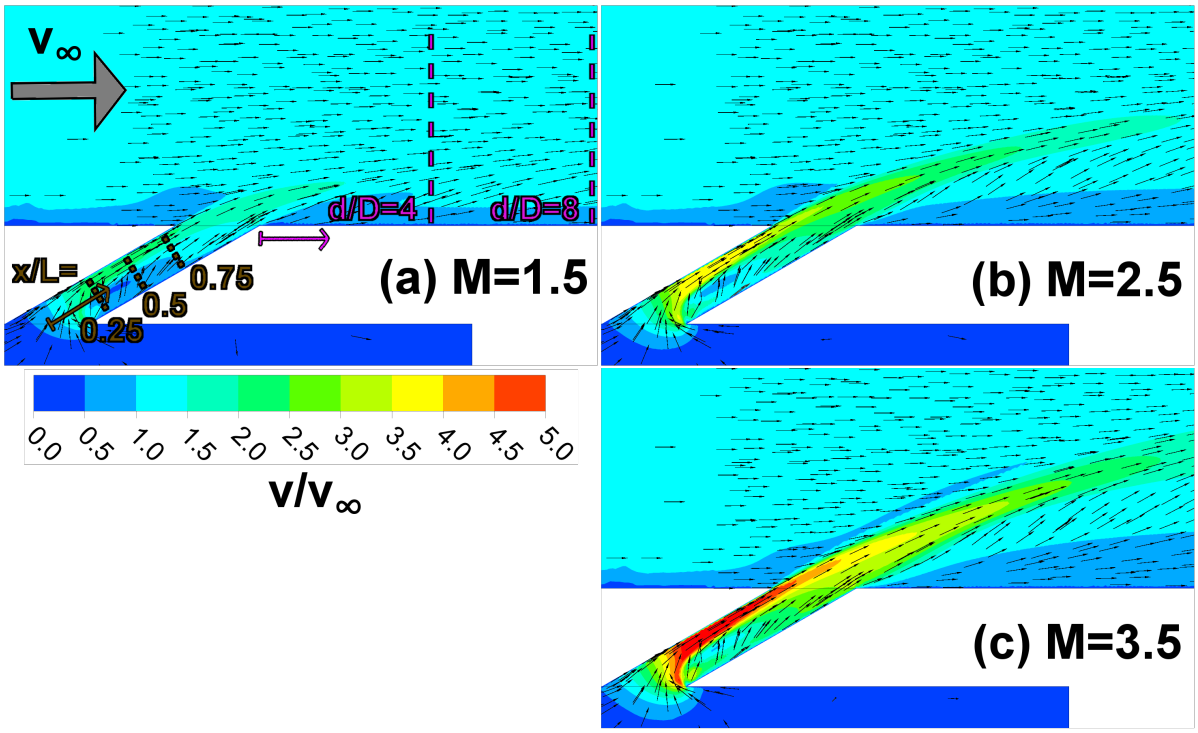


Figure 2.1: RANS CFD results showing absolute flow velocity contours and directional arrows for a single, streamwise-blowing film cooling hole at three blowing ratios. The planes interrogated in Figures 2.2 and 2.3 are indicated.

ence of counter-rotating 'kidney vortices' on the underside of the jet, illustrated in the author's CFD results of Figures 2.1 to 2.3 for the streamwise-inclined cooling hole in Figure 2.1. In these simulations, the $k-\epsilon$ turbulence model with enhanced wall functions was used. The mesh consisted of unstructured, tetrahedral elements with refinements near the hole inlet, in the coolant jet path, inside the hole, and adjacent to the hole wall, resulting in a total element count of approximately 10.9 million. A mesh independence study was not conducted since the intention was merely to qualitatively replicate the results of previous CFD studies in the literature.

Leylek and Zerkle [27] first published the results of similar RANS CFD simulations and showed that the acute angle formed in the blade material where the hole meets the coolant plenum acts as a separation point, causing a region of slow-moving air on the side of the cooling hole which is downstream with respect to the mainstream flow (for a streamwise-inclined hole such as in Figure 2.1). This fluid forms counter-rotating vortices within the hole itself, which grow to fill more of the hole as they travel toward its exit, and which

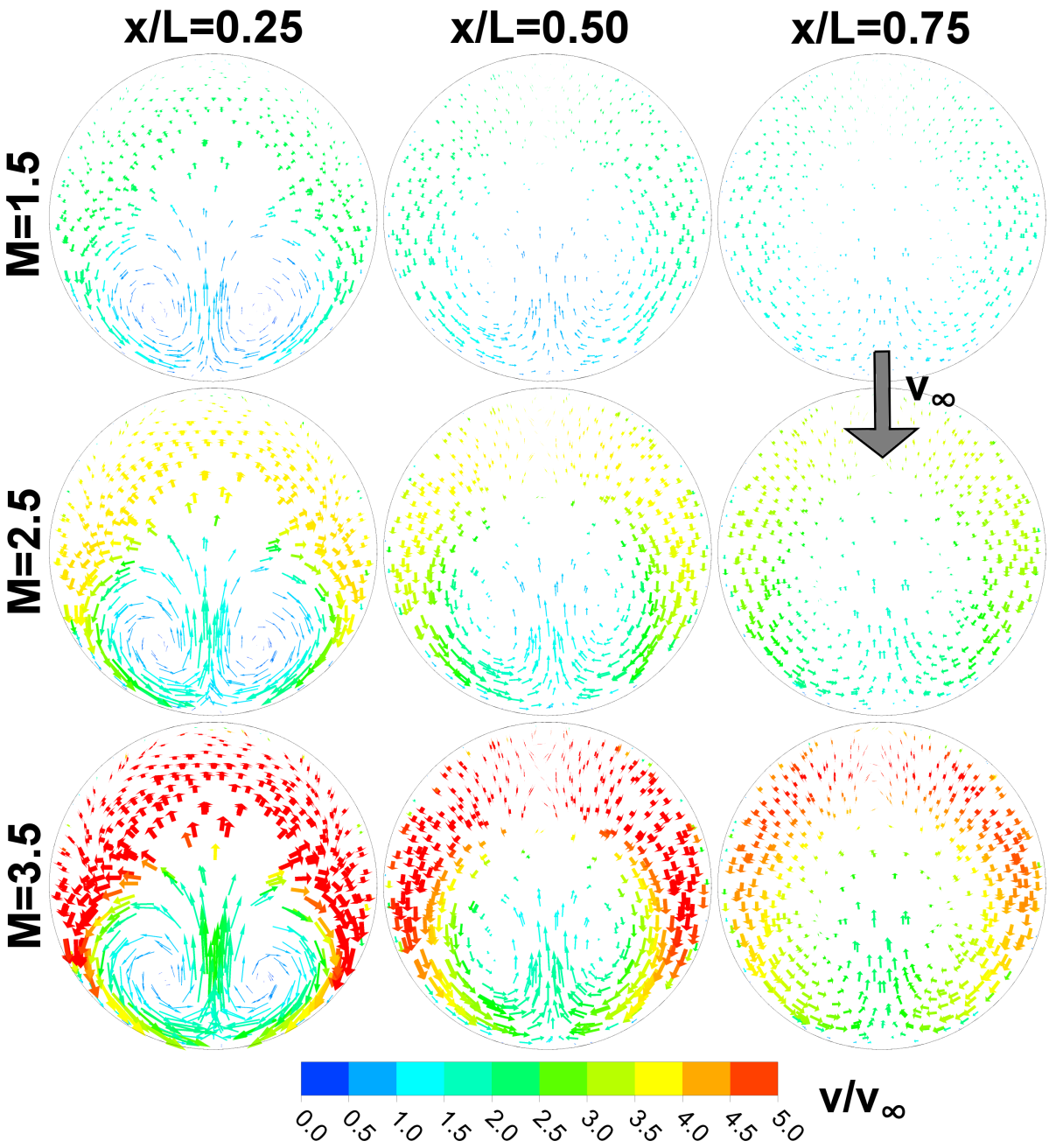


Figure 2.2: RANS CFD results showing growth of vortices within a streamwise-blowing film cooling hole at three blowing ratios. x is the distance along the hole centreline from the hole inlet, and L is the hole length.

are stronger for higher blowing ratios (see Figure 2.2). These vortices cause the rest of the fluid to accelerate as it proceeds up the hole due to the increasing effective blockage presented by the slower fluid. The velocity gradient at the interface of the vortices and the faster, 'jetting' fluid generates high turbulence intensities, and at high blowing ratios, this turbulence generation is greater than that between the mainstream flow and the expelled coolant jet, which reduces as the jet and mainstream velocities equalise. Since the length-

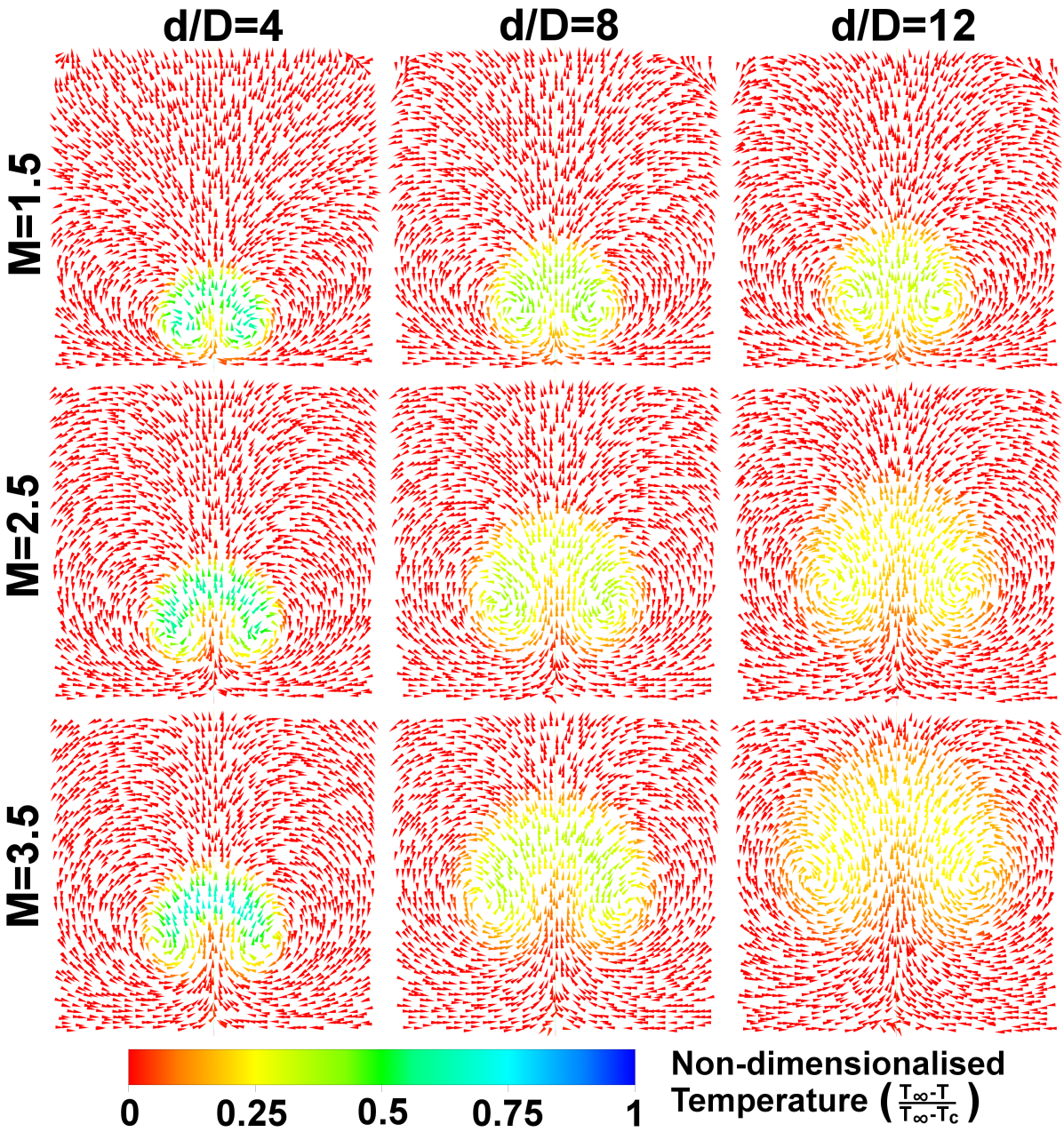


Figure 2.3: RANS CFD results showing development of counter-rotating kidney vortices downstream of a single, streamwise-blowing film cooling hole at three different blowing ratios. d is the distance downstream from the hole exit's downstream edge and D is the hole diameter.

to-diameter ratio of most film cooling holes is low, the flow in the pipe does not have time to become fully developed, and so these features influence the ejection of coolant from the end of the hole. The high momentum jetting fluid towards the upstream of the hole exit tends to lift off over the slower blockage fluid. Walters and Leylek [28] showed that the vorticity within the cooling holes is the origin of the kidney vortices which draw hot mainstream flow underneath coolant jets, reducing their film effectiveness even when

they are attached to the surface. Figure 2.3 shows the predicted evolution of the kidney vortices downstream of the film cooling hole illustrated in Figure 2.1 for three different blowing ratios. Lower blowing ratio jets lift off less, expand less in cross section, and entrain less mainstream gas (as evidenced by the lower jet core temperatures achieved at locations far downstream of the cooling hole). When film coolant injection is not purely streamwise, the kidney vortices formed are asymmetrical.

2.5 Hole Geometry

2.5.1 Hole Position, Spacing, and Angling

Film cooling holes are arranged in streamwise consecutive rows, since single rows usually produce film effectiveness which rapidly decays downstream as coolant mixes with the hot mainstream, and because too many holes in a single row may compromise structural integrity [15]. The distance between corresponding points of two holes within a row is known as the pitch, and this is often maintained or at least similar along an entire row. The holes in each alternate row may be slightly offset from those of its neighbours in the direction perpendicular to the mainstream flow (spanwise). This permits individual film coolant jets to pass between downstream jets, increasing their residence time close to the cooled surface and contributing to the formation of a cohesive film. The optimal amount of this offset, known as 'stagger', depends on the path of the jet, in turn determined by the hole shapes and angles, as well as the blowing ratio. Holes close to the leading edge of an aerofoil tend to be angled relative to the streamwise direction (known as the compound angle), often by as much as 90° (known as radial film cooling holes). This helps to spread the local coolant in the spanwise direction (i.e. laterally), preventing regions between holes from being entirely neglected due to the absence of any upstream coolant ejection. Farther downstream, the holes tend to be oriented streamwise. Goldstein and Jin [29] showed that compound angling delays film lift-off compared to streamwise injected jets. The angle between the central line through the hole and the cooled surface is known as the surface angle, which is crucial in determining the component of jet momentum away from the surface, and hence the propensity for jet lift-off.

Cresci et al. [30] investigated two rows of cylindrical, staggered, endwall film cooling holes injecting streamwise at a 45° surface angle, and measured the downstream velocity and turbulence profiles for three different hole pitches. They found that lower pitch holes produce greater near-wall momentum which persists farther downstream because of reduced mixing with the mainstream flow when jets merge to create a cohesive film. As a result, subsequent rows have suppressed jet lift-off because of the increased local mainstream mass flow rate and hence reduced local blowing ratio. Lower pitch holes reduced the distance of peak turbulence intensity from the endwall, and increased the decay of intensity downstream.

2.5.2 Hole Shape

The most studied and simplest to produce film cooling holes are cylindrical. Many variations have been proposed and tested, with the most common used in practice being the 'fan-shaped', laterally diffusing exit hole. The holes may also diffuse slightly in the streamwise direction. Diffusing hole shapes reduce the coolant jet exit velocity, which discourages lift-off at any given blowing ratio (which can be compared fairly to cylindrical hole blowing ratios on the basis of equal coolant mass flow rates), improving film effectiveness [31, 32]. Their wider exits also spread the ejected coolant over a wider tract of the cooled surface. Despite these benefits, diffusing holes have not been universally adopted and are usually only employed in certain regions of a turbine aerofoil, due to their increased manufacturing costs and potentially reduced component structural integrity. For example, due to their higher exit velocities, radially blowing cylindrical holes in the low mainstream momentum leading edge region can achieve the same amount of lateral spreading of the local coolant with a lower density of holes. The benefits of fan-shaped cooling holes can also apply to compound-angled cooling holes [33, 34]. If fans are too wide, separations may occur within the hole exits, causing imperfect coolant spreading and increased heat transfer coefficients which can more than offset the effectiveness gains [35].

Another cooling geometry often used to cool pressure side trailing edges is the slot, which provides still superior coolant coverage via a spanwise line of coolant discharge which is essentially uninterrupted except for nearby periodic, mechanically supportive walls [36, 37]. Sargison et al. [38] proposed a row of cylindrical holes which converge together into a slot at a shared exit, enhancing the mechanical strength compared to conventional slots. Other geometric variations which have been researched include entrenched hole exits [39], 'arrowhead-shaped' hole exits with streamwise diffusion only on their sides [40], cylindrical holes with triangular tabs protruding over their downstream edges [41], reverse-blowing holes [42], vortex suppression holes injecting additional coolant with opposed vorticity (small holes branching from each main film cooling hole [43], or unique holes with opposite but equal compound angling [44]), and intersecting film cooling holes which create additional pressure losses and increase internal heat transfer [45, 46].

2.6 Leading Edge Film Cooling

In order to achieve adequate local film coolant coverage, a greater density of film cooling holes is required at an aerofoil's leading edge than at surface locations downstream, because of the absence of coolant accumulated from upstream cooling holes. This region of densely packed holes is known as the 'showerhead' and typically consists of six to eight closely spaced rows of cylindrical film cooling holes ejecting radially [15]. The challenge of providing sufficient cooling is further exacerbated by the low mainstream flow momentum in the stagnation region, which increases the local effective blowing ratios and hence the amount of coolant jet lift-off. This situation is illustrated in Figure 2.4, which presents the results of a reduced-domain (only the four most upstream hole rows) leading edge film cooling simulation detailed in section 6.3. Velocity vectors in a plane orthogonal to the spanwise direction of the NGV split around the leading edge stagnation line, and their magnitudes are very low nearby it. Coolant jet temperature contours from the first pressure side row of film cooling holes show the relatively high surface angle radial jets lifting off under these conditions and rapidly mixing with the hot mainstream. Coolant streamlines show the partial return of coolant to the surface farther downstream by the accelerating mainstream, especially on the suction side.

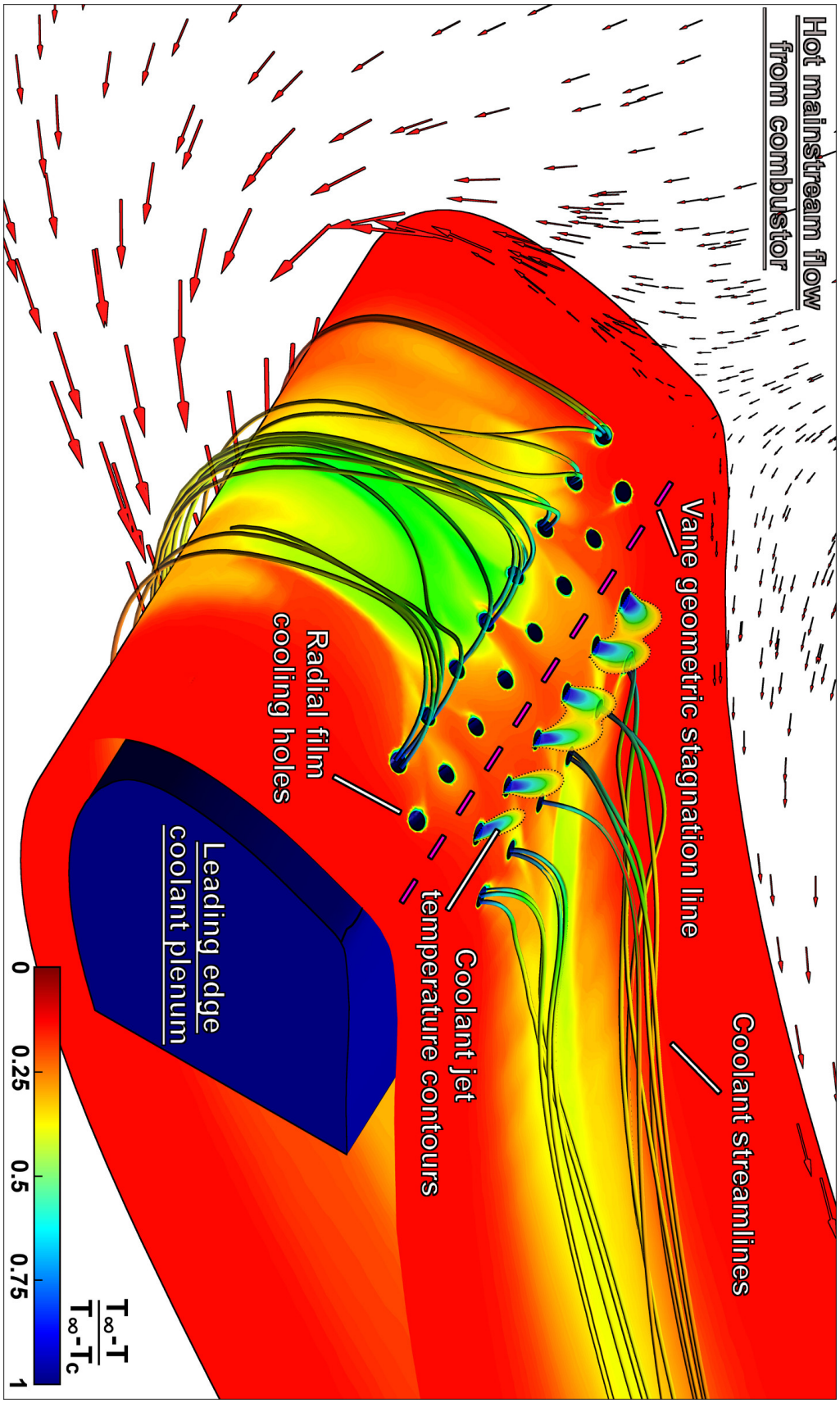


Figure 2.4: Results of a RANS CFD leading edge film cooling simulation performed by the present author. Owing to the significant lift-off of the modelled stagnation region coolant jets, the local and downstream NGV surface temperatures are well above the coolant feed temperature.

Cutbirth and Bogard [47] investigated a film-cooled NGV geometry and found that a dense, six-row showerhead of radial holes with 25° surface angles produced a step rise in local film effectiveness between two of the tested blowing ratios, due to the formation of a cohesive film after the jets acquired sufficient momentum to interact with those from laterally adjacent holes. The effectiveness continued to improve even for very high blowing ratios. Elevated turbulence intensity caused a reduction in the effectiveness at and nearby the showerhead, since increased mixing with the hot mainstream increases the temperature of the coolant film.

Semi-circular leading edges with flat afterbodies and zero angle of attack were once frequently used to approximate the mainstream flow conditions around real aerofoil leading edges, though more recently have become less common owing to the limited engine-realism of the flow except very close to the geometric stagnation line. Mick and Mayle [48] presented film effectiveness distributions on such a geometry with two rows of staggered, radial film cooling holes just downstream of the stagnation line on one side. In contrast with the results of Cutbirth and Bogard, the spanwise averaged effectiveness downstream of the showerhead was reduced at the higher tested blowing ratios, owing to increased jet lift-off. Film effectiveness gains were not realised because of the reduced density of showerhead holes (row count and spacing) and unrealistic mainstream flow pattern. This demonstrates the importance of a high density of radial holes at the leading edge for achieving good local film cooling, and the importance of realistic aerofoil geometry (especially for measurements of the downstream effects of leading edge film cooling). Mehendale and Han [49] performed a similar semi-circular leading edge study considering also the effects of elevated mainstream flow turbulence. They confirmed that the effectiveness of leading edge coolant more rapidly decreases downstream in the presence of higher freestream turbulence. They also showed that, even for turbulence levels around 12% (slightly lower than expected at the combustor-turbine interface), the additional turbulence due to film cooling on the leading edge is small and thus no longer greatly increases the heat transfer

coefficient beyond its uncooled values. This fact is the reason why the strongly interacting arrangement of radial jets is acceptable and widely used on NGV leading edges – it provides relatively high effectiveness with little additional augmentation of heat transfer coefficient given the highly turbulent mainstream flow from the combustor.

2.7 Mainstream and Surface Effects

The higher velocities of suction side mainstream flow significantly reduce the local blowing ratios of suction side jets (though the lower exhaust pressures also slightly increase the coolant jet mass flow rates, partially offsetting this). This means that these jets tend to stay well attached compared to pressure side jets. Increasing the aerofoil coolant mass flow rate tends to decrease suction side effectiveness as a slightly greater amount of coolant will escape from the surface as the jet exit velocities increase. However, the pressure side jets which tend to be already substantially escaping the surface achieve higher effectiveness because of the increased coolant mass flow rate, especially where the jets blow towards the surface by virtue of its concave curvature. These facts were demonstrated experimentally by Ito et al. [50].

Turbulence is well known to have a significant effect on heat transfer to solid surfaces, because of its role in increasing the near-wall fluid temperatures via increased mixing with the mainstream flow. Ames [51] investigated the effects of turbulence parameters on NGV heat transfer, finding that both increased turbulence intensity and turbulence length scale can significantly increase the heat transfer, particularly on the leading edge and pressure side. Van Fossen et al. [52] investigated heat transfer on NGV leading edges and found that, compared to isotropic turbulence, anisotropic turbulence increases heat transfer by up to 33% in the stagnation region. Jumper et al. [53] showed that mainstream turbulence levels of the order expected at the outlet of an annular combustor have little effect on the film effectiveness immediately downstream of a cooling hole on a flat plate, but that the increased mixing between the film and mainstream causes a decay in effectiveness as the film proceeds downstream. Later, Schmidt and Bogard [54] showed that the extent to

which the effectiveness near the hole and farther downstream is diminished by increased mainstream turbulence depends upon the momentum flux ratio. The optimal momentum flux ratio increases for a more turbulent mainstream, because of the improved transportation of coolant back to the surface. Saumweber et al. [55] investigated the effects of mainstream turbulence intensity on the film cooling performance of both cylindrical and fan-shaped holes in a single row on a flat plate. They found that elevated turbulence reduced the film effectiveness due to cylindrical holes, except above a critical blowing ratio, after which effectiveness was increased. This is attributed to the greater lateral spreading of coolant jets and a return of lifted-off coolant back to the surface. Across the same range of blowing ratios, fan-shaped holes only exhibited effectiveness reductions because the jets from the entire row were already laterally dispersed to the extent that they coalesced, and did not sufficiently lift off to benefit from the turbulence-enhanced return of coolant back to the surface. Drost and Bölcs [23] found that mainstream flow turbulence has only small effects on suction side film effectiveness and heat transfer coefficient. However, in the presence of high mainstream flow turbulence, surface roughness on the suction surface can trigger an earlier boundary layer transition to turbulence, increasing heat transfer [56]. On the pressure surface, for sufficiently low coolant jet momentum, heat transfer coefficient decreases and effectiveness increases with increased mainstream turbulence intensity because of increased coolant diffusion within the boundary layer [23], and surface roughness introduces little additional heat transfer [12]. During long-term gas turbine operation, a gradual increase in the roughness of the thermal barrier coating (known as spallation) on an aeroengine NGV can result due to the combined effects of frequent thermal cycling and deposition of ingested particles [57].

2.7.1 Combustor-Turbine Interactions

In a real gas turbine engine the actual mainstream flow conditions at the inlet to the nozzle guide vanes are determined by features of the combustor; in particular, the dilution port and endwall film coolant flows. The inlet profiles of temperature and turbulence produced are typically highly non-uniform. Dilution port flows are responsible for controlling the

heat release which takes place centred on the combustor's discrete fuel injectors, and as such they tend to produce colder and higher turbulence intensity regions at the vane inlet which are equally spaced around the circumference of the annulus and biased towards the midspan [**?**, 58]. Aside from increasing the near-endwall turbulence and providing film cooling, the additional flow momentum due to the injection of endwall film coolant just upstream of the vanes eliminates classical cross-passage vortices [59]. These vortices would otherwise disturb the near-endwall suction side film coolant. Instead, the endwall coolant washes the near-endwall vane surfaces, reducing or eliminating the need for vane films in these regions. Some additional findings from various recent combustor-turbine interactions experiments are discussed in section 3.1 as a prelude to the introduction of the experimental wind tunnel used in the present studies which features both combustor dilution ports and endwall film cooling.

2.8 Computational Modelling of Film Cooling

2.8.1 Reynolds-Averaged Navier-Stokes Studies

Due to the importance of jet trajectory and mixing with the mainstream for film cooling performance, Reynolds-Averaged Navier–Stokes (RANS) CFD predictions can be highly sensitive to the turbulence model employed during calculations. These CFD predictions tend to be poor, and even in the simplest case of a flat plate with a single, streamwise cylindrical hole, the lateral spreading of coolant is usually under-predicted, while the centreline cooling effectiveness is over-predicted. Nevertheless, the cancellation of these two errors frequently yields a good laterally averaged film effectiveness prediction [15]. Ferguson et al. [60] compared various turbulence models and near-wall treatments with experimental results, finding that in general the case of a separated jet is especially poorly modelled by RANS. Just downstream of the cooling hole, centreline film cooling effectiveness is greatly overestimated by all $k - \epsilon$ turbulence model wall function treatments, though results similar to those from experiments are obtained farther downstream than about 15 hole diameters. The use of a two-layer zonal model instead of a wall function reduced the

overestimation but still did not capture the characteristics of the experimental data near the cooling hole. No models successfully predicted experimental heat transfer coefficients along the entire centreline.

The earliest CFD simulation of leading edge film cooling in the open literature appears to be the 1995 study of He et al. [61]. The semi-cylindrical leading edge featured two rows of staggered, 30° surface angle radial cooling holes to each side of the stagnation line, and the authors used a $k - \epsilon$ turbulence model with wall functions. The mainstream inlet turbulence intensity was 0.5%, and a coolant inlet plenum was not modelled. Rather, a velocity was specified at an internal cross section of each individual cooling hole which gave blowing ratios to match those of a prior experiment conducted on the same geometry [62]. The pressure gradient around the leading edge caused non-uniform flow at the cooling hole exits, with the effect being stronger at the forward row where the gradient is stronger. Radial injection formed smaller vortices farther downstream from the cooling holes and farther away from the cooling surface than did simulated streamwise injection, reducing coolant lift-off. For the lower of two blowing ratios tested, the coolant from the first row passed between the holes of the next, resulting in better film coverage than when an increased blowing ratio sent this coolant towards the second row holes. The CFD film cooling effectiveness results agreed better with experimental results in the case of the low blowing ratio, suggesting that accuracy is reduced when more jet interaction is modelled.

2.8.2 Large Eddy Simulation Studies

Improved predictions can be made with the significantly more computationally intensive Large Eddy Simulation (LES). The two-part study of Rozati and Tafti [63] also differs from that of He et al. in their use of a cooling geometry with only one row of 30° spanwise inclined cooling holes on each side of a cylindrical leading edge. Rather than utilising a symmetry condition about the stagnation line, the full geometry is simulated and flow properties at equivalent positions near the surface on either side of the leading edge are cross correlated. This serves as a test which affirms the assumption implicit in experi-

ments and simulations with only half of the domain, that coolant-mainstream interactions on one side of the leading edge are unaffected by the dynamics on the other side with respect to effectiveness and heat transfer coefficient measurements and predictions. By employing two different coolant feed turbulence profiles, it is shown that the nature of the NGV-internal coolant flow can affect the quality of the NGV-external film cooling predictions. When the feed coolant turbulence levels were unrealistically low, the spanwise averaged cooling effectiveness was overpredicted, as was the extent of the region of very high effectiveness emanating from the hole leading edge. Examination of temperature profiles downstream of the hole suggests that this may be due to unrealistically successful diffusion of coolant back towards the cooled surface for the case of unrealistically low inlet coolant turbulence. They also observed that in the presence of unsteady jet-mainstream interactions, the stagnation line is not stationary as is commonly assumed. However, the motion of the stagnation line is on time scales too long compared to the turbulence time scales for complete simulation to be feasible.

In a study of the effects of blowing ratio on particle deposition onto NGV leading edges, Sreedharan and Tafti [64] simulated with LES another cylindrical leading edge with radial cooling holes with 45° surface angles, with a row on the geometric stagnation line and one row to each side, at a range of blowing ratios. They found that increasing the blowing ratio at the stagnation line reduced the spanwise averaged adiabatic effectiveness because of increased jet penetration into the mainstream, but contributed to increasing the effectiveness farther downstream because of the coolant being redirected onto the surface by the mainstream. The same effects were observed at the second row.

2.8.3 Hybrid and Direct Numerical Simulation Studies

Sakai et al. [65] modelled a semi-cylindrical leading edge with a flat after-body and two rows of staggered, 30° surface angle radially inclined cooling holes on either side. They used RANS with three different variants of the $k - \omega$ turbulence model, as well as Detached Eddy Simulation (DES), which is an LES approach employing, in this case, a

Spalart-Allmaras RANS turbulence model in the near-wall region (the first practical usage of such a technique appeared in the study of Shur et al. [66] of a high angle of attack aerofoil). All three RANS implementations gave very similar laterally averaged film cooling effectiveness results, and more closely resembled previous experimental results than did the DES. However, DES achieved better results on the hole centreline farther downstream than 5 hole diameters, where pure RANS models significantly overestimated the effectiveness. DES also better modelled the far-downstream lateral spread of coolant and hence the lateral effectiveness distributions. This is also strongly represented in the spanwise cross-sectional temperature distribution results, which show an unrealistically round jet of coolant downstream of the hole. Visualisation of the corresponding cross-sectional velocity fields shows that, unlike DES, the RANS models did not capture the vortices responsible for lateral coolant transport.

Voigt et al. [67] compared RANS, Unsteady RANS (URANS), and Scale-Adaptive Simulation (SAS, which selectively switches to LES-like behaviour in unsteady flow regions) to experimental results for a single reattaching jet from a cylindrical hole. Of the three tested RANS turbulence models, the best was $k - \epsilon$ Explicit Algebraic Reynolds Stress Model which had velocity errors of less than 20%. URANS and SAS unsteady models were able to improve velocity errors to below 10%, since the three-dimensional unsteadiness of the jet-in-crossflow is better captured by these methods, which are also almost 100 times more computationally demanding. Direct Numerical Simulation (DNS) CFD is far more demanding still and is hence the most rarely used in film cooling simulations. However, its additional accuracy can nevertheless make it useful for studying effects unlikely to be adequately captured by RANS, LES, or their derivatives. Muldoon and Acharya [68] used DNS to investigate the effects of sinusoidal pulsing of the film coolant delivery. Pulsing at higher frequencies was found to reduce the turbulence generated in the wake behind the jet and hence to improve the film effectiveness compared to the case of constant blowing ratio. Fluctuating and constant blowing ratios are compared on the basis of time-averaged coolant flow rate.

In addition to unsteadiness, simulations of film cooling for design purposes must also contend with additional flow complexity from sources such as mainstream flow turbulence, endwall secondary flows, and aerofoil curvature. Due to inaccuracy in the modelling of the turbulent kidney vortices, lift-off of the coolant jet may not be captured, resulting in drastic overestimation of the film cooling effectiveness immediately downstream of the hole, such as in the study of Leylek and Zerkle [27]. Conjugate CFD models attempting to compute cooled aerofoil metal temperatures typically also simulate the flow through internal cooling features in order to accurately capture internal heat transfer, compounding the modelling challenges and computational requirements. In a study by Chandran and Prasad [69], the metal temperature of an NGV leading edge with showerhead film cooling and internal impingement cooling was modelled with a finite element mesh informed by internal and external RANS CFD flows. Even the spanwise averaged results for dimensionless metal temperature differed by up to 6% from the authors' corresponding experimental results, suggesting still greater localised CFD prediction errors. Despite the ongoing limits to the viability of CFD as an accurate, independent design tool for aerofoil cooling systems, it has yielded a great deal of information about the mechanisms which underlie fundamental coolant behaviour.

2.8.4 CFD Strategy of the Present Work

Given the experimental apparatus and aims of the present work, CFD techniques more time-consuming and computationally intensive than RANS were not viable. However, as has been seen, RANS performs poorly in the prediction of film behaviour even for much simpler geometries than the cooled leading edges considered in the present work. It also performs poorly in the prediction of cooling hole discharge coefficients, as discussed in section 7.4. Therefore, quantitative validation of CFD results was not pursued, and RANS CFD was used primarily with the goal of supplementing various experiments by providing qualitative insights into the relevant flows.

2.9 Conclusions from Existing Literature and Contributions of the Present Work

The film effectiveness and heat transfer coefficient are frequently measured with techniques requiring two separate experiments and reliant on an assumption of a sufficient material thickness which may prevent their use on certain experimental geometries. Among the present work's contributions is an infrared, single-experiment technique for determining both of these film cooling performance parameters for essentially any film-cooled geometry, regardless of material thickness. The calibration procedure for the infrared measurements is novel in its accounting for the variation across the observed surface of extraneous, reflected infrared radiation. This variation is caused by the non-uniformities of temperature and material thermal emissivity within sophisticated wind tunnel experiments such as combustor simulators.

Among the many possible film cooling hole geometric concepts, holes which blow in reverse against the mainstream have received fairly considerable attention in recent academic literature. This study proposes and investigates a novel usage of such holes in which they are placed in two rows near to but on opposite sides of the cooled aerofoil's geometric stagnation line. By staggering the two rows of holes, the coolant jets can criss-cross over the stagnation line without lifting off very far from the surface, providing excellent film effectiveness in this notoriously difficult-to-cool region. An additional geometric innovation considered herein is the use of coolant supply passage partitions (or passage 'inserts') to increase the coolant feed pressures to holes at risk of hot gas ingestion by reducing the feed pressures to holes at lower risk (those with lower exhaust pressures). Such considerations of the margin of pressure between hole inlets and exits are rarely considered in academic literature.

While the effects of turbulence on film effectiveness have previously been investigated only for simple, film-cooled flat plate and cylindrical leading edge geometries, one of the contributions of the present work has been to measure the effects of engine-representative

dilution port turbulence on representative NGV leading edge films. The most important finding is that lifted-off jets in the stagnation region have their effectiveness contributions significantly enhanced by the mainstream turbulence (by up to 0.2). Another achievement involving interactions between the combustor and the nozzle guide vanes is the removal of mainstream temperature variations due to dilution ports from vane film effectiveness measurements. This process permitted the effects of dilution port mainstream turbulence to be assessed independently of the apparent film effectiveness due to the dilution port temperature profiles. Another means of eliminating this confounding factor from the film effectiveness measurements would be to match the mainstream and dilution port temperatures while maintaining a film coolant temperature difference, however this requires more than one flow heater, increasing rig complexity and cost.

Chapter 3

Oxford Combustor-Turbine Interactions Rig

In this chapter, the sophisticated wind tunnel used in the experiments of the present studies is introduced, preceded by a discussion of similar apparatuses from previous studies in the context of their experimental goals. Several design and procedural modifications to the wind tunnel are described which were required during the present experiments.

3.1 Introduction to Combustor-Turbine Rigs

Since film cooling performance is highly dependent on the properties of the flow arriving at the cooled components, NGV leading edge film cooling performance can be most accurately assessed in the presence of upstream devices which simulate the flow conditions at the exit of real gas turbine combustors. Most researchers seek to optimise simulation realism without using real engine temperatures and pressures, since this is usually prohibitively expensive and reduces possibilities for optical access and *in situ* instrumentation. Experiments are usually conducted on scaled-up, engine-representative geometries, since this improves the possible resolution of measurements and permits matching of heat transfer and aerodynamic dimensionless quantities such as Reynolds number even at the lower pressures and temperatures. Furthermore, it may facilitate certain transient heat transfer experiments by increasing the thickness of test bodies through which thermal pulses will penetrate. It has long been established that the combustion process itself presents a negligible contribution to overall combustor turbulence, in both annular and

can combustors. Multiple researchers have employed Laser Doppler Anemometry (LDA) or pressure transducers at the exits of real engine combustors, at multiple fuel-to-air ratios and operating conditions, and found no differences in outlet turbulence between these and the corresponding non-reacting cases [70, 71, 72]. This crucial finding validated the subsequent work on developing combustor simulators which would permit investigation at reasonable laboratory temperatures of the effects of combustor exit flows on high pressure turbines (HPTs). Thole et al. [73] were among the first to employ an 'active' annular (typical of aeroengines) combustor simulator of jets-in-crossflow rather than 'passive' turbulence generators comprised of a grid of straight bars. They compared the turbulence generation capabilities of both types and found that the turbulence intensities achievable with combustor simulators were much higher (and thus more engine-representative) and also more easily adjustable by means of jet mass flow rate control. The results from many subsequent simulators and experiments performed with them have been published in the open literature, and the following is merely a sample of more recent work.

3.1.1 Examples of Previous Combustor-Turbine Rigs

Cha et al. [74] present experimental results from a fully annular, Rich-burn, Quick-mix, Lean-burn (RQL) combustor rig. It includes fuel spray nozzles (FSNs), an annular combustor liner, and combustor wall tiles, and was tested both with and without the presence of uncooled NGVs. Velocity fields at three planes perpendicular to the bulk flow (just upstream and downstream of the endwall film cooling holes and just downstream of the NGV trailing edges) were obtained with a five-hole probe. Also employed is a 'passive scalar tracing' technique, whereby trace quantities of gaseous CO_2 are seeded into the FSNs and the CO_2 concentration is measured downstream via a probe delivering to an infrared CO_2 gas analyser. Since the vast majority of the heat release in an RQL combustor is completed well before the NGV inlet, the distribution of CO_2 concentration after the intervening turbulent mixing is taken to correspond well with the NGV inlet temperature profile of a real engine with a reacting flow. Aided by RANS CFD simulations of the rig, it is concluded that due to the highly three-dimensional motion of the observed

CO_2 concentrations, inlet profile generators without dilution jets modelled after those in a real engine combustor cannot adequately reproduce the temperature distributions at the NGVs. Typically, dilution ports inject ahead of the FSNs and the high turbulence mixes these regions to be cooler than the regions between consecutive FSNs (the 'hotspots'). Realistic, opposed dilution ports are needed to generate not only the high turbulence intensities, but also the correct turbulence length scales at the NGVs of a real RQL combustor. Comparison of tests both with and without NGVs demonstrated the significant impact of NGV pressure fields on the combustor flow. The velocity profile is substantially altered even farther upstream than the endwall film cooling holes, while the turbulence intensities and length scales are only significantly influenced nearer to the NGVs.

Barringer et al. [75] developed a combustor simulator to study how combustor exit flows affect flow development and heat transfer within a fully annular HPT rig. The single-stage turbine is of a typical aeroengine scale, and is spun up by a starting motor before testing begins, and held at a constant speed by an eddy current brake during the test. The flow matches relevant dimensionless parameters including Reynolds number, Mach number, pressure ratio, momentum flux ratios, and dimensionless rotational speed. This is made possible in an experimental testing scenario by a short duration, 'blow-down' flow arrangement, in which a tank of heated and pressurised nitrogen gas is stored and then released through a fast-acting valve, passing through the test section and then into evacuated collection tanks, producing between one and five seconds of steady flow conditions in the test section. The combustor simulator consisted of three concentric annuli, mimicking an annular combustor; the middle annulus represented the combustor liner interior, while the surrounding annuli provide flow to staggered dilution ports and endwall film cooling holes of two and five rows, respectively. One finned-tube heat exchanger in each of these latter two annuli allowed the outer and inner injected flows to be independently and variably cooled, while five pairs of rotating, concentric, identically slotted discs produced variable blockages and allowed flexible control of all momentum flux ratios. Among other published results obtained from this setup are data regarding the effects of combustor

exit radial stagnation pressure and temperature profiles on the heat transfer around a rig NGV, as measured by thin film heat flux gauges at each of three span locations (near the hub, midspan, and tip). Results showed that more distorted vane inlet temperature profiles (with lower temperatures toward the endwalls due to the endwall film cooling holes) have little effect on the midspan heat transfer, but decrease the heat transfer around the entirety of the vane surfaces near the endwalls. Tests with similar vane inlet temperature profiles but different levels of near-endwall stagnation pressure show that increasing the stagnation pressure near the endwalls with film cooling lowers heat transfer to the spanwise extremes of the vane surfaces, though beyond an upper limit to this stagnation pressure, the heat transfer begins to increases again.

The simulator of Barringer et al. [76] was designed with a target outlet stagnation pressure profile obtained from an earlier, large-scale simulator (enlarged approximately 9 times from a real annular combustor). This simulator is essentially a linear wind tunnel with advanced flow preconditioning, ending with a linear NGV cascade of only two passages (a central NGV with an additional pressure and suction surface forming each of the adjacent working section walls). It operates with only a single axial fan to drive flow. To generate the cooling air flows in the combustor simulation section upstream of the NGV location, two panels split the tunnel into an upper, middle and lower passage corresponding respectively to the combustor flow regions radially outside of the liner, within the liner, and inside of the liner. The central passage begins with a perforated plate to set the mass flow rate split between each section. The flow in this passage is then heated and straightened before entering the liner simulator section, which receives the cooler air from the upper and lower passages via two rows of dilution holes and several rows of endwall film cooling holes drilled into the panels which separate the three passages. Within each main supply chamber, each cooling component also requires a separate smaller chamber to ensure the correct flow splits. This arrangement does not permit dynamic adjustment of the various coolant mass flow rates, restricting the usefulness of the rig in performing parametric studies on the effects of coolant ejection properties.

3.2 Overview of the Oxford Combustor-Turbine Interactions Rig

The Oxford Combustor-Turbine Interactions Rig (CTI rig) was designed by Cresci et al. [30, 77, 78] to enable engine-representative aerothermal research to be conducted on a two-passage NGV cascade with a scale enlarged from an aeroengine by approximately 4.5 times. Its upstream combustor simulator features opposed dilution ports and both inner (hub) and outer (tip) endwall film cooling (45° surface angle, streamwise blowing) at the locations indicated in Figure 3.1. The inner and outer endwall cooling are also known as the RIDN and RODN (Radial Inner/Outer Discharge Nozzle). The central vane's leading edge is supplied with film coolant from the inner side. The mainstream flow is created by a downstream suction fan, while the coolant features are fed by a separate blower fan via a branching pipe system. Hand-operated butterfly valves on each branch permit individual control of the coolant mass flow rate to each of the five cooling features. These are measured by an orifice plate in each branch according to European Standard ISO 5167-2 [79], while the combustor inlet mass flow rate is measured by a pitot tube. The readily varied momentum flux ratios at the dilution ports and endwalls are denoted by J_D and J_E, respectively. The mainstream is heated by an electric heater mesh between the bellmouth

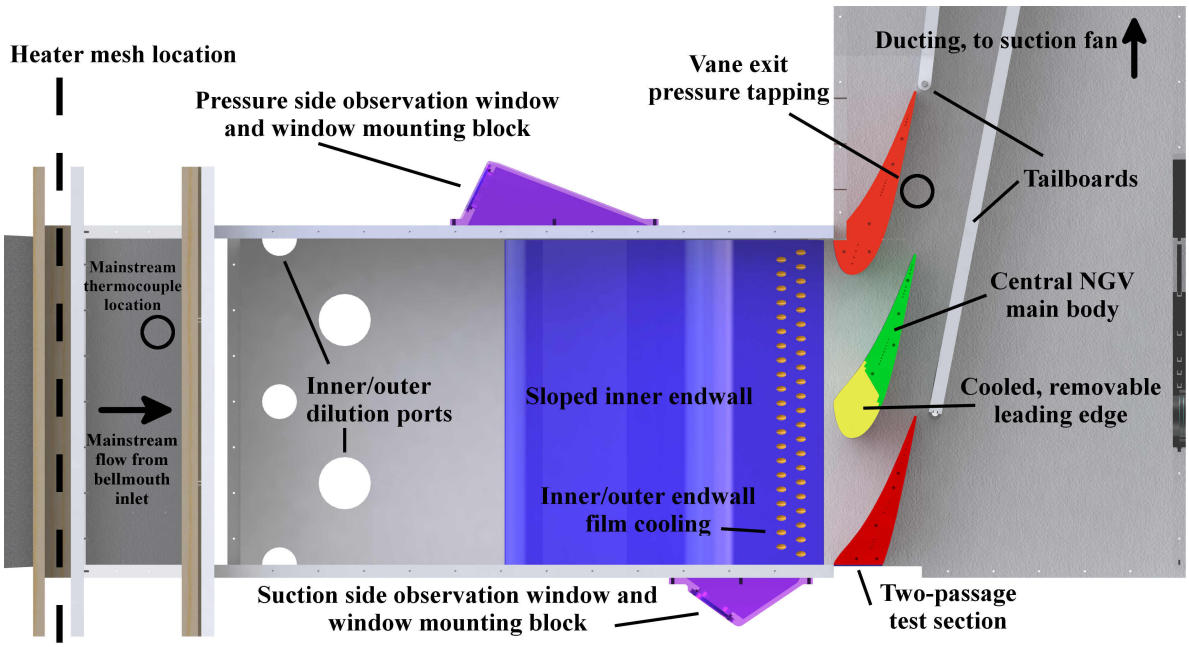


Figure 3.1: Oxford Combustor-Turbine Interactions Rig with main features indicated.

inlet of the wind tunnel and the entrance to the combustor simulator. When activated, this causes a temperature rise of approximately 40 K above ambient. A study in which four thermocouples were placed at different positions just downstream of the heater mesh confirmed that there are no significant variations across the temperature profile due to uneven heating.

Due to heat loss through the rig walls, the temperature just upstream of the NGV cascade is slightly lower than that measured by the thermocouple just downstream of the mesh (even with no dilution or endwall coolant flow). During a test in which thermocouples were temporarily placed in the flow just upstream of the cascade, this temperature drop was measured as approximately 1 K for the mesh and suction fan settings used throughout the present studies. This is corrected for during the calculations of film effectiveness and heat transfer coefficient. Since the blowing fan causes a rise in temperature of approximately 12 K, the rig is substantially non-isothermal even before the heater mesh is activated. Flow temperatures are recorded by a thermocouple downstream of the heater mesh and also within each coolant feed plenum. One of the rig's film-cooled leading edge test pieces was instrumented with a thermocouple within its coolant passage, which measured temperatures below those at the corresponding coolant plenum by a flow rate-dependent amount of up to approximately 2 K. Rather than instrument every test piece with an internal thermocouple, the already instrumented one was used to estimate this discrepancy as a function of the NGV coolant mass flow rate, such that a correction could be applied to the plenum thermocouple measurement in order to more accurately determine the temperature of the film coolant jets.

While the perspex from which the majority of the rig is constructed is transparent to visible spectrum light, it is opaque to infrared radiation. Two Germanium, infrared-transparent windows allow two infrared cameras to observe the central NGV leading edge. The windows are mounted on 3D-printed, angular blocks attached to opposite sides of the simulator. One permits observation of the leading edge suction side, and the other primarily of the pressure side, with some overlap near the stagnation region.

The NGV geometry is a linear extrusion of a modern aeroengine NGV midspan cross section, with an aspect ratio of 1.04, pitch-to-chord ratio of 0.977, and exit flow angle of 74°. Upstream of the cascade, the inner endwall contracts by approximately half an NGV span, while the outer endwall is flat. Diffusing tailboards downstream of the cascade can be adjusted to achieve a periodic pressure distribution as measured by pressure tappings on the central vane and surrounding half-vanes. Tailboards are a popular approach to reducing the flow field differences between large-scale, linear cascades and their fully annular equivalents (e.g. [80, 81, 82, 83]). A core feature of the CTI rig is that the central vane's leading edge is a separate, removable piece, permitting rapid and simple performance testing of different film cooling geometries. Furthermore, two different types of test pieces are used: 3D-printed resin for pressure measurements both within the coolant feed passage and on the external surface, and machined, high density foam for infrared film cooling effectiveness measurements. Both types are shown in Figure 3.2(a), and a view of the cascade from within the combustor simulator is shown in Figure 3.2(b). Appendix A presents a detailed description of how the Oxford CTI rig is operated during experiments.

3.2.1 Pressure Leading Edge Test Pieces

The 3D-printed NGV leading edges used all feature a single cooling hole design, with nine streamwise-injecting hole rows. The leading edge test pieces are each 287 mm long, which is at present too long to be manufactured in one piece by most desktop stereolithography 3D printers; the 'Formlabs Form 2' printer used in this project is only able to print objects of lengths up to around 175 mm. Therefore, it was necessary to produce leading edge inserts in two pieces each and then glue them together. To prevent the tapping hoses from interfering with either coolant inlet flow or mainstream flow, the pressure tappings in these models must lead out of the NGV via the side opposite the film coolant inlet. Pressure tappings are unable to traverse the boundary between the two glued pieces, since the gluing process would likely result in their becoming blocked. However, it is experimentally necessary to take pressure readings inside the NGV coolant passage near its

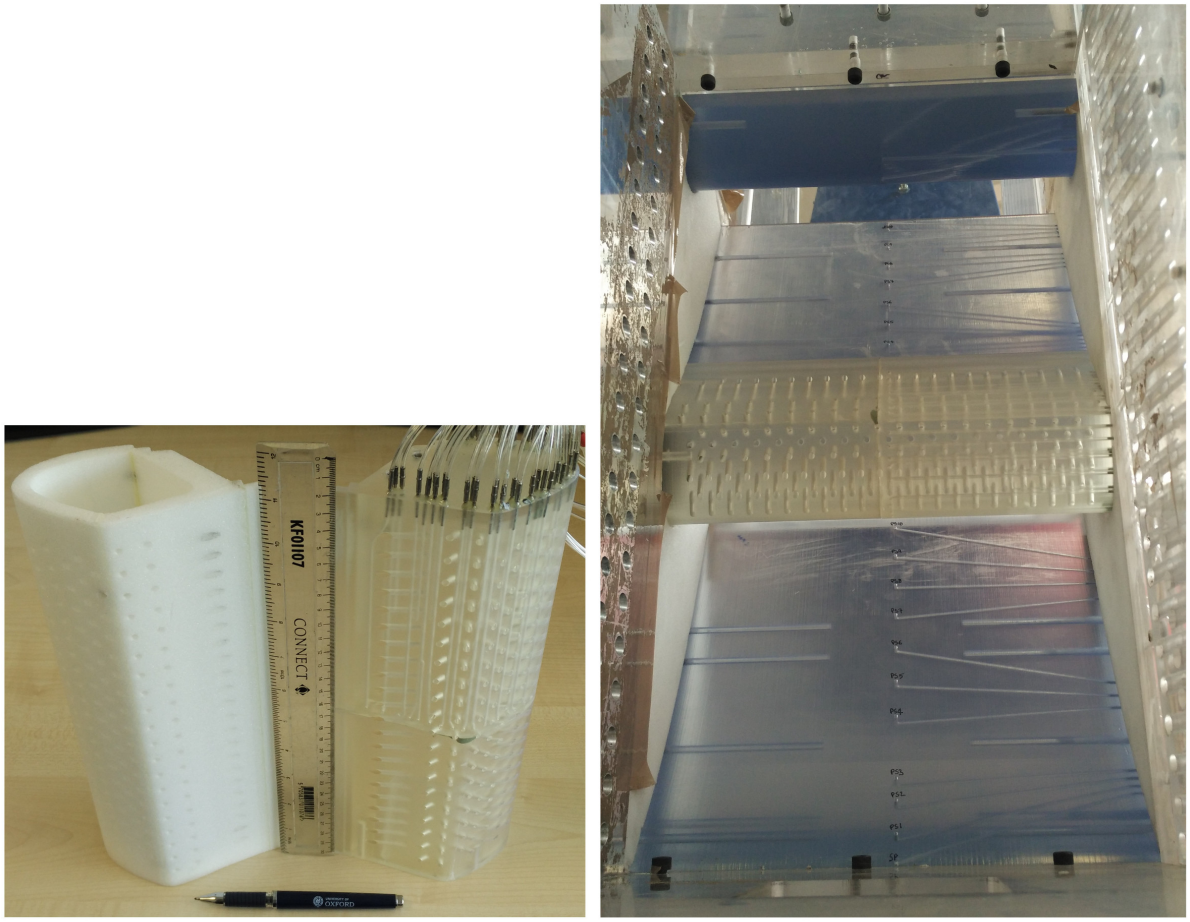


Figure 3.2: (a) Rohacell film effectiveness (left, before painting) and 3D-printed resin pressure (right) leading edge test pieces. (b) View looking downstream at the NGV cascade with a pressure test piece inserted.

inlet, farther than 175 mm away from the tapping exit end of the model. To deal with this issue, two separate leading edge inserts are needed, each consisting of two pieces: an 'inlet' piece of 137 mm length (fractional spanwise position $s = 0 \rightarrow 0.477$) and a 'main' piece of 150 mm length ($s = 0.477 \rightarrow 1$). As shown in Figure 3.3, one inlet piece features internal tappings near the coolant inlet at both $s = 0.15$ and $s = 0.30$, all of which exit the piece at its interface with the matching main piece. Before gluing, these tapping exits are fitted with tubing which is fed through hollows in the main piece, passing the tubes through the rest of the leading edge to exit at the side opposite the coolant inlet. The second inlet piece features no pressure tappings, and its main piece has external tappings at $s = 0.5$ and internal tappings at $s = 0.75$.

The main disadvantage of the limited 3D printing manufacture length is that a complete set of measurements along the entire span requires replacement of one leading edge insert with the other. Owing to the design of the rig, this is not a highly time-consuming operation. A significant advantage of having two models is that there are overall more pressure tappings fit into the two models than could be fit into a single 287 mm model, since in any one model there is a limit on how many pressure tappings can be successfully routed in a spanwise direction between the cooling holes. Each of the three spanwise locations of internal tappings consists of 15 measurements around the cooling supply passage, and the external tappings are 28 in number, making for a total of 73 pressure tappings. A single-piece design previously additively manufactured by a third party and used by Cresci [78] was able to accommodate just 44 tappings.

3.2.2 Film Effectiveness Leading Edge Test Pieces

Infrared film effectiveness measurements are made on leading edges machined out of 'Rohacell', a range of proprietary, high density, polymethacrylimide foams, of which the 'Rohacell 110IG-F' variety is used in this study ($\rho = 110\,\mathrm{kg/m^3}$). The low thermal con-

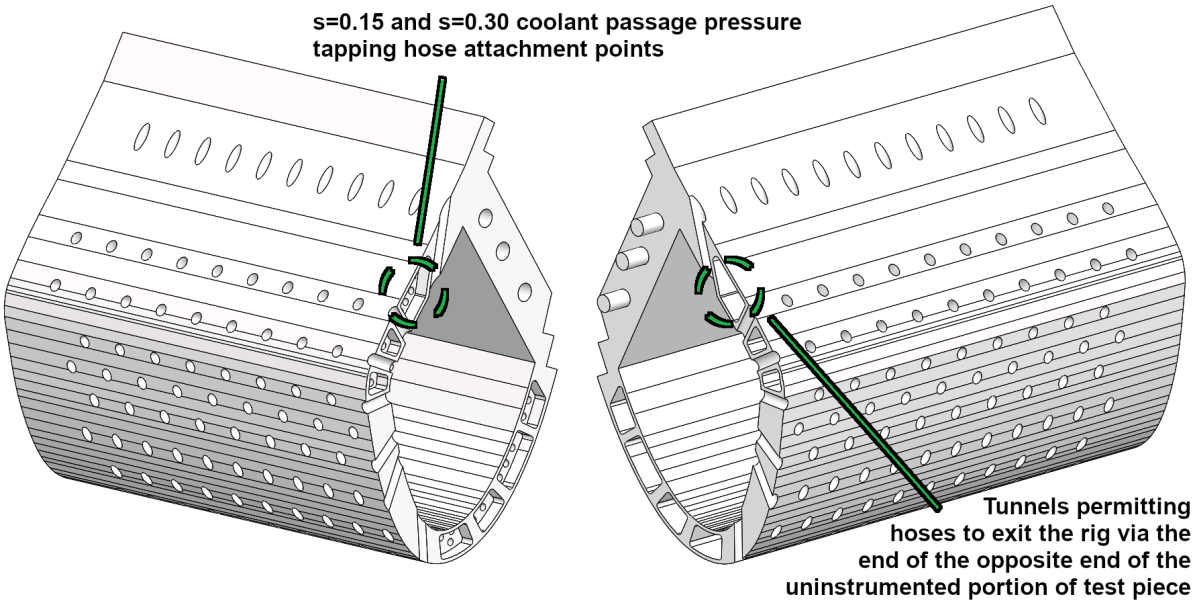


Figure 3.3: The 'inlet' (left) and 'main' (right) pieces of the pressure model containing internal tappings at $s = 0.15$ and $s = 0.30$ within the 'inlet' piece. In order to exit the rig, the pressure tapping hoses must pass through spanwise cavities in the 'main' piece.

ductivity of this material means that surface temperatures measured on its cooled surface approximate the adiabatic wall temperature used to define the film effectiveness. The Rohacell test pieces were machined from blocks of Rohacell with a 4-axis CAD/CAM machine in the Oxford Thermofluids Institute's workshop. Each was manufactured in two halves (this time split in a plane through the geometric stagnation line, rather than spanwise) so that the 277 mm long coolant passage could be hollowed out by the limited tool length of the machine. Where compound-angled film cooling holes were required, the test pieces were sent to a third party for drilling by a 5-axis CAD/CAM machine. After manufacturing, the Rohacell test pieces were spray-painted black using a repeatable technique which produced a uniform application of the paint across all of the painted surfaces. As discussed in the following chapter, this increases and standardises the infrared emissivity of the test pieces and allows for more accurate surface temperature measurements.

The structural capability of the Rohacell foam to withstand the pressure differential between the coolant and mainstream flows was confirmed by the author ahead of experiments by numerical modelling of the expected stress field. Pressure measurements from the pressure test pieces were used to infer approximate internal and external pressure distributions on an ANSYS Mechanical structural model with the mechanical properties of Rohacell [84], the results of which are shown in Figure 3.4. Hole-internal pressures are assumed to be uniform and equal to those within the coolant passage, when in reality they would be less. The maximum coolant mass flow rate used produces a maximum predicted strain of only 0.18%, which is small compared to the nominal breaking elongation of 3.0% [85].

3.2.3 Rig Modifications by the Author

In the course of the present work, the author made the following major additions and modifications to the Oxford CTI rig and related software:

1. Design and production of numerous pressure and film effectiveness leading edge test pieces, and an additional test piece facilitating an advanced infrared measurement calibration.
2. Addition of a leading edge coolant plenum separate from the RIDN coolant plenum, permitting simpler control of the mass flow rates to these two cooling features.

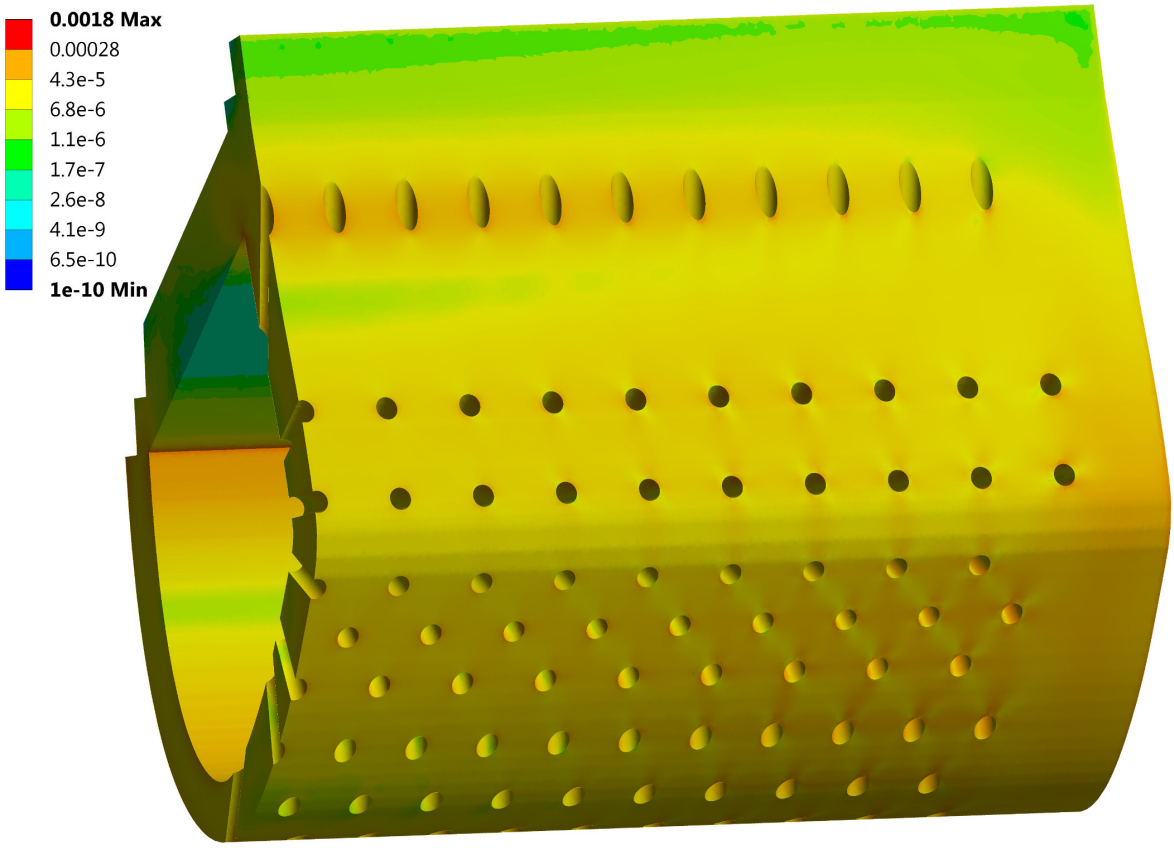


Figure 3.4: Predicted strain in a Rohacell test piece under typical rig differential pressure conditions.

3. Addition of three infrared viewing windows - one above the combustor simulator for observing the cascade's central NGV leading edge pressure side, one below it for observing the leading edge suction side, and one behind the cascade for observing the far suction side (not used in the present studies).

4. Creation of a LabVIEW program to simultaneously trigger recording of the two infrared cameras' video feeds and the various rig thermocouple readings.

5. Streamlining and data readout and export additions to the existing CTI rig mass flow rate measurement LabVIEW program.

6. Video and thermocouple data reduction MATLAB scripts, and a one-dimensional finite element approach to determining the vane heat transfer coefficient distributions based on experimental temperature data.

3.3 Effect of Dilution Port Mass Flow Rates on Cascade Aerodynamics

Figure 3.5 shows the measured NGV pressure ratio (Equation 3.1) and capacity (Equation 3.2) relative to no-dilution for two different amounts of dilution port flow and at a range

of Reynolds numbers (based on the vane throat flow properties and chord length) and in the absence of vane and endwall film cooling ($J_E = M = 0$).

$$PR = \frac{p_{01}}{p_2} \tag{3.1}$$

$$\Gamma = \frac{\dot{m}_1\sqrt{T_{01}}}{p_{01}} \tag{3.2}$$

$\dot{m}_1$ and T_{01} are the cascade inlet mass flow rate and total temperature, respectively. p_{01} is the cascade inlet total pressure, taken as the maximum static pressure measured at any tapping on the externally pressure-tapped leading edge test piece; the relevant tapping is at the midspan of the geometric stagnation line. p_2 is the vane exit static pressure, measured at an endwall pressure tapping indicated in Figure 3.1. Although these unique tapping positions do not account for flow non-uniformities, qualitative trends relevant to combustor design are still observed. The pressure ratio is reduced by dilution port flow due to the incomplete mixing of this flow with the mainstream (and associated ongoing total pressure loss) until well after the vane cascade. Boundary layer losses in a turbine cascade are also increased by mainstream turbulence [86]. The magnitude of the pressure loss is increased by both greater inlet flow rate (i.e. Reynolds number) and greater dilution port flow rate because both of these changes increase the magnitudes of the shear stresses between the mainstream flow and the jets-in-crossflow. Since the flow is unchoked and the inlet total pressure is reduced relative to the outlet static pressure, increasing Reynolds number also reduces the cascade mass flow rate for a given total pressure (i.e. capacity), though the dependency on the dilution port flow rate is not resolved due to the limited precision of the mass flow rate and total temperature measurements.

3.4 Technique for Controlling Two Coolant Feeds with a Single Plenum

For most of the experiments contained in this work, two plena supplied coolant separately to the NGV leading edge and the RIDN. This resulted in relatively low uncertainties for mass flow rate measurements. However, for the early studies presented in chapter 7 (be-

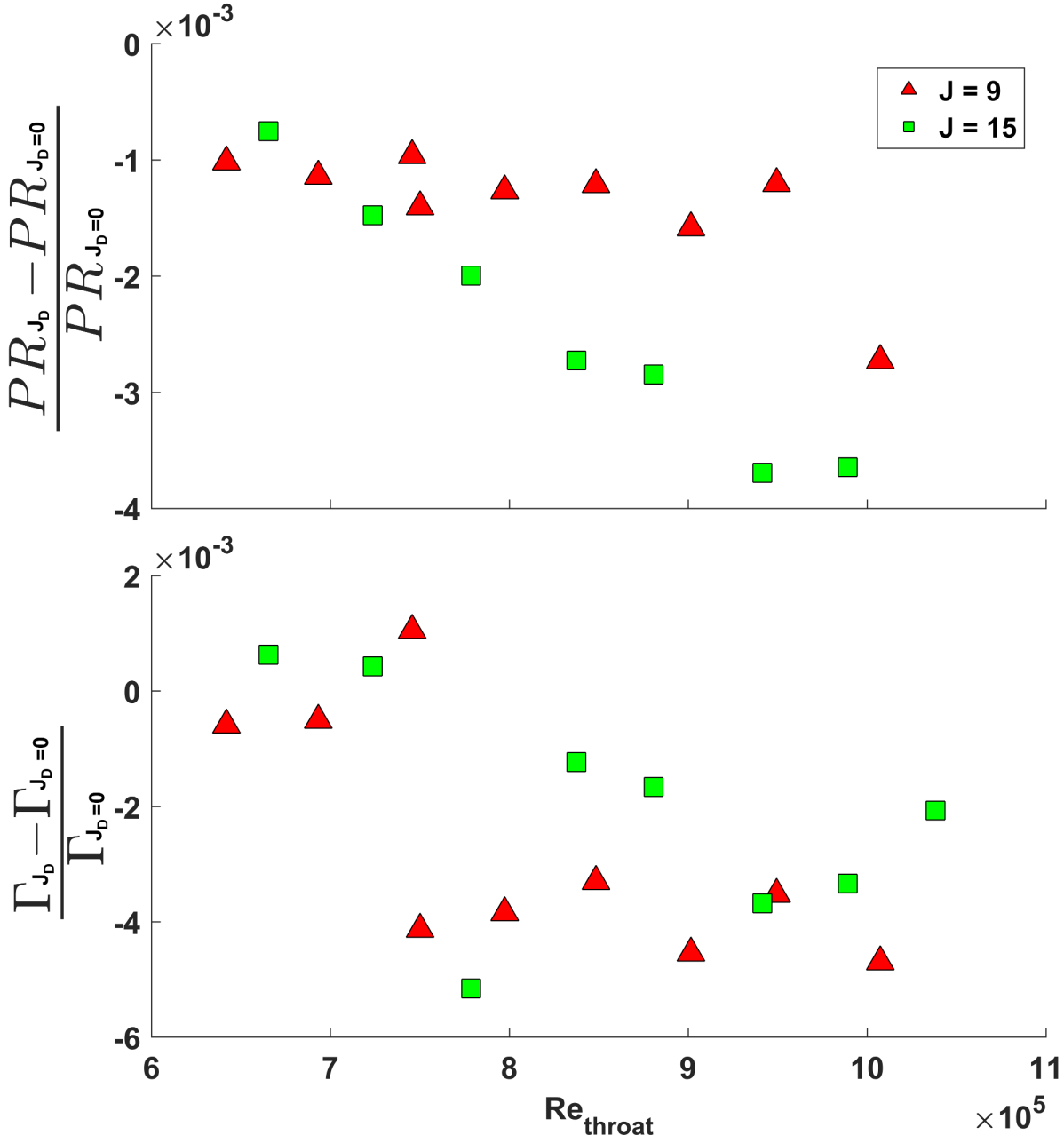


Figure 3.5: The effects of dilution on NGV pressure ratio and capacity ($J_E = M = 0$).

fore the construction of a separate NGV plenum) an approach developed by Cresci [78] was used, in which the NGV coolant and the RIDN coolant were supplied by the same plenum located within the aluminium chamber which features the sloping inner endwall. In this arrangement, in order to determine the coolant mass flow rate to each cooling feature, the author installed and calibrated a set of perforated plates, fitted to the inlet of the leading edge coolant passage, as detailed below.

Pressure tappings required to directly measure the pressure in the chamber supplying the NGV and RIDN can not readily be implemented owing to the considerable difficulty of drilling through the thickness of the aluminium casing. This pressure is instead inferred from prior experimental measurements with the perspex supply chamber exhausting coolant to the atmosphere, as illustrated in Figure 3.6(a). The combined pressure losses of the supply chamber (rapid expansion from the supply hose into the chamber itself, followed by a baffle plate) are measured with use of a static pressure tapping near the end of the supply hose. The total pressure at this location is inferred from the measured static pressure, the cross-sectional area of the hose, and the coolant density and mass flow rate. The latter was varied in order to produce a stagnation pressure loss calibration curve for the full range of available mass flow rates to the coolant supply chamber. In this arrangement, the pressure loss can be calculated as in Equation 3.3.

$$\Delta p_{0,loss} = p_{0,hose} - p_{0,plenum} = (p_{s,hose} - p_{s,atm}) + \frac{1}{2}\rho(v_{hose}^2 - v_{plenum}^2) \tag{3.3}$$

v_{plenum} refers to the velocity of the jets through the baffle plate holes, calculated according to the mass flow rate and the total combined hole area. With the supply chamber attached to the rig, the pressure loss data makes known the total pressure in the aluminium plenum feeding the leading edge and the RIDN. The flow split is controlled by adjusting the amount of blockage at the leading edge passage inlet with various perforated plates. The actual mass flow rate through a perforated plate is related to the ideal mass flow rate by Equation 3.4:

$$\dot{m}_{actual} = C_d \dot{m}_{ideal} = C_d A \rho v_{ideal} = C_d A \sqrt{2\rho(p_0 - p_s)} \tag{3.4}$$

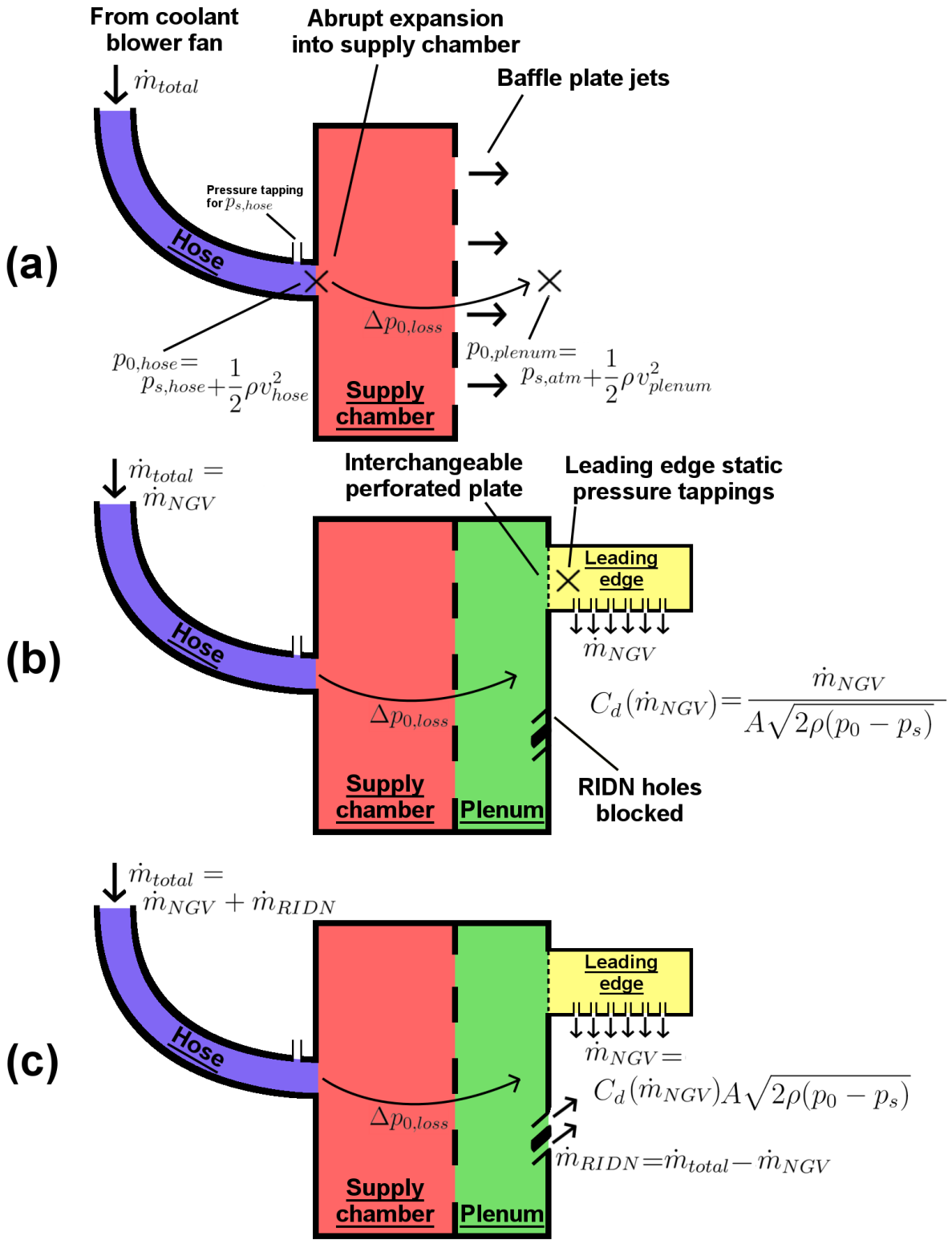


Figure 3.6: (a) Determining flow rate-dependent supply chamber and baffle plate total pressure losses by exhausting to atmosphere. (b) Blocking RIDN holes to measure flow rate-dependent leading edge discharge coefficients. (c) Using known total pressure losses and discharge coefficients to determine flow split.

where A is the combined area of the plate holes, p_0 is the upstream stagnation pressure, p_s is the downstream static pressure, and the density ρ is approximately constant for low Mach number flows (based on the maximum leading edge coolant mass flow rate and minimum plate area, the maximum coolant Mach number was approximately 0.23). The discharge coefficient C_d is always less than unity, owing to hole inlet flow separations which reduce the effective hole areas. For cases without significant crossflow at the hole inlets or outlets, the extent to which these effects occur depends only upon the mass flow rate through the holes under consideration. The static pressure within the passage was taken as the average of the internal pressure tappings located at 30% of span from the passage inlet. With the RIDN coolant holes blocked, a range of known mass flow rates is passed through the NGV for each of several perforated plates positioned over the inlet to the NGV coolant passage, as shown in Figure 3.6(b). For each perforated plate, C_d data is curve-fitted against the mass flow rate. When the RIDN holes are unblocked as in Figure 3.6(c), the coolant mass flow rate through the NGV can be calculated in an iterative process from knowledge of the $C_d(\dot{m}_{NGV})$ of the passage inlet with its current perforated plate. The plate is chosen which gives the desired flow split through the RIDN and the leading edge film cooling.

3.5 Predicting the Nondimensional Parameters for Heated Flow

Prior to a transient heater mesh experiment, the two rig fans are turned on and the coolant mass flow rates adjusted to achieve the leading edge blowing ratio and endwall and dilution port momentum flux ratios desired for the test. When the heater mesh is turned on however, the density of the mainstream flow decreases, as does its mass flow rate, since at a given rotational speed the centrifugal suction fan draws a roughly constant volume flow rate. Hence the blowing ratio and momentum flux ratio (Equations 2.7 and 2.8) both change when the heater mesh is turned on, as does the throat Reynolds number:

$$Re_{throat} = \frac{\rho_{throat} v_{throat} c_{NGV}}{\mu_{throat}} \tag{3.5}$$

It is therefore desirable, for each of these dimensionless mass flow rate parameters, to be able to predict the cold (unheated) set point which will result in a particular hot (heated) value for the parameter. To this end, the combustor simulator inlet mass flow rates and temperatures were measured both hot and cold for the fan rotational speed and heater mesh voltage settings used throughout the experiments contained in this work, resulting in the ratios $\frac{m_{inlet,cold}}{m_{inlet,hot}} \approx 1.116$ and $\frac{T_{inlet,cold}}{T_{inlet,hot}} \approx 0.917$. Using only these empirical values, theoretical estimates can be made of each of the component ratios in Equations 3.6 through 3.8, thus finally giving ratios for the three dimensionless mass flow rate parameters:

$$\frac{M_{cold}}{M_{hot}} = \frac{\rho_{\infty,hot}}{\rho_{\infty,cold}} \frac{v_{\infty,hot}}{v_{\infty,cold}} \approx 0.925 \tag{3.6}$$

$$\frac{J_{cold}}{J_{hot}} = \frac{\rho_{inlet,hot}}{\rho_{inlet,cold}} \frac{v_{inlet,hot}^2}{v_{inlet,hot}^2} \approx 0.914 \tag{3.7}$$

$$\frac{Re_{throat,cold}}{Re_{throat,hot}} = \frac{\rho_{throat,cold}}{\rho_{throat,hot}} \frac{v_{throat,cold}}{v_{throat,hot}} \frac{\mu_{throat,hot}}{\mu_{throat,cold}} \approx 1.138 \tag{3.8}$$

where properties with the subscript '∞' are mass-averages of the inlet and dilution coolant properties, and properties with the subscript 'throat' are mass-averages of the inlet, dilution port, and leading edge film coolant properties. These constant ratios imply proportional relationships between the cold set points and resulting hot targets. The relationships were successfully validated experimentally by recording the parameters both before and after turning on the heater mesh for various experiments across a variety of coolant mass flow rates. Figure 3.7 shows that the experimental data fit well with the semi-empirical, proportional relationships (straight, black lines) except in the case of the Reynolds number. However, since the Reynolds number variations are small with regards to their potential to affect the measured film cooling performance (as shown in section 5.5), accurately predicting its correct cold set point is relatively unimportant.

3.6 Mass Flow Rate Uncertainty Analysis

The combustor inlet mainstream velocity uncertainty is calculated according to the uncertainties in the pitot tube velocity equation measurands. The coolant mass flow rate

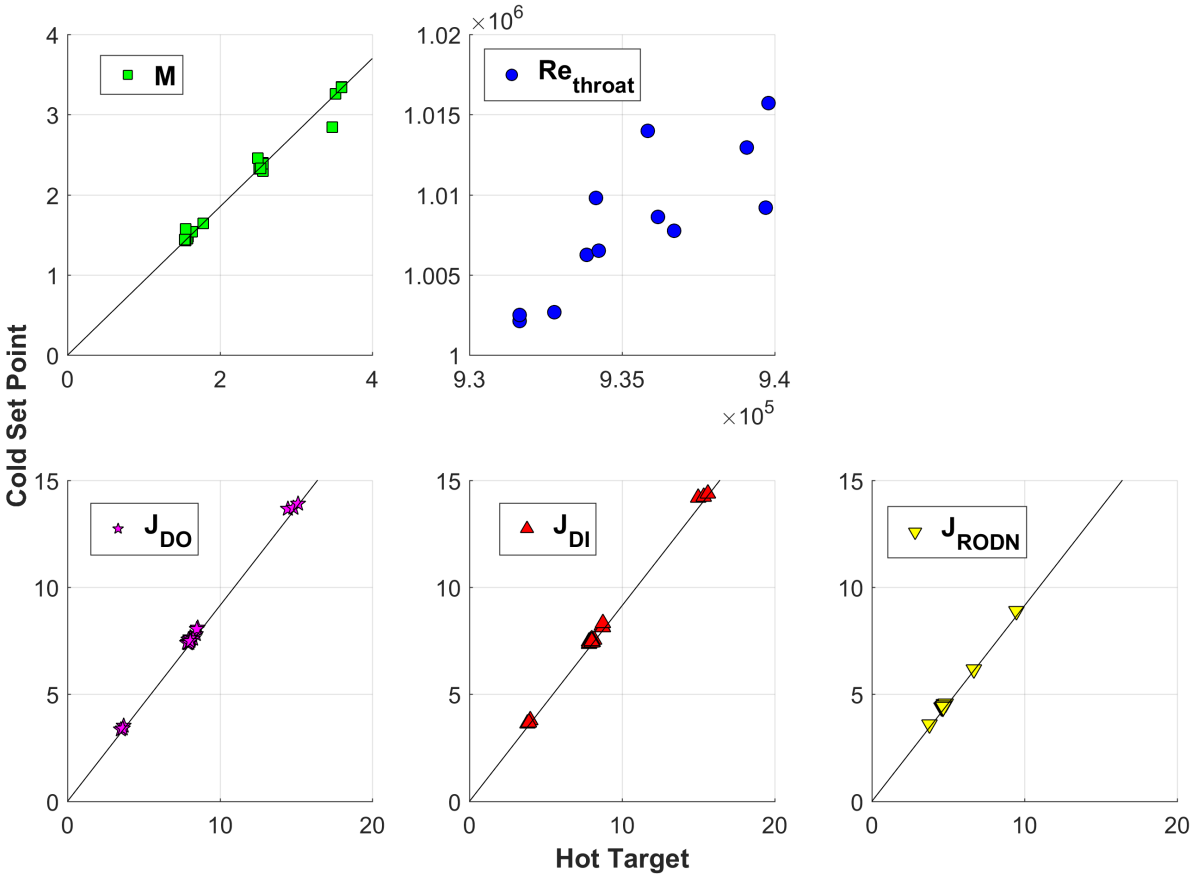


Figure 3.7: Experimentally observed variations between cold and hot dimensionless mass flow rate parameters, which fit well with the semi-empirical proportional relationships for M and J but not Re_{throat}.

uncertainties are calculated in accordance with the orifice plate uncertainty procedures detailed in European Standard ISO 5167-2 [79]. The facility is designed for easy removal and replacement of the central vane's leading edge, and some leakage from the film coolant plenum around the leading edge test pieces into the mainstream is unavoidable. An additional leading edge mass flow rate uncertainty is assigned to account for this. The maximum possible leakage area is estimated as equal to approximately 2% of the combined cooling hole area. Since the mass flow rate is proportional to the flow area (Equation 3.4), the reported leading edge blowing ratios also overestimate the true values by a maximum of approximately 2%. Coolant mass flow rates are reported as dimensionless quantities (J_D, J_E, M) dependent on the mainstream velocities near the injection points, and uncertainty is propagated from both coolant and mainstream flow velocities and densities. Since the endwall and vane film cooling lie downstream of the dilution ports, the local

mainstream flow uncertainties include components propagated from the uncertainty in both the combustor inlet and dilution port mass flow rates. Moreover, since the coolant mass flow rates are controlled with hand-operated valves and the predictions of the heater mesh activation parameter changes are imperfect, there is always a small deviation of the measured nominal quantity from its target value, and these deviations were included in the uncertainty estimates. The resulting maximum percentage uncertainties in the J_D, J_E, and M values reported herein are approximately 5%, 4% and 10%, respectively. For these, roughly 1%, 1%, and 4% are due to manual valve adjustment discrepancies, while the remainder is the cumulative bias uncertainty in underlying measurements. The valve issue is proportionally more significant for the blowing ratio because the NGV leading edge receives a much lower coolant mass flow rate than the other two cooling features. The uncertainties for quantities derived from leading edge surface temperature and pressure measurements are discussed in sections 5.3 and 7.3.4, respectively.

3.7 Window Analysis

The flow field effects of the additional cavities produced by the two window mounting blocks were determined to be negligible by comparison of two RANS CFD simulations of the combustor simulator; one with and one without the cavities. Their presence produced less than 1% variation in both the predicted exit turbulence and temperature profiles. The mesh independence of each case was determined by the negligible change in these exit profiles with additional mesh fidelity increases. Germanium infrared-transparent windows represent a significant financial investment for a fragile component, which warranted a careful study of their structural integrity and thermal state ahead of their actual installation into the rig. The thermal gradients within the windows also affect the variation of infrared emissions across the window. As shown in Figure 3.8, each window frame is simply a round portion of aluminium tightened down onto its window and two sealing gaskets by four screws. The gasket-window-gasket arrangements are compressed into round recesses in the window blocks at the locations indicated in Figure 3.1. The aluminium frame does not meet the window block i.e. it has no intended 'fully tightened' state.

This has the advantage that if replacement gaskets or windows are needed, they need not necessarily be of exactly the same widths as the initially chosen components, because the frame height can be changed accordingly via the positions of the tightening bolts. The 'Klinger Statite' gasket material of 0.8 mm thickness was chosen from the product catalogue of Klinger Ltd. [87] on the basis of low cost and low sealing pressure, since this reduces the stresses in the windows. The ASME gasket factors for Klinger Statite permitted the calculation of an estimated required sealing pressure, and hence of the required axial force and equivalent torque on each of the four window frame bolts [88]. An FEA model of the window frame setup was run with these bolt forces applied as equivalent pressures on the bolt washers. The stresses in the Germanium window yielded a minimum Mohr-Coulomb failure safety factor of approximately 1.70, suggesting safety from brittle failure [89]. Although it is possible to use a torque wrench to estimate the axial force in each bolt and hence ensure that the gaskets are theoretically sealed, in practice the bolts are tightened gradually until the windows no longer audibly leak.

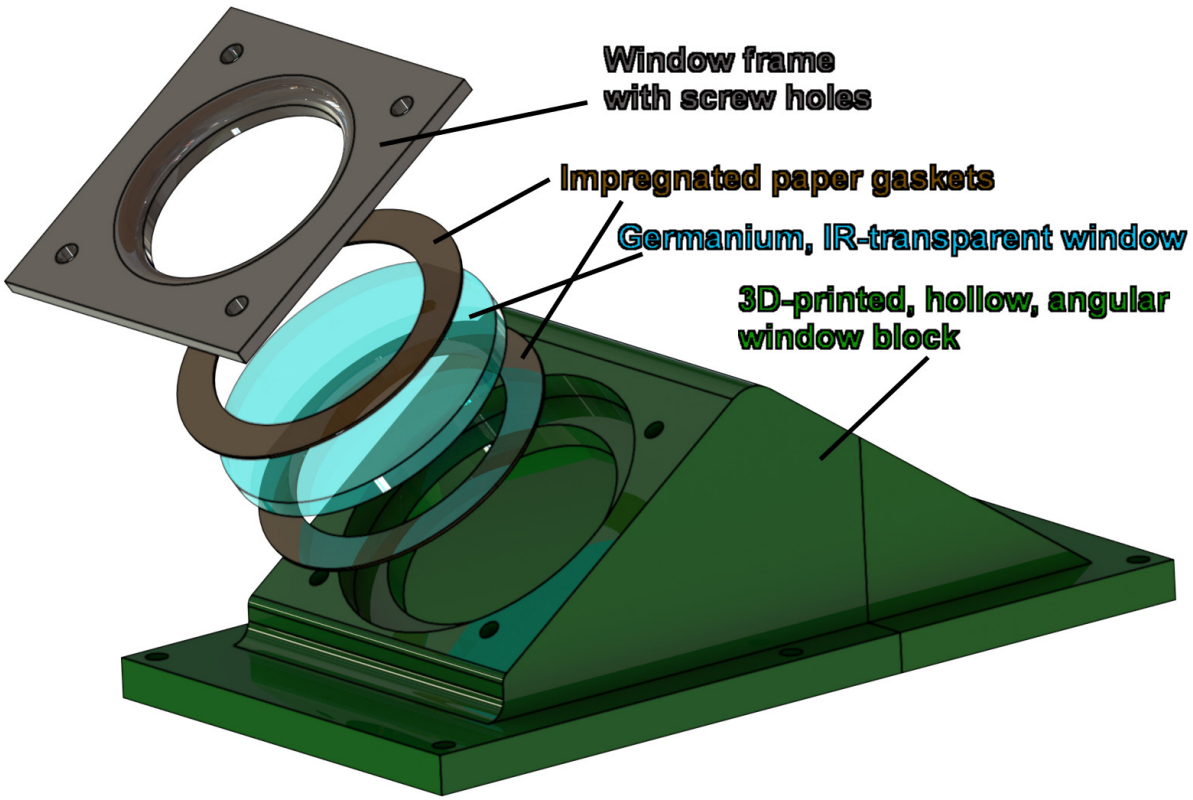


Figure 3.8: Germanium windows (blue) as assembled within a window block (green) with two gaskets and an aluminium window frame.

A conjugate heat transfer CFD calculation was conducted in order to obtain an estimate of the experimental temperature and stress distributions within the windows under steady-state, heated rig conditions. The CFD calculation is a reduced domain so as to allow improvement of the mesh fidelity in and around the window. The domain is reduced in the streamwise direction by importing inlet (velocity components and temperature) and outlet (pressure and total temperature) profiles from a larger, full domain rig simulation (section 5.5.2), as well as by the inclusion of only one window cavity. This simulation was performed before the final design of the angular window block was completed, however the results remained useful for the purposes of ensuring the suitability of the Germanium windows. The external surfaces of the perspex, window frame, window, and gaskets are modelled as being convectively cooled by the atmosphere (assuming $T_{aw,atm} = 20\,^{\circ}\mathrm{C}$ and $h = 10\,\mathrm{W\,m^{-2}\,K^{-1}}$), with the remaining boundaries considered adiabatic. The imposed inlet and resultant outlet temperature profiles, as well as a cross section of the mesh with the corresponding cross section of the computed temperature field, are shown in Figure 3.9. As the dilution port coolant is highly mixed with the mainstream by the time it reaches the window location, both the solid and fluid temperatures are nondimensionalised using the simulator inlet (hot) and dilution coolant (cold) reference temperatures.

Clearly visible are the three fluid domain mesh densities, increasing toward the window and the other two adjacent cavities. An enhanced view of the indicated mesh region is shown in Figure 3.10. Convergent solution of the problem required an extremely fine mesh on the 0.8 mm thick gaskets, driving up the element count to a total of 38.1 million. Due to the difficulty of growing prisms in the fluid zone adjacent to both the window and the thin, fluid-side gasket, combined with the complex flow field and turbulence produced in and around the window recess, the local convective heat transfer is unlikely to have been modelled with great accuracy. However, under these circumstances, the range of temperatures predicted within the window is only around 1 K. The solid temperature field results were used in a mechanical model which also simulated the pressure applied to the window

and frame by their fastening bolts. The predicted minimum Mohr-Coulomb failure safety factor in the window reduced to approximately 1.25, which is still ample given the conservatively high gasket-sealing bolt pressures applied. These predictions suggested that the window would survive rig operating conditions and that the spatial variations in the window infrared emissions would be small (though these are nevertheless implicitly calibrated for by the technique described in chapter 4). The conjugate simulation assumed that the rig was at steady-state when heated, so the predicted window temperature rise was approximately 15 K. In fact, during the 60 second transient rig tests, a thermocouple on the curved side of the suction side window indicated a temperature increase of only a few Kelvin during this time, suggesting lower thermal stresses than were predicted.

Another pair of windows was simultaneously added to the rig but not used during the present studies. They permit observation of the far suction side of the central vane. As can be seen in Figure 3.1, windows are required in both the perspex wall downstream of the cascade and one of the tailboards. As shown in Figure 3.11, interlocking blocks of different sizes allow each window to be shifted up and down without significantly altering the aerodynamics of the surfaces. The perspective through the tailboard window limits the combined observable region to a thin strip surrounding the suction side midspan.

3.8 Film Effectiveness Conductivity Correction

Rohacell 110IG-F is the variety of high density polymethacrylimide foam used to manufacture film effectiveness leading edge test pieces for the present studies. It has a very low thermal conductivity of just $k = 0.032\,\mathrm{W\,m^{-1}\,K^{-1}}$ [90], which serves to increase the Biot number of these test pieces, thus increasing the internal thermal gradients, or equivalently, reducing the effect on surface temperatures of conduction relative to convective heat transfer. The intention is that during film cooling experiments, the local surface temperatures on the hot-gas side of the Rohacell will approximate the adjacent fluid adiabatic wall temperatures, which can be used to calculate a low-error measurement of the film cooling effectiveness distribution. The use of the adiabatic wall temperature is ubiquitous

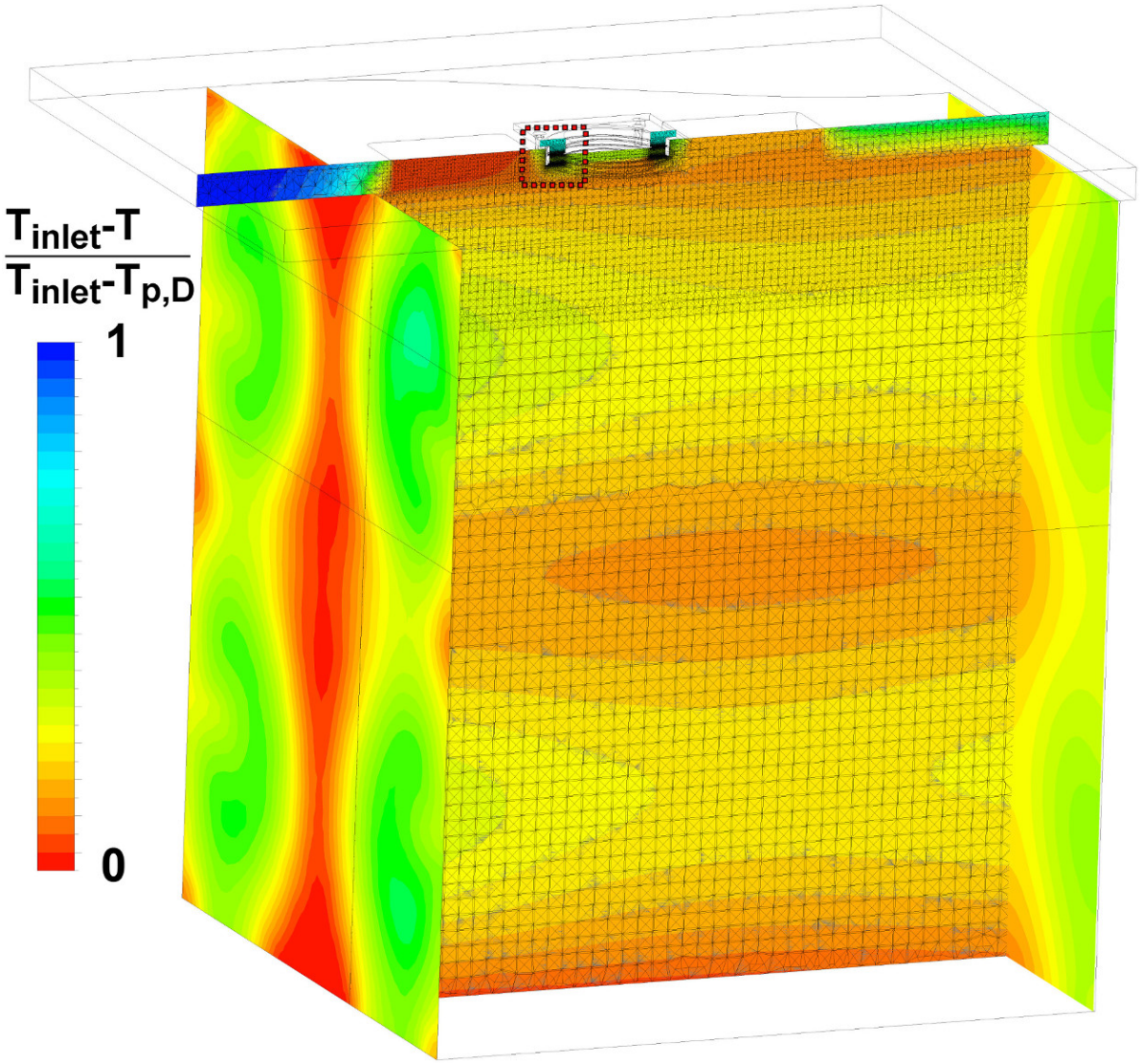


Figure 3.9: Inlet fluid temperature profile boundary condition (left), mesh and temperature result cross section (middle) and outlet fluid temperature result (right) for the reduced domain, conjugate CFD simulation of the window frame during heated rig operation. Dilution port coolant $T_{p,D}$ and combustor simulator inlet T_{inlet} reference temperatures.

in film cooling studies, because it is a simply replicable way to quantitatively compare the surface cooling effects of various films. For computational studies, conductive modelling of the solid bodies is not necessary when determining adiabatic wall temperatures. Moreover, given sufficient flow field similitude, effectiveness values are valid at engine conditions, allowing accurate predictions of film temperature distributions for engine design purposes.

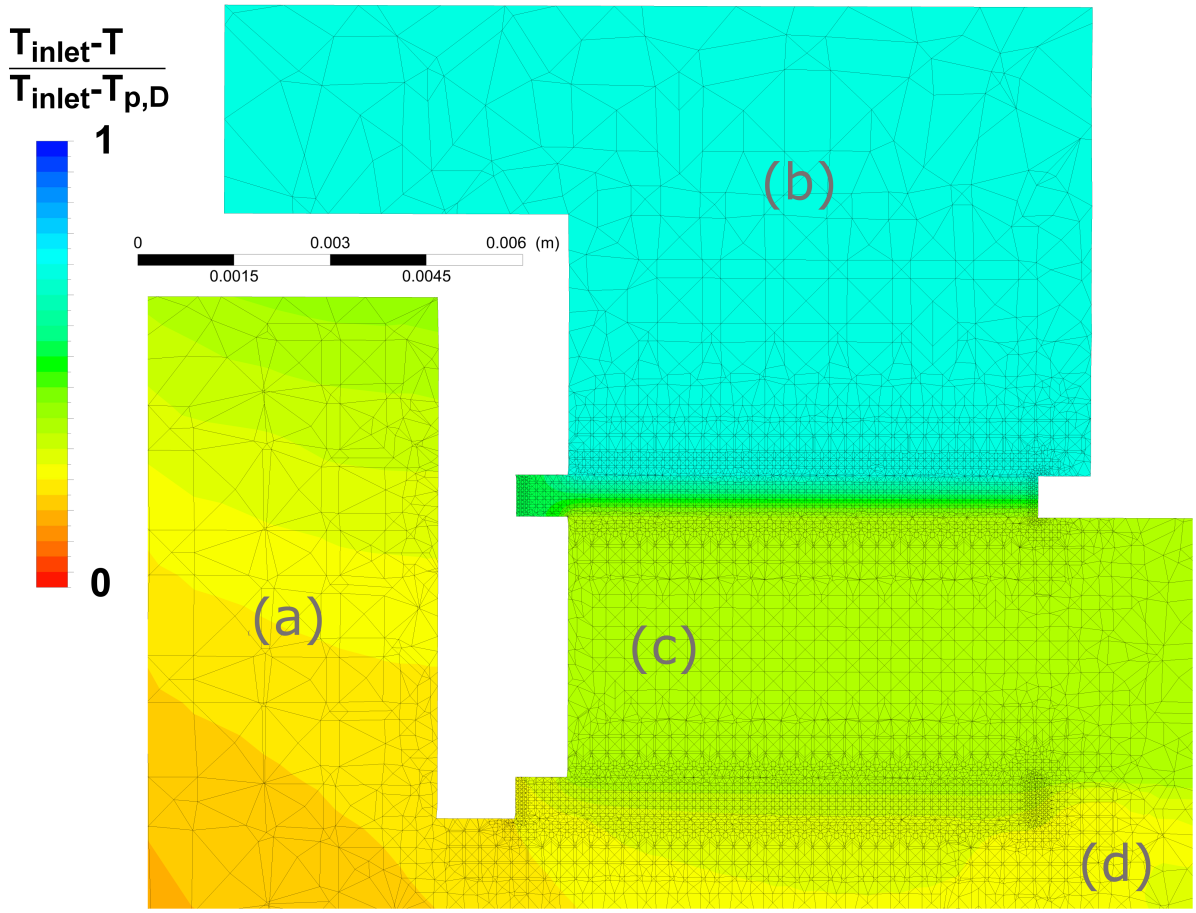


Figure 3.10: Close-up of the mesh region indicated in Figure 3.9, showing (a) perspex (b) window frame (c) Germanium window (d) fluid, and the high mesh density gaskets.

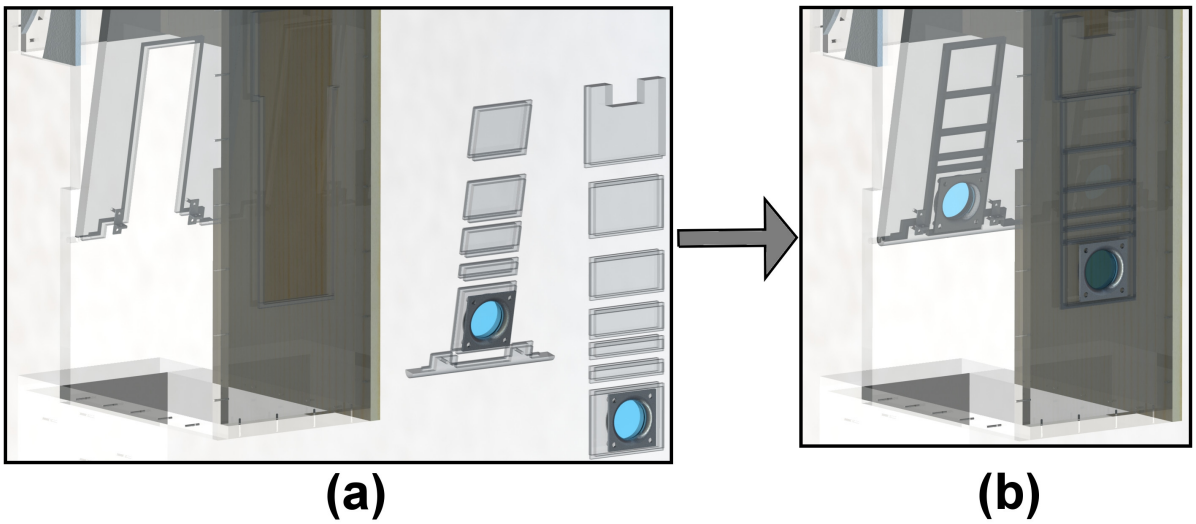


Figure 3.11: Two adjustable height windows facilitating downstream suction side observations on the central NGV.

3.8.1 Analytical and Computational Studies of Film Effectiveness Conduction Error

Two types of one-dimensional analysis were used to assess the assumption that the hot-gas side surface temperature of the experimental Rohacell leading edges exactly equals the flow adiabatic wall temperature: an analytical heat resistance model and a transient finite difference model. From these, values were determined for a film effectiveness correction parameter, $\eta_{correction}$, which equals the difference between the theoretical and measured (based on a surface temperature) effectiveness values. It was found that because of the relatively thin leading edge wall (9 mm), the effects of conduction do significantly influence the film effectiveness measurements, despite the low thermal conductivity of the test piece material. Specifically, conduction through the wall due to convective heat transfer within the leading edge coolant passage means that the effectiveness based on external surface temperature measurements is overestimated. The true adiabatic film effectiveness is defined with the adiabatic wall temperature T_{aw} according to Equation 2.2. However, the experimentally measured temperature is always a surface temperature T_s on a low conductivity solid such as Rohacell, which without correction for solid conduction effects permits calculation only of the 'surface film effectiveness' defined according to Equation 3.9.

$$T^* = \frac{T_\infty - T_s}{T_\infty - T_c} \tag{3.9}$$

The correction between these two quantities can be defined as the nondimensionalised difference between the two temperature distributions T_{aw} and T_s, as per Equation 3.10.

$$\eta_{correction} = \frac{T_{aw} - T_s}{T_\infty - T_c} \tag{3.10}$$

Then the corrected film effectiveness is given by Equation 3.11.

$$\eta = \frac{T_\infty - T_s}{T_\infty - T_c} - \frac{T_{aw} - T_s}{T_\infty - T_c} = T^* - \eta_{correction} \tag{3.11}$$

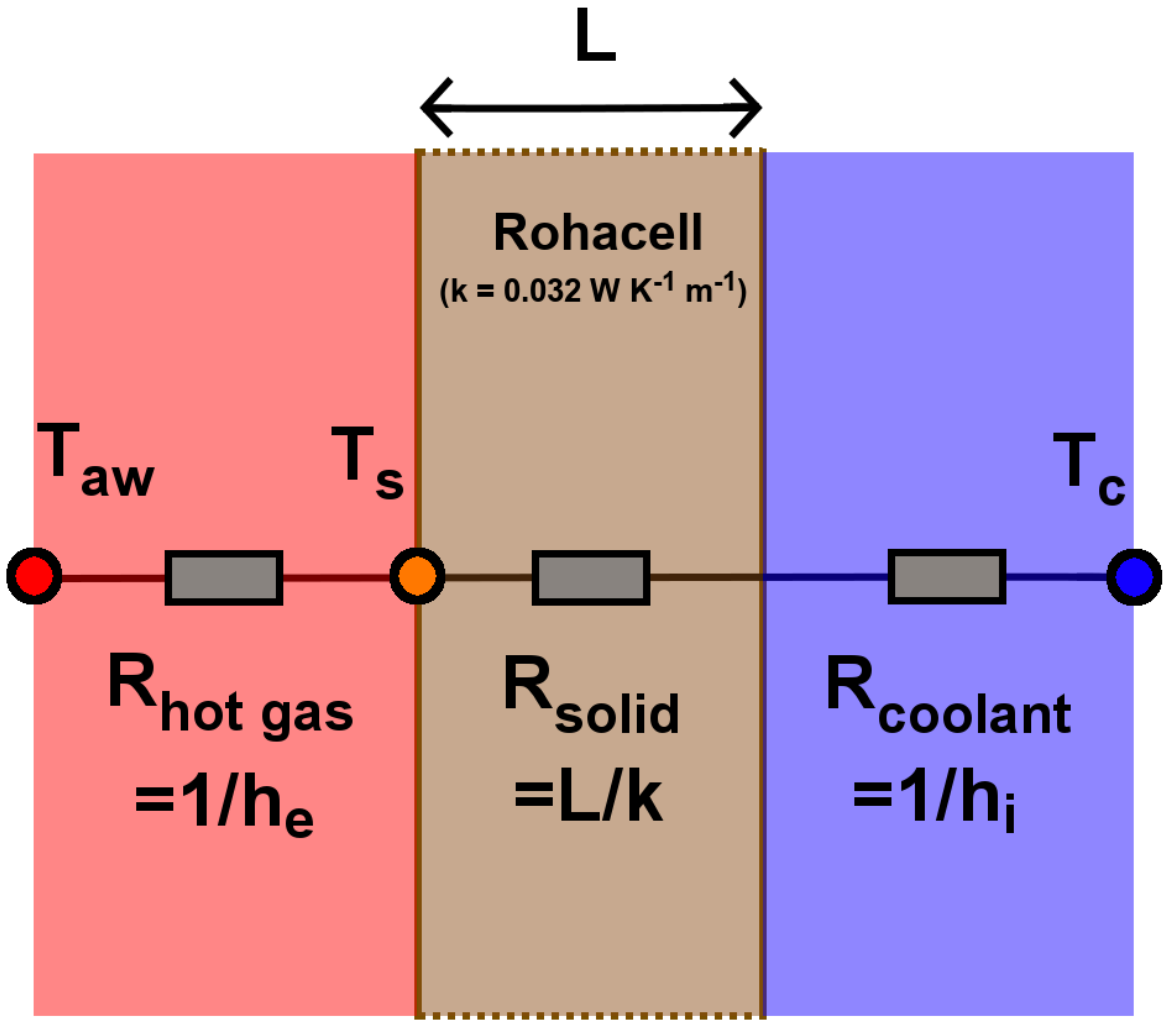


Figure 3.12: One-dimensional thermal resistances model for steady-state analysis of a solid with convective heat transfer on both sides. h_e and h_i are the external (hot gas) and internal (coolant) heat transfer coefficients, respectively. L is the solid wall thickness.

An analytical expression for the theoretical effectiveness correction can be determined using the one-dimensional heat resistance model illustrated in Figure 3.12. To begin, the correction is expressed as the product of the two fractions in Equation 3.12.

$$\eta_{correction} = \frac{T_{aw} - T_c}{T_\infty - T_c} \times \frac{T_{aw} - T_s}{T_{aw} - T_c} \tag{3.12}$$

The first of these is simply one minus the film effectiveness, as shown in Equation 3.13.

$$\frac{T_{aw} - T_c}{T_\infty - T_c} = \frac{T_{aw} - T_\infty + T_\infty - T_c}{T_\infty - T_c} = 1 + \frac{T_{aw} - T_\infty}{T_\infty - T_c} = 1 - \eta \tag{3.13}$$

At steady-state (during which film effectiveness measurements are made) the temperature differences in the second fraction are each equal to the sum of the thermal resistances between those temperatures (see Figure 3.12).

$$\frac{T_{aw} - T_s}{T_{aw} - T_c} = \frac{\frac{1}{h_e}}{\frac{1}{h_e} + \frac{L}{k} + \frac{1}{h_i}} = \frac{1}{1 + \frac{Lh_e}{k} + \frac{h_e}{h_i}} \tag{3.14}$$

Substituting Equations 3.13 and 3.14 into Equation 3.12 yields the theoretical expression for the effectiveness correction, Equation 3.15.

$$\eta_{correction} = \frac{1 - \eta}{1 + \frac{Lh_e}{k} + \frac{h_e}{h_i}} \tag{3.15}$$

Substituting Equation 3.15 into Equation 3.11 yields an analytical expression for the effectiveness in terms of the nondimensionalised surface temperature T^*, Equation 3.16.

$$\eta = \frac{1 + \frac{Lh_e}{k} + \frac{h_e}{h_i}}{\frac{Lh_e}{k} + \frac{h_e}{h_i}} T^* - \frac{1}{\frac{Lh_e}{k} + \frac{h_e}{h_i}} \tag{3.16}$$

The external convective heat transfer coefficient h_e was estimated with the Hilpert correlation for cylinders in cross flow [91] (Equation 3.17, in which k_{air} is the thermal conductivity of air, D is the estimated equivalent cylinder diameter, and $C(Re)$ and $n(Re)$ are empirical constants tabulated for various Reynolds number ranges).

$$h_e = \frac{k_{air}}{D} C(Re) \times Re^{n(Re)} \tag{3.17}$$

The internal coolant passage wall heat transfer coefficient h_i was estimated with the Dittus-Boelter equation for internal pipe flows with $Re > 2000$ [91] (Equation 3.18, in which k_{air} is the thermal conductivity of air, D_H is the hydraulic diameter of the coolant passage, and Pr is the Prandtl number of air.

$$h_i = 0.023 \, \frac{k_{air}}{D_H} \, Re^{0.8} \, Pr^{0.4} \tag{3.18}$$

Figures 3.13 and 3.14 show the subsequent results from Equation 3.15 for two values of film effectiveness and a range of hypothetical material thicknesses and thermal conductivities. Higher effectiveness values reduce the required correction because of the reduced thermal potential between the gases on either side of the wall. The correction is also lower for higher thickness and lower thermal conductivity. Unfortunately, the conductivity is limited by the available materials which also exhibit sufficient stability under machining. The scope for increasing the thickness of the CTI rig's Rohacell test piece walls is also limited by the size of the rig and the requirement for realistic film cooling hole lengths and feed conditions. Moreover, the hyperbolic shape of the curves in Figure 3.14 shows that further test piece thickness increases would yield relatively little additional reduction in the $\eta_{correction}$ parameter, whose value for the CTI rig Rohacell test pieces is approximately $\eta_{correction} = 0.032$ when the true film effectiveness is zero. $\eta_{correction}$ was also successfully determined by applying identical convective heat transfer boundary conditions to a computational heat conduction model. A one-dimensional, explicit method transient finite difference code was written in MATLAB. The time integration was forward difference and the spatial integration was the second order central difference. The spatial and temporal discretisations were of constant size and were sufficiently small that smaller steps made negligible difference to the solution. The solid temperature distribution is initialised by assuming a depthwise linear change between the hot and cold driving gas temperatures at the external and internal surfaces respectively, though in fact the initialisation does not affect the steady-state solution. Using the external surface temperatures predicted as the solid temperature distributions approached steady-state, the results for $\eta_{correction}$ presented in Figures 3.13 and 3.14 were closely reproduced.

The one-dimensional case considered ignores the possible effects of cooling holes, whose internal convective cooling accelerates the local conduction of heat away from the ostensibly adiabatic external vane surface. However, as is visible in the film effectiveness results of Figure 3.15 and subsequent chapters, the rings of affected area around each hole are much thinner than the diameter of the holes. While sophisticated corrections could

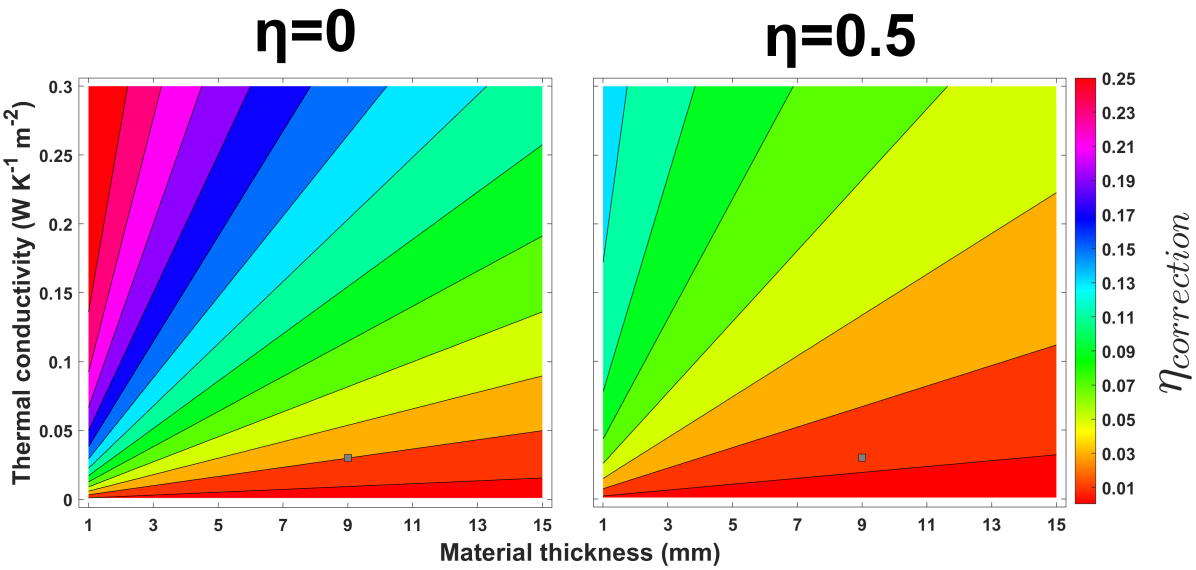


Figure 3.13: Contours of the nondimensionalised discrepancy between test piece driving gas temperature and surface temperature, for two values of film effectiveness and various material thicknesses and conductivities. CTI rig Rohacell test piece performance indicated on each plot.

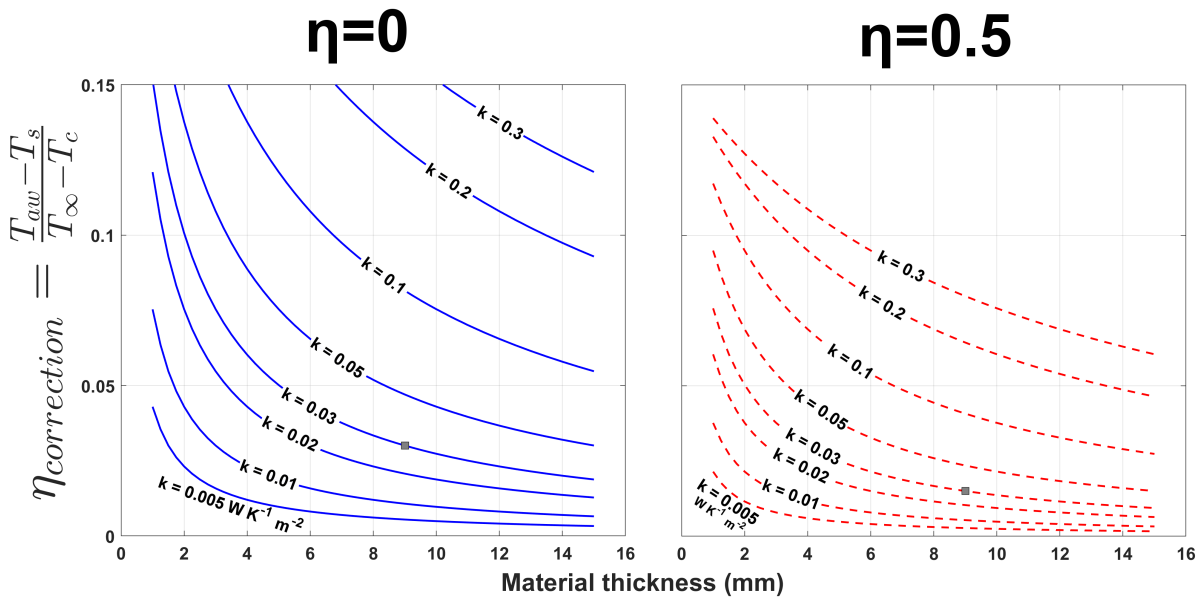


Figure 3.14: Curves representing the data in Figure 3.13.

in principle be developed for these regions, it is simpler just to exclude them from data processing operations such as lateral averaging.

3.8.2 Experimental Correction with Conduction Images

Ultimately, the effects of conduction were captured experimentally in the present film cooling experiments. The technique developed offers several important advantages over the one-dimensional analytical and computational approaches:

1. Corrections are determined uniquely at every position of the observed aerofoil surface, permitting spatial variations in the required correction.
2. No assumptions are made about surface heat transfer coefficient values, which in fact vary slightly both around the aerofoil surface and along the coolant passage.
3. No assumption is made about the thermal conductivity of the Rohacell, which has an associated uncertainty and is in fact a weak function of temperature.

The technique proceeds as follows. A Rohacell leading edge test piece with no film cooling holes (referred to as the 'calibration model') is installed into the rig. The mainstream temperature is made as uniform as possible by sealing the dilution ports and endwall film cooling holes. This temperature $T_{aw,cond}$ is then treated as the driving adiabatic wall temperature across the entire external surface. Leading edge film coolant is supplied as usual but vented to atmosphere through a large opening in the end of the calibration model. Due to its lack of film cooling holes, the measured leading edge external surface temperature reduction below the mainstream temperature is then entirely due to conduction of heat towards the coolant passage. This surface temperature distribution due to conduction is nondimensionalised as a conduction factor $\gamma(\mathbf{x})$ according to Equation 3.19.

$$\gamma(\mathbf{x}) = \frac{T_{aw,cond} - T_s(\mathbf{x})}{T_{aw,cond} - T_{c,cond}} \tag{3.19}$$

The conduction correction parameter is found to have a slight dependence on the leading edge coolant mass flow rate, so that separate corrections are used for different blowing ratios. Its value is for the most part higher (up to 0.1) than the correction value of 0.032 determined analytically for zero true effectiveness, owing to the analytical model's uncertainties in the HTC estimates and material thermal conductivity. The infrared cameras are kept rigidly fixed between experiments, and in subsequent experiments featuring cooling, the now spatially variant adiabatic wall temperature is calculated from the surface temperature measurements and the conduction factor, by rearrangement of Equation 3.19.

$$T_{aw}(\mathbf{x}) = \frac{T_s(\mathbf{x}) - \gamma(\mathbf{x})T_c}{1 - \gamma(\mathbf{x})} \tag{3.20}$$

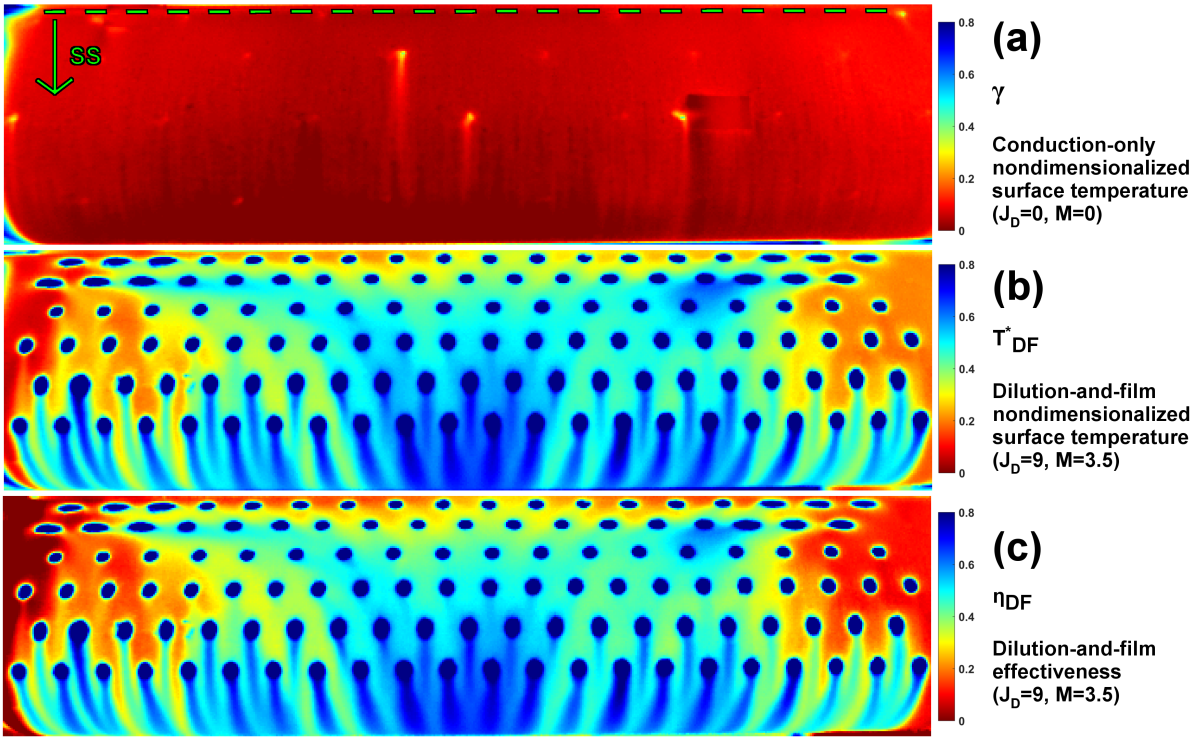


Figure 3.15: An example of the experimental test piece thermal conductivity correction used ($J_D = 9$, $J_E = 0$, $M = 3.5$).

This is then nondimensionalised into the corrected film effectiveness:

$$\eta(\mathbf{x}) = \frac{T_\infty - T_{aw}(\mathbf{x})}{T_\infty - T_c} \tag{3.21}$$

An example of the conduction correction data is shown in Figure 3.15. The subscript 'DF' indicates that the experiments feature both dilution ports (D) and leading edge films (F) but no endwall film cooling. Figure 3.15(a) shows the conduction correction parameter used to determine the corrected effectiveness in Figure 3.15(c) which corresponds to the uncorrected effectiveness in Figure 3.15(b). Clearly when the effect of heat conduction into the film-cooled surface is taken into account, the effectiveness is globally reduced compared to the uncorrected measurements.

Substitution of Equation 3.20 into Equation 3.21 yields the corrected effectiveness as a linear function of the uncorrected effectiveness T^*, as shown in Equation 3.22.

$$\begin{aligned}\eta(\mathbf{x}) &= \frac{T_\infty - \frac{T_s(\mathbf{x}) - \gamma(\mathbf{x})T_c}{1-\gamma(\mathbf{x})}}{T_\infty - T_c} \\ &= \frac{T_\infty}{T_\infty - T_c} - \frac{T_s - T_\infty + T_\infty - \gamma(\mathbf{x})T_c}{(T_\infty - T_c)(1-\gamma(\mathbf{x}))} \\ &= \Big[\frac{T_\infty}{T_\infty - T_c} - \frac{T_\infty - \gamma(\mathbf{x})T_c}{(T_\infty - T_c)(1-\gamma(\mathbf{x}))}\Big] + \Big[\frac{1}{1-\gamma(\mathbf{x})}\Big]T^*\end{aligned} \tag{3.22}$$

Comparing the coefficients of T^* with Equation 3.16 and rearranging gives Equation 3.23 for the experimental conduction factor $\gamma(\mathbf{x})$ in terms of the test piece conductive and convective heat transfer properties, which is equal to the analytically derived $\eta_{correction}$ for $\eta = 0$.

$$\gamma(\mathbf{x}) = \frac{1}{1 + \frac{Lh_e}{k} + \frac{h_e}{h_i}} \tag{3.23}$$

In section 4.7, a novel HTC measurement technique is elucidated by which the uncooled external leading edge HTC was measured to be around $h_e \approx 60\,\mathrm{W\,m^{-2}\,K^{-1}}$ (though varying slightly across the surface). This compares favourably with the Hilpert correlation (Equation 3.17) prediction of $h_e \approx 63\,\mathrm{W\,m^{-2}\,K^{-1}}$. The corresponding internal HTC can be estimated by also substituting into Equation 3.23 the thickness of the Rohacell walls, their nominal thermal conductivity, and the experimentally measured value of the conduction factor ($L = 0.009\,\mathrm{mm}$, $k = 0.032\,\mathrm{W\,m^{-1}\,K^{-1}}$, $\gamma(\mathbf{x}) = 0.1$). This results in an internal HTC of $h_i \approx 22\,\mathrm{W\,m^{-2}\,K^{-1}}$, and also implies a Rohacell test piece Biot number of $Bi \approx 17$ (based on the external HTC). This is approximately half what is estimated with the Dittus-Boelter equation, a discrepancy which is likely due in large part to the insufficient flow development in the coolant passage for this equation to truly apply, and the presence of flow extraction by film cooling holes. This ratio of $\frac{h_e}{h_i} \approx 3$ would be lower in a real leading edge where the internal HTC would be bolstered by impingement jets or turbulation elements.

By using the conduction correction parameter as measured on the uncooled leading edge, it is implicitly assumed for corrections to the present cooling experiments that the HTCs

remain unchanged due to film cooling. In fact, the external HTCs tend to increase, while the effects of flow extraction from the coolant passage on internal HTCs have not been measured. Assuming that the internal HTCs do not change significantly, and given that the external HTCs only rise significantly on the suction side in regions of very high effectiveness (where the effect of any correction is small), the uncooled correction factor is still applicable without significantly affecting the final results. However, the technique could potentially be further improved by using known, spatially variant, film-cooled external and internal HTCs to determine more accurate correction factors from the uncooled ones.

3.9 Conclusions

This chapter has described the workings of the Oxford Combustor-Turbine Interactions Rig. Its dilution ports, endwall film cooling and sophisticated, interchangeable NGV leading edge test pieces have generated novel insights into the combustor-turbine engine environment and resulted in the development of new experimental techniques. The first insight discussed in this chapter is that the pressure ratio and capacity of the NGV cascade are slightly reduced by the presence of the upstream dilution port coolant flow. The second is that the limited wall thickness of engine-representative NGV leading edge test pieces means that even when they are constructed from a low thermal conductivity material such as Rohacell, there is still a film effectiveness conduction error of up to 0.1.

Three novel techniques useful to the operation of the CTI rig were developed:

1. Controlling the mass flow rates of two different cooling features from a single feed plenum. This requires pressure measurements both upstream and downstream of a pressure loss component (e.g. perforated plate) for just one of the cooling features. Initially the other feature must be sealed so that air flows only through the instrumented feature, and the discharge coefficient of the pressure loss component is measured as a function of the known mass flow rate. After the second feature is unsealed, this permits estimation of the flow rate through the instrumented feature

based on the measured pressure losses. The second feature's mass flow rate is then the difference between the total mass flow rate upstream of the supply plenum, and the estimated flow rate of the instrumented feature.

2. Theoretical and empirical prediction of changes to the rig's dimensionless mass flow rate parameters when the heater mesh is switched on. This is useful as a means of saving heater power while adjusting the rig's various coolant mass flow rates and also as a means of prolonging the heater's working life. The empirically recorded hot-from-cold parameter relationships were highly linear, matching the theoretical predictions closely.

3. Experimental correction for film effectiveness conduction errors. With the infrared cameras kept stationary after a surface temperature measurement on a film-cooled test piece, the test piece is replaced by one with no film cooling holes. The experiment is then repeated with the dilution ports and endwall film cooling holes sealed so that a known, uniform hot gas driving temperature is applied to the entire leading edge. This permits the calculation of a conduction correction parameter over the entire test piece surface of interest, which can then be used to correct the film effectiveness data on a pixel-by-pixel basis. An advantage of the experimental technique over a theoretical correction is that the test piece material thermal conductivity and the internal and external heat transfer coefficients do not need to be known in advance. Furthermore, the correction is spatially variant and can in principle take into account any local variations in the internal or external heat transfer coefficients, or even the test piece thermal conductivity.

Chapter 4

Infrared Thermography

In this chapter, the theory of infrared thermography for surface temperature measurement in the Oxford Combustor-Turbine Interactions (CTI) rig is developed into a calibration methodology which includes a camera black-body calibration, experimental determination of the grey-body properties of the test surfaces and optical pathways, and a novel test piece for determining the spatial distribution of radiation reflected from the vane surface of interest. The requirement to perform this type of spatially resolved calibration is clarified by quantifying the error which would be expected if a leading edge film effectiveness experiment were to be carried out in the CTI rig in the presence of a cooled endwall, but without a spatial calibration. Finally, a novel technique is described for the determination from a single heated test of both key film effectiveness performance parameters; the film effectiveness and the heat transfer coefficient. The technique makes use of the specific advantages of infrared transient surface temperature measurements, and does not require assumptions about the material thickness underlying the test surface or the uniformity with depth of its initial temperature distribution. This relieves constraints on the design of film cooling test pieces and reduces uncertainty in the results. The calibration technique was published in a paper for an international conference [92] and a related journal paper [93], and the single-test film performance measurement technique has been accepted for publication by a journal [94].

4.1 Introduction to Full-surface Temperature Measurement

In this study, infrared (IR) thermography has been used to obtain highly detailed, full-surface temperature measurements on film-cooled leading edges. In the field of turbomachinery heat transfer research, several other technologies are also often employed for such measurements, and their principles, advantages, and disadvantages are outlined below.

1. **Infrared**

   Collisions between atoms and molecules cause all baryonic matter to passively expel electromagnetic radiation generated by the resulting accelerations of charges and oscillations of electric dipoles. Since this process represents a transformation of matter's internal thermal energy, the radiation is known as thermal radiation. Infrared thermography is the imaging of temperature distributions, usually of the surfaces of solid bodies, by observation of IR region thermal radiation, which is the thermal radiation most strongly emitted by matter near room temperature.

2. **Liquid crystals and thermographic phosophors**

   Certain chiral organic molecules known as liquid crystals can, within specific temperature ranges, form into layers which stack with a temperature-dependent pitch. A given pitch results in a narrow-banded, wavelength-selective reflection [95]. Substances reflecting in the visible spectrum thus exhibit a temperature-dependent colour play when illuminated by white light. When suitably encapsulated, such substances can be thinly painted onto an experimental surface to provide surface temperature measurements by recording any transient colour changes with a conventional digital video camera. During a transient driving gas temperature rise, the temperature indicated by the crystals lags the temperature of the underlying surface by a short timespan of order 3 ms [96]. A similar though less frequently used technique employs thermographic phosphors. These substances are instead illuminated by ultraviolet laser light which excites electrons in the phosphor to higher energy states. These then return to their original state via pathways which include photon emissions in the visible spectrum (fluorescence).

3. **Thermal paint**

   Thermal paints undergo irreversible colour changes dependent on the maximum temperature they have reached. The colour changes are due to the creation of new compounds by the decomposition at elevated temperatures of constituent mineral phosphates, carbonates, and aluminates [97]. By applying paints to engine test components and running them at engine or engine-representative conditions, the surface temperatures reached can be deduced afterwards by examination of the distribution of paint colours. The mineral decomposition and hence the colours generated may have a dependence on the time of exposure to elevated temperatures, which must be included in the colour-temperature calibrations.

4. **Pressure-sensitive paint**

   Although not a direct measurement of surface temperature, this technique is still widely used to measure film effectiveness. Pressure-sensitive paints (PSPs) include complex organic molecules which are capable of absorbing light of one wavelength (typically blue or ultraviolet) and subsequently emitting this energy as light of a higher wavelength (typically red) [98]. However, the presence of molecular oxygen creates reaction pathways for the excited molecules to return to their original state without a photon emission. The two competing molecular relaxation mechanisms mean that, when appropriately illuminated, the paint emits with greater intensity for lower partial pressures of oxygen, and vice-versa. Observation of this intensity (e.g. with a charge-coupled device camera [99]), combined with a calibration which takes into account its slight temperature dependence, permits highly localised measurements of oxygen partial pressures. When a non-oxygen foreign gas is injected as a film coolant onto a surface coated with a PSP, the oxygen partial pressure indicates the mass-fraction of coolant at a given location, which is taken to approximate the film effectiveness in what is termed a 'mass/heat transfer analogy'.

After careful consideration of the literature and the techniques used in the Oxford Thermofluids Institute and similar laboratories, the author compiled Table 4.1 of the merits and drawbacks of the different techniques.

Table 4.1: The key advantages and disadvantages of various full-surface temperature measurement techniques with respect to film cooling experiments.

Technology	Advantages/Disadvantages
Infrared	**Advantages**: • Transient temperature measurements • Wide temperature range with a single calibration • Relatively simple paint application • No need for illumination of test surface **Disadvantages**: • Expensive capital costs (camera, lenses, and IR-transparent windows) • Accuracy depends upon ability to account for reflections and the properties of the optical pathway
Liquid crystals and thermographic phosphors	**Advantages**: • Transient temperature measurements • Relatively inexpensive equipment **Disadvantages**: • Degradation of active molecules over time - recoating required • Limited temperature range with any given coating • Requires highly uniform illumination - difficult on curved surfaces
Thermal paint	**Advantages**: • No *in-situ* optical access required • Accuracy independent of the experimental optical scenario **Disadvantages**: • No transient temperature measurements (film effectiveness only) • Low accuracy due to limited colour contours • New test piece and coating required for every experiment
Pressure-sensitive paint	**Advantages**: • Relatively inexpensive equipment • No experimental heating required **Disadvantages**: • Not a true temperature measurement (film effectiveness only) • Degradation of organic molecules over time - recoating required • Requires foreign gas and supply apparatus • Requires highly uniform illumination - difficult on curved surfaces

The curvature of the NGV leading edge and the presence of the combustor simulator makes uniform illumination difficult. Furthermore, the CTI rig's large size would require a substantial mass flow rate of foreign gas in order to achieve engine-representative Reynolds numbers and blowing ratios. For these reasons, liquid crystals and PSPs were considered unviable. Thermal paints were discounted because the need to replace test pieces after each experiment would have greatly escalated the cost and time requirements of experiments for the present work, since each film-cooled leading edge has been tested across a range of leading edge and combustor coolant flow rate conditions. Moreover, thermal paints are usually developed by industry for experiments at far higher temperatures than can be achieved in the CTI rig. Thus IR thermography was chosen as the most suitable full-surface temperature measurement technique for its flexibility and relative simplicity of deployment. The high initial cost of the CTI rig's dual IR camera setup was partially offset by the use of existing cameras in the Oxford Thermofluids Institute, such that only one camera was purchased specifically for the present work.

4.2 Two Types of Infrared Cameras

The spatial and temporal resolution capabilities of IR cameras have continually improved since the beginning of their widespread commercialisation in the late 1980s [100], which combined with reducing costs has made them increasingly popular in turbomachinery heat transfer research in recent years. The FLIR A655sc cameras used in this study each feature a 640×480 focal plane array (FPA) of microbolometers, with each corresponding to a pixel of observed surface temperature. Each pixel's position on the FPA is described by a vector of two integers, $\boldsymbol{x}$. A microbolometer is a micron-scale plate of material (most commonly vanadium oxide [101]) with a strongly temperature-dependent resistance and a rapid approach to equilibrium temperature for a given incident IR radiative power. The slight differences in construction between these detectors are corrected for by the camera's internal software by adjusting for the differences in the offset and slope of each detector's voltage characteristic, so that all such characteristics become essentially identical [102]. Factory-calibrated corrections for the camera's own internal thermal emissions onto the

FPA are constantly applied on the basis of temperature sensors within the camera. The voltages of each microbolometer are digitised as values between 0 and 16384 (2^{14}), known as the raw counts $R(\boldsymbol{x})$.

A second type of IR camera features semiconducting detectors which produce a current due to the excitation of valence electrons into the conduction band by incident IR photons. Such electron transitions are also possible due to the internal thermal energy of the detectors, and cryogenic cooling of the FPA is necessary to reduce the noise of internal thermal effects relative to the effects of the IR signals of interest. The advantages of cooled IR cameras include higher resolutions, lower pixel response times (permitting much higher frame rates), and higher temperature sensitivity [103]. However, cryocoolers are expensive and take time to sufficiently cool the semiconductor FPA before the camera can be used. Microbolometer IR cameras are therefore used in this study since they are the cheaper and more versatile of the two types.

4.3 Thermal Radiation Theory

4.3.1 Interactions Between Infrared Radiation and Matter

To achieve accurate IR measurements in most practical situations, it is not sufficient to consider only the thermal radiation originating from the surface of interest, since this surface will also reflect some proportion of the thermal radiation incident on it from other surfaces. Additionally, the radiative properties of any optics involved in the observations must be taken into account, in order to determine the true radiative power of the IR radiation thermally emitted from surfaces of interest, and hence the temperature distributions on those surfaces.

All real bodies absorb, reflect, and transmit certain proportions of incident electromagnetic radiation, dependent on both wavelength and angle of surface incidence. Since they are as such not perfect black-body emitters, they are referred to as 'grey-bodies'. For most

materials, the wavelength dependence is negligible across the range relevant to infrared thermography [102]. These proportions are known as absorptivity (α), reflectivity (ϱ), and transmissivity (τ), respectively, and can be represented by values between zero and one, which under the assumption of weak dependence on wavelength and incidence angle results in the relationship:

$$\alpha + \varrho + \tau = 1 \tag{4.1}$$

According to Kirchoff's law of thermal radiation, a body in thermodynamic equilibrium with its surroundings must be emitting the same amount of radiation as it is absorbing, and is said to have emissivity (ϵ) equal to its absorptivity (which is also true to a good approximation for most non-equilibrium applications [104]):

$$\epsilon = \alpha \rightarrow \epsilon + \varrho + \tau = 1 \tag{4.2}$$

An idealised absorber/emitter is known as a black-body, which reflects and transmits no incident radiation (all incident radiation is internally absorbed and balanced by an exactly equal amount of emission i.e. $\alpha = \epsilon = 1, \varrho = \tau = 0$). Experimental test pieces for IR observations are typically painted black in order to maximise the absorptivity and emissivity. This minimises the transmissivity and reflectivity of the surfaces of interest, and hence the proportion of extraneous IR radiation (i.e. not emitted by the test surface) reaching the IR sensor from the surroundings. In fact, the IR transmissivity of most solids is effectively zero:

$$\tau = 0 \rightarrow \epsilon + \varrho = 1 \tag{4.3}$$

However, since no paint can render an object a perfect black-body ($\epsilon < 1$), there will be some appreciable amount of reflection ($\varrho > 0$) from a test piece surface of IR radiation emitted by bodies surrounding the test piece. A calibration is therefore necessary to account for the portion of camera-incident radiation not solely due to the thermal emissions of the observed test piece, in order to improve the accuracy of the temperature measurements on its surface.

4.3.2 Planck's Law and the Stefan-Boltzmann Law

Derivation of the infrared calibration used in the present work begins with the laws of black-body thermal radiation. At any given temperature, all black-bodies thermally emit electromagnetic radiation with a unique spectral power density (or 'spectral radiance', B_λ), defined as the radiated power of a unit of wavelength per unit solid angle, per unit surface area of emission, and having units of $\mathrm{W\,sr^{-1}\,m^{-3}}$. The spectral radiance is described by Planck's law (which can be derived from quantum and statistical mechanics arguments for a cavity with conducting walls and in thermodynamic equilibrium):

$$B_\lambda(\lambda, T_{bb}) = \frac{2hc^2}{\lambda^5} \frac{1}{e^{hc/(\lambda k_B T)} - 1} \tag{4.4}$$

where h is the Planck constant, c is the speed of light in the medium into which emission occurs, λ is a spectral component wavelength, k_B is the Boltzmann constant, and T_{bb} is the temperature of the black-body. With increasing temperature, the energy density at all wavelengths increases, though the emissions are progressively biased to the shorter wavelengths (higher energies). As shown in Figure 4.1, this wavelength of maximum energy density slowly decreases with increasing temperature. Objects near to room temperature emit almost entirely in the IR spectrum. At around 800 K, most materials begin to exhibit sufficient radiative power in the visible spectrum to be detected by human eyes as a red glow [105]. Integration of Planck's law over the irradiated half-sphere and the entire wavelength spectrum yields the Stefan-Boltzmann law for the radiant power emitted per unit surface area (or 'radiosity', j) by a black-body at temperature T_{bb}:

$$j_{bb} = \sigma T_{bb}^4 \tag{4.5}$$

where $\sigma = \frac{2\pi^5 k_B^5}{15h^3c^2} \approx 5.67 \times 10^{-8}\,\mathrm{W\,m^{-2}\,K^{-4}}$ is the Stefan-Boltzmann constant. The emissivity, ϵ, of a real grey-body is defined as the fraction of its radiative power compared to that of a black-body at the same temperature, T, such that its radiosity is given by:

$$j_{gb} = \epsilon \sigma T^4 \tag{4.6}$$

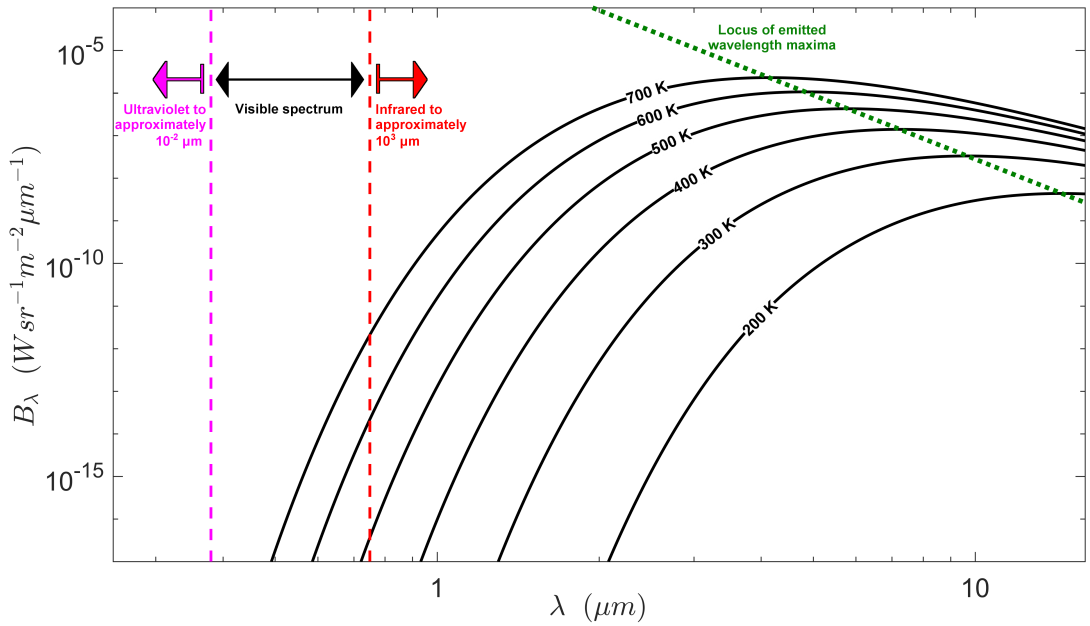


Figure 4.1: Graphical illustration of Planck's law, showing that an ideal black-body in thermal equilibrium and near room temperature emits thermal radiation mainly in the infrared spectrum. Spectrum boundaries from [1].

4.3.3 Grey-body Analysis in the CTI Rig

Using the Stefan-Boltzmann law and the grey-body properties of the CTI rig test piece, its surroundings, and the optical pathway, a detailed mathematical expression for the surface temperature of interest can be derived from consideration of the components of radiative power incident on the individual microbolometer receivers of the IR cameras (i.e. pixels, each with a vector coordinate $\boldsymbol{x}$ within the FPA) [102]. Figure 4.2 illustrates these components.

1. **Test surface emissions**, $P_s = \xi\tau \times A_s\epsilon\sigma T_s^4$

   The radiative power, P_e, emitted by the small portion of test piece surface area A_s which exactly fills the field of view of one pixel, $\boldsymbol{x}$, is given by:

$$P_e(\boldsymbol{x}) = A_s(\boldsymbol{x}) \times j_{gb}(\boldsymbol{x}) = A_s(\boldsymbol{x})\epsilon\sigma T_s^4(\boldsymbol{x}) \tag{4.7}$$

   where T_s is the average temperature of that small region and $j_{gb}(\boldsymbol{x})$ is its grey-body radiosity. For the remainder of this chapter, the explicit indication of the

pixel-dependent quantities is removed for simplicity:

$$P_e = A_s \times j_{gb} = A_s \epsilon \sigma T_s^4 \tag{4.8}$$

Two reducing factors, ξ and τ, must be applied to P_e in order to obtain P_s, the power of test surface-emitted radiation incident on the camera microbolometer:

$$P_s = \xi\tau \times A_s \epsilon \sigma T_s^4 \tag{4.9}$$

The view factor $\xi \ll 1$ is the fraction of P_e which is directed towards the relevant pixel. This is necessarily small, in accordance with the small solid angle subtended by a point on the test surface area element and the pixel's equivalent receiving area on the infrared window. The transmissivity, $\tau < 1$, is the combined attenuation of this power due to the window and air in the optical pathway.

2. **Test surface reflections**, $P_R = \xi\tau(1-\epsilon) \times A_s \sigma T_R^4$

   $(1-\epsilon)A_s \sigma T_R^4$ is the radiant flux reflected by a test surface element of area A_s which exactly fills the field of view of a pixel. Since the test piece is opaque, the reflectivity of the test surface is given by $\varrho = 1 - \epsilon$. ξ and τ are as described above. Since the temperatures and emissivities of the surrounding rig vary spatially, and since reflection from the test surface is some combination of diffuse and specular, the 'effective reflected temperature' T_R cannot be computed directly. It is a virtual temperature of a hypothetical, ideal black-body emitter surrounding the observed test surface, which would result in an equivalent reflected power as that which is reflected towards the pixel in question.

3. **Optical pathway emissions**, $P_{opt}(T_{window}, T_{air}, d)$

   The optical pathway (including the IR-transparent window and the heated air in the combustor simulator) between the test surface and the camera is also optically active, emitting some amount of infrared radiation throughout. This power contribution is expected to be small, owing to the high transmissivities and correspondingly low emissivities of these optical components.

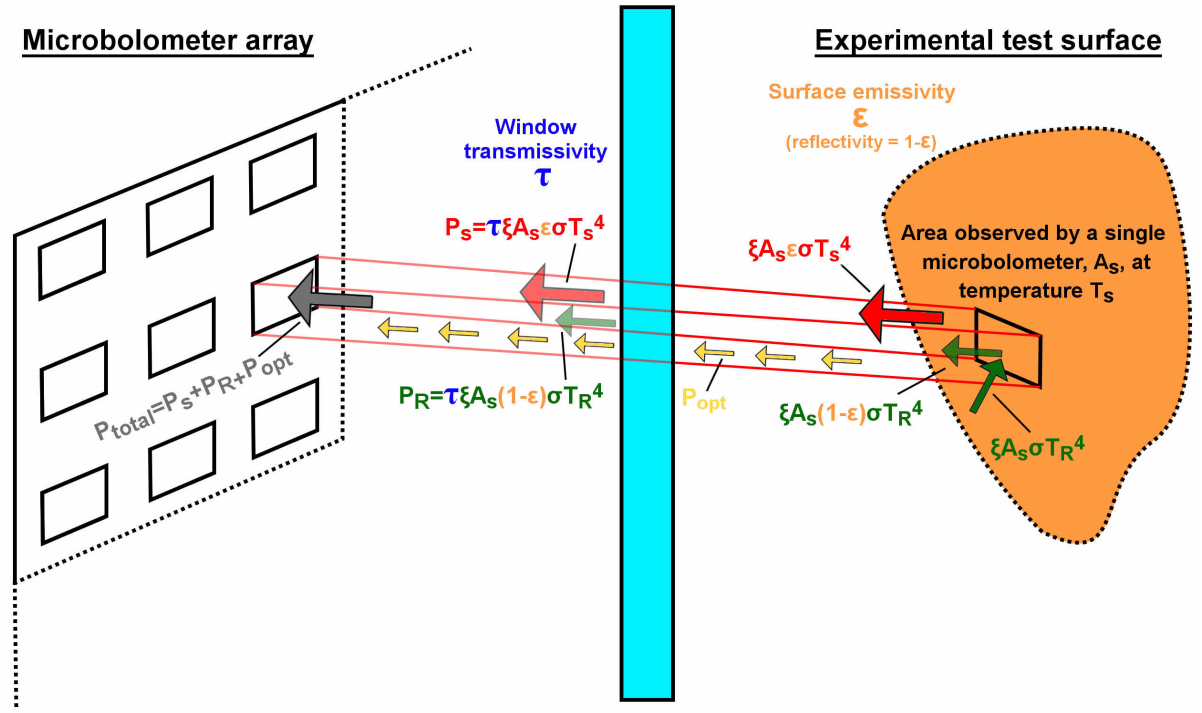


Figure 4.2: Three sources of infrared radiation incident upon an IR camera's individual microbolometer from a small surface area on a test surface. The test surface emissions (P_s) are attenuated by the window. The test surface reflections (P_R) are attenuated first by their reflection from the surface and then by the window.

Since the IR camera is calibrated to output an effective black-body temperature T_{bb} (refer to section 4.4), the total power received by a pixel can be expressed as:

$$P_{total} = \xi A_s \sigma T_{bb}^4 \tag{4.10}$$

which is equal to the sum of the component sources of radiative power, such that:

$$P_{total} = \xi A_s \sigma T_{bb}^4 = \xi\tau \times A_s \epsilon \sigma T_s^4 + \xi\tau(1-\epsilon) \times A_s \sigma T_R^4 + P_{opt} \tag{4.11}$$

Rearrangement yields the following expression for the test surface temperature:

$$T_s = \sqrt[4]{\frac{\sigma T_{bb}^4 - \left[\sigma(1-\epsilon)\tau T_R^4 + \frac{P_{opt}}{\xi A_s}\right]}{\sigma\tau\epsilon}} \tag{4.12}$$

Though unknown, the product ξA_s is assumed to be some approximately constant value for any pixels observing an in-focus test surface, since the camera raw count output is

known to have negligible dependency on the range at which a surface is viewed. As noted above, the effective reflected temperature T_R and the received emissive power due to the optical pathway P_{opt} are also extremely difficult to estimate. A desirable practical alternative is to measure the combined quantity $\sigma(1-\epsilon)\tau T_r^4 + \frac{P_{opt}}{\xi A_s}$. A localised measurement of this quantity is possible if the camera-observed black-body temperature T_{bb} can be referenced to a known surface temperature, T_w, at a nearby reference surface thermocouple. Then, by rearrangement of Equation 4.12, and normalisation as per Kirollos and Povey [106] by the factor $(1-\tau\epsilon)$, the above quantity can be determined by:

$$q^* = \frac{\sigma T_{bb}^4 - \sigma\tau\epsilon T_w^4}{1-\tau\epsilon} \tag{4.13}$$

Further borrowing from Kirollos and Povey [106], this term is referred to as the 'surrounding radiance'. While the thermal emissions of its surroundings do indeed increase the net radiance of a test surface, the 'surrounding radiance' as measured does not strictly have the units of radiance ($\mathrm{W\,sr^{-1}\,m^{-2}}$), since in this formulation no account has been taken of the effective solid angle subtended by a point on the test surface and an individual camera pixel. It is rather a measure of the camera-perceived (i.e. via the black-body calibration of section 4.4) *radiosity* of the test surface not due to its own thermal emissions, having units of $\mathrm{W\,m^{-2}}$. In the CTI rig, this extraneous radiosity is primarily due to reflection off the test piece of thermal radiation emitted from the wind tunnel walls, rather than the emissions of the optical pathway, which are typically small for highly IR-transparent media. Using the practical definition of the measured surrounding radiance in Equation 4.13, the working equation for IR surface temperature measurements in the present study is as follows:

$$T_s = \sqrt[4]{\frac{\sigma T_{bb}^4 - (1-\tau\epsilon)q^*}{\sigma\tau\epsilon}} \tag{4.14}$$

Emissivity, ϵ, and transmissivity, τ, can reasonably be treated as constants under the conditions of the CTI rig, and their measurement is discussed in section 4.5. However, since the surrounding radiance, q^*, is a strong function of the temperatures in the rig, this is ideally measured separately for each run.

4.4 Black-body Calibration

The black-body calibration maps the camera's digitised voltage outputs (raw count, $R(\boldsymbol{x})$) to the temperature of an observed ideal black-body, T_{bb}. This stage of the calibration is independent of the true emissivity of the test surface and the amount of radiation it reflects, as well as the transmissivity of the optical pathway. These effects are taken into account during the grey-body calibration, which then maps T_{bb} to the surface temperature, T_s.

By design, the raw count output of each FLIR A655sc IR camera (discussed in section 4.2) is highly linear with the radiosity of an observed black-body, such that:

$$j_{bb} = \sigma T_{bb}^4(\boldsymbol{x}) = c_1 R(\boldsymbol{x}) + c_2 \tag{4.15}$$

The constants c_1 and c_2 were determined using the enclosed cylindrical cavity shown in Figure 4.3, which was spray-painted a thick black inside and out. This minimised the amount of thermal radiation entering the cavity from outside, under which condition the interior resembles an ideal black-body when isothermal [104]. Painting and instrumentation of the inside of the cavity was made possible by 3D-printing it in two halves which were glued together after painting and insertion of a thermocouple into the side wall. Except for a periscope-like aperture, the cavity was entirely submerged in warm water, which caused it to remain essentially isothermal during the water's slow temperature decrease. The aperture is inclined to allow the IR camera to view inside the isothermal cavity without water vapour fogging or heating the camera and lens. An in-wall thermocouple measured the cavity temperature, which is taken as a black-body temperature, T_{bb}, while the camera simultaneously recorded corresponding raw count values $R(\boldsymbol{x})$ from pixels through the aperture. These raw count values were averaged for each T_{bb} measurement and the results yielded the constants c_1 and c_2 via linear regression. This process was repeated for both of the IR cameras used in film cooling experiments (cameras A and B) and with two lens types (focal lengths $f = 13.1\,\text{mm}$ and $f = 24.6\,\text{mm}$). As shown in Figure 4.4, the linear fits were found to vary slightly between the camera systems used

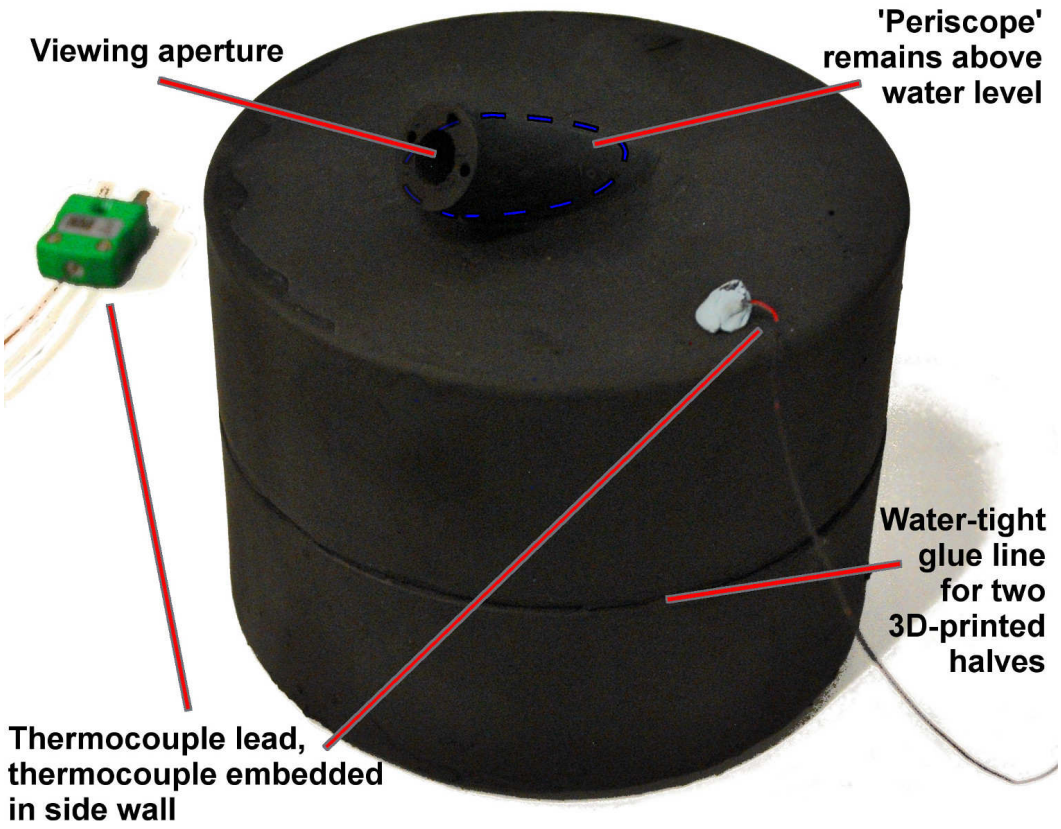


Figure 4.3: 3D-printed cavity black-body used to calibrate the black-body temperature corresponding to IR camera raw count outputs.

during the study, due to their subtly different optical properties. Experimental surface temperature data have therefore been processed with the black-body calibration constants appropriate to their acquisition device. Also considered with a third camera (C) and a single lens ($f = 13.1\,\text{mm}$) was the effect of the camera observation distance, d, on the black-body calibration. For a given black-body cavity radiosity (as calculated according to the thermocouple temperature), the camera receives more thermal radiation (as indicated by the raw counts) when it is closer to the cavity, due to reduced attenuation by the reduced length of the air optical pathway. Since the effect is small, and can be corrected for during the grey-body calibration procedure, the distances used in the black-body calibrations were not carefully matched to those which are fixed by the CTI rig IR camera positions relative to the observed NGV leading edge.

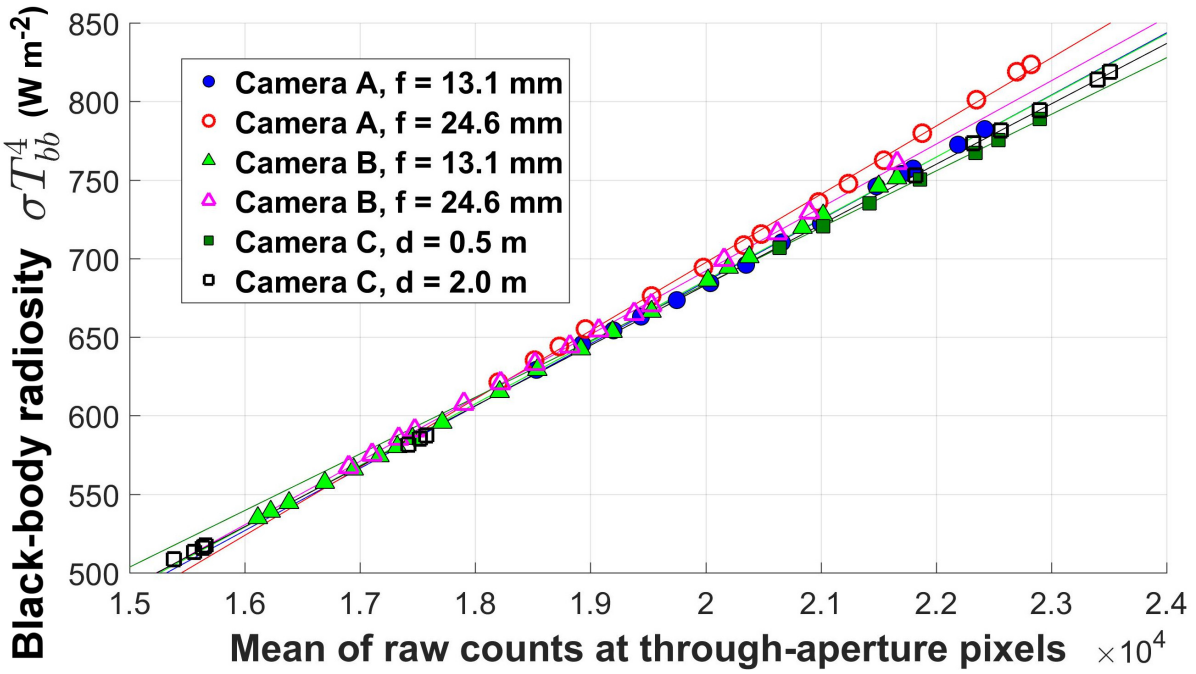


Figure 4.4: Linear black-body calibration relationships for cameras A and B used for CTI rig surface temperature measurements (each with two different lenses) and a third camera C illustrating viewing distance dependence.

4.5 Grey-body Calibration

The grey-body calibration maps the hypothetical black-body temperatures, T_{bb}, (determined by the black-body calibration) to the final IR surface temperature measurements, T_s. As per Equations 4.13 and 4.14, this requires measurements of the following quantities:

1. Emissivity of the test surface, ϵ.
2. Transmissivity of the optical pathway between the test surface and the IR camera sensor (air and IR-transparent window), τ.
3. Normalised surrounding radiance i.e. the camera-incident radiosity due to reflections from the test surface of radiation emitted by the surroundings, q^*.

It will be shown that the emissivity and transmissivity can each be treated as constant for CTI rig experiments. However, since the thermal radiation emitted by the test surface surroundings depends on their temperature distribution, the surrounding radiance must be measured for each heated experiment.

4.5.1 Dependence of Emissivity on Observation Angle

The emissivity of a real surface typically drops off with higher viewing angles from the surface normal, though for most surfaces there is little variation for viewing angles below 60° [107]. Tests were conducted on the viewing angle dependence of the emissivity of the black paint used to coat all of the leading edge test pieces in the present study (*Autotek Very High Temperature*). An aluminium plate of dimensions approximately $100 \times 100 \times 5\,\text{mm}$ was instrumented with two surface thermocouples on one side and then uniformly painted. The camera was fixed to observe the painted plate (at short range and with no additional optics) and the plate was rotated between tests such that the camera observed it at angles to the surface normal from 0° to 80°. For each test, the plate was heated with a heat gun and then allowed to cool slightly in order to become isothermal. Once it had cooled to approximately 35 K above the ambient temperature T_{amb} the two thermocouple temperatures $T_{w,1}$ and $T_{w,2}$ were recorded, as were the corresponding mean T_{bb} values measured by the camera at pixels nearby the surface thermocouples. These values were used to estimate the emissivity on the assumptions that the transmissivity of the short air optical pathway between the plate and the camera was approximately unity ($\tau = 1$) and that the thermal emissions of the optical pathway were negligible ($P_{opt} = 0$) i.e. the radiosity not due to the plate's thermal emissions is due only to reflections from the painted plate of the emissions of surrounding black-bodies at a highly uniform ambient temperature T_{amb}. Then Equation 4.11 can be simplified to:

$$T_{bb}^4 = \epsilon T_w^4 + (1 - \epsilon) T_{amb}^4 \tag{4.16}$$

This can be rearranged to give the following expression for the emissivity of the painted plate surface:

$$\epsilon = \frac{T_{bb}^4 - T_{amb}^4}{T_w^4 - T_{amb}^4} \tag{4.17}$$

At each observation angle, the above calculation was performed once for each thermocouple, and the two results were averaged. The results for emissivity as a function of the viewing angle are shown in Figure 4.5(a). The emissivity begins to reduce slightly

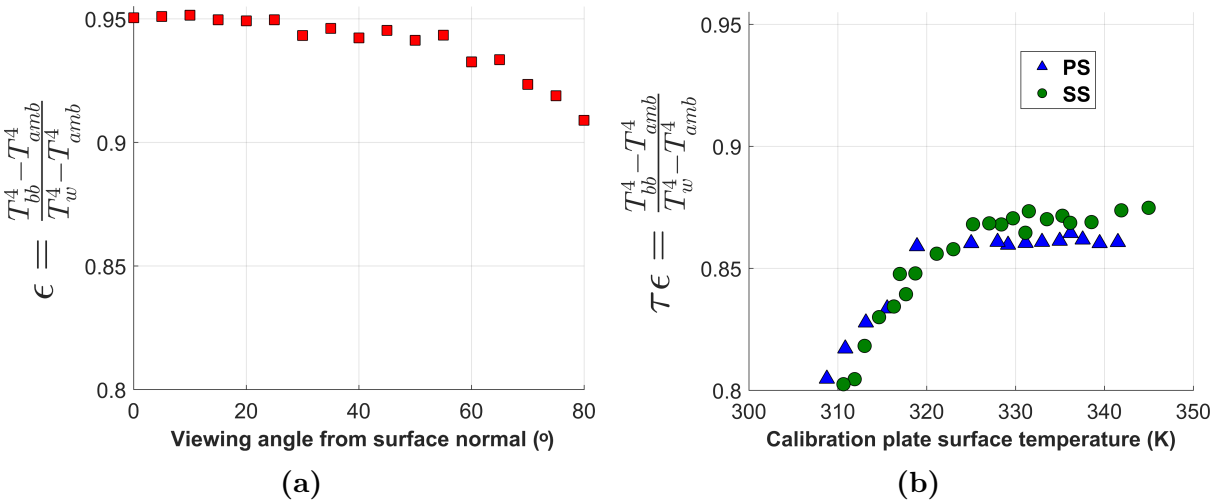


Figure 4.5: (a) Black paint emissivity as a function of viewing angle, as measured on a flat aluminium plate at a constant temperature and (b) Combined transmissivity-emissivity factor as a function of plate temperature, plate viewed through the rig IR-transparent windows at a constant viewing angle.

starting at a viewing angle of around 30°. However, only beyond a viewing angle of approximately 60° does the reduction exceed one percent of the original value. This finding suggests that, so long as the viewing angles in the CTI rig experiments do not exceed 60°, the emissivity can reasonably be treated as a constant, which somewhat simplifies the processing of IR surface temperature data. The goal of observing the entire central leading edge of the CTI rig without exceeding this angle was the main consideration when choosing the positions of the two IR-transparent windows. A MATLAB script was used to investigate the observation angle distributions achieved for various pairs of window positions, in a plane orthogonal to the cascade span. It was desirable for the cameras to be placed at the midspan so that IR surface temperature data could be laterally averaged without requiring any image transformation. By targeting an in-plane maximum observation angle of 40°, it was ensured that the observation angles for surface regions near the endwalls were also all below 60°. The two window positions chosen are shown in Figure 4.6.

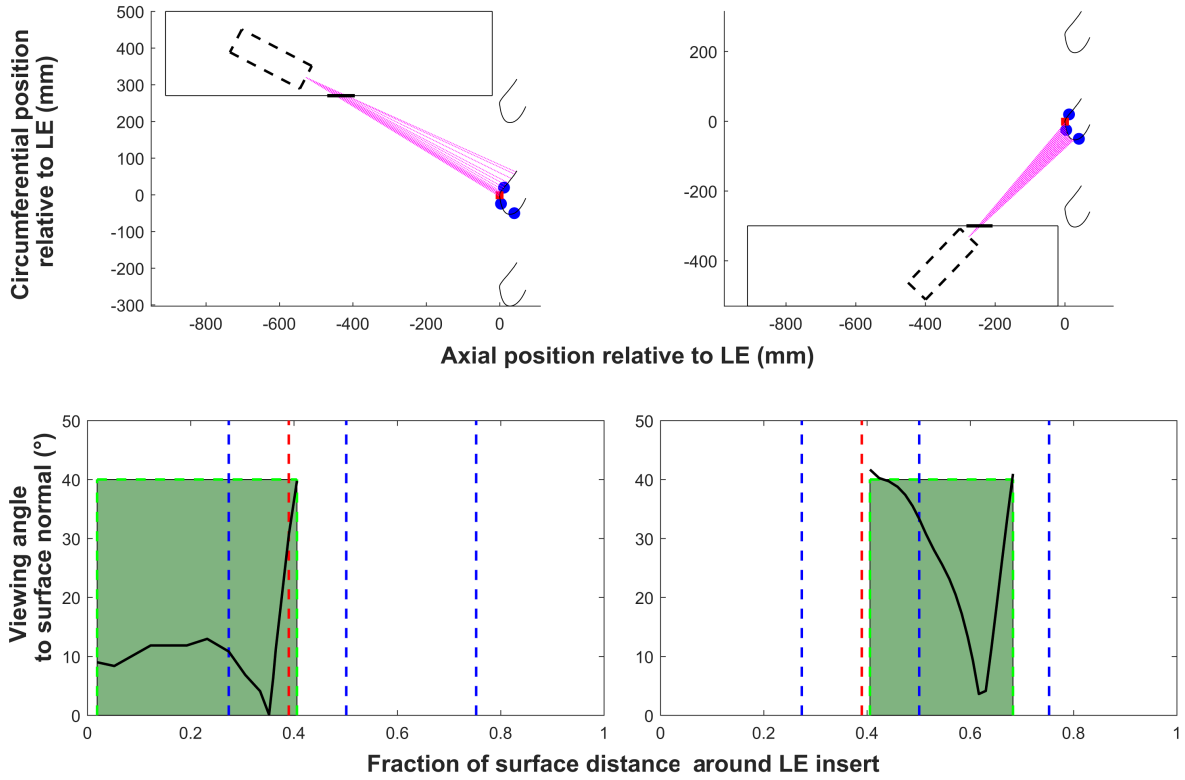


Figure 4.6: The distribution of observation angles with the test piece surface normals around a cross section of the central NGV leading edge for the two camera positions in the CTI rig.

4.5.2 Dependence of Window Transmissivity on Temperature

The IR-transparent windows used are Germanium with a 75 mm diameter, 5 mm thickness, and an anti-reflective coating which increases the transmissivity of the window by reducing the amount of radiation in the nominal wavelength range of 3 to 12 µm which is reflected from the window. Germanium windows are a cost-effective option suitable for low temperatures. The transmissivity of Germanium windows decreases with increasing temperature and they are recommended for use below 100 °C [108]. However, a thermocouple glued to the side of one of the rig windows detected a temperature rise of just 1.5 °C above ambient temperature during a typical heated experiment in the CTI rig. Furthermore, in an experiment akin to the above emissivity experiment, the window transmissivity was measured as essentially unchanged between ambient temperature (22 °C) and when the window was heated by a hot air gun (40 °C). For these reasons, the window transmissivity can also reasonably be treated as a constant in the CTI rig.

Given the constancy of both the transmissivity and the emissivity, and their appearance only as a combined product, $\tau\epsilon$, in Equations 4.13 and 4.14, these quantities can also be measured together as that combined product. This approach removes the need for independent experimental assessments of each quantity, which aside from being convenient also reduces the overall surface temperature measurement uncertainty. By conducting the measurement *in-situ* and individually for each camera, any transmissivity variation between the two different optical pathways can potentially be measured. These tests were carried out by placing the painted, aluminium plate at the approximate position of the leading edge, and heating it with a heat gun. As the plate cooled, simultaneous measurements were periodically taken of the two surface thermocouple temperatures and their corresponding, camera-observed black-body temperatures. A mathematical expression for the product ($\tau\epsilon$) can be derived by again assuming that the radiation reflected from the plate was emitted by black-body surroundings at the measured ambient temperature T_{amb}. The addition of the window to the optical pathway reduces the transmissivity but also increases the thermal emissions of the optical pathway. The P_{opt} term in Equation 4.11 can be estimated by assuming that the window's negligible reflectivity is approximately zero ($\varrho = 0$). Then from Equation 4.3, it follows that the window's emissivity is $\epsilon = 1 - \tau$. Since the window is also at the ambient temperature, $P_{opt} = \xi A_s \sigma (1 - \tau) T_{amb}$, and Equation 4.11 can be simplified to:

$$T_{bb}^4 = \tau\epsilon T_w^4 + \tau(1 - \epsilon) T_{amb}^4 + (1 - \tau) T_{amb}^4 \tag{4.18}$$

This can be rearranged to give the following expression for the transmissivity-emissivity of the system:

$$\tau\epsilon = \frac{T_{bb}^4 - T_{amb}^4}{T_w^4 - T_{amb}^4} \tag{4.19}$$

Figure 4.5(b) shows the results for both the pressure and suction sides. Below a plate temperature of about 325 K the $\tau\epsilon$ product appears to be non-constant because of the breakdown at near-ambient temperatures of the assumptions leading to Equation 4.20. However, above this plate temperature the results are essentially constant, and the mean

of these results yields the estimates $(\tau\epsilon)_{PS} = 0.86$ and $(\tau\epsilon)_{SS} = 0.87$. The slightly higher value for the suction side may be due to its shorter distance of air in the optical pathway, though slight differences in the transmissivities of the two windows may also have an effect. Any slight spatial deviation from these essentially constant values used to calculate surface temperatures could potentially be compensated for by the appearance of a bias in the surrounding radiance distribution discussed in the following section.

4.5.3 Surrounding Radiance Test Piece

The surrounding radiance term q^* of Equation 4.14 varies spatially due to the non-uniform temperatures and grey-body properties of the CTI rig combustor simulator components which surround the leading edge test surface. The rig's removable central vane leading edge facilitated investigation of this spatial variation across the leading edge. A Rohacell leading edge test piece absent of film cooling holes was instrumented with an array of flat, K-type thermocouples, distributed across both the pressure and suction sides, as shown in Figure 4.7. To minimise the flow disturbance of the thermocouples, small holes in the test piece were drilled such that the wires tunnel through the surface from within the leading edge coolant passage, and only a short length of thermocouple emerges from each hole before being flattened down and glued to the external surface. The thermally conductive glue has a negligible effect on the thermocouple readings, which can be shown by extending the steady state analysis in Equation 3.14 and making use of the experimentally attained heat transfer coefficients mentioned in section 3.8.2. The thickness of the glue is estimated as $L_g = 5\,\text{mm}$ and according to the manufacturer its thermal conductivity is approximately $k_g \approx 0.65\,\text{W}\,\text{m}^{-1}\,\text{K}^{-1}$ [109]. Therefore, at steady state:

$$\frac{T_{g,s} - T_s}{T_{aw} - T_c} = \frac{\frac{L_g}{k_g}}{\frac{1}{h_e} + \frac{L}{k} + \frac{L_g}{k_g} + \frac{1}{h_i}} \approx 0.002 \tag{4.20}$$

i.e. the variation of temperature through the glue is only around 0.2% of the difference between the two driving gas temperatures. The thermocouple surface temperatures, in conjunction with the corresponding nearby mean black-body temperatures detected by



Figure 4.7: IR calibration leading edge test piece (a) before painting and (b) after painting.

the IR cameras, are used to calculate the transient surrounding radiance near each thermocouple which follows an activation of the heater mesh. Transient surrounding radiance measurements are essential for the calculation of transient surface temperatures, and thus heat transfer coefficients. For the calculation of film effectiveness at steady-state, only the final, plateaued surrounding radiance is required. CTI rig tests last for approximately 50 seconds after heat-on, based on the observation that this time is sufficient for the surrounding radiance to reach a plateau, i.e. for the rig interior to reach an approximately constant temperature.

The absence of film cooling on the leading edge surrounding radiance test piece reduces the ambiguity of which pixels of T_{bb} data adequately represent the corresponding thermocouple T_w data, and the results are relatively insensitive to the rectangle sizes. However, it is still necessary to exclude the optically anomalous tip of each thermocouple from its averaged nearby T_{bb} value. A MATLAB script has been used which allows manual selection of appropriate pixels by production and manipulation of images such as Figure 4.8.

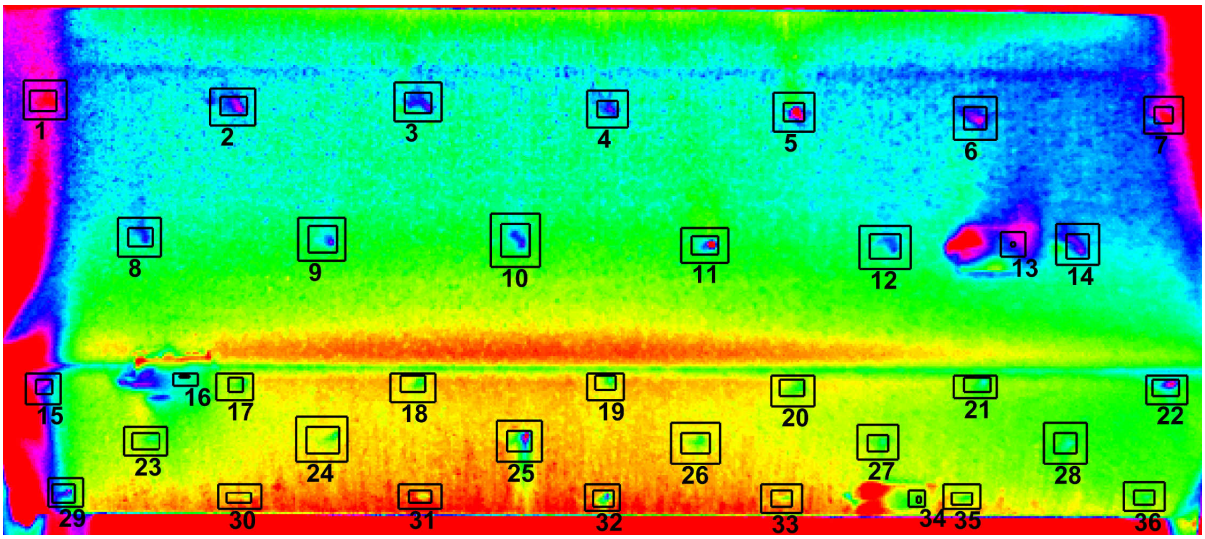


Figure 4.8: MATLAB-generated interface for manually selecting regions around surface thermocouples at which to average pixels to determine corresponding T_{bb} data (pressure side camera). The average for each thermocouple is the mean of all the pixels bounded between its pair of roughly concentric rectangles. Since at this stage of analysis surface temperatures are not known, the colour contouring is by camera raw count (scale omitted).

The inner rectangle containing a visible thermocouple is excluded from the average T_{bb} of pixels within the outer rectangle.

Each surrounding radiance value (calculated according to Equation 4.13) is assigned to the pixel coordinate on which its thermocouple was centred. These point surrounding radiance values are interpolated to the remaining pixels in order that the calibration can be applied to the entirety of the experimental vane surfaces. Several methods of interpolating the data in two dimensions were investigated using MATLAB, but finally an inbuilt interpolation function was chosen. Some of the test piece thermocouples reside within high temperature gradient areas very close to the endwalls, caused by small amounts of leakage into the rig from the NGV coolant plenum (left, inner endwall) and from the atmosphere where the removable leading edges are removed and replaced (right, outer endwall). The surrounding radiance results from such thermocouples are excluded from the interpolation because of the difficulty in selecting nearby pixels from which to calculate a camera-observed black-body temperature which corresponds to the thermocouple-measured surface temperature. The need to interpolate could be avoided by using a full surface temperature measurement technique such as liquid crystals or thermographic

phosphors, but in the CTI rig these would still have the disadvantages listed in Table 4.1, as well as the requirements of conventional digital cameras in addition to the infrared cameras, and software to transform and pixel-match video data measured from slightly different vantage points. However, perhaps the most severe disadvantage would be the narrow range of temperatures over which measurements are typically possible, which would prevent the reliable acquisition of transient surrounding radiance measurements.

The magnitudes of the surrounding radiance distribution during any given experiment depend on the temperatures of the surrounding rig features. These, in turn, depend on the heater mesh voltage, the rig mass flow conditions, the test duration, and to a smaller extent, the ambient temperature and the preheating of the rig due to recent tests. Due to these last factors, when the surrounding radiance test piece is replaced with another, uninstrumented test piece, the spatial distribution of surrounding radiance may change slightly from that which was measured. In practice, it has been assumed that the surrounding radiance is the same for any heated test on the same day and at the same mesh voltage and combustor simulator mass flow rate condition, and an additional component of uncertainty has therefore been added to the surrounding radiance measurements. In order to ascertain this additional uncertainty in the surrounding radiance distribution due to the removal of the calibration test piece, a series of consecutive, heated tests were carried out with the calibration test piece in place, and the surrounding radiance measurements compared. The maximum steady-state surrounding radiance variation between these runs as calculated at each thermocouple was approximately 17% of the maximum spatial variation detected during a single run on the pressure side, and 8% on the suction side. Therefore, the uncertainty in the surrounding radiance due to the replacement of the calibration test piece with a film-cooled one is small compared to the additional spatial certainty gained, verifying the utility of the spatial calibration.

4.6 Accuracy Advantage of a Spatial Infrared Calibration in the CTI Rig

The calibration leading edge test piece was used to investigate the effects on the IR calibration of changing the dilution port and outer endwall film cooling momentum flux ratios (J_D and J_E, respectively). Changes to the calibration are expected when rig wall temperatures change, since this affects the surrounding radiance levels. For a range of J_E, the interpolations from the at-thermocouple surrounding radiance values during the steady-state test phase are normalized by the mean surrounding radiance of the pressure side $J_D = J_E = 0$ case, and shown in Figure 4.9. The contemporaneous full-field blackbody temperatures as seen from the suction side camera are also presented, which serve to indicate the relative temperatures of the cooled endwall (right) between tests. The distributions of surrounding radiance are relatively unaffected by changes to the dilution port momentum flux ratio (so these results are omitted). This is because the dilution ports inject cool air perpendicularly to the combustor walls and do not significantly change their surface temperature distribution. For all of the cases in Figure 4.9, $J_D = M = 0$.

For $J_E = 0$, the supply plenum was sealed at its inlet, rather than at the holes themselves. This means that the ambient temperature air in the plenum still provides some cooling to the endwalls by mixing with the mainstream flow and by natural convection within and at the entrance to the holes. This endwall cooling reduces its IR radiosity, causing the diminished amount of reflected radiation detected on the calibration test piece near this endwall. Endwall film cooling with $J_E = 4$ significantly expands the vane surface region experiencing reduced reflections and exacerbates the peak reduction, because the endwall temperature and hence its IR emissions are considerably reduced. The two subsequent J_E each increase the temperature of the endwall surface between the cooling holes. These locally increased thermal emissions partially offset the reduction of reflections from the test piece, especially on the vane surface very close to the endwall. The temperature rise of this portion of the endwall is due to its external face's considerable thermal contact with both endwall coolant (in the plenum) and ambient air. Due to the temperature rise

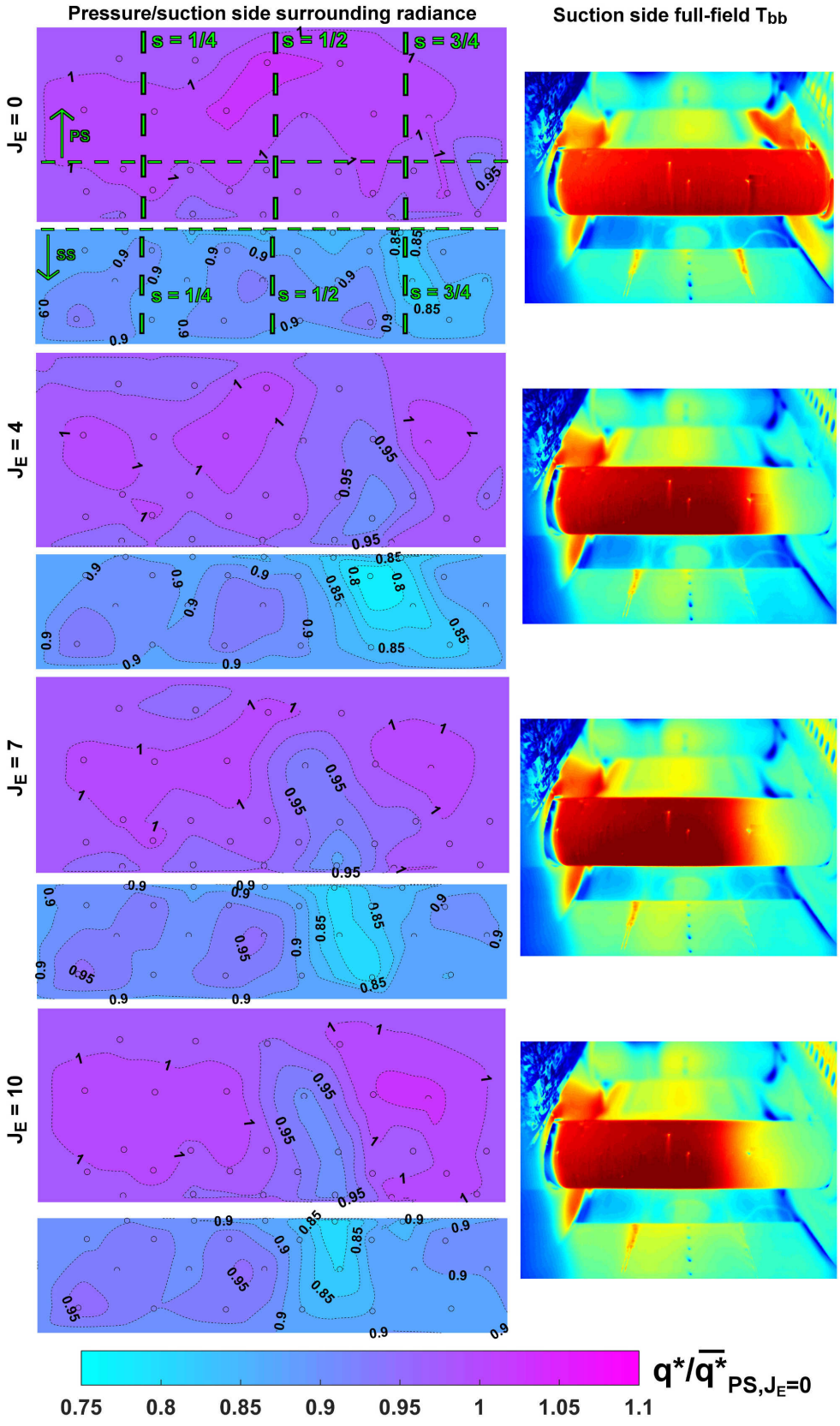


Figure 4.9: Normalised surrounding radiance distributions for outer endwall film cooling momentum flux ratios $J_E = 0$, 4, 7, 10. Pressure and suction side views with spanwise positions indicated (left), and full-field IR camera black-body temperatures from suction side view (right) to indicate endwall coolant's effect on vane. For these cases, $J_D = M = 0$.

through the blower fan which supplies it, the coolant is typically around 13 K warmer than ambient. Thus, as the mass flow rate of coolant to the plenum increases, so too does the net convective heat transfer to the piece of endwall in question. Its increase in temperature with increasing J_E may also be partly due to the increasing surface entrainment of hot mainstream gas as the jets lift off more prominently from the surface near their holes of origin. This specific flow rate dependence of the surrounding radiance distribution may merely be an idiosyncrasy of the CTI rig and its construction; the significant finding is the local reduction of vane reflections when endwall film cooling is used.

To illustrate the potential importance of a spatial calibration in a combustor simulator wind tunnel with endwall film cooling, the film-cooled effectiveness distribution has been calculated on the suction side three times; once with the measured surrounding radiance distribution, once with a uniform surrounding radiance value equal to the mean of the distribution, and once with a uniform surrounding radiance value equal to the maximum measured by a single thermocouple. The latter two cases can be considered as typical and worst-case scenarios, respectively, in terms of the error in film effectiveness due to neglecting the spatial variation in the amount of extraneous IR radiation reflected from the test piece. Two distributions of the error are calculated as the pixel-wise difference between the spatially-calibrated result and each of the two constant surrounding radiance cases, and are shown in Figure 4.10. These results show that if a single surface thermocouple were used for the IR calibration, the maximum possible error across the calculated effectiveness distribution would be approximately 0.05, while the expected maximum error for a randomly placed reference thermocouple would be approximately 0.03.

4.7 An Experimental-Numerical Method for Transient Infrared Measurement of Film Effectiveness and Heat Transfer Coefficient in a Single Test

An experimental technique for assessing film cooling performance has been developed which can determine both film effectiveness and heat transfer coefficient (HTC or h) distributions from a single infrared experiment. These parameters are the two most

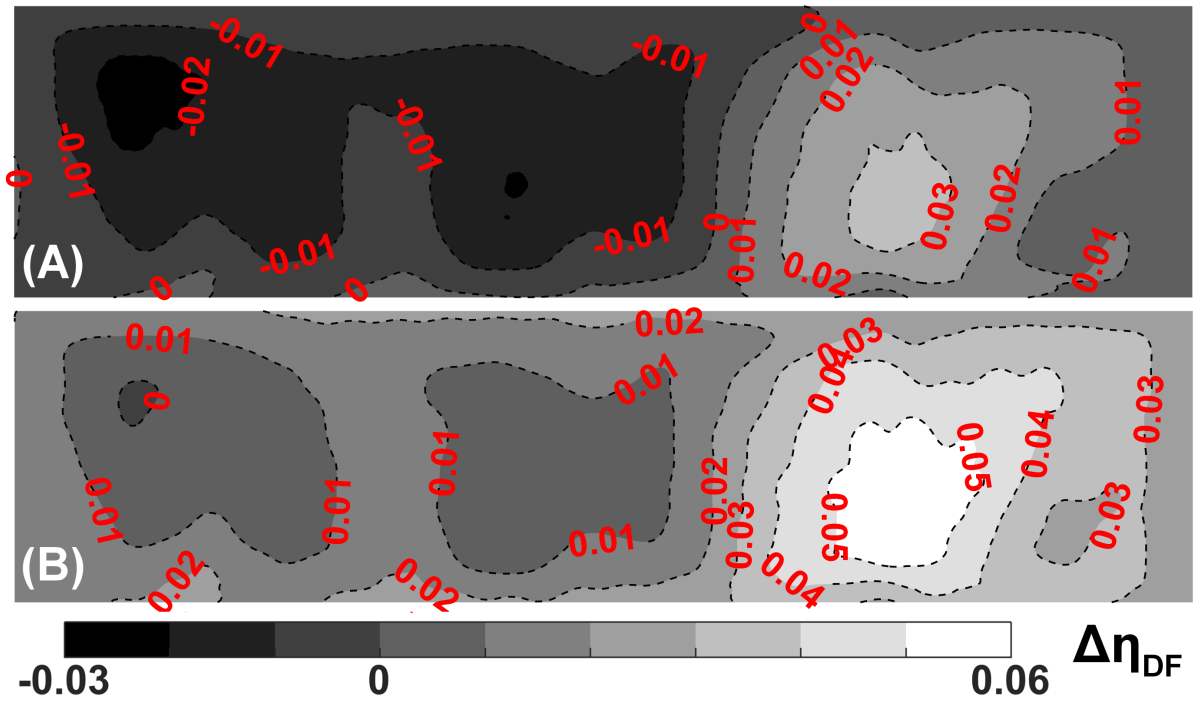


Figure 4.10: Contours of suction side film effectiveness discrepancy for $J_D = 9$, $J_E = 7$, $M = 1.5$ when calculated with a spatial calibration compared to calculation with (a) mean surrounding radiance (b) minimum surrounding radiance.

commonly used in film cooling literature to evaluate the performance of films, and their determination conventionally requires two separate experiments, increasing experimental time requirements while reducing the accuracy of results. First, the film effectiveness is determined in the single experiment's steady-state phase (utilising the low thermal conductivity of the test piece). Then, the effectiveness is used to calculate the distribution of the transient phase driving gas temperatures, which is applied to a finite difference conduction model. Initial guesses for HTC levels are iteratively refined until the surface temperature histories predicted by the finite difference model match those which were experimentally observed. Unlike conventional methods based on one-dimensional, analytical heat transfer solutions, this technique does not require assumptions about the material thickness underlying the test surface or the uniformity with depth of its initial temperature distribution. This relieves certain experimental constraints and reduces uncertainties.

4.7.1 Previous Techniques

Most commonly, two separate experiments are used to determine the full-surface distributions of the film effectiveness and HTC, and several assumptions are made leading to an easily soluble equation involving both T_{aw} and h (Equation 4.21). t is the time after the mainstream temperature rise begins, and k and α are the thermal conductivity and diffusivity of the test piece solid, respectively):

1. The driving gas temperature rises instantaneously at the beginning of the test from the initial surface temperature T_i to T_{aw}.
2. The conduction into the solid from the heated (film-cooled) side is essentially one-dimensional.
3. The thermal pulse does not reach the opposite surface ('semi-infinite' substrate).
4. The solid initially has temperature T_i at all depths.

$$\frac{T_s(t) - T_i}{T_{aw} - T_i} = 1 - \exp\Big(\frac{h^2 \alpha t}{k^2}\Big)\mathrm{erfc}\Big(\frac{h\sqrt{\alpha t}}{k}\Big) \tag{4.21}$$

A perfectly instantaneous driving temperature rise can never be achieved in real experiments, so modifications to this model have been made which take into account its transient rise (e.g. [96, 110]). However, the remaining assumptions still introduce certain experimental constraints and uncertainty in the results. The single-test technique proposed in this section is not subject to these assumptions, and it therefore offers more flexibility in experimental design and potentially lower result uncertainties.

In a two-test technique, authors such as Vedula and Metzger [111] and Du et al. [112] used a thermochromic liquid crystal (TLC) colour transition to detect at which time each surface location reached the corresponding transition temperature. The first test had the temperature of the film coolant and mainstream both equal to a constant T_{aw}, allowing solution of Equation 4.21 for h. The second test used heated coolant to create a temperature difference with the mainstream, producing a driving temperature distribution T_{aw} which could be solved for by substitution into Equation 4.21 of the known h distribution.

Chambers et al. [113] developed a three-test technique and applied it to impingement cooling experiments. In one test, both air supplies are heated, while in the second and third tests, only one or the other is heated. Each of the second and third tests can be combined with the first test to generate a pair of equations in the two unknowns. Regions of low effectiveness use the test in which the non-coolant stream is heated to determine HTC, and regions of high effectiveness the test in which the coolant stream is heated. In this way, a long-duration temperature transient is available for the entire surface, where otherwise regions of either very high or very low effectiveness would not produce reliable HTC results. The effects of the changing density ratio between the two streams were observed to be negligible for the combinations of temperatures used. The authors noted that if the two mixing temperatures can be closely matched during the first test, then the HTCs (but not the effectiveness) can be determined with just a single test.

A single-test TLC technique was proposed by Licu et al. [114] in which a wide-band TLC coating yields full-surface temperatures for a longer duration transient, allowing calculation of both T_{aw} and h distributions as a function of time. They noted that the use of a full temperature transient reduces measurement noise and captures the time-averaged behaviour of unsteady flows. Chyu and Hsing [115] proposed an earlier single-test technique using thermographic phosphors, also employing their relatively wide-band temperature capabilities to produce transient T_{aw} and h distributions.

Ekkad et al. [116] proposed an infrared technique yielding both parameters in a single test and applied it to measurements of a single film cooling hole on a cylindrical leading edge with a flat afterbody. Similar to a two-test approach, they employed two infrared images of the test piece surface temperature captured at two different times in a single, transient heated experiment to generate two simultaneous equations which were then solved for the two unknowns T_{aw} and h. They identified the advantages of IR over temperature-sensitive coatings, namely that the test surface paint does not need frequent reapplication or calibration, the temperature range is much broader, and the initial sur-

face temperature distribution is easily obtained. They also identified the advantages of single-test experiments over two-test experiments; since only a single operating condition is required, experimental time, complexity, and uncertainty are all reduced. More recently, authors such as Chen et al. [117] and Hayes et al. [118] have used many frames of IR data from a single test to determine the distributions of both parameters, making use of an iterative, least-squares regression to satisfy with minimal error the many resulting equations of the Equation 4.21 form.

4.7.2 Outline of the Novel Technique

The proposed technique for determining both the film effectiveness and the HTC with a single heated experiment requires that the film-cooled test piece be of a low thermal conductivity, such that the surface temperature quickly plateaus (i.e. a steady state is reached). During this time, the surface temperature approximates the adiabatic wall temperature, T_{aw}, which defines the film effectiveness according to Equation 2.2. As described in section 3.8.2, in the CTI rig a correction is used to improve this approximation by accounting for conduction effects in the Rohacell leading edge test pieces, the material properties of which are known from manufacturer data sheets [90].

With the film effectiveness known, external HTCs are determined from the preceding transient phase of the test (when the film-cooled surface temperatures are still rapidly increasing). At each pixel of IR camera data, the temperature distribution through the thickness of the test piece is modelled by a transient, one-dimensional, finite difference (FD) conduction model. This resembled the FD scheme used in chapter 3, with forward difference time integration and second order central difference spatial integration. The spatial and temporal discretisations were of constant size and were sufficiently small that smaller steps made negligible difference to the external HTC solutions. Once again the solid temperature distribution is initialised by assuming a depthwise linear change, though in this case the initial external surface temperature is known at each pixel from the IR camera data, while the initial internal surface temperature can be determined from an

analytical steady state solution (or alternatively from a preliminary transient simulation until steady state). Convective heat transfer boundary conditions (Equation 2.1) are used for both the internal (coolant plenum) side and the external (film-cooled) side. All of the parameters describing these boundary conditions are known, except for the external HTC. Guesses for this unknown are improved by running FD simulations for the pixel in question until the predicted surface temperature history closely matches the surface temperature history observed by the IR camera. The closeness of fit is measured by the sum of the (signed) errors at each of the known surface temperature history data points. The strategy for updating the HTC guesses is explained below, and seeks to minmise the closeness of fit error metric. The internal driving gas temperature is the NGV coolant temperature T_c, which is essentially constant everywhere and throughout an entire test. The internal HTC is estimated as a constant attained with the Dittus-Boelter equation for internal pipe flows. The final results for external HTC were found to have very low sensitivity to the internal HTC, justifying the use of this estimation. The low impact of the internal heat transfer boundary condition on the unknown external HTC parameter suggests that, despite the low thickness of the Rohacell leading edge test pieces, their thermal conductivity is sufficiently low to justify the semi-infinite assumption common to the conventional analytical method of determining the film-cooled HTC (Equation 4.21). This aspect of the novel technique would nevertheless become advantageous for the same experiment at a smaller scale but the using the same vane material (smaller leading edge Biot number).

The film effectiveness distribution is used to estimate the external driving gas temperatures at each pixel throughout the transient phase of the test, calculated according to a rearrangement of the definition of film effectiveness:

$$T_g(\mathbf{x}, t) = T_\infty(t) - \eta(\mathbf{x}) \times (T_\infty(t) - T_c) \tag{4.22}$$

The reference hot temperature, $T_\infty(t)$, is the mass-averaged temperature of the combustor simulator inlet flow (heated by the heater mesh) and the flow from the dilution ports.

This does not undergo a perfect step temperature rise because of initial heat conduction from the heater mesh into its brass electrical connectors and from the mainstream into the rig walls. Crucial to the use of Equation 4.22 is the assumption that the steady-state film effectiveness is valid throughout the transient. This is true in the present experiments because the film coolant jet physics remain relatively unchanged throughout the transient because of the small variations in the blowing ratio and coolant-to-mainstream density ratio. As calculated in section 3.5, these are each approximately 8% ($\frac{M_{hot}}{M_{cold}} \approx 1.08$ and $\frac{\rho_c/\rho_{\infty,hot}}{\rho_c/\rho_{\infty,cold}} = \frac{T_{\infty,cold}}{T_{\infty,hot}} \approx \frac{T_{inlet,cold}}{T_{inlet,hot}} \approx 0.92$).

An iterative algorithm was devised to refine an initial pair of HTC guesses, $(h_1, h_2)_0$, until the pair of improved guesses, $(h_1, h_2)_N$, converges to within a small tolerance. The initial guesses are chosen to span the full range of expected HTC values in the domain, since the algorithm assumes that the true HTC lies somewhere in between. Each HTC guess is applied to the FD model external surface to produce an external surface temperature history prediction $T_{s,p}(t)$ intended to resemble the true history $T_{s,t}(t)$ captured by the camera. A simple error metric E is used to evaluate the closeness of each fit:

$$E = \sum_{\Gamma} (T_{s,p} - T_{s,t}) \tag{4.23}$$

where Γ is the set of infrared temperature data points within the time period considered. Increasing the HTC guess will always produce a surface temperature prediction which is at all times greater than the previous prediction. This has two importance consequences for the algorithm. Firstly, the signed error metric is natural to the algorithm; a positive error metric indicates that $T_{s,p}(t)$ lies entirely or primarily above $T_{s,t}(t)$ and that the associated HTC guess is too high (and vice-versa). Secondly, for an unsigned error metric there would be potentially three predicted histories satisfying a given summed error (slightly above the true history, slightly below it, and intersecting it, refer to Figure 4.11). So the signed metric is also advantageous in that it only locates the latter of these, which is also the one with the smallest maximum absolute error at any point. The algorithm closely resembles the bisection technique for approximating the value of a root of a function which is known

to have a root in a given domain [119] (in which case the error metrics are simply the function evaluated at each of the current guesses). The algorithm proceeds as follows at each iteration, and an example of the convergence towards an answer for a single pixel is presented in Figure 4.11. The symbols $\cap$ and $\cup$ refer to logical 'and' and 'or', respectively.

1. For each of the current guesses $(h_1, h_2)_n$ perform the FD calculation leading to the predicted surface temperature history.
2. Get the error metrics $(E_1, E_2)_n$ for the current guesses.
3. Determine new guesses $(h_1, h_2)_{n+1}$ according to $(E_1, E_2)_n$:
   (a) If $(E_1 > 0 \cap E_2 < 0) \cup (E_1 < 0 \cap E_2 > 0)$
   i.e. one predicted history lies above and the other below the true history:
   $h_{1,n+1}$ = mean of guesses $(h_1, h_2)_n$
   $h_{2,n+1}$ = guess $(h_1, h_2)_n$ with the lowest error metric (absolute value)
   (b) If $(E_1 > 0 \cap E_2 > 0)$
   i.e. both predicted histories lie primarily above the true history:
   $h_{1,n+1}$ = minimum of guesses $(h_1, h_2)_n$
   $h_{2,n+1}$ = minimum of guesses $(h_1, h_2)_{n-1}$
   (c) If $(E_1 < 0 \cap E_2 < 0)$
   i.e. both predicted histories lie primarily below the true history:
   $h_{1,n+1}$ = maximum of guesses $(h_1, h_2)_n$
   $h_{2,n+1}$ = maximum of guesses $(h_1, h_2)_{n-1}$
4. If $(h_{1,n+1} - h_{2,n+1})$ is less than the tolerance value, the solution is the mean of guesses $(h_1, h_2)_{n+1}$, otherwise return to (1) with the updated guesses.

4.7.3 Advantages of the Novel Technique

The algorithm described above resembles that used by Coletti et al. [120] and later Ryley et al. [121] to determine HTC distributions on ribbed internal cooling geometries. They used a commercial, transient finite element code and full-surface temperature data (obtained by IR and TLC, respectively) on their complex, three-dimensional (3D) geometries to iteratively refine initial guesses for full-surface HTC distributions. This was intended to improve upon the constraint of 1D geometry imposed by the common analytical solution (Equation 4.21), while the present technique employs numerical PDE solutions to avoid the analytical solution's initial temperature and semi-infinite substrate assumptions. It

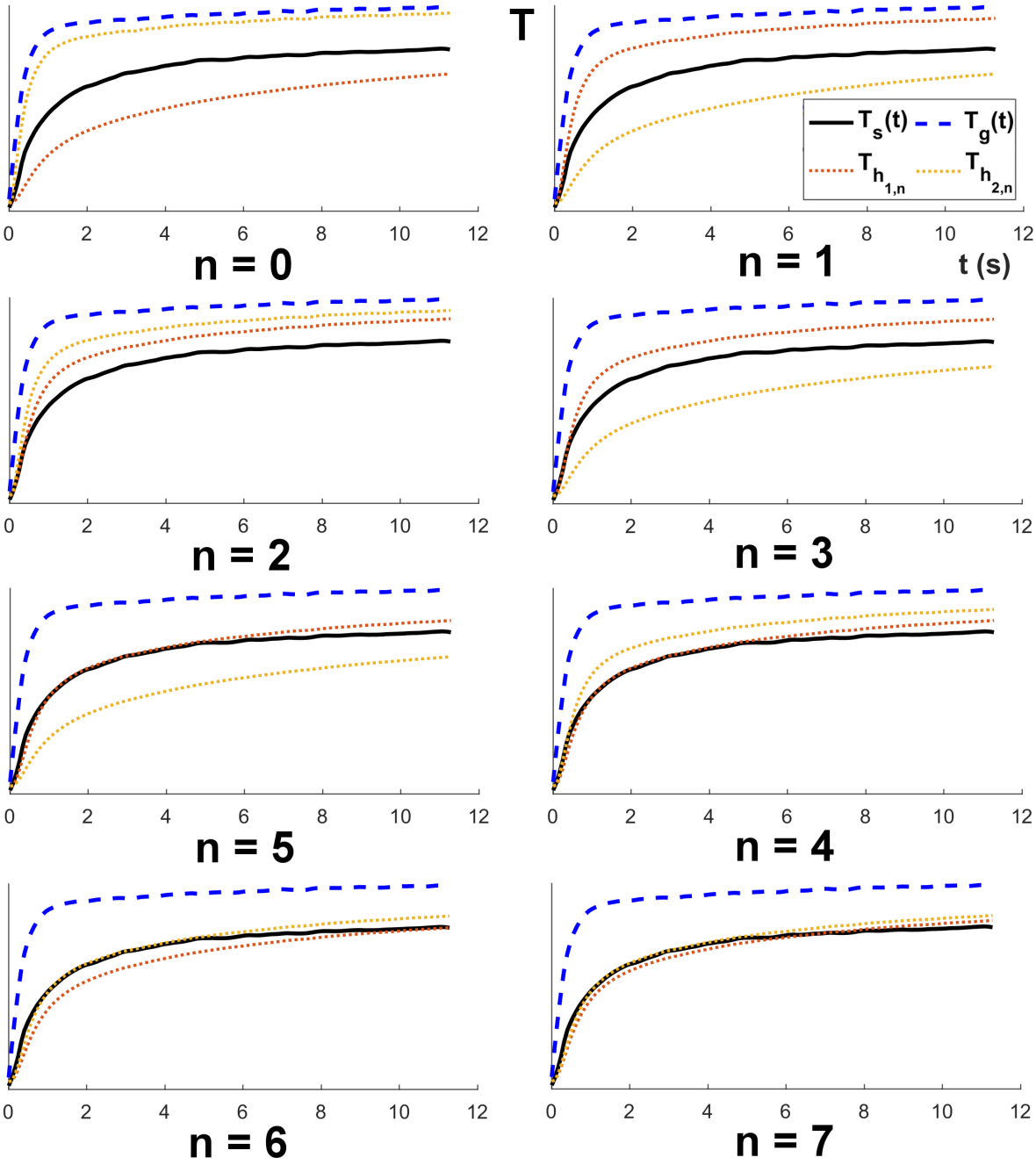


Figure 4.11: Iterative progress of the HTC-finding algorithm, showing convergence of FD-predicted surface temperature histories towards the measured surface temperature history for a single pixel.

also differs from these past numerical applications by being simple to implement without a commercial finite element code, and in the technique by which the distribution of transient gas driving temperature is determined from the steady-state film effectiveness measurement (Equation 4.22).

Avoidance of the analytical solution assumptions confers significant practical advantages to the novel technique. Firstly, the test piece material can be much thinner. This consideration is important to experimental setups such as the CTI rig, whose wall thickness cannot be increased without significantly affecting the film cooling hole lengths and inlet conditions. Secondly, the test piece can have a depth-wise initial temperature gradient. The CTI rig again offers an example of how this can be essential to a given experiment, in that the blower fan used to supply coolant increases the temperature of the coolant above atmospheric. Before the heater mesh is turned on, the leading edge test pieces are therefore initially exposed to warmed air inside the coolant plenum and predominantly atmospheric air on the external, film-cooled surface. This creates initial depth-wise temperature gradients inside the leading edge test piece which are modelled at each pixel in the FD HTC calculation as a linear temperature gradient between the two sides (the initial external surface temperature is known at each pixel from the IR camera data, while the initial internal surface temperature is determined from an analytical steady state solution). In the present experiments, using the FD model and assuming that the temperature throughout the thickness at each pixel is uniformly equal to that pixel's initial surface temperature results in HTC over-predictions of up to 7%. Increasing the test surface thickness in the FD model to be essentially semi-infinite further increases this maximum error to over 30%. This illustrates the importance in the present experiments of accounting for the initial temperature gradient and the true thickness of the test pieces.

The novel technique can, for appropriately simple geometries, be easily extended to a reduced-domain 3D code. This was done in order to assess the influence on HTC results of the 1D conduction assumption. The domains were rectangular prisms comprised of the

same number of nodes in the wall thickness direction as in the 1D case, but additional nodes in the surface directions to correspond to the additional surface temperature pixel data available. The pixel for which HTC was calculated remained as the central external surface node, and the unique pixel-wise gas temperature histories calculated according to Equation 4.22 were applied to their appropriate nodes. The coolant plenum nodes were all subject to the aforementioned convective boundary condition, while the sides of the domain were adiabatic. Regardless of the size of the domain, the results indicated HTC variations consistently less than 2% from the 1D model, justifying the use of the latter. So long as convergence is achieved, the choice of time step makes a negligible difference to results, while the nodal distance used produces results consistently less than 1% different from those produced with smaller distances. In section 5.5, the technique is applied to three leading edge designs and the film effectiveness and HTC results are compared.

4.8 Conclusions

A leading edge covered by a dense array of thermocouples was observed with the Oxford CTI rig infrared cameras in order to measure the infrared radiation reflections across the entire leading edge surface under different combustor coolant flow rate conditions.

- Dilution ports were found to have a negligible effect on the reflected radiation because the jets penetrate away from the combustor walls and have little effect on their temperatures.

- Endwall film cooling significantly reduces the surface temperatures and thus thermal emissions of the endwall. This in turn reduces the amount of radiation which reflects to the camera via the nearby vane surface.

- Since only the portion of vane surface near to the cooled endwall is affected, a separate calibration in this region is essential. It was shown that using only a single vane-surface calibration thermocouple in the CTI rig could lead to effectiveness errors of up to 0.05.

Additionally, a new technique has been developed for determining both film effectiveness and heat transfer coefficient from a single heated film cooling experiment.

- In the steady state phase, surface temperature data yield the film effectiveness, which is then used to determine the distribution of driving gas temperatures throughout the transient phase.

- These are applied to a transient, 1D, finite difference model of the test piece material. The pixel-wise solution for heat transfer coefficient is determined by refining guesses until the computationally predicted surface temperature history fits optimally with the experimentally observed one.

- Unlike conventional techniques, there is no need to assume that the test piece thickness is essentially semi-infinite or initially uniform in temperature, permitting the use of thin-walled test pieces with unequal initial temperatures on the film-cooled and internal surfaces.

- An alternative approach which has not been considered herein would be to apply the known external surface temperature history as the external boundary condition, determine the predicted near-surface heat flux q'' as a function of time, and then calculate the HTC as a function of time using the known adiabatic wall temperature history and Equation 2.1.

Chapter 5

Radial Showerhead Film Cooling Measurements Downstream of Combustor Dilution Ports

In this chapter, stagnation region film cooling holes blowing in the radial direction (along the NGV spanwise direction) are investigated for three experimental leading edge models. The models differ in the spanwise distributions of surface angles of the radial holes. The film cooling effects of each tested model are combined with the dilution port temperature profile as manifested on the surface of the central leading edge. An experimental strategy has been developed for uncoupling the effects of these two cooling flows on the leading edge adiabatic wall temperatures. This approach has enabled study of the effects of dilution port turbulence on leading edge film cooling performance in a manner which is independent of the temperature profiles also generated by the dilution ports. Reference images without leading edge film cooling are used to capture the effects of the dilution ports acting alone. These are compared to images taken with both leading edge film cooling and the same amount of dilution. The further cooling effects on top of those in the reference images are imputed to the leading edge film cooling. It is found that the film effectiveness due to lifted-off jets from higher surface angle radial cooling holes can be enhanced by dilution port turbulence by up to 0.2, independent of the temperature profiles generated by the dilution ports. The main results from this chapter were included in two papers for international conferences [92, 122] and a related journal paper [93].

5.1 Introduction

Modern jet engine NGVs are typically film-cooled on their leading edges by a densely spaced array of cylindrical film cooling holes blowing at a substantial compound angle to the local mainstream flow direction (i.e. $\beta \approx 90°$, see Figure 5.2(c)). Since the blowing is thus aligned approximately with the radial direction of the turbomachine, such film cooling holes are known as 'radial'. The stagnation region's lack of upstream film cooling holes and propensity for film coolant lift-off (due to low mainstream flow momentum) mean that this densely packed, radially blowing arrangement is crucial to achieving acceptable local external gas temperatures. Two adjacent NGV aerofoils are usually cast in a single piece with their endwalls. This maximises structural integrity at the points where the aerofoils meet the endwalls, and facilitates more precise control over the NGV throat area. However, this presents a problem for the production of radial film cooling holes by laser drilling, as the presence of the endwalls prevents the laser head from accessing the entire span from angles which will produce radial holes with low surface angles. This is the angle between a line through the hole's centreline and its projection down onto the aerofoil surface (angle α, see Figure 5.1). Holes with lower surface angles tend to produce jets which improve adjacent and downstream cooling performance by staying more completely attached to the surface, particularly close to the stagnation region where there is minimal mainstream flow momentum to return coolant to the vane surface. Three types of arrangement are possible regarding the direction of radial film cooling hole blowing, as illustrated in Figure 5.1:

1. All of the radial holes blow towards a single endwall. The radial holes near that endwall are necessarily at very high surface angles. This arrangement may cause a substantial migration of coolant towards this endwall, such that farther downstream, there will be a paucity of coolant near to the other endwall. This and the lack of NGV film coverage very near to the neglected endwall may require a significant asymmetry in the amount of endwall film cooling required.

2. The radial holes blow towards their nearest endwall, with a reversal of blowing direction occurring somewhere near the blade midspan. Holes near both endwalls are necessarily at very high surface angles. Moving downstream, coolant migrates towards each endwall, and an increased hole density may be required near the blowing direction transition point in order to ensure adequate midspan surface cooling.

3. The radial holes blow away from their nearest endwall and towards the midspan, with a reversal of blowing direction occurring somewhere near the midspan. Depending on the details of the machining process, this may permit the machining of low surface angle radial holes right up to this transition point, or they may have to increase in surface angle near the midspan. Moving downstream, coolant migrates towards the midspan.

5.1.1 Radial Film Cooling Geometries

In the present study, arrangement 3 is referred to as an 'opposed' radial showerhead configuration. Three leading edge test pieces (labelled as RAD-A, RAD-B, and RAD-C and shown in Figure 5.2) were designed to investigate the opposed configuration with respect to the effects on film cooling effectiveness of radial hole surface angles which gradually increase towards the midspan. This was originally motivated by industrial

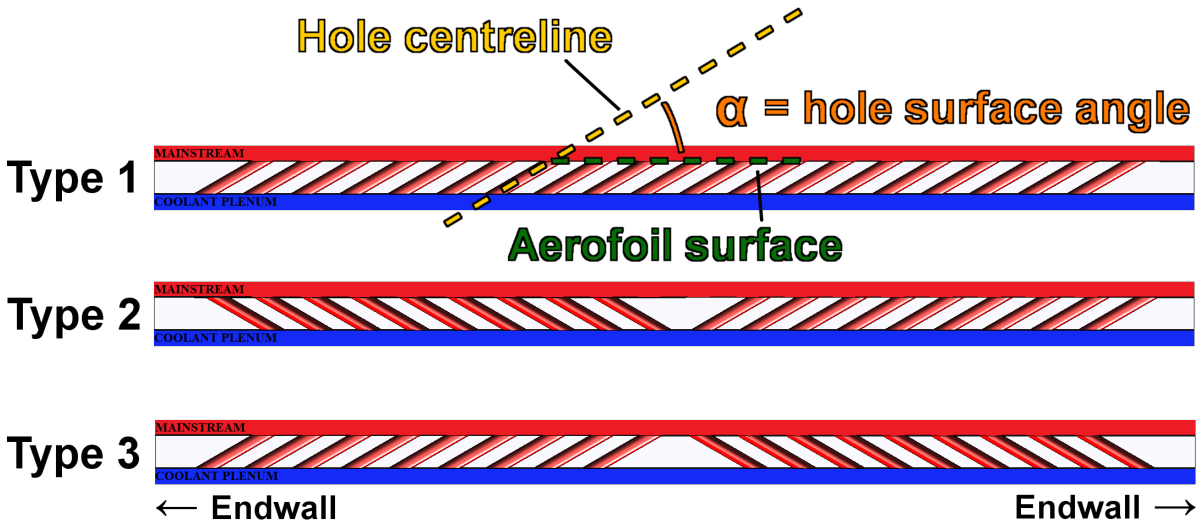


Figure 5.1: Hole row cross sections illustrating the three possible types of arrangement of radial cooling holes, and showing the definition of the hole surface angle.

Table 5.1: Hole pitch, surface distance of exit centre from stagnation line, and hole length by row, normalised by hole diameter, for all three radial cooling models.

Hole row	P/D	S/D	L/D
PS3	3.5	-15.6	6.4
PS2	4.0	-6.3	2.8 - 5.6
PS1	4.0	-2.1	2.7 - 5.4
SS1	4.0	1.9	2.7 - 5.4
SS2	4.0	4.4	2.8 - 5.6
SS3	4.0	6.9	3.5
SS4	3.4	10.4	3.5
SS5	3.4	13.8	4.3
SS6	3.4	17.3	4.3

interest in this common arrangement, specifically in the penalised performance near the midspan. The dilution port and endwall film cooling combustor flows were found to have significant impacts on the performance of these geometries. The three pressure side and six suction side hole rows are labelled from 'PS3' to 'SS6' as shown in Figure 5.3. Model RAD-A has no compound hole angling, and acts as a baseline reference for performance of showerhead injection which is aligned with the surface normal. Models RAD-B and RAD-C feature radial cooling holes in the four rows nearest the geometric stagnation line (PS2-SS2), while the remaining hole rows are streamwise and identical to those in Model RAD-A. Model RAD-B has very low surface angle radial cooling holes right up to the midspan, and so represents the performance that might be achieved if endwall obstruction were not an influence on the hole machining process. Model RAD-C is more representative of a typical in-engine opposed radial showerhead, having radial cooling holes of three different surface angles, with the higher surface angles occurring towards the midspan (see RAD-C in Figure 5.2). Figure 5.3 shows the hole angles in a cross-sectional plane orthogonal to the spanwise direction, which are common to all three of the models. Table 5.1 shows the pitch, surface distance of hole exit centres from stagnation line, and hole length for each row, normalised by the hole diameter. Only the lengths vary between the three models, owing to the changes in radial hole surface angles.

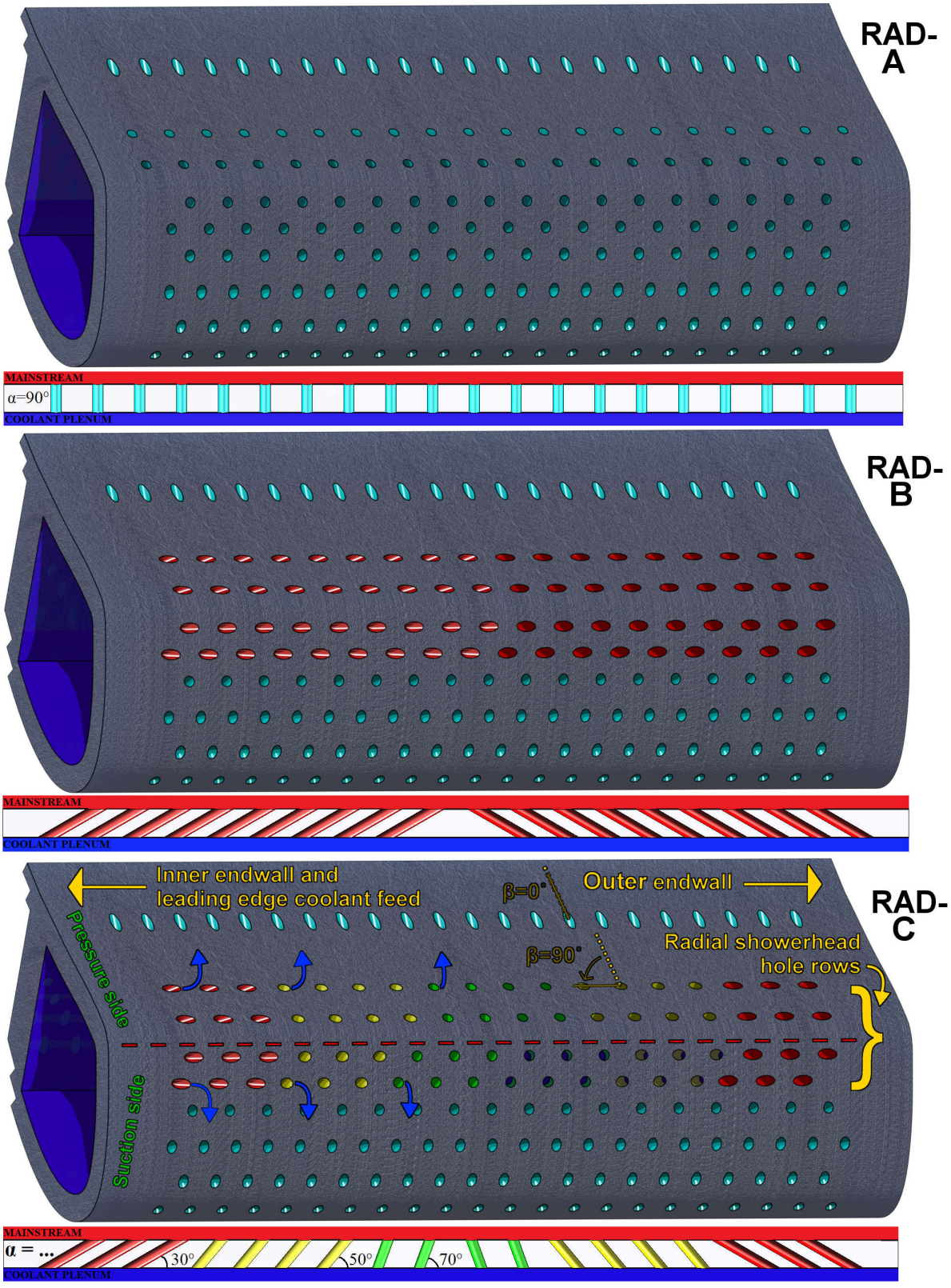


Figure 5.2: Three removable NGV leading edge test pieces showing their varying spanwise distributions of surface angles (α) of the PS2-SS2 radial holes (compound angles $\beta = 90°$).

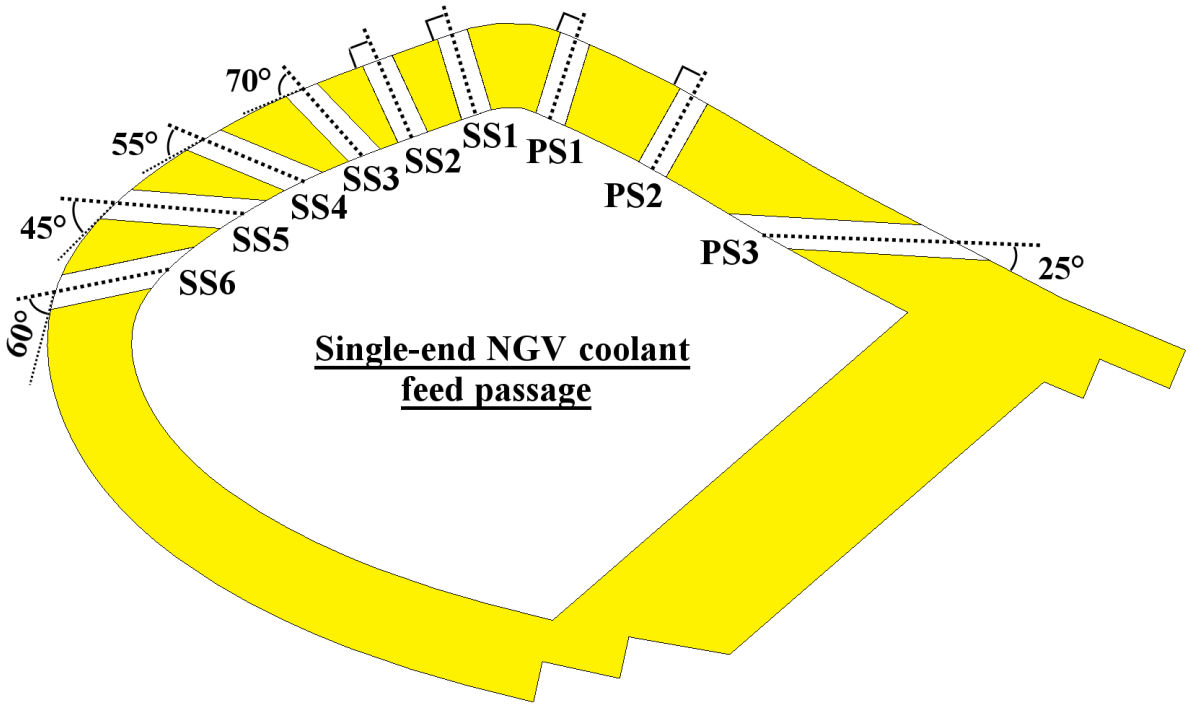


Figure 5.3: Hole angles in a cross-sectional plane, consistent for all three radial models.

5.2 Upstream Temperature Profile Correction

In addition to the conduction effects described in section 3.8, the measurement of film effectiveness is complicated by non-uniformity of the temperature profile approaching the NGV cascade. Based on a single adiabatic wall temperature measurement, the true cooling effects of the film cannot be fully uncoupled from the simultaneous effects of the dilution port jets, which have not had time to fully mix with the mainstream when they arrive at the cascade. The adiabatic wall temperature in the presence of both dilution and films is denoted by the subscript 'DF', and is normalised according to Equation 5.1:

$$\eta_{DF}(\mathbf{x}) = \frac{T_{\infty,DF} - T_{aw,DF}(\mathbf{x})}{T_{\infty,DF} - T_{c,DF}} \tag{5.1}$$

where the hot and cold reference temperatures are the mass-averaged temperature of the combustor inlet and dilution port flows ($T_{\infty,DF}$) and the leading edge coolant temperature ($T_{c,DF}$), respectively. Figure 5.4 shows suction side, conduction-corrected effectiveness measurements both with and without dilution port flow and a fixed blowing ratio of $M = 3.5$. Among other changes, there is an apparent improvement in the effectiveness

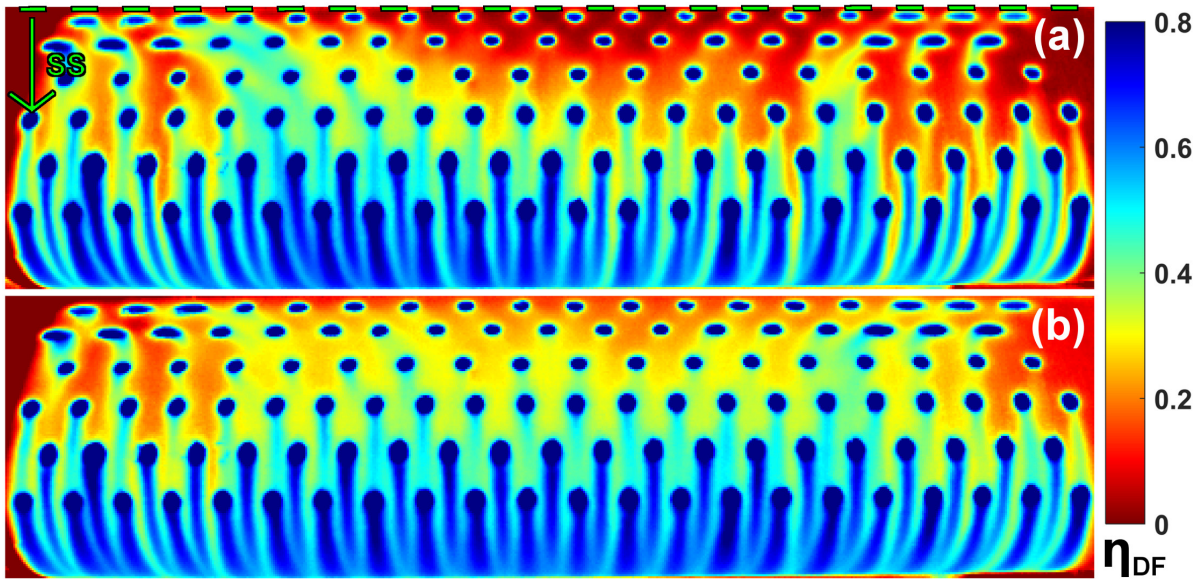


Figure 5.4: Film effectiveness for two dilution port flow rates, including the influence of the two vane inlet temperature profiles. $J_E = 0$, $M = 3.5$. (a) $J_D = 0$ and (b) $J_D = 9$.

near the midspan stagnation line (top middle) in the presence of dilution ports. However, it is not clear how much of this change is due to the altered temperature profile, and how much is due to the altered turbulence profile. An experimental technique has been developed for isolating the cooling effects of the films from those of the dilution ports. These isolated effects can then be used to assess the effectiveness performance of films under the different mainstream turbulence conditions produced by different dilution port mass flow rates. Another method would be to match the mainstream and dilution port temperatures while maintaining a film coolant temperature difference, however this would require more than one flow heater, increasing rig complexity and cost. As with the conduction correction method, the technique makes use of secondary experimental images to process the primary data, and is carried out separately on both the pressure and suction sides. The basic measurement of film-cooled surface adiabatic wall temperature in the presence of both film cooling and a mainstream temperature profile caused by upstream dilution ports is denoted by $T_{aw,DF}$ (this is determined from a corresponding infrared surface temperature measurement, $T_{s,DF}$, using the experimental conduction correction method outlined in section 3.8.2). If the vane adiabatic wall temperature distribution due only to the same particular amount of dilution (without films) $T_{aw,D}$ is also known, the additional cooling effect of the films under those conditions is indicated by the difference

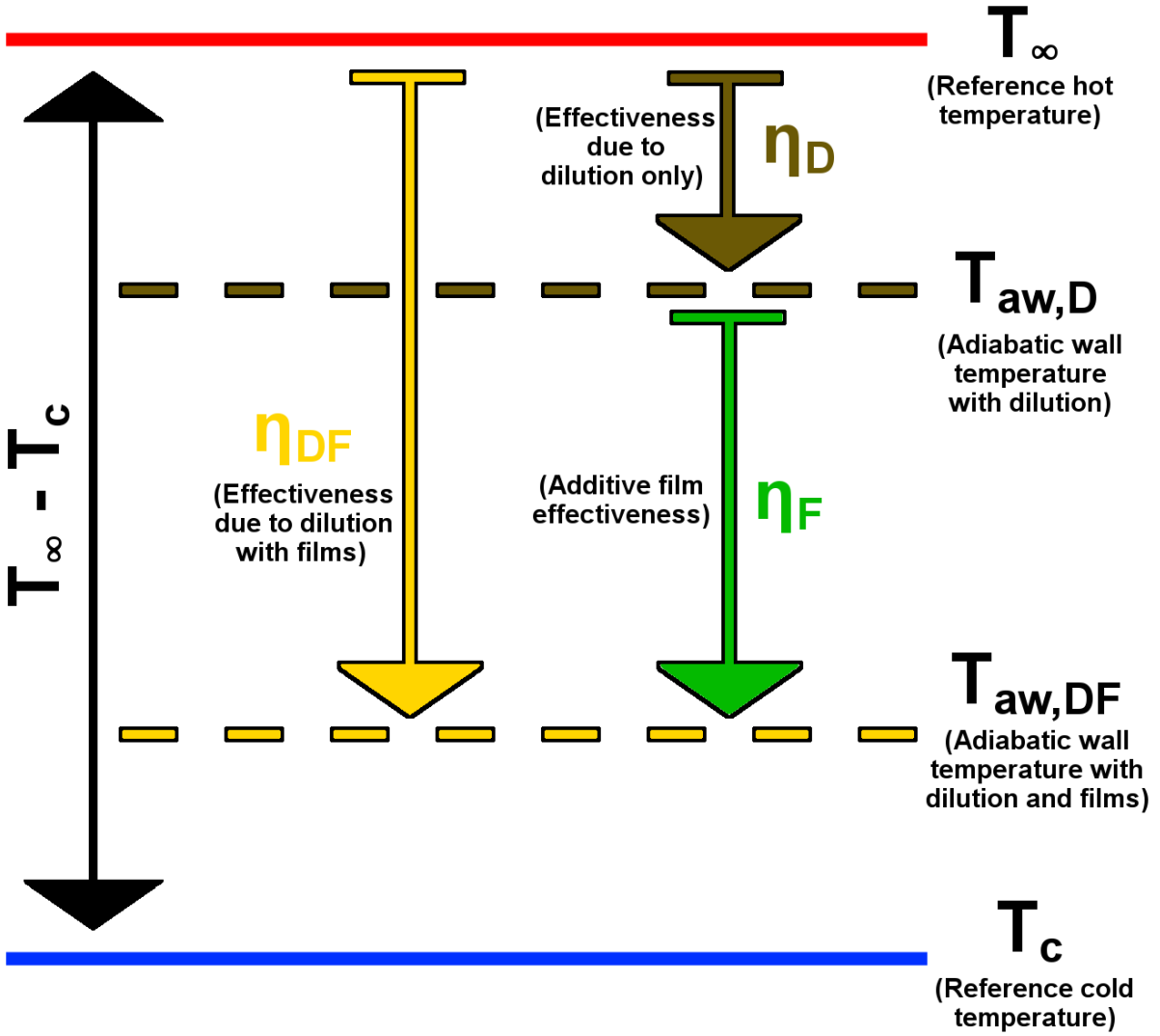


Figure 5.5: Conceptualisation of the additive film effectiveness as the additional temperature reduction when films are turned on with pre-existing upstream dilution.

of the two distributions. This quantity, when nondimensionalised, is referred to as the 'additive film effectiveness' η_F i.e. the film effectiveness additional to the artificial effectiveness caused by dilution port coolant flow. This concept is illustrated in Figure 5.5. In other words, the additive film effectiveness is the additional temperature drop of the dilution-and-films combination relative to the adiabatic wall temperature for the dilution acting by itself, normalised by the difference in reference temperatures for the experiment with films, according to Equation 5.2:

$$\eta_F(\mathbf{x}) = \frac{T_{aw,D}(\mathbf{x}) - T_{aw,DF}(\mathbf{x})}{T_{\infty,DF} - T_{c,DF}} \tag{5.2}$$

The hot and cold reference temperatures are the mass-averaged temperature of the combustor inlet and dilution port flows ($T_{\infty,DF}$) and the leading edge coolant temperature ($T_{c,DF}$) respectively. In order to account for potential small changes in operating conditions between the D and DF experiments, the dilution-only adiabatic wall temperature ($T_{aw,D}$) is measured on the uncooled calibration leading edge model and its nondimensionalised effectiveness calculated according to Equation 5.3.

$$\eta_D(\mathbf{x}) = \frac{T_{inlet,D} - T_{aw,D}(\mathbf{x})}{T_{inlet,D} - T_{p,D}} \tag{5.3}$$

This dilution-only experiment instead makes use of the combustor inlet temperature ($T_{inlet,D}$) as a hot reference temperature, since this is not a strong function of the dilution mass flow rate and it maintains a positive nondimensionalised quantity. Furthermore, it makes use of the dilution port coolant temperature ($T_{p,D}$) as a cold reference temperature, since vane film coolant is not present. These different reference temperatures for the dilution-only experiment mean that the relative magnitude of η_D is slightly misrepresented in the illustrative Figure 5.5. The corresponding dilution-and-films reference temperatures $T_{inlet,DF}$ and $T_{p,DF}$ are then used to attain the condition-corrected vane cooling contribution of the dilution ports for this case. Rearrangement of Equation 5.3 for $T_{aw,D}$ and substitution into the additive effectiveness definition yields Equation 5.4.

$$\eta_F(\mathbf{x}) = \frac{T_{inlet,DF} - \eta_D(\mathbf{x}) \times (T_{inlet,DF} - T_{p,DF}) - T_{aw,DF}(\mathbf{x})}{T_{\infty,DF} - T_{c,DF}} \tag{5.4}$$

Before the dilution port temperature profile $\eta_D(\mathbf{x})$ is employed in Equation 5.4, the visible calibration model thermocouples (some of which leak trace amounts of coolant through the thermocouple wire tunnels, see Figure 5.10) are spatially smoothed. An example of the process for determining the additive effectiveness at a particular combination of blowing ratio and dilution momentum flux ratio is illustrated in Figure 5.6. The relevant nondimensionalised dilution port vane surface temperature profile Figure 5.6(b) is applied to the suction side dilution-and-films effectiveness Figure 5.6(a). This yields the additive effectiveness Figure 5.6(c). Comparison of the additive film effectiveness for $J_D = 9$ in

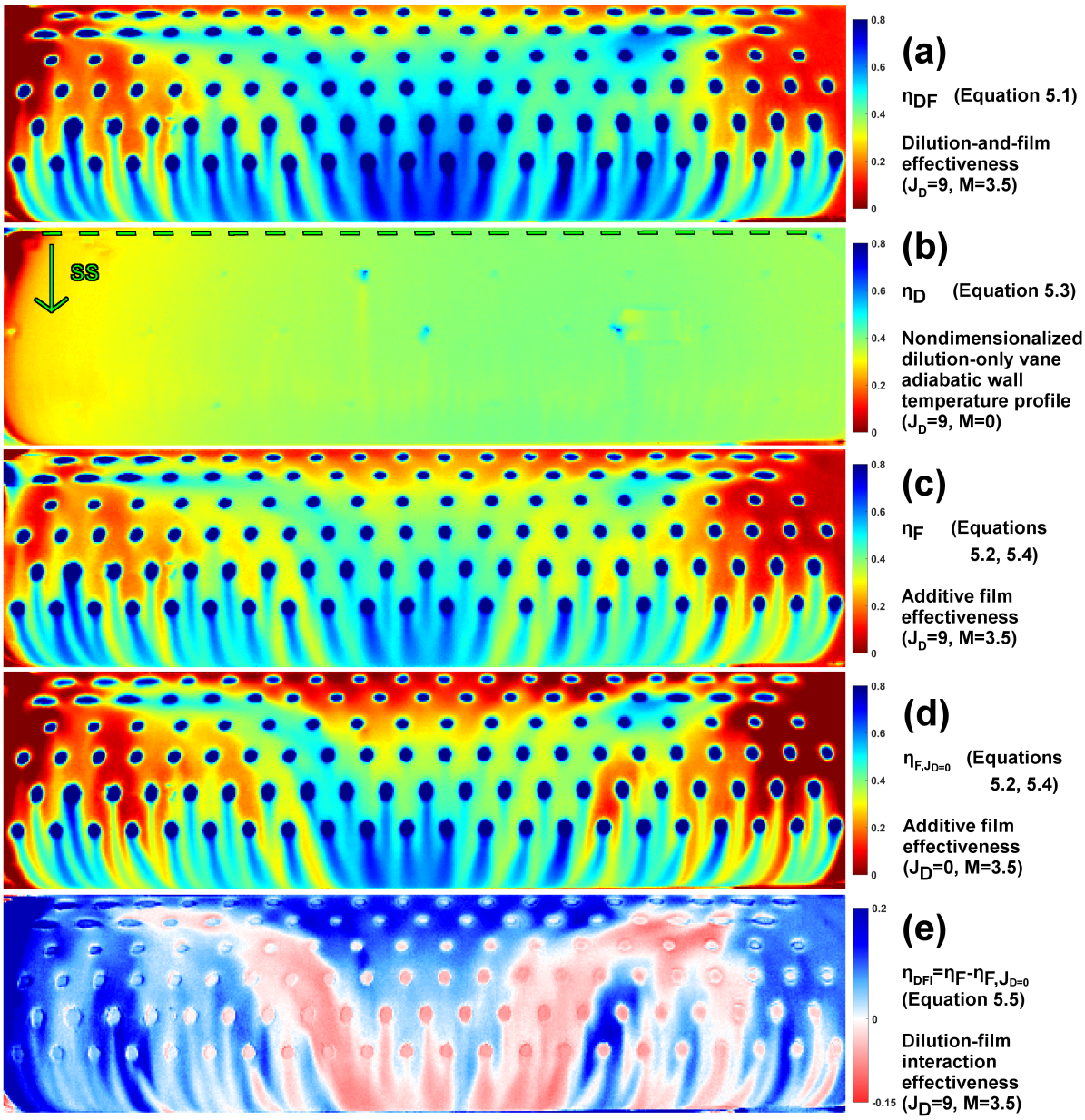


Figure 5.6: An example of the film effectiveness data processing used. Note the different colour scale employed for DFI images. Positive/negative DFI effectiveness indicates that dilution port turbulence enhances/diminishes local film effectiveness, the mechanisms for which are discussed in section 5.5.

Figure 5.6(c) and $J_D = 0$ in Figure 5.6(d) reveals that the addition of NGV leading edge films causes a greater film effectiveness gain near the radial showerhead in the presence of dilution than in its absence. This gain is independent of the two different dilution port temperature profiles (essentially constant in the $J_D = 0$ case) by virtue of their prior subtractions from the film data. This film performance improvement can be more clearly visualised by the difference map of the two cases shown in Figure 5.6(e) and defined as

the 'dilution-film interaction effectiveness' (DFI effectiveness):

$$\eta_{DFI} = \eta_F - \eta_{F,J_D=0} \tag{5.5}$$

The DFI effectiveness for a given dilution port momentum flux ratio (or indeed for any generalised upstream flow condition e.g. including endwall film coolant) represents the change in leading edge film effectiveness relative to a no-dilution case which is caused by aspects of the dilution other than its effect on the vane inlet temperature profile i.e. its effect on the vane inlet turbulence.

5.3 Film Cooling Uncertainty Analysis

In this section, the uncertainties in the various surface temperature and heat transfer coefficient measurements are discussed. The uncertainties for quantities derived from rig mass flow rate and pressure measurements are discussed in sections 3.6 and 7.3.4, respectively.

5.3.1 Film Effectiveness

The uncertainties in the effectiveness measurements η_D (nondimensionalised adiabatic wall temperature profile on the vane due to dilution ports only) and η_{DF} (film effectiveness with dilution) are calculated from the propagated uncertainties in the camera black-body output, thermocouple readings, grey-body product $\tau\epsilon$, and surrounding radiance measurements. Regions of higher vane surface temperatures typically exhibit lower uncertainties. Table 5.2 reports the minimum and maximum uncertainties for these two quantities, as well as those implied for the derived quantities additive film effectiveness (η_F) and dilution–film interaction effectiveness (η_{DFI}). As discussed in section 4.5.3, the present experiments assume that the repeatability of the experimental conditions is sufficiently accurate that the spatial infrared calibrations do not change significantly once the calibration test piece has been replaced by an uninstrumented, film-cooled test piece. The maximum expected surrounding radiance variations are included in the film effectiveness uncertainty estimates.

Table 5.2: Uncertainties for dilution-only, dilution-and-films, additive, and dilution-film-interaction effectiveness results. The uncertainties vary slightly both between cases and within individual images, resulting in the reported overall maxima and minima.

	η_D	η_{DF}	η_F	η_{DFI}
Max	0.019	0.029	0.035	0.049
Min	0.016	0.024	0.029	0.041

5.3.2 Heat Transfer Coefficients

The uncertainties in external HTCs were estimated using the perturbation method described by Moffat [123]. The variables driving uncertainty in the HTC calculation procedure were surface temperature, material thermal diffusivity, and surface-gas temperature time error, as well as the film effectiveness, coolant temperature and mainstream temperature used in the calculation of the driving gas temperatures. The uncertainty contributions of each for a single example experiment are provided in Appendix Appendix B. By far the largest contributors to HTC uncertainty are the surface temperature and the film effectiveness. This is apparent in the maps of uncertainty, δ_{HTC}, in Figure 5.7 for both the PS and SS since they resemble the corresponding maps of film effectiveness presented in section 6.4.2. This leads to uncertainties of approximately 9% to 18% on the pressure side and 10% to 60% on the suction side. The lower uncertainties occur near pressure side and upstream suction side film rows and are broadly consistent with uncertainties reported in previous, single-row HTC studies. Regions of very high effectiveness (within and after the final SS rows) exhibit greatly elevated HTC uncertainty because they experience a relatively small temperature rise after the mainstream becomes heated. The HTC uncertainties could be reduced with a greater mainstream-to-coolant temperature difference, or by also conducting an experiment with only the coolant heated, as per Chambers et al. [113].

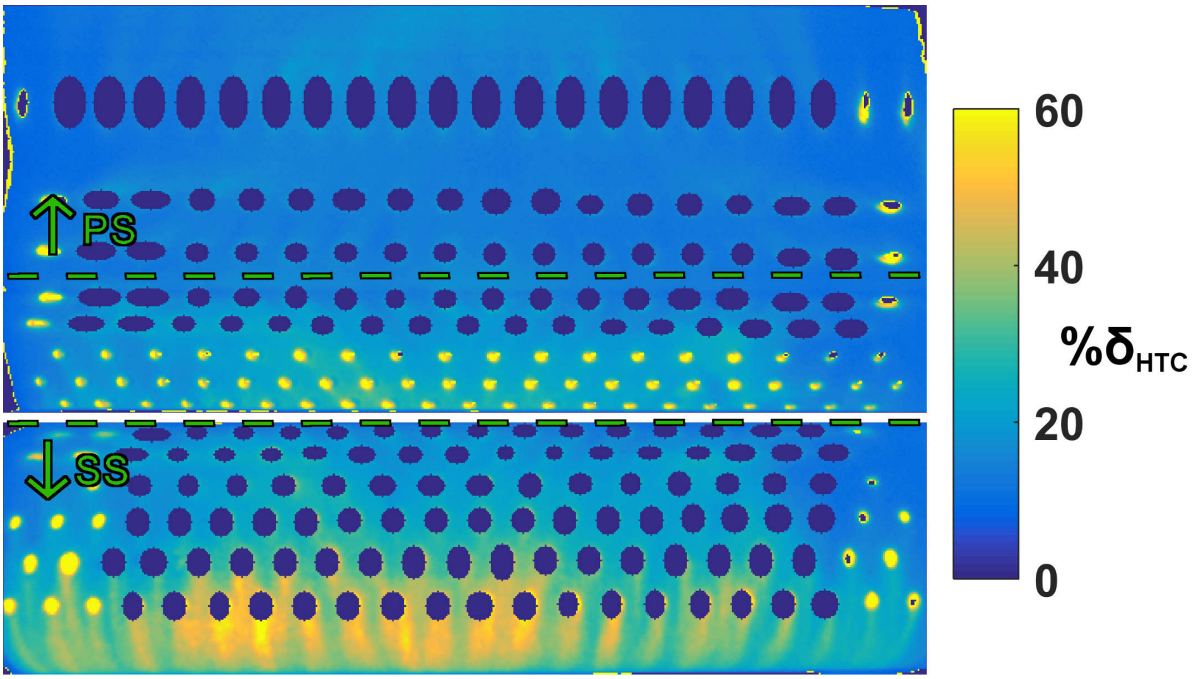


Figure 5.7: Percentage HTC uncertainties on the PS and SS on one of the film-cooled leading edge models investigated ($M = 3.5$, $J_D = 9$). Geometric stagnation line indicated.

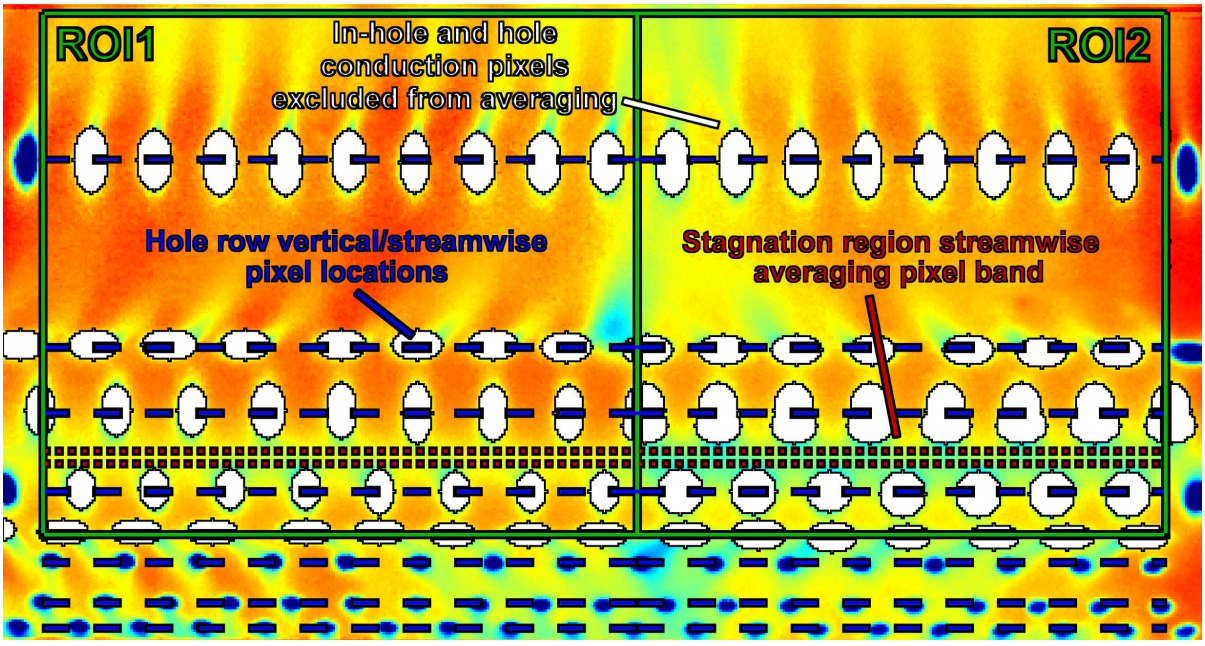


Figure 5.8: The two regions of interest (green lines), stagnation region (red dashed lines), and hole row locators (blue lines) used in producing averages of thermographic measurements.

5.4 Data Averaging Methodology

To produce averaged film effectiveness and heat transfer coefficient values, a simple MATLAB graphical output is used to choose and verify the regions over which averaging takes place for each test image. An example for a pressure side film effectiveness image is shown

in Figure 5.8. The in-hole pixels and nearby pixels strongly affected by in-hole convective cooling are excluded from averages (indicated by white spaces in the image data). Two regions of interest (ROIs, green lines) are chosen which correspond with the two spanwise halves of each model. The production of separate averages in each of these regions is especially useful for the analysis of leading edge film effectiveness models presented in chapter 6 whose halves each feature distinct cooling geometries. Area averages are taken as the average of all the pixels within a ROI. Within each ROI, streamwise and spanwise averaging are also conducted (meaning averaging along streamwise and spanwise line segments, respectively). Spanwise averaging is also known as lateral averaging in some film cooling literature. In the present studies, such averaging is possible simply by averaging along lines of pixels; no image warping is necessary owing to the midspan positions of the IR cameras and their careful alignment before each experiment (such that the top and bottom edges of each image are parallel with the hole rows, which always each lie at a constant streamwise position). The spanwise positions (s between 0 and 1) of streamwise-averaged data points are inferred by a simple linear interpolation with the spanwise positions of two hole centres. Since the streamwise positions of the hole breakouts relative to the leading edge stagnation line are known (blue lines), the streamwise positions of spanwise-averaged data points can be estimated (and hence the curvature of the vane surface accounted for) by linear interpolation. For a given experiment the process is performed on both the pressure side and the suction side. Since the pressure side camera also observes some of the suction side, a small portion of it is also included in the pressure side spanwise average. The overlap region where both results have been calculated is averaged and smoothed before plotting. The final average taken is a streamwise average confined to a thin strip between the PS1 and SS1 hole rows (red lines). This is useful in comparing the capabilities of various geometries to achieve high film effectiveness near to the geometric stagnation line, which is the main focus of chapter 6. In this chapter, only HTC laterally averaged results are presented. Detailed and averaged radial geometry film effectiveness results are reserved for chapter 6 to facilitate comparisons with the effectiveness results of the alternative leading edge geometries proposed therein.

5.5 Results

Film effectiveness and heat transfer coefficient images for a given model, blowing ratio, and dilution port momentum flux ratio are acquired in a single heated, 'hybrid transient-steady' experiment (section 4.7) using unique, spatially-resolved infrared calibrations (section 4.6) and conductivity corrections (section 3.8.2), and the relevant dilution port temperature profile correction (section 5.2). Three blowing ratios and four dilution port momentum flux ratios are investigated. Endwall film cooling was not used ($J_E = 0$). The mainstream suction fan speed was kept constant during these tests, such that changes to the dilution port and leading edge coolant mass flow rates resulted in a range of Reynolds numbers (based on the vane throat flow properties and chord length) of 8.52×10^5 to 1.02×10^6. Owing to this Reynolds number variation across experiments, it was necessary to conduct additional tests to determine the influence of Reynolds number on film effectiveness results. A study was conducted in which no combustor coolant flowed ($J_D = J_E = 0$) and the blowing ratio was fixed ($M = 1.5$) but two suction fan speeds were used, each achieving approximately one of these two Reynolds number extremes. Figure 5.9 shows the difference map of the leading edge film effectiveness distributions achieved in these two tests. Most of the observed leading edge pressure surface experienced a change in measured film effectiveness of less than 0.005, and only highly localised regions changed by more than 0.02. Therefore, Reynolds number effects on film effectiveness in the present studies are considered negligible compared to the rival effects of film coolant mass flow rates and dilution port flow field changes. This also suggests that in general any slight departures of experimental rig vane Reynolds numbers from those of corresponding real engines will only generate second order differences in the respective film effectiveness distributions, implying an element of leeway in the choice of rig size and fan specifications given near-standard atmospheric operating conditions.

5.5.1 Dilution Port Temperature Profiles

The dilution port temperature profiles as manifested on the leading edge are captured with the no-films calibration test piece. Figure 5.10 shows NGV leading edge adiabatic

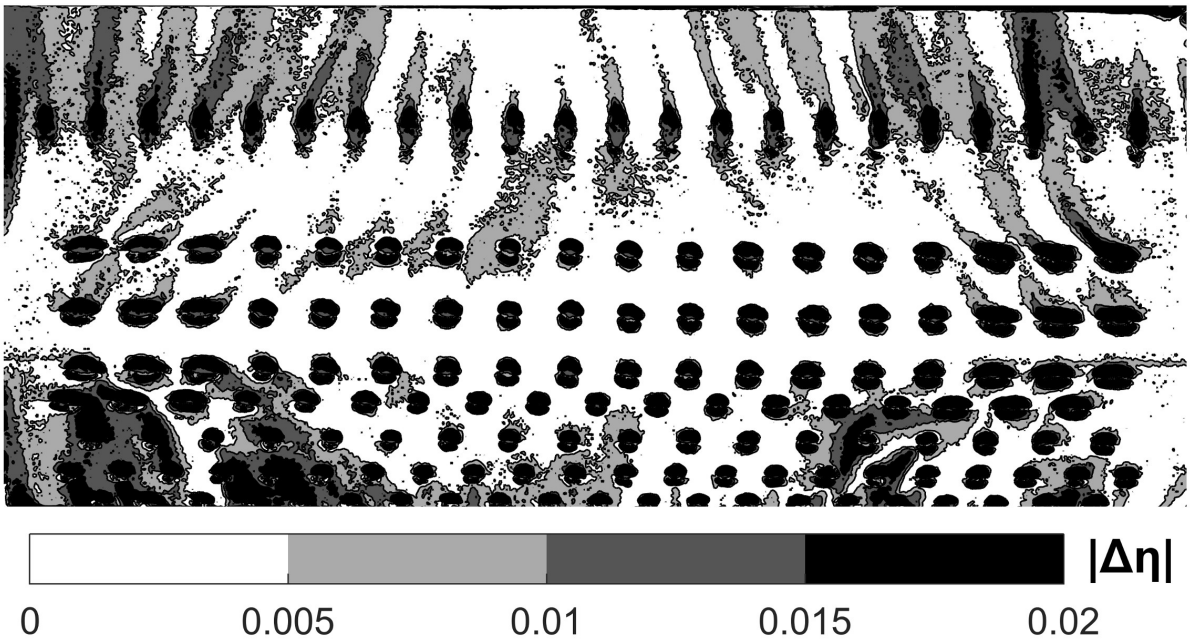


Figure 5.9: Contours of absolute change in pressure side film effectiveness due to a change of Reynolds number from 8.5×10^5 to 1.0×10^6. $J_D = J_E = 0$, $M = 1.5$.

wall temperatures (surface temperature results corrected for conduction effects) nondimensionalised according to Equation 5.3 for three dilution port momentum flux ratios and no NGV or endwall film cooling. The approximate position of the geometric stagnation line is indicated for both the pressure side and the suction side views. For $J_D = 4$, the greater mass flow through the outer dilution ports (right side) due to their slightly larger combined hole area creates a distinct cool patch. The sloped combustor liner wall on the inner wall (left) may also act to disperse the inner dilution port coolant or direct it away from the central vane. For $J_D = 9$, the most engine-representative case, the outer dilution port coolant has clearly penetrated farther into the mainstream, and a more uniform temperature profile is created. The still greater coolant penetration and mass flow rate for $J_D = 15$ produces the most uniform profile.

5.5.2 CFD Simulation of Dilution Port Momentum Flux Ratios

To enhance the interpretation of the experimental results on the dilution ports' effects on leading edge film effectiveness, RANS CFD simulations were performed whose domain featured the combustor inlet, dilution ports, and the vane cascade without leading edge film cooling. All three experimental dilution port flow rates were simulated, with the

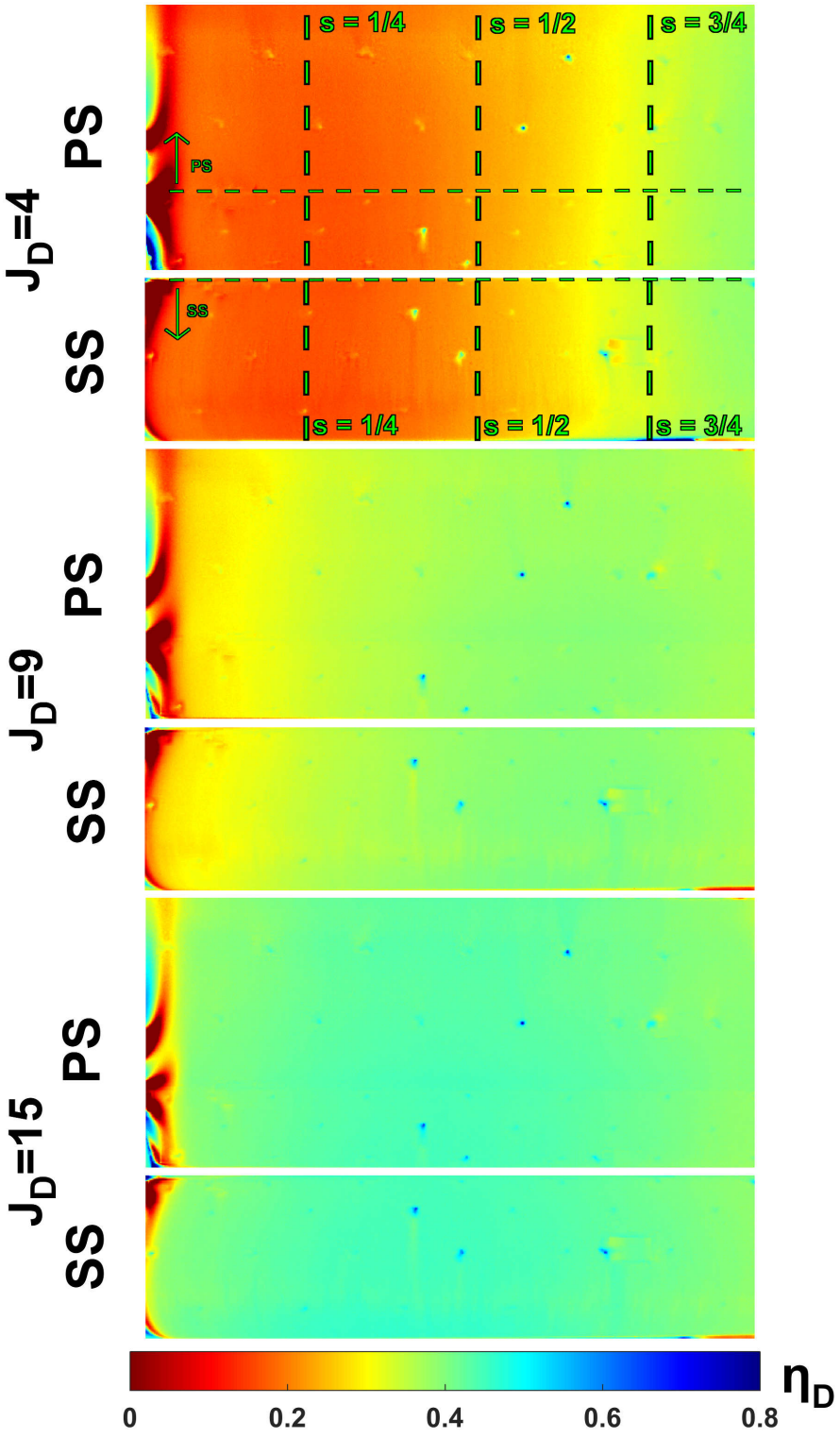


Figure 5.10: Nondimensionalised vane adiabatic wall temperature profiles due to dilution ports. $J_D = 4$, 9, 15, $J_E = 0$, $M = 0$. $\eta_D(\mathbf{x}) = \frac{T_{inlet,D} - T_{aw,D}(\mathbf{x})}{T_{inlet,D} - T_{p,D}}$ (Equation 5.3).

temperature and mass flow rate boundary conditions identical to those recorded during experiments. Additional refinement (to 18.3 million elements) of the 12.3 million element CFD mesh used produced little change in the results, and the Standard $k-\epsilon$ turbulence model used did not produce significantly different results compared to a trial case with the k–ω Shear Stress Transport model. Figure 5.11 shows a cross section through the centre of the 12.3 million element mesh and the refinements in the dilution port mixing and vane leading edge zones (also used but not shown are refinements in the dilution port holes). Figure 5.12 shows that the CFD closely predicts the experimentally observed dilution port temperature profiles (Figure 5.10) as manifested on the central leading edge. Cha et al. [74] compared a RANS $k-\epsilon$ simulation of an engine-realistic combustor with dilution ports to corresponding LES and experimental results. They found that although the RANS simulation quantitatively overpredicted turbulence intensity, it adequately predicted the experimental results in terms of its relative distribution just upstream of the vane inlet. The corresponding predictions of the present simulations prove useful to understanding the results for DFI effectiveness in the following section. Figure 5.13 presents contours of CFD-predicted turbulent kinetic energy (TKE) at three normalised vane spanwise positions (also indicated for reference on the experimental results in Figure 5.10) and for the three experimentally tested momentum flux ratios. As the dilution port momentum flux ratio increases, there is a clear increase in the TKE at all three planes. For $J_D = 4$ and $J_D = 9$, there is relatively little turbulent kinetic energy produced by the dilution ports at $s = \frac{1}{4}$ compared to $s = \frac{3}{4}$, but for $J_D = 15$ the spanwise distribution of turbulence is more equal. The asymmetry at lower J_D is due to the smaller combined dilution port area of the inner relative to the outer, as well as the sloped inner endwall, which places the inner dilution ports at a spanwise coordinate of $s = -\frac{1}{2}$, while the outer dilution ports are at $s = 1$. At low J_D, the inner endwall coolant jets have insufficient momentum to substantially penetrate to $s = \frac{1}{4}$.

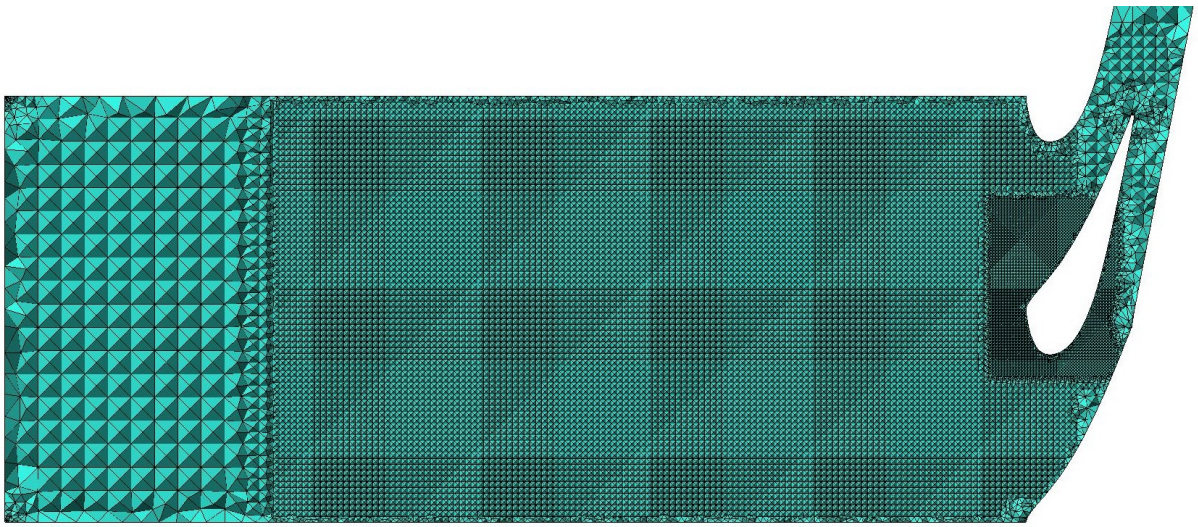


Figure 5.11: 12.3 million element CFD mesh used to predict temperature profiles on the CTI rig's central NGV leading edge due to dilution ports.

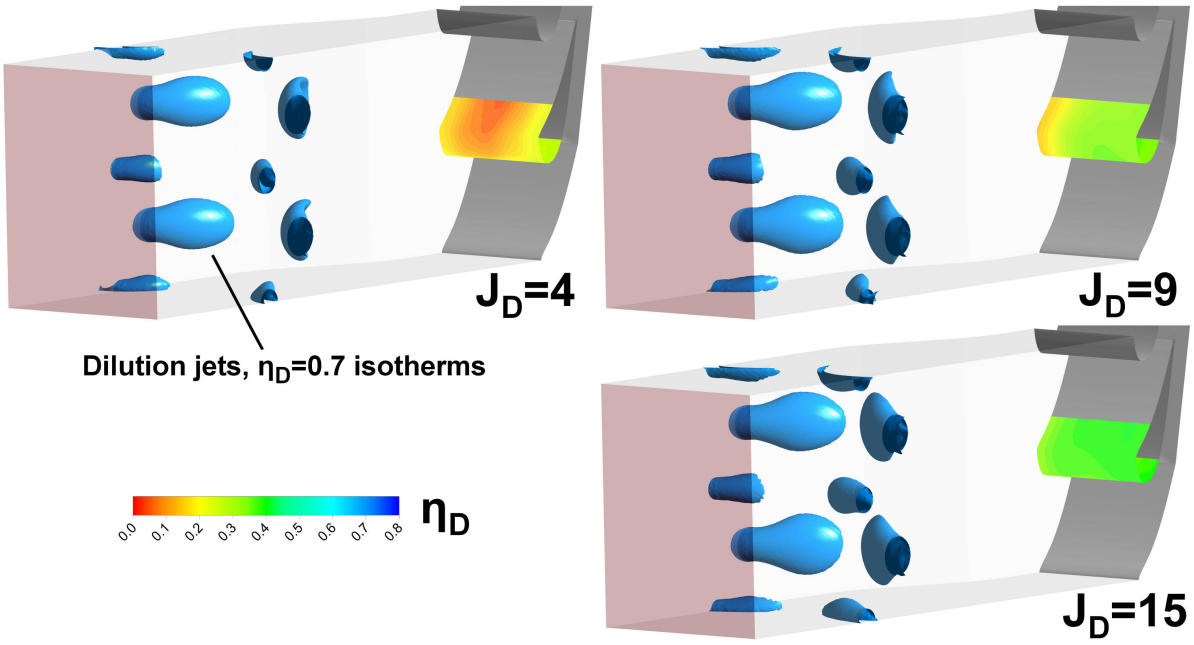


Figure 5.12: CFD-predicted nondimensionalised vane adiabatic wall temperature profiles due to dilution ports. Isotherms show the increasing penetration of dilution jets into the mainstream with increasing momentum flux ratio. $J_D = 4$, 9, 15, $J_E = 0$, $M = 0$. $\eta_D(\mathbf{x}) = \frac{T_{inlet,D} - T_{aw,D}(\mathbf{x})}{T_{inlet,D} - T_{p,D}}$ (Equation 5.3).

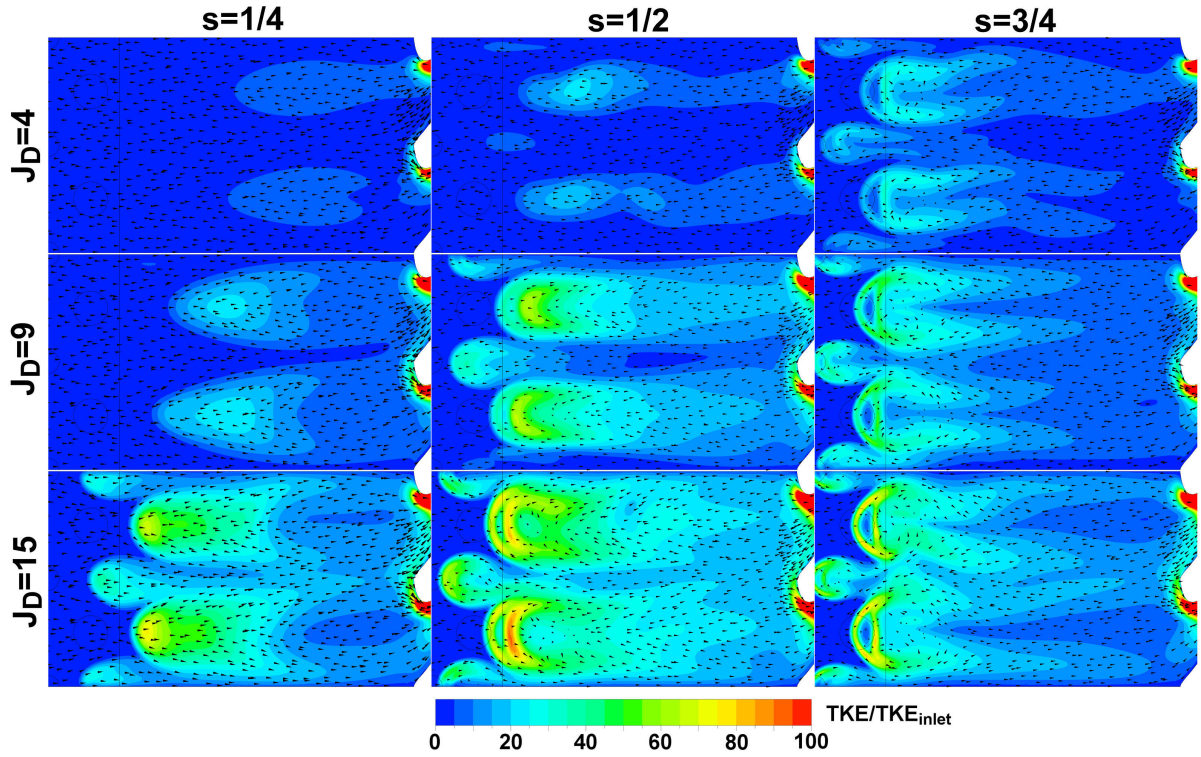


Figure 5.13: Contours of CFD-predicted turbulent kinetic energy (TKE) in the combustor simulator in planes orthogonal to the NGV spanwise direction. $s = \frac{1}{4}, \frac{1}{2}, \frac{3}{4}$ and $J_D = 4, 9, 15$.

5.5.3 Dilution-Film Interaction Effectiveness

Figures 5.14 through 5.19 present the DFI effectiveness results for all three radial leading edge test pieces at three dilution port momentum flux ratios and three leading edge blowing ratios. Figure 5.14 indicates the approximate position of the geometric stagnation line for both the pressure side and the suction side views. The no-dilution reference for each blowing ratio's data is the $J_D = 0$ additive film effectiveness for the same blowing ratio. The additive effectiveness of the final pressure side hole row (PS3) jets tends to decrease due to the action of the dilution port turbulence, owing to the accelerated removal of coolant from these attached jets by mixing with the mainstream. However, for cases with strong and highly uniform additive effectiveness gain at the radial showerhead, this decrease is offset or even reversed, especially in the gaps between those PS3 holes (and their jet paths) which lie directly downstream of the showerhead gains. This indicates that the turbulence-augmented, near-surface mixing of upstream radial coolant jets also produces downstream cooling effects as this coolant passes between the downstream jets. The expected reduction of attached jet effectiveness due to dispersion of the jet coolant

may be obscured for some jets by the altered interactions between rows; turbulent removal of coolant from the upstream jets also changes the paths of these jets and hence their interactions with downstream jets.

On the suction side the final three rows (SS4-SS6) are attached to varying extents (more attached farther downstream and for lower blowing ratios). The effectiveness due to these jets is therefore susceptible to decrease in the presence of elevated turbulence from dilution port flow. At all blowing ratios, greater amounts of dilution tend to reduce the spanwise variation in its effects on additive film effectiveness. This is most obvious for model RAD-A (Figures 5.14 and 5.15) since it only features streamwise-blowing films, and can be understood in terms of the CFD results indicating spanwise turbulence variation. For $J_D = 4$, turbulence is only significantly elevated near to the outer endwall, so the effects of coolant jets more rapidly mixing with the hot mainstream are most prevalent there. As the dilution flow rate increases, the turbulence near the midspan and inner endwall is also significantly increased, resulting in a more evenly diminished spanwise suction side effectiveness. Model RAD-C exhibits increases (or offset reductions) of the suction side effectiveness near to the endwalls over the no dilution cases. This is due to the competing effect of the passage downstream of coolant being removed from the low surface angle radial jets by the increased mainstream turbulence. This effect can be seen in Figures 5.18 and 5.19, where the effectiveness surrounding jets from low surface angle holes is enhanced due to the increased local extraction and mixing of jet coolant as the dilution port flow increases. This effect also explains the two higher blowing ratios' two prominent (especially for $J_D = 9$ and $J_D = 15$) suction side streaks, within which dilution reduces the effectiveness of the film coolant. The increased turbulence removes lateral momentum from the upstream coolant, causing it to remain closer to the endwalls during its passage downstream. A single pressure side streak is also clearly visible on the pressure side of model RAD-B, which is generated by the same effect and narrows with increasing blowing ratio.

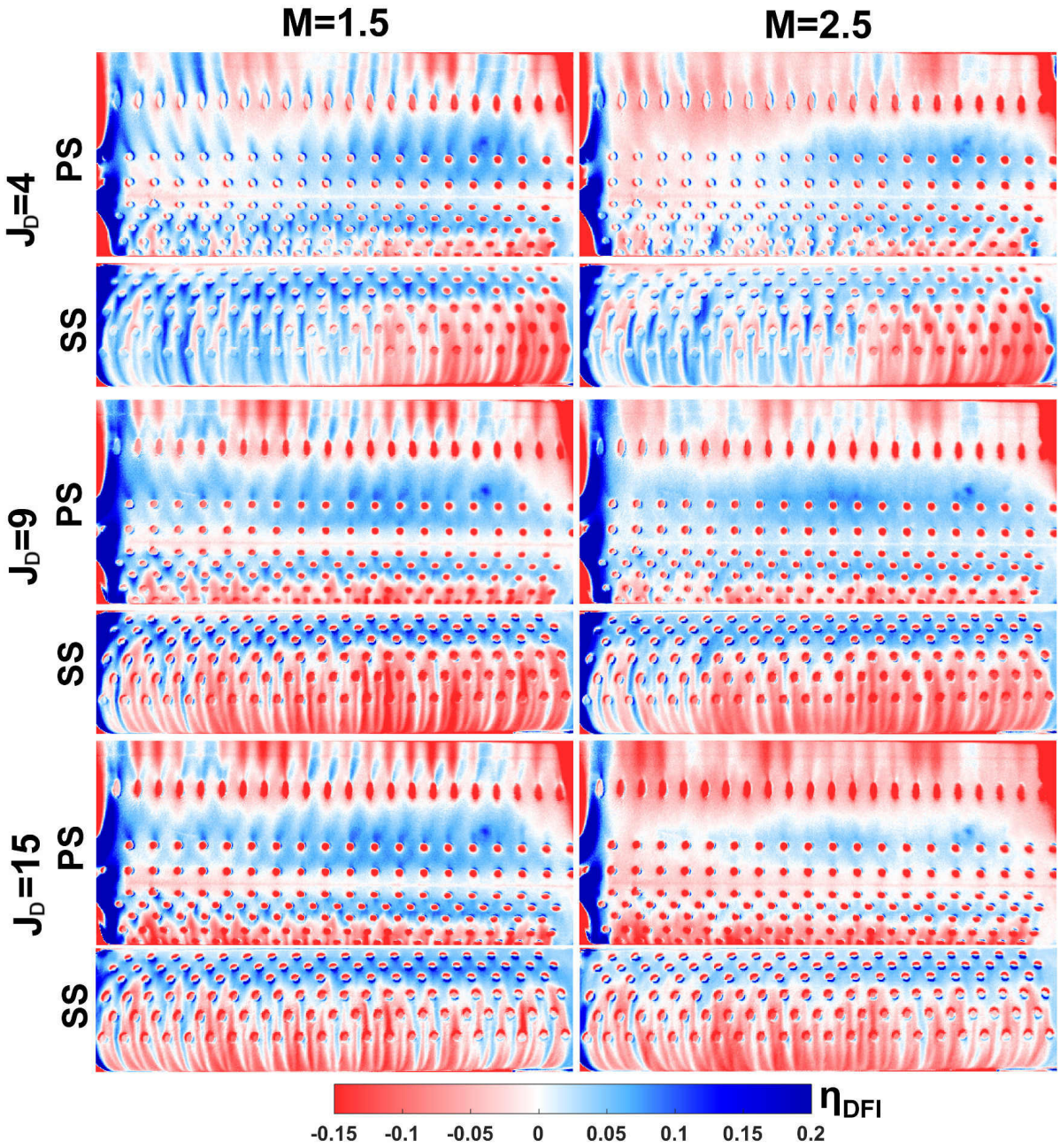


Figure 5.14: DFI effectiveness for model RAD-A at $M = 1.5$ and 2.5, and three dilution momentum flux ratios, $J_D = 4$, 9, 15. The DFI effectiveness represents the gain in effectiveness of the leading edge film due to the dilution port turbulence.

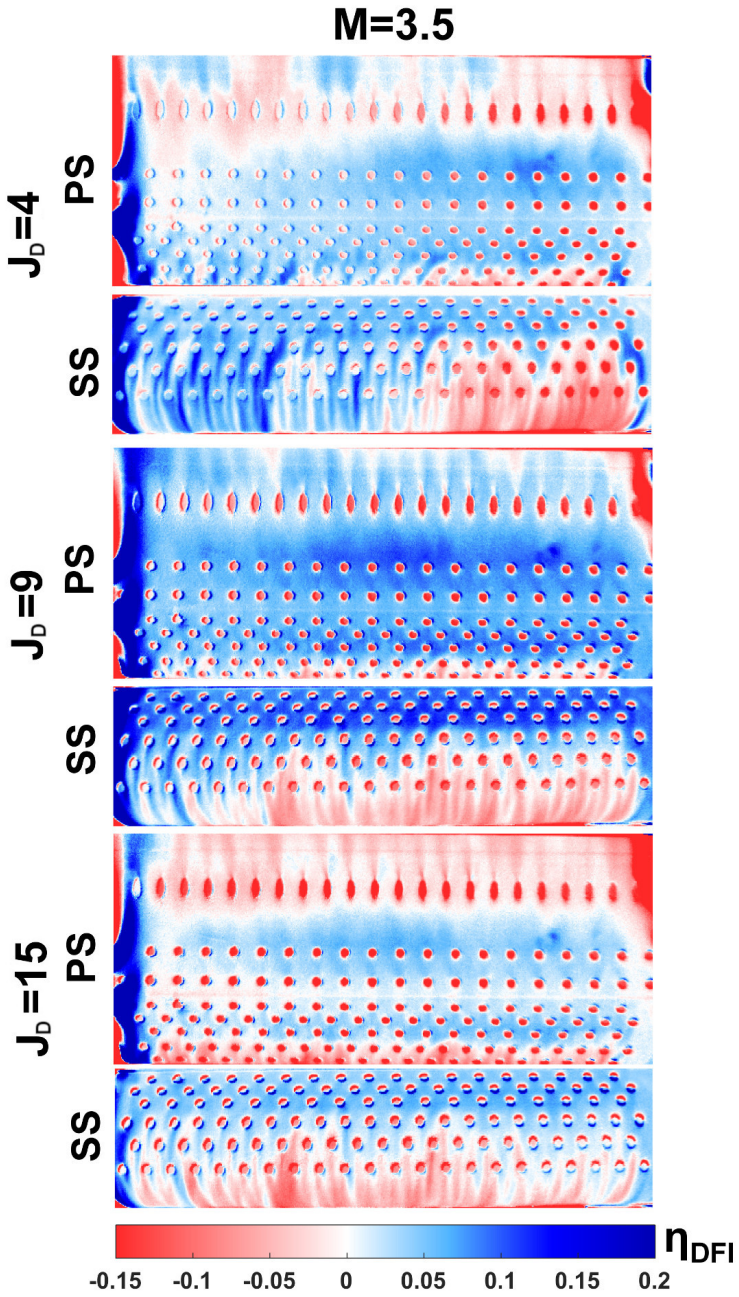


Figure 5.15: DFI effectiveness for model RAD-A at $M = 3.5$ and three dilution momentum flux ratios, $J_D = 4$, 9, 15.

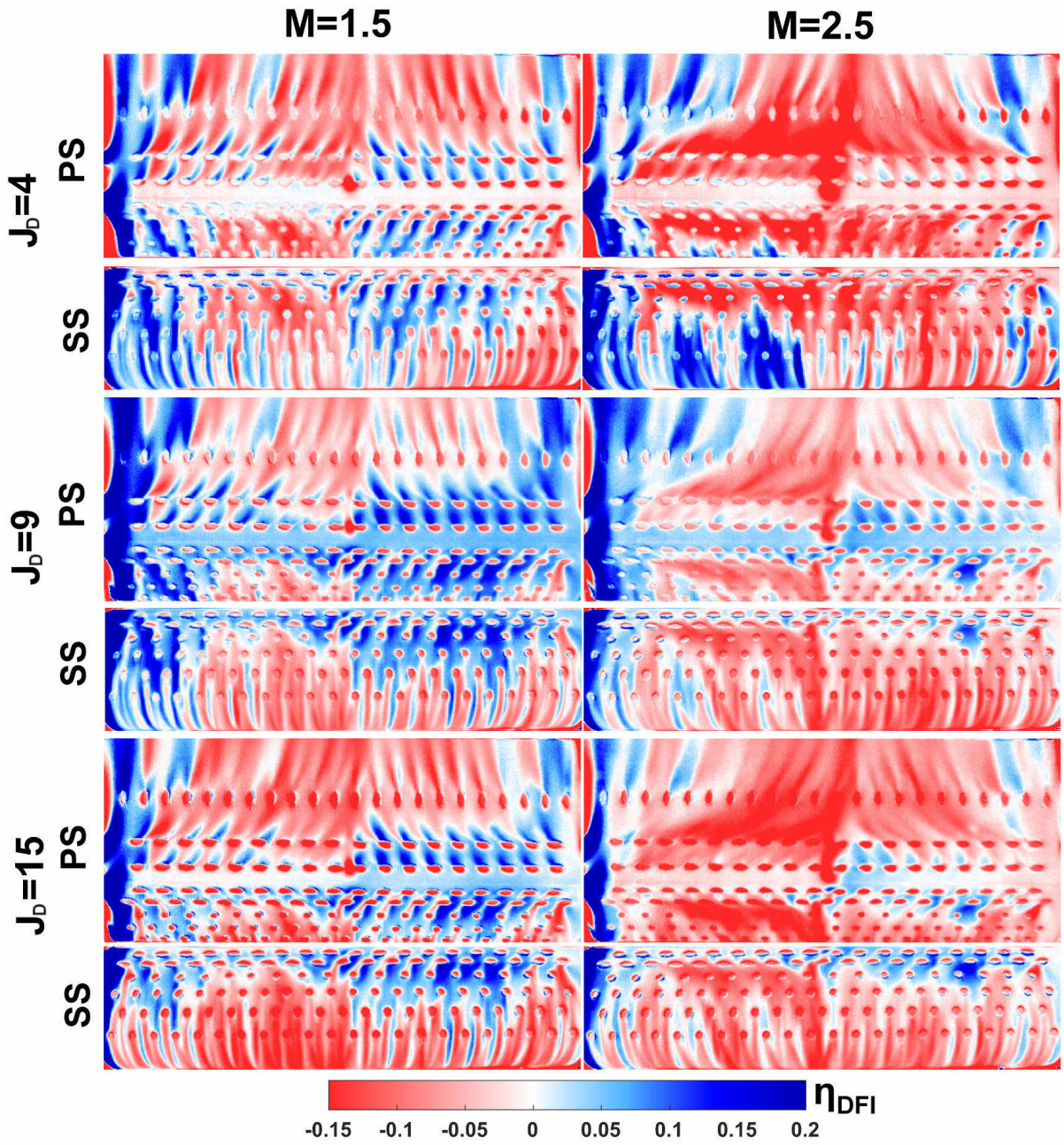


Figure 5.16: DFI effectiveness for model RAD-B at $M = 1.5$ and 2.5, and three dilution momentum flux ratios, $J_D = 4$, 9, 15.

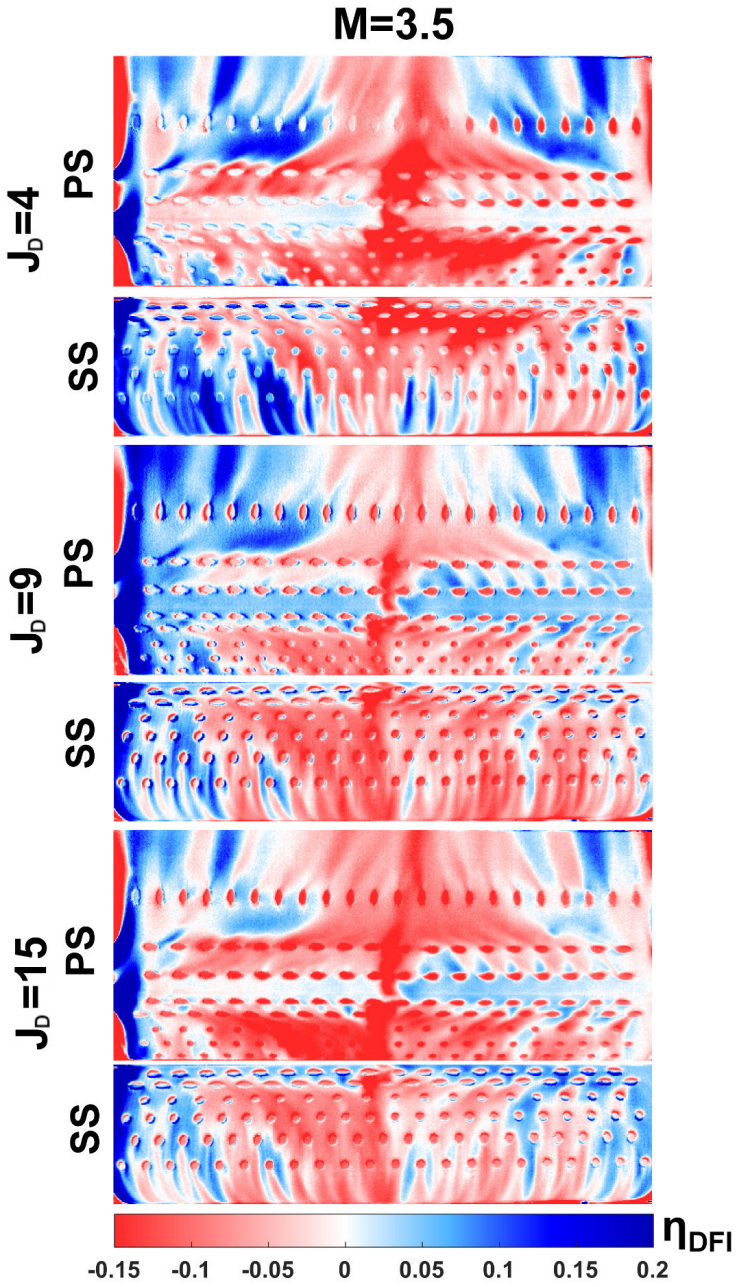


Figure 5.17: DFI effectiveness for model RAD-B at $M = 3.5$ and three dilution momentum flux ratios, $J_D = 4$, 9, 15.

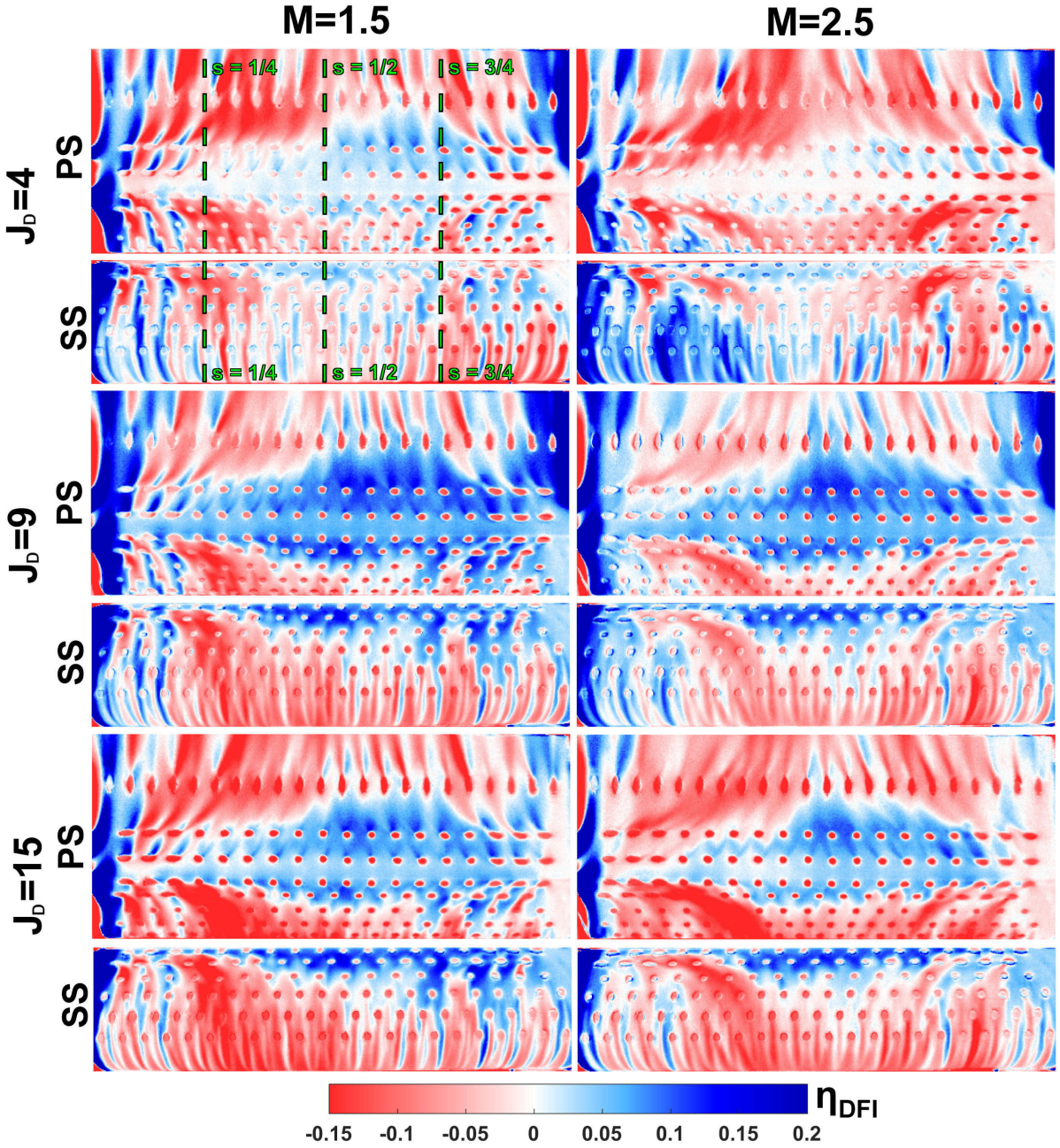


Figure 5.18: DFI effectiveness for model RAD-C at $M = 1.5$ and 2.5, and three dilution momentum flux ratios, $J_D = 4$, 9, 15.

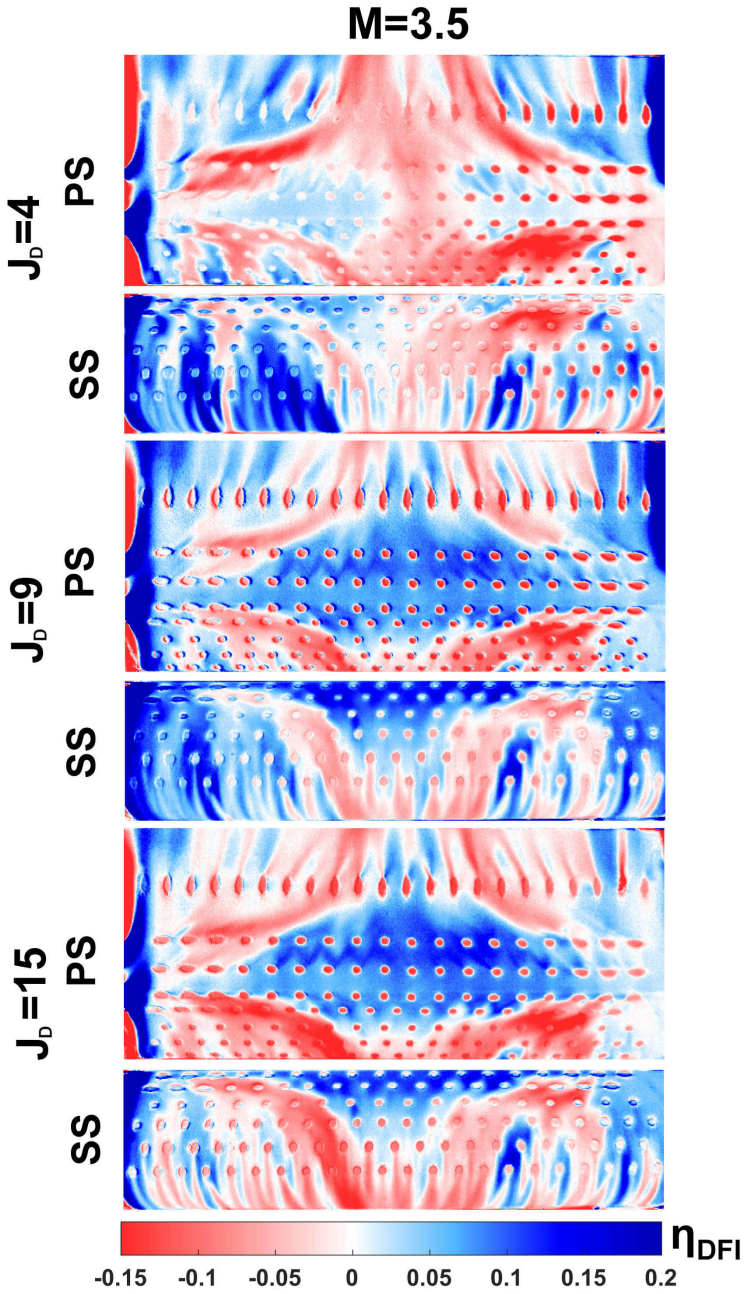


Figure 5.19: DFI effectiveness for model RAD-C at $M = 3.5$ and three dilution momentum flux ratios, $J_D = 4$, 9, 15.

Since film effectiveness is typically at its lowest within and nearby the showerhead (e.g. Figure 5.4), the changes brought about by dilution are proportionally the greatest and hence are most significant in this region. Due to its spanwise-uniform hole alignments, model RAD-A experiences uniform effectiveness gains in this region due to dilution. These gains are due to the turbulence-enhanced near-hole mixing of lifted-off jets also observed on flat plates by Schmidt and Bogard [54], and others. Because the jets are lifted off, additional turbulence results in further dilution of the mainstream before it reaches the aerofoil surface. RAD-B is more prone to experiencing showerhead effectiveness reductions because the attached jets from the low surface angle radial holes have more coolant removed by turbulence and swept downstream. Near the midspan region of the RAD-C showerhead, all but the lowest dilution momentum flux ratio demonstrate greater film effectiveness increases than on the RAD-A showerhead, of up to 0.2. This is due to the intermediate surface angles of the midspan radial holes. Like the RAD-A showerhead holes, the jets are detached. However, the slightly lower surface angle means that they remain closer to the surface before they are swept downstream, increasing the extent of turbulent mixing near the point of ejection. Across the range investigated, the blowing ratio has little influence on the magnitude of the effect, but at higher blowing ratios the improved region extends downstream around the midspan on both the pressure and suction sides. The higher jet hole exit velocities increase the near-surface shear stresses and hence the amount of coolant which is locally extracted to remain resident near to the surface as it progresses downstream.

5.5.4 Heat Transfer Coefficients

Heat transfer coefficients are nondimensionalised as Frossling number according to Equation 5.6:

$$Fr = \frac{hw}{k_f \sqrt{Re_w}} \tag{5.6}$$

Past studies reporting this quantity on cylindrical leading edges used the cylinder diameter as the characteristic length (e.g. Mick and Mayle [48] and Sen et al. [34]). By analogy, the vane leading edge axial width w (defined by the axial line segment intersecting both

the geometric stagnation point and the suction surface) is used in this study. k_f is the fluid thermal conductivity and Re_w is the Reynolds number based on the mainstream approach velocity and the aforementioned characteristic length w. Figures 5.20(b) and 5.21(b) show the Frossling number distributions on model RAD-C for $M = 3.5$ and $J_D = 9$. Due to convective cooling inside of holes and conduction effects visible in the effectiveness images Figures 5.20(a) and 5.21(a), the film effectiveness and hence driving gas temperatures are not accurately known in the immediate vicinity of each hole exit (approximately 20% of a hole diameter). Therefore, the hole exits and their immediate surroundings are intentionally excluded from HTC calculations. These near-hole HTCs could be obtained more accurately with a fully 3D finite element approach in which appropriate assumptions were made about the convection within the holes. The HTCs are clearly elevated towards the inner endwall (left), especially around SS5 and SS6, due to the slightly higher mainstream velocity generated by the inner endwall contraction, identified by Cresci et al. [124].

Figures 5.22 and 5.23 present laterally averaged Frossling number for all three radial models across all three blowing ratios and four dilution port momentum flux ratios. Due to the low acceleration on the pressure side, the HTC is relatively flat, increasing modestly with the elevated mainstream turbulence of higher dilution flow rates and the elevated local turbulence of higher film coolant mass flow rates. Suction side HTCs increase rapidly as the mainstream flow accelerates, producing more turbulence due to increasingly vigorous shear stresses with subsequent rows of film jets. After the final hole row, the ability of a turbulent boundary layer to grow begins to reduce the HTC. The suction side HTCs also tend to increase with higher dilution and film coolant flow rates. Model RAD-A tends to produce the highest suction side HTCs. Since this model experiences the greatest stagnation region jet lift-off and hence the most significant shear and mixing, this suggests a strong dependence of suction side HTCs on the turbulence generation by upstream film jets.

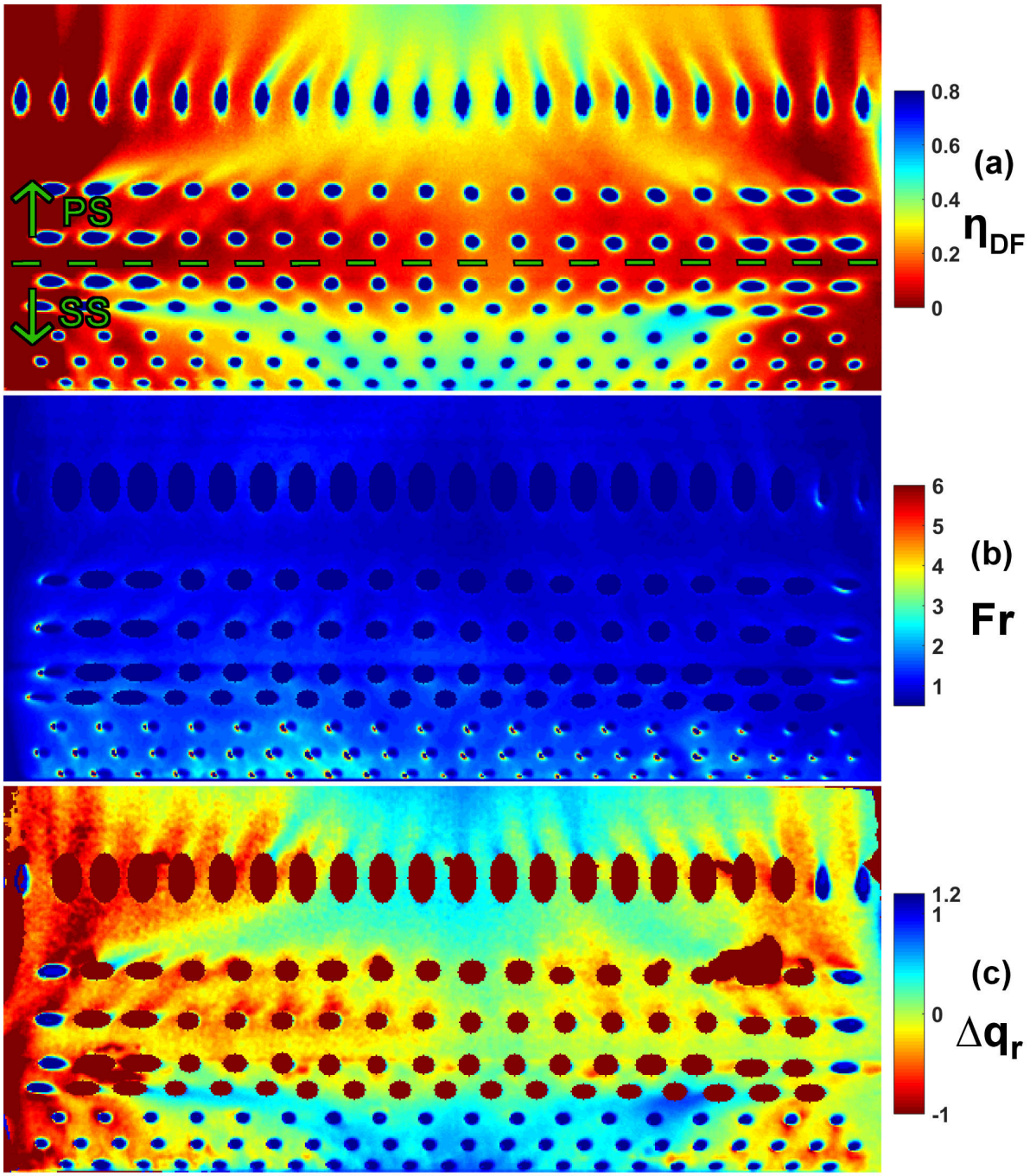


Figure 5.20: (a) Film effectiveness (b) Frossling number, and (c) estimated net heat flux reduction on the pressure side of model RAD-C. $M = 3.5$, $J_D = 9$, $J_E = 0$.

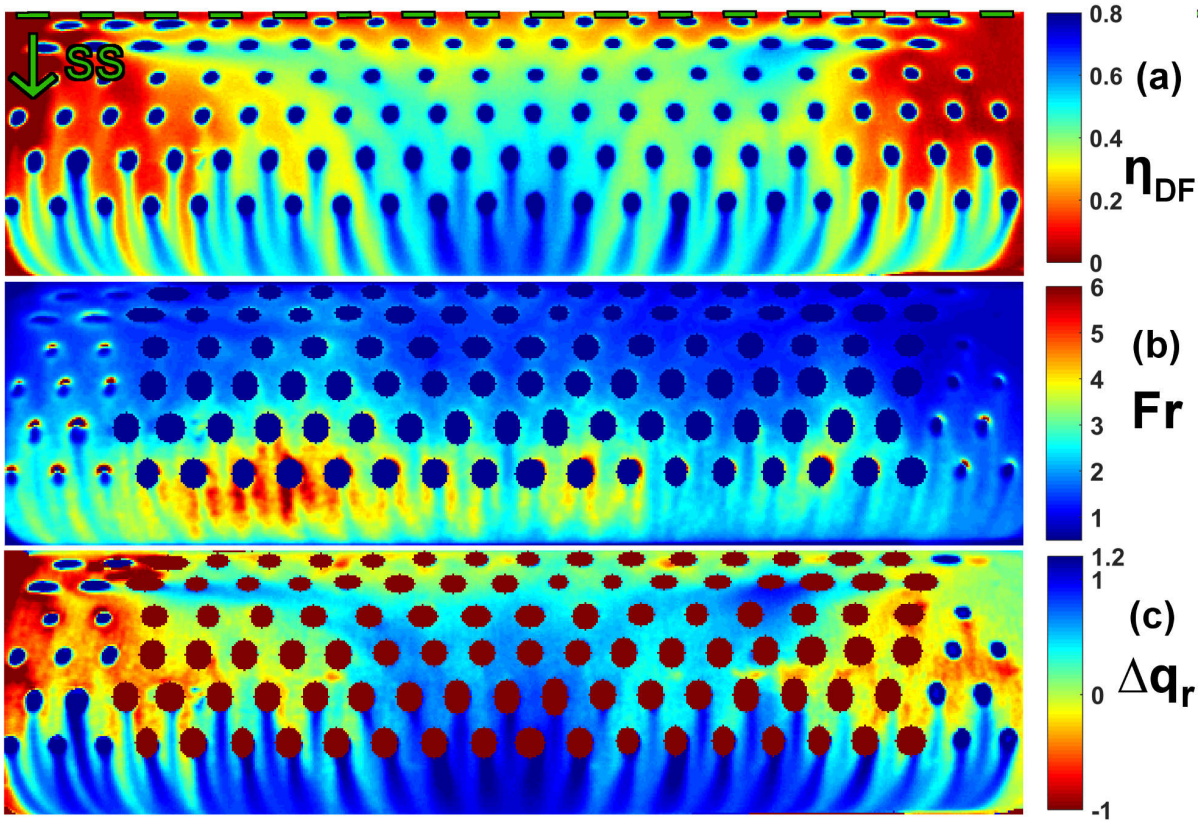


Figure 5.21: (a) Film effectiveness (b) Frossling number, and (c) estimated net heat flux reduction on the suction side of model RAD-C. $M = 3.5$, $J_D = 9$, $J_E = 0$.

5.5.5 Net Heat Flux Reduction

As discussed in section 2.1, the efficacy of a film cooling design can also be assessed in terms of the net surface heat flux reduction Δq_r, defined in Equation 2.4. Since the material properties and internal heat transfer coefficients of the Rohacell test pieces are not engine-representative, the true distribution of overall cooling effectiveness is unknown. However, the distribution of the net surface heat flux reduction can still be estimated using the common estimation of overall cooling effectiveness $\phi = 0.6$, and surface measurements of uncooled HTC, h_0, as determined with the calibration leading edge test piece. Figures 5.20(c) and 5.21(c) show the resulting pressure and suction side images, respectively, for model RAD-C at a single coolant flow rate condition. The strong resemblance to the relevant film effectiveness distributions indicates the dominance of film effectiveness over HTC in predicting heat fluxes in film cooling scenarios.

5.6 Conclusions

Gas turbine engine combustors produce inhomogeneous profiles of both temperature and turbulence at the NGV inlet, both of which must be taken into account in the design of NGV cooling films. The temperature profile affects the amount of surface cooling required, while the turbulence profile affects the performance of the coolant jets which must provide that cooling. In these experiments, the effects of combustor dilution port temperature profiles on NGV leading edge film effectiveness were accounted for in order to isolate the effects of the dilution port turbulence on the film cooling across a range of dilution port mass flow rates. The film cooling geometries tested featured radial showerheads with various spanwise distributions of radial cooling hole surface angle.

- Low surface angle radial jets are attached to the surface and tend to have their effectiveness diminished by additional dilution port turbulence since the mainstream is able to remove more coolant from the jet. The extracted coolant remains relatively close to the surface and may still contribute to effectiveness downstream from where it was extracted.

- When the surface angle and blowing ratio are high enough, jets lift off but mainstream turbulence acts to return some of the coolant to the surface. The effectiveness gain thus produced by the turbulence is greater for higher turbulence intensity and also for particular intermediate surface angle radial holes than for those which are orthogonal to the surface, because of the greater proximity of the jet trajectory to the surface.

- Owing to this effect, a test piece with radial hole surface angles lower near the endwalls and higher near the midspan (representative of a common engine scenario) achieved near its midspan showerhead the greatest (approximately 0.2) and most uniform rise in film effectiveness due to dilution port turbulence.

- Due to the inherent difficulty of achieving good film coverage in this region, it is the leading edge region where film effectiveness gains are most needed.

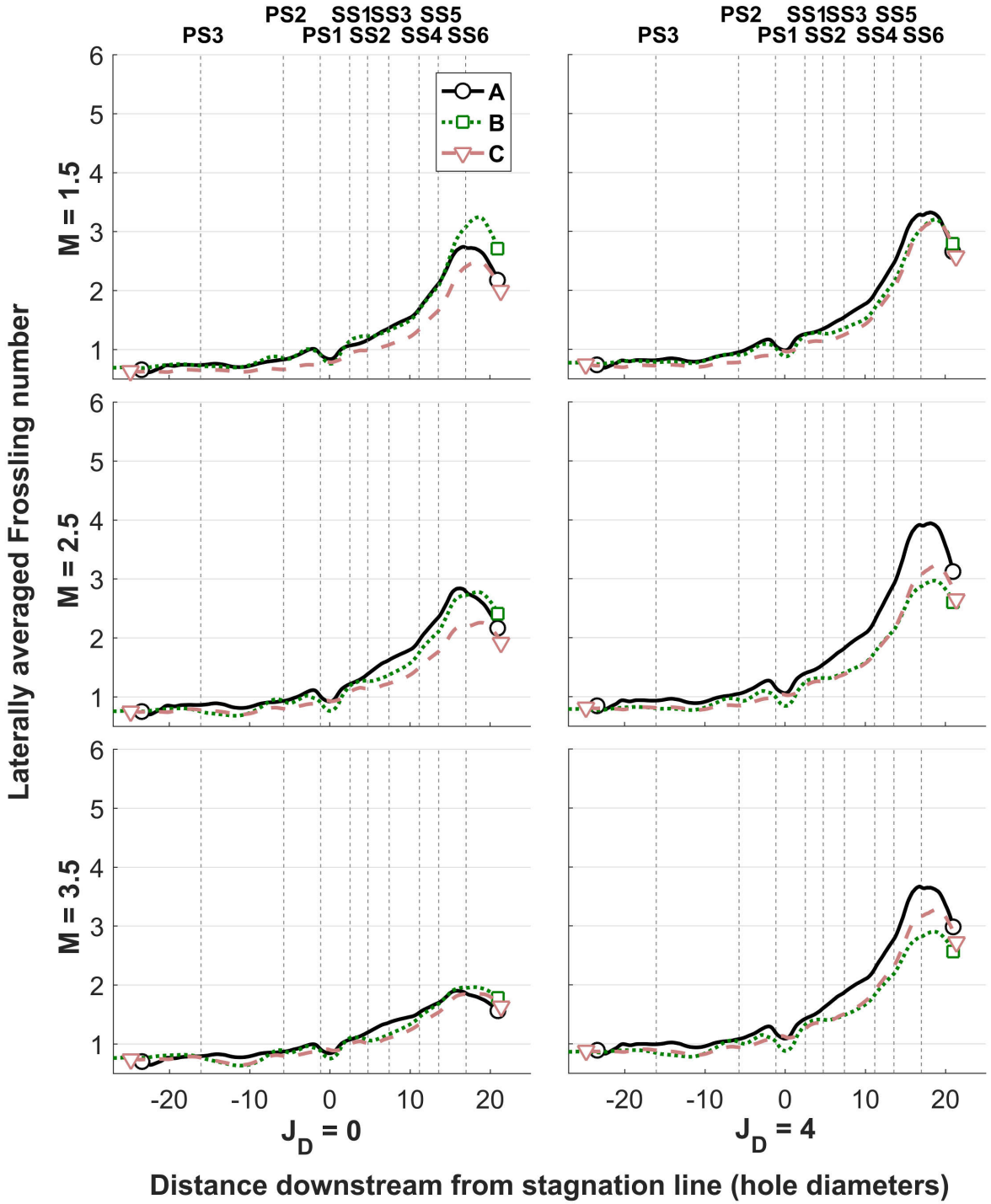


Figure 5.22: Laterally averaged Frossling number for all three radial showerhead leading edge models. $M = 1.5, 2.5, 3.5$, $J_D = 0, 4$.

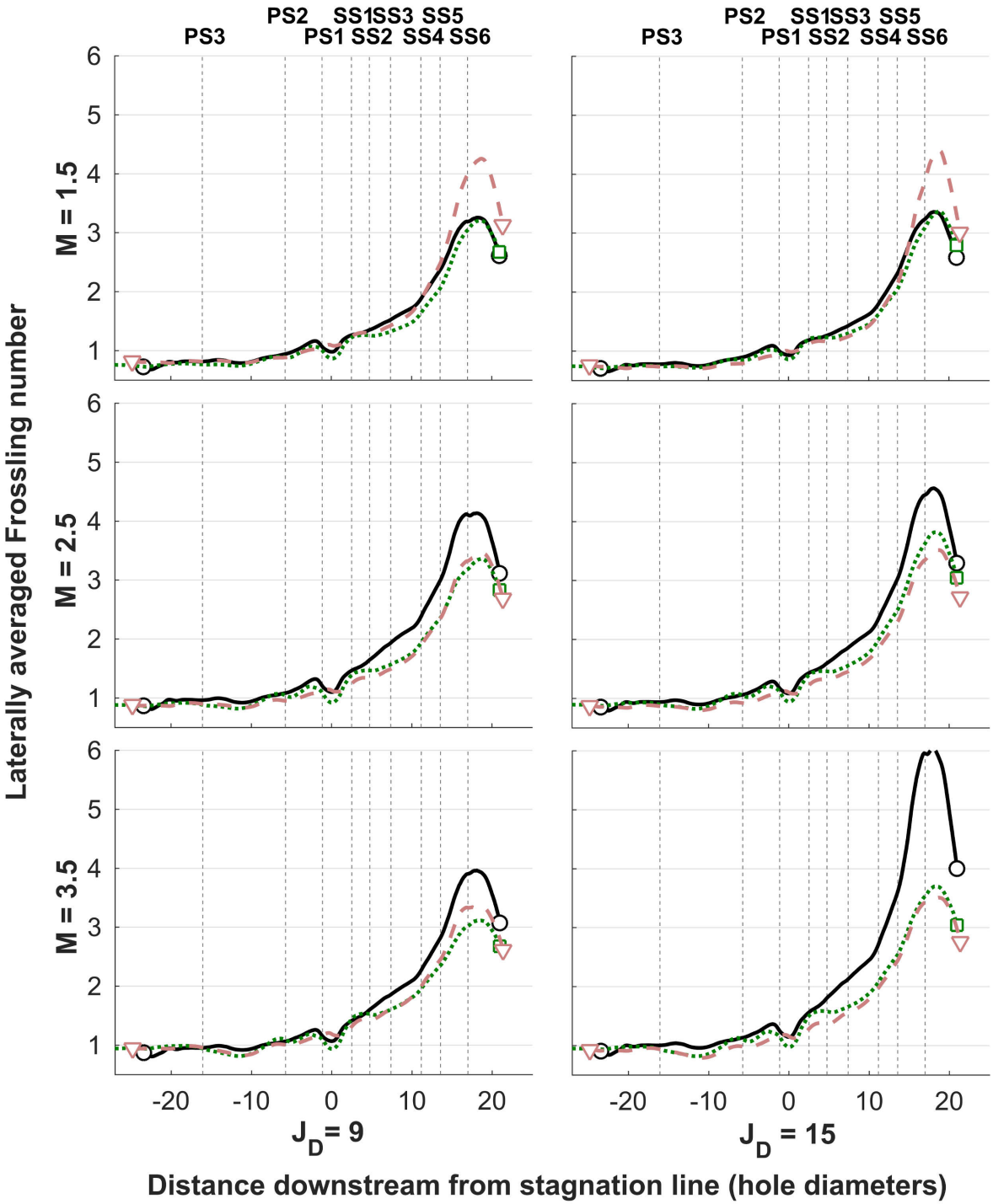


Figure 5.23: Laterally averaged Frossling number for all three radial showerhead leading edge models. $M = 1.5, 2.5, 3.5$, $J_D = 9, 15$.

- These strong interactions between the stagnation region film coolant and the dilution port flow indicate the importance of combustor design with respect to NGV leading edge film cooling performance.

- Combustor geometry design decisions which increase the film effectiveness by increasing the degree of stagnation region film mixing could reduce the quantity of cooling air required in this demanding region, leading to engine efficiency benefits.

- However, although the radial showerhead film effectiveness gain due to dilution is optimised for intermediate surface angle radial holes, lower surface angle attached jets still tend to produce slightly better area-averaged film effectiveness in absolute terms (as presented in the following chapter).

- Thus, absent machining limitations necessitating higher surface angle holes, low surface angle radial holes at the midspan may still produce optimal overall cooling.

- Of three tested film-cooled NGV leading edge geometries, the one without radial inclination of the four most upstream hole rows experienced higher downstream heat transfer coefficients because of the increased turbulence produced by the upstream jets' increased penetration into the mainstream.

- Film effectiveness dominates in predictions of net heat flux reduction due to leading edge film cooling.

Chapter 6

Reverse-Blowing Films Crossing Over the Aerofoil Stagnation Line

In this chapter, a novel leading edge film cooling approach is investigated, and its performance quantified. In conventional designs, the region near the geometric stagnation line is typically between the two most upstream film hole rows, which each emit coolant in the downstream direction on their respective sides of the aerofoil. This region is thus relatively starved of coolant flow and adequate cooling is achieved inefficiently with a high density of holes expelling a large amount of coolant in order to mix with and dilute the nearby mainstream flow, a process which is augmented by combustor turbulence, as demonstrated in chapter 5. Drawing inspiration from recent literature on reverse-blowing film cooling holes, the film cooling geometries in this chapter were designed by the author with a view to improving upon this situation by blowing coolant from each side of the NGV stagnation line to the other in a criss-cross pattern. This is found to be capable of producing much higher effectiveness near the stagnation line than the more conventional designs of chapter 5, as well as comparable downstream effectiveness. A method is also described for using experimental film effectiveness data to estimate the proportion of the mainstream which interacts with NGV leading edge film coolant, and the proportion of coolant from the two most upstream film hole rows which reaches the stagnation line.

6.1 Introduction and Motivation

The spanwise-averaged film cooling effectiveness on a conventionally film-cooled NGV leading edge has a distinct minimum between the two foremost rows of radially inclined holes which straddle the geometric stagnation line (e.g. [125]). The leading edge model RAD-C investigated in the previous section and shown again in Figure 6.1 is an example of a conventional radial geometry suffering from this local minimum. While the exact location of the pressure stagnation line may be unsteady, the mainstream flow is essentially split such that the majority of the first pressure side row coolant is swept downstream on the side from which it originated, and likewise for the suction side. As such only a very small amount of coolant is able to traverse the region between these two hole rows, though it has been shown in the previous chapter that this quantity has a significant dependence on the nature of the mainstream turbulence and the radial film holes, potentially allowing some optimisation via the design of both the combustor and the leading edge film holes. One alternative design features a row of film cooling holes machined directly on the geometric stagnation line. However, owing to flow field changes with engine condition, the true position of the time-averaged stagnation line is not perfectly fixed, and its unsteadiness at a given engine condition may also significantly influence the performance of such a hole row. Therefore, it is difficult to achieve consistent and well-characterised performance with this design.

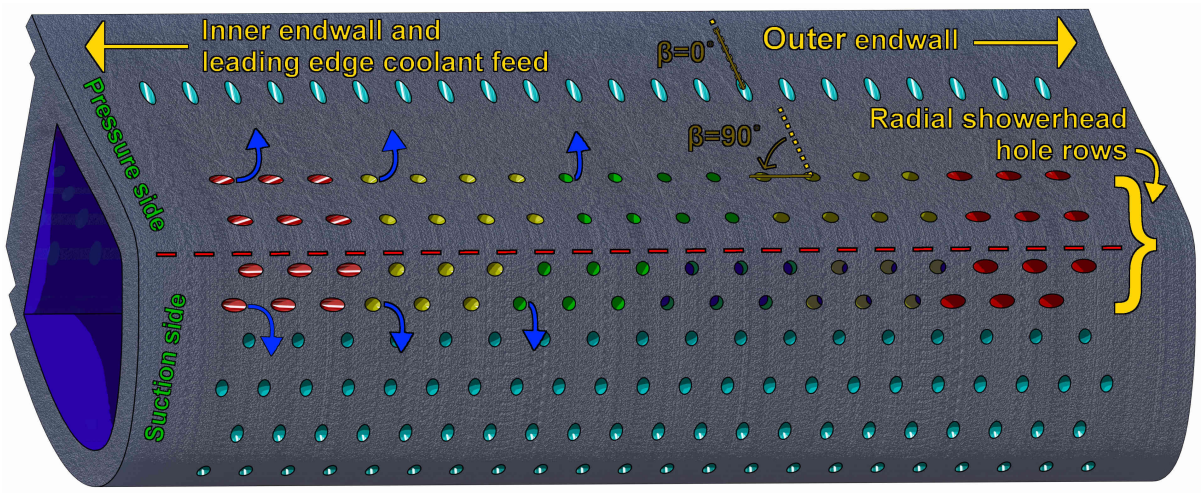


Figure 6.1: An example of a conventional, radially film cooled leading edge, illustrating how the PS1 and SS1 coolant is swept downstream away from the stagnation line.

This chapter investigates the possibility of blowing coolant from each of the two rows straddling the geometric stagnation line (PS1 and SS1) around the stagnation line to the opposite side of the aerofoil, with the goal of achieving improved film effectiveness between these two rows while simultaneously improving (or at least not significantly diminishing) the film cooling performance farther downstream. The holes in the two rows are staggered in an attempt to minimise the extent to which the jets obstruct each other's passage over the stagnation line. For the brief time in which this coolant has not yet crossed over, its direction of travel opposes that of the local mainstream flow. Hence, these designs are herein referred to as both 'cross-over' and 'reverse-blowing'. The relatively low mainstream momentum near the stagnation region tends to promote coolant jet lift-off, however the initially opposed momentum of the mainstream may partially reduce this. Further lift-off control is potentially available from hole intersection pressure losses. The reverse-blowing rows PS1 and SS1 are necessarily machined in the opposite streamwise sense to their immediately downstream rows. Since they are also positioned in a region of high curvature and high hole density, they are highly prone to intersect with the holes of the downstream rows. It is also possible to engineer additional intersections between holes within a reverse-blowing row, which creates holes which blow with a component towards one another as per the research of Fletcher [45] and Nowlin [126] (see Figure 6.2(c)). An additional possible benefit of cross-over films is improved consistency of film behaviour at different engine operating conditions. The position and transient behaviour of the stagnation line may vary slightly with the engine condition, which for a conventional, radial leading edge film cooling design may significantly alter nearby effectiveness distributions due to the coolant jets' minimal amount of initial streamwise momentum.

Reverse-blowing film cooling is a relatively recent research concept, with the first study in the academic literature being Li's 2010 flat plate numerical simulation [42]. The blowing ratio and hole surface angle were varied for a single cylindrical hole blowing both directly with and directly against the mainstream flow, and results indicated that reverse-blowing

tends to increase the coolant's lateral spreading, providing a higher laterally averaged film effectiveness. Later numerical studies also reported this result for cylindrical holes on aerofoil surfaces (Shetty et al. [127]) and fan-shaped holes on a flat plate (Subbuswamy et al. [128]), but noted reduced centreline effectiveness compared with equivalent forward-blowing holes. Chen et al. [129] experimentally investigated single rows of film cooling holes on a flat plate. Results showed that the effectiveness of reverse-blowing holes was less sensitive to blowing ratio and density ratio changes than the effectiveness for equivalent forward-blowing holes, and that in terms of effectiveness levels, cylindrical holes benefited more from reversal than did fan-shaped holes. Park et al. [130] experimentally studied two rows of staggered film cooling holes on a flat plate with three arrangements: both rows blowing forward, both blowing backwards, and the first row blowing backwards, second row blowing forwards. The latter was found to produce the highest effectiveness levels. Prenter et al. [131] experimentally measured the centreline plane mean flow field as well as thermal fields and film effectiveness for a hole in a single row of cylindrical, reverse-blowing holes. They determined that the coolant lateral spreading is assisted by the separation at the downstream side of the hole inlet. This separation creates faster moving fluid at the upstream side of the hole exit. The blockage generated by this faster coolant shields the slower moving coolant from the mainstream, permitting it to spread laterally before it is swept downstream. Heat transfer coefficients for reverse-blowing holes were measured to increase compared to those for forward-blowing holes, and in conjunction with improved effectiveness levels resulted in comparable net heat flux reduction. To the author's knowledge, the present study is the first in the academic literature to investigate reverse-blowing holes on an aerofoil leading edge, and hence also the first to propose cooling near the stagnation line by having the reverse-blown jets cross over it.

6.2 Cooling Hole Geometries

Three Rohacell leading edges (labelled as REV-A, REV-B, and REV-C) were designed to investigate the leading edge reverse-blowing concept. To maximise the breadth of performance data collected, each model was divided into two spanwise halves (A1/A2, B1/B2,

C1/C2) each featuring different PS1 and SS1 reverse-blowing film cooling hole arrangements, as described in Table 6.1. Figure 6.2 presents digital renders of these three models, illustrating the above geometric information as well as the compound angles β present on their PS2-SS2 hole rows. The hole colouration of these rows indicates the nature of the inter-row intersections (between PS1/PS2 and SS1/SS2 holes): no intersection (green), half intersection (yellow), full intersection (red). Owing to the importance of hole surface angle in determining film effectiveness via its effect on jet lift-off (discussed in section 2.4), this parameter was kept as a constant 30° for all of the reverse-blowing holes across all three models. Since models REV-B and REV-C feature compound-angled PS1 and SS1 holes, their hole angles in the plane orthogonal to the NGV span are reduced, as shown in Figure 6.3. The hole pitch and hence the density of holes is also kept constant, though in the case of REV-C the spacing between adjacent holes alternates, but the double-pitch remains the same as that of the other models' PS1 and SS1 rows. The spanwise and streamwise positioning of the PS2 and SS2 hole rows changes slightly between models in order to achieve the full variety of inter-row intersection conditions in all three models and to maintain the 30° surface angle for all of the reverse-blowing holes. Table 6.2 reports the pitches P, streamwise distances downstream of the geometric stagnation line S, and hole lengths L for all nine hole rows of all six reverse and radial models tested. Where very small row variations exist, some values were modified for table compactness, however all of the given values are accurate to within $0.1D$.

Table 6.1: Characteristics of reverse-blowing cooling hole rows (PS1 and SS1) on the three reverse-blowing models designed for experiments. Hole stagger and spacing are expressed in terms of the hole diameter D.

Leading edge model	**Spanwise half 1 (left/radial inner)**	**Spanwise half 2 (right/radial outer)**
REV-A	Streamwise cylindrical	Streamwise fan-shaped
REV-B	Parallel compound angled, zero stagger	Parallel compound angled, $1D$ stagger
REV-C	Opposed compound angled, $3D$ opposed hole spacing	Opposed compound angled, $4.6D$ opposed hole spacing

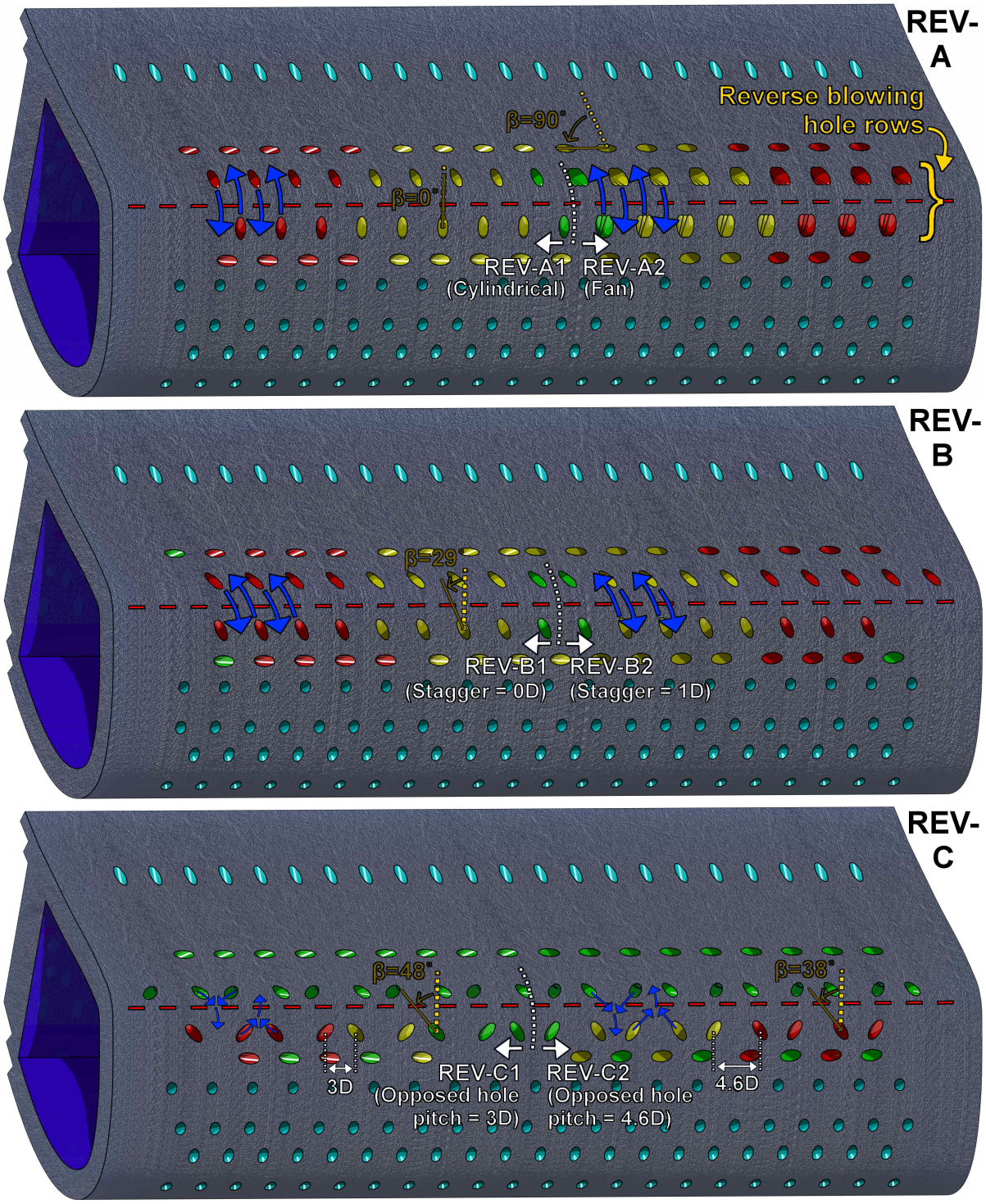


Figure 6.2: Three leading edge test pieces with reverse-blowing PS1 and SS1 hole rows blowing in various criss-cross patterns over the stagnation line. The PS2 and SS2 rows blow radially. Hole colouration indicates the nature of the inter-row hole intersections.

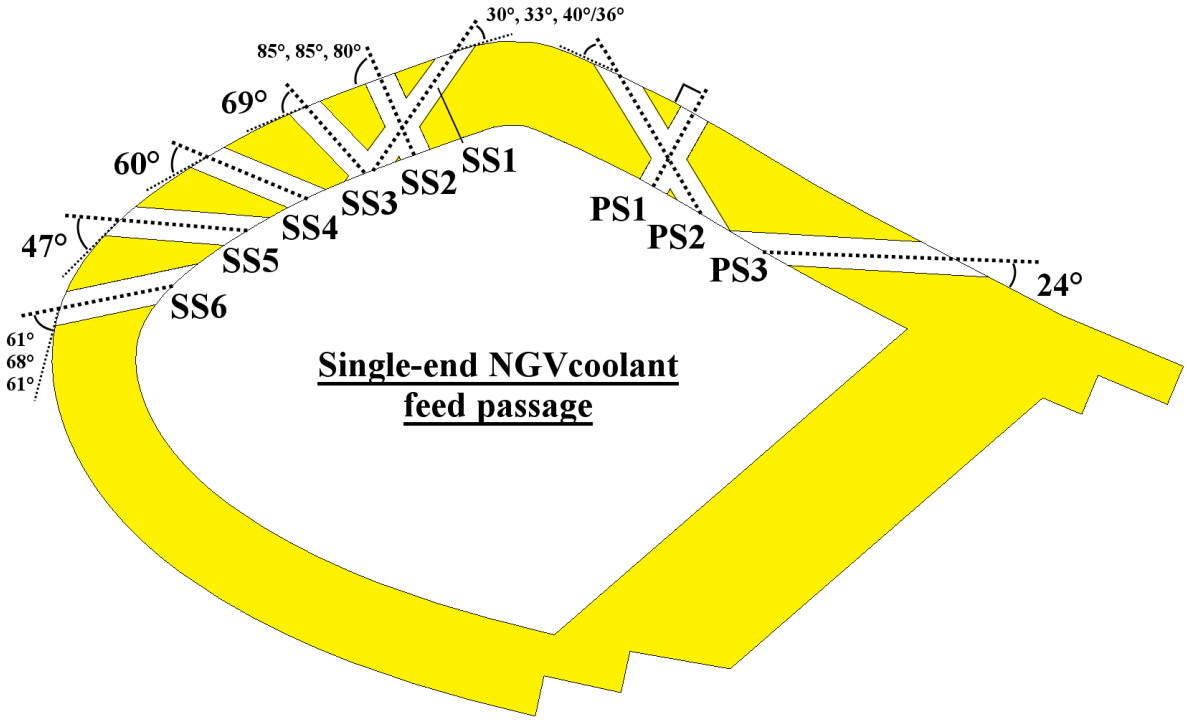


Figure 6.3: Hole angles in a cross-sectional plane, with some slight variations between the three reverse-blowing models (listed in order REV-A,B,C).

Table 6.2: Hole pitch P, surface distance of hole exit centre from stagnation line S, and hole length L by row, normalised by hole diameter D, for radial and reverse-blowing models.

Hole row	P/D	S/D		L/D	
Rows \ Models	ALL	REV-A,B,C	RAD-A,B,C	REV-A,B,C	RAD-A,B,C
PS3	3.5	−16.2	−15.6	6.3	6.4
PS2	4	−5.8	−6.3	5.3	5.3[v]
PS1	4[i]	−1.1[ii]	−2.1	6.8[iv]	5.3[v]
SS1	4[i]	2.4	1.9	5.5	5.3[v]
SS2	4	5.2[iii]	4.4	5.3	5.3[v]
SS3	4	7.4	6.9	2.8	3.5
SS4	3.4	11.1	10.4	3.1	3.5
SS5	3.4	13.6	13.8	4.1	4.3
SS6	3.4	17.0	17.3	3.7	4.3

i. REV-C1 3.0 and REV-C2 4.6 ii. REV-B -2.3, iii. REV-C 4.8,
iv. REV-B 6.4 and REV-C 5.7, v. $\alpha = 60°$ 2.8, 40° 3.5, 20° 5.3

6.3 CFD Study of Radial and Cross-Over Film Cooling Geometries

Steady-state, RANS CFD simulations of the six radial and cross-over leading edge film cooling geometries have been performed using ANSYS Fluent (and ANSYS ICEM for octree meshing) in order to gain insight into the jet physics dictating their performance and to gauge the accuracy of single-PC simulations against experimental results. In order to reduce the mesh element count and hence the computational requirements, the domain was reduced from the full rig geometry to a mass flow rate inlet boundary condition plane between the dilution ports and the cascade, and a pressure outlet boundary condition plane at the tailboard exit. The coolant feed is an additional mass flow rate inlet boundary condition at the beginning of the coolant passage (i.e. neglecting the true rig coolant feed geometry) and a second pressure outlet at the end of the passage can be adjusted to create a rig-representative cross-flow within the passage. Moreover, only the central 50% of the span was modelled, and a reduced selection of adjacent film cooling holes from the PS2 to SS2 rows. An example of the domain for model RAD-B is shown in Figure 6.4 along with the walls and boundary condition locations.

6.3.1 Mesh, Model, and Boundary Condition Studies

Model RAD-B at a single blowing ratio was used to test the effects of mesh density at feasible element counts. Refinements were applied predominantly within the holes and near the leading edge surface to achieve models with 6.3, 12.1, and 16.6 million tetrahedral elements. Qualitatively, isosurfaces of coolant temperature appeared essentially unchanged between the coarsest and densest meshes, suggesting essentially unchanged jet trajectories. The leading edge film effectiveness calculated for the densest case still varied from the second densest case by up to around 0.5 in very small regions, but the variation was negligible over most of the surface. Given the requirement to simulate three blowing ratios for each geometry, the 12.1 million element refinement settings were used for all of the final test cases in order to reduce computational time, despite its imperfect mesh independence in terms of film effectiveness predictions. The use of in-hole prism layers at

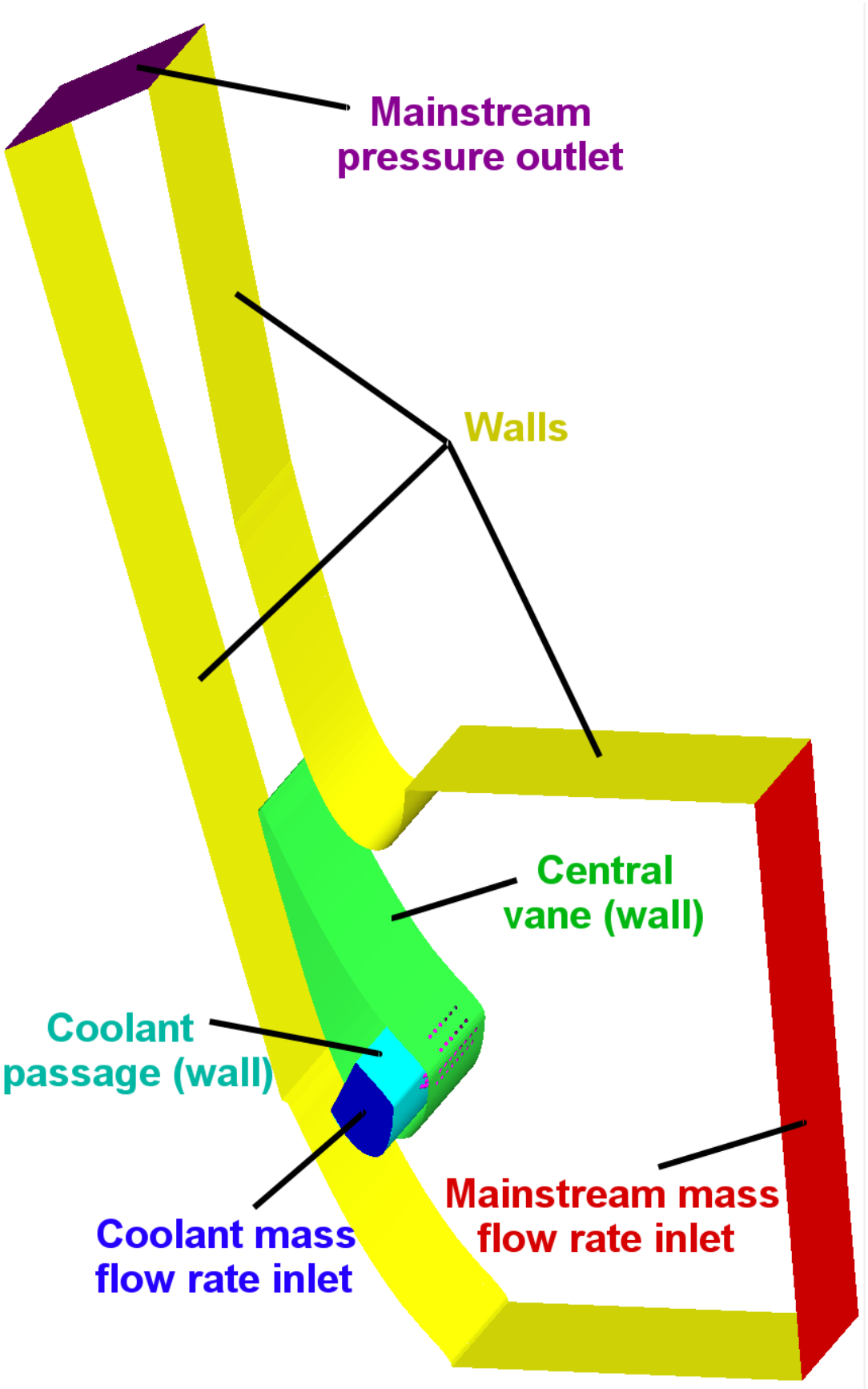


Figure 6.4: Model RAD-B CFD reduced domain geometry with walls and boundary condition locations indicated. The coolant pressure outlet is on the hidden end of the coolant passage.

a given mesh size was found to make relatively little solution difference, so prisms were not generated in the final meshes. A case with no internal cross-flow was also tested, which removed the requirement to adjust the coolant outlet pressure to achieve the correct hole mass flow rates. The film effectiveness results were changed by up to approximately 0.1 nearby the hole exits in the outer spanwise half of the vane, so cross-flow was modelled for all of the final simulations. The $k-\epsilon$ Realizable turbulence model with enhanced wall functions was used, and comparison with $k-\omega$ was not possible since these models exhibited relatively poor convergence properties. The mainstream inlet turbulence intensity was set to 18%, and reducing it to 5% produced relatively small effectiveness differences of up to just 0.02.

6.4 Results

6.4.1 Detailed Effectiveness - Reverse-Blowing Geometries

Figures 6.5 and 6.6 show the experimental film effectiveness performance of models REV-A, REV-B, and REV-C at three different blowing ratios. Figure 6.5 indicates the approximate position of the geometric stagnation line for both the pressure side and the suction side views. For all of the experiments in this chapter, the dilution port momentum flux ratio is kept at a constant $J_D = 9$, and the endwall film cooling is off ($J_E = 0$). The film effectiveness is corrected for the influence of the upstream temperature profile according to the method described in section 5.2. At the lowest blowing ratio, only the REV-A1 and REV-B2 cylindrical holes produce significant effectiveness between the PS1 and SS1 hole rows, indicating the greatest amount of coolant cross-over. However, the REV-A2 diffusing holes produce effectiveness levels in this region comparable to those of cylindrical holes at higher blowing ratios. On both the pressure and suction sides there is a fairly significant increase in the effectiveness from $M = 2.5$ to $M = 3.5$ between the first and second hole rows, where cooling must be predominantly due to jets from the first row of the opposite side. There is a lesser increase in these locations for the cylinders. For all blowing ratios, the fan holes also produce a more cohesive film between PS2 and PS3,

suggesting the influence of additional coolant from upstream. This may also be partially caused by coolant swept off the PS1 jet boundaries before it can cross over, especially for the lowest blowing ratio. These results suggest that the reduced exit velocity and lift-off of diffusing holes is highly beneficial to the ability of reverse-blowing jets to locally cool and then cross the stagnation line. The importance of low lift-off in avoiding reverse-blown jet retardation and reversal is due to the rapidly increasing mainstream flow momentum away from the vane surface nearby the stagnation line. Figure 6.7 shows how the mainstream momentum rapidly increases away from the geometric stagnation line between the PS1 and SS1 hole rows, and the REV-A1/A2 CFD coolant streamline predictions show how the slightly reduced surface angle of the jet as it issues from the diffusing holes (A2) can cause tighter coolant trajectories after cross-over compared to the cylindrical holes (A1). The effectiveness results of Figures 6.5 and 6.6 also show that REV-B achieves similar performance to REV-A1, while REV-C performs poorly both between PS1 and SS1 and farther downstream. REV-C does however achieve very high localised effectiveness where two PS1 or SS1 opposed coolant jets collide. The effects on film effectiveness of different intersection types between hole rows can in principle be determined from the detailed experimental results for reverse-blowing models. However, the results suggest very little influence from these intersections, with the only apparent difference being a slight reduction in stagnation region effectiveness for REV-A and REV-B where first and second rows fully intersect. For the reverse-blowing rows of these models, in order to achieve lateral components of jet velocity while maintaining a constant surface angle, the angle between the mainstream bulk approach velocity and the hole angles in the plane orthogonal to the spanwise direction must reduce relative to model REV-A. This reduction is visible in Figure 6.7 and is also indicated in Figure 6.3. The CFD streamlines suggest that this results in more coolant lift-off and reversal than occurs for model REV-A, especially for REV-C which features the greatest compound angling. These effects contribute to the lower stagnation region effectiveness values. REV-B streamlines suggest that higher blowing ratios reduce the fraction of PS1 and SS1 coolant which is swept backwards rather than crossing over, though the other two models show a small amount of coolant reverse at all

blowing ratios. The streamlines of all models indicate that higher blowing ratios produce less tight cross-over trajectories, though from the the experimental results it is clear that this is more than adequately offset by the increased coolant mass flow rates. While the trends observed in the results of the present CFD simulations help to explain some of the experimentally observed cooling performance, the predictions of film effectiveness are not accurate enough to be useful. Comparing the detailed $M = 3.5$ CFD (Figure 6.8) and experimental (Figure 6.6) film effectiveness results, the effectiveness underneath the jet near-hole trajectories is significantly overestimated, suggesting an underestimation of the initial lift-off. The regions between rows have less uniform effectiveness than in experiments, suggesting also an underestimation of the jet dispersion. These RANS behaviours are consistent with the findings of the film cooling review by Bogard and Thole [15].

6.4.2 Detailed Effectiveness - Radial Geometries

Figures 6.9 and 6.10 show the film effectiveness performance of the RAD-A,B,C radial film cooling leading edge models (described in section 5.1.1) at three different blowing ratios. The effectiveness advantages of RAD-B and RAD-C over RAD-A discussed in section 5.5.3 are evident. All of the radial models clearly underperform even model REV-C in terms of stagnation line cooling. Among the three, RAD-B has the most consistent film development downstream, owing to its low surface angle radial holes. However, these also cause very high accumulation of coolant towards the midspan on both the downstream PS and SS, such that REV-A achieves more even film coverage, albeit with a lower midspan peak effectiveness. This suggests more efficient usage of crossed-over, streamwise-blown coolant than coolant which is blown in an opposed radial configuration, even at very low surface angles. This is because the radially blown coolant accumulates towards the midspan where individual jets compete for space with their neighbours, neglecting the near-endwall leading edge surface while also propelling much of the midspan coolant to a great distance from the surface. The CFD-predicted streamlines of Figure 6.11 show that greater lateral momentum of the opposed radial jets generates stronger midspan coolant vortices. This formation enhances midspan effectiveness downstream of the showerhead at

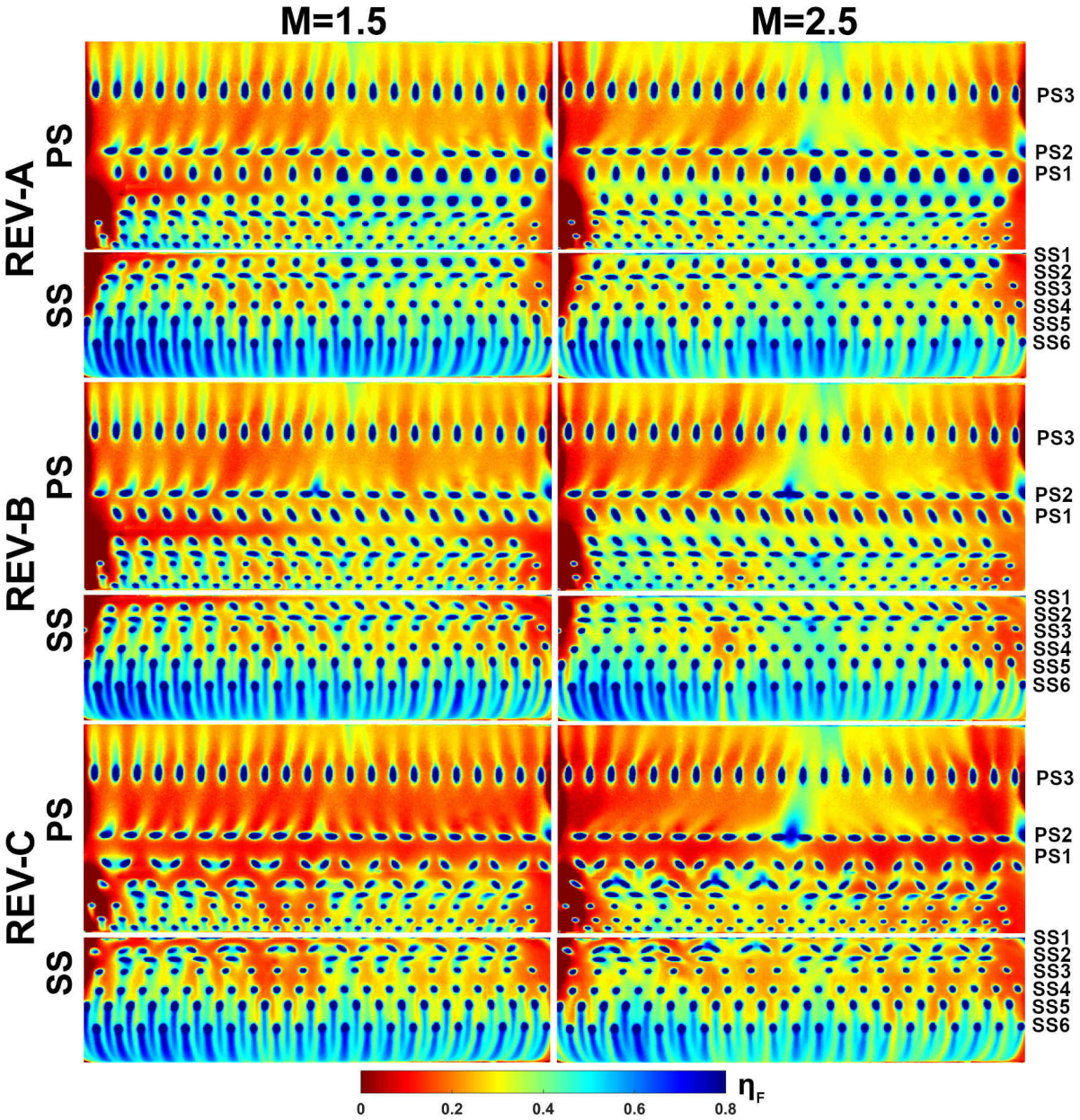


Figure 6.5: Film effectiveness for models REV-A,B,C at $M = 1.5$ and 2.5, $J_D = 9$.

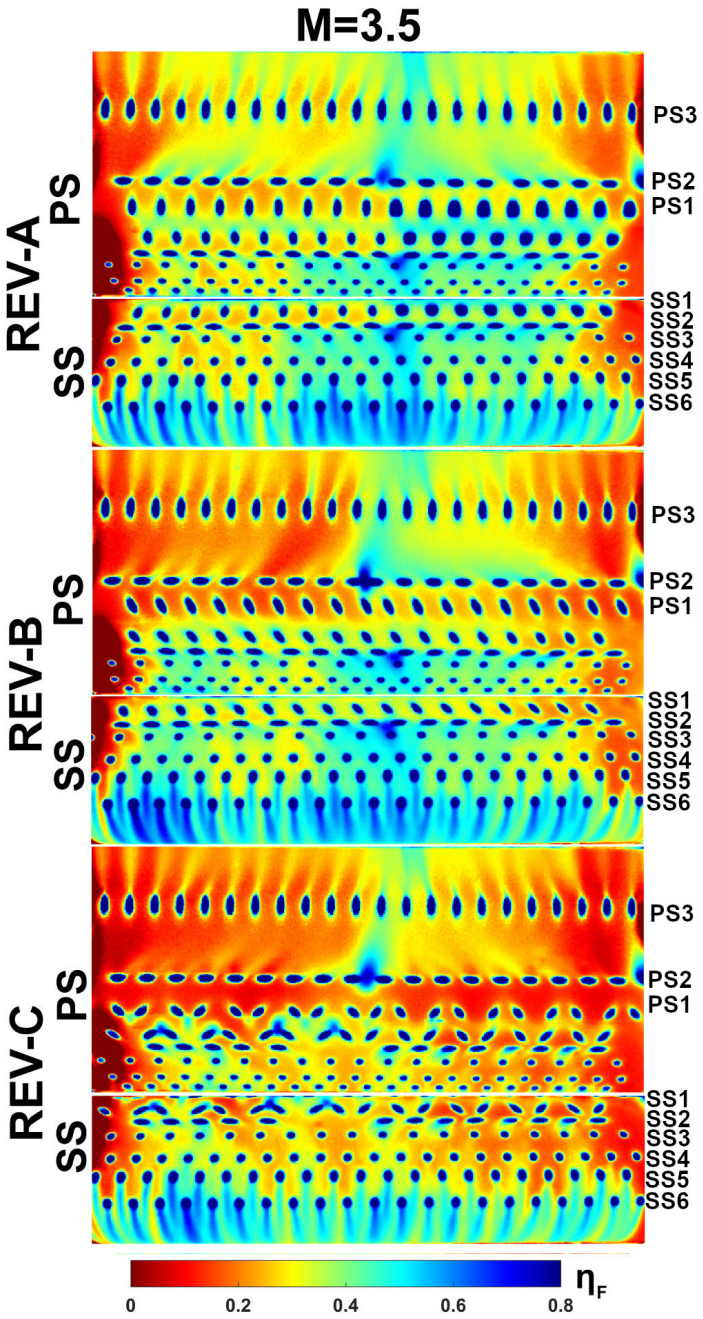


Figure 6.6: Film effectiveness for models REV-A,B,C at $M = 3.5$, $J_D = 9$.

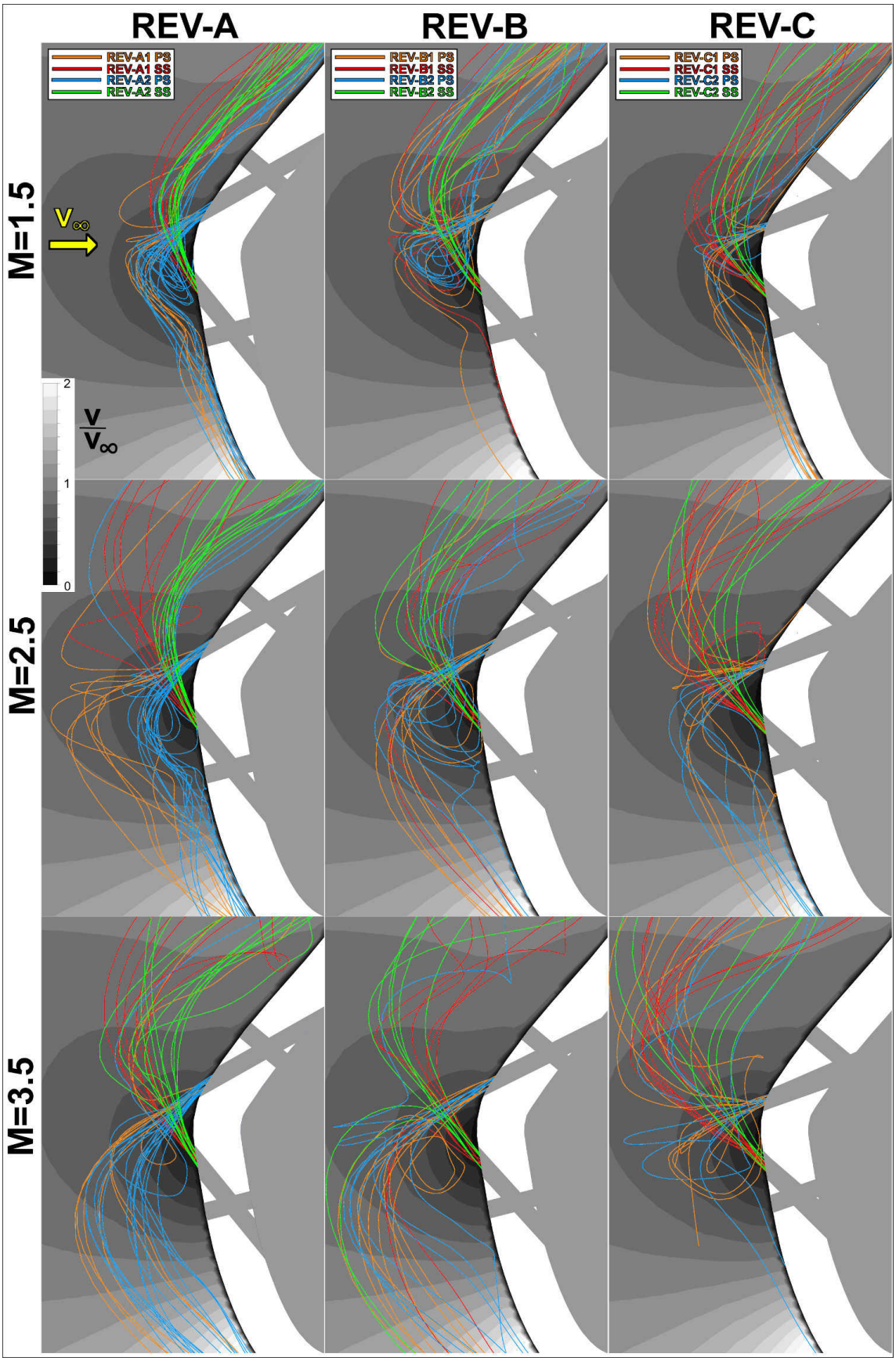


Figure 6.7: Streamlines of coolant from the PS1 and SS1 reverse-blowing holes of models REV-A1/A2,B1/B2,C1/C2, at three blowing ratios, according to steady RANS CFD simulations. The mainstream flow velocity magnitude is shown as a grey-scale contour.

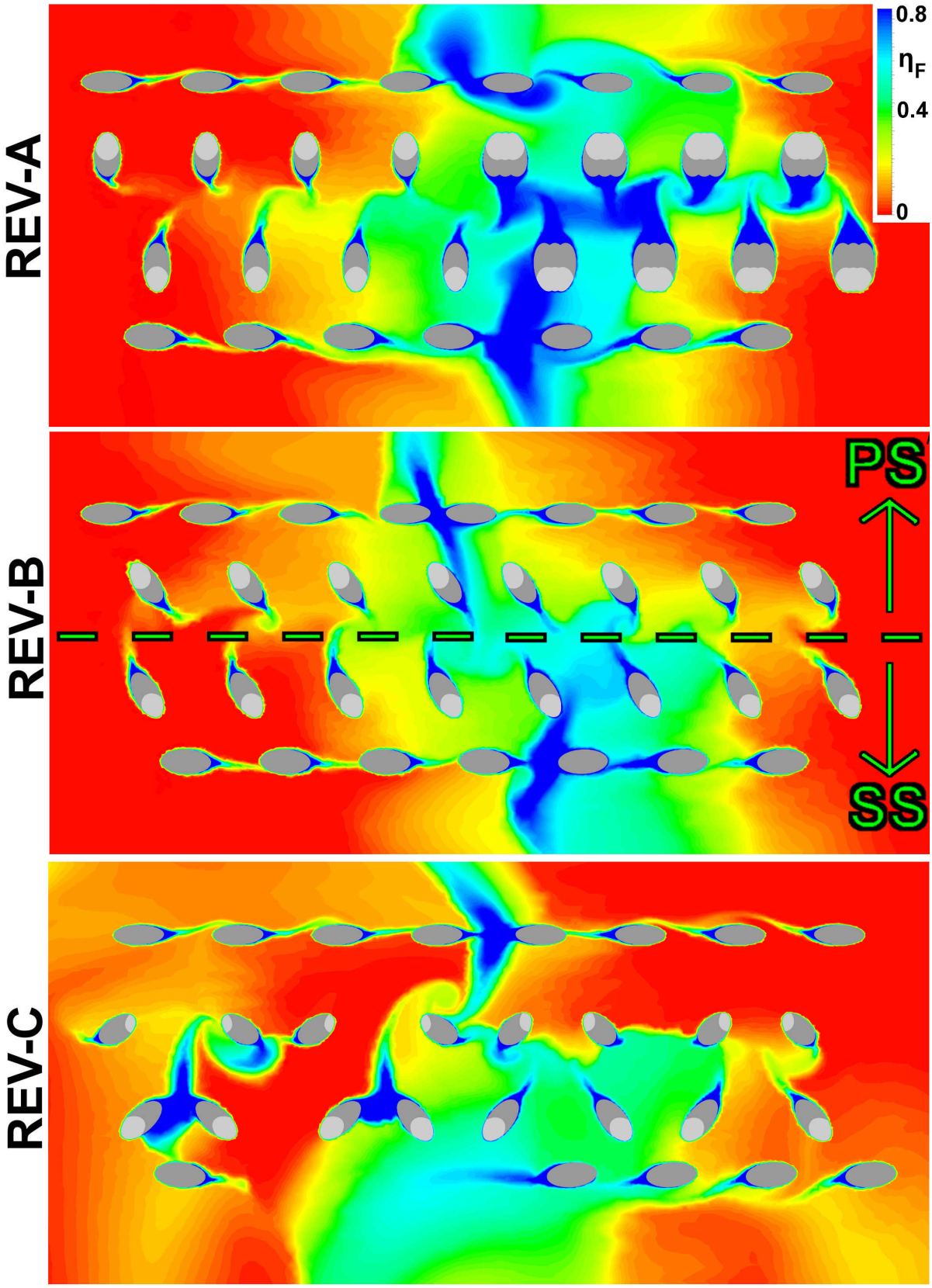


Figure 6.8: Detailed near-midspan stagnation region film effectiveness predictions for models REV-A,B,C, $M = 3.5$, according to steady RANS CFD simulations.

the expense of downstream effectiveness nearer the endwalls. It is also clear from Figure 6.11 that there is very little coolant cross-over relative to the reverse-blowing models, congruent with the significantly lower stagnation line effectiveness.

6.4.3 Stagnation Line Performance

Figure 6.12 shows the effectiveness achieved along the stagnation line by each of the Rohacell leading edge models. Averages are produced from experimental results according to the methods of section 5.4. The REV-A1 and REV-B1 stagnation line effectiveness at

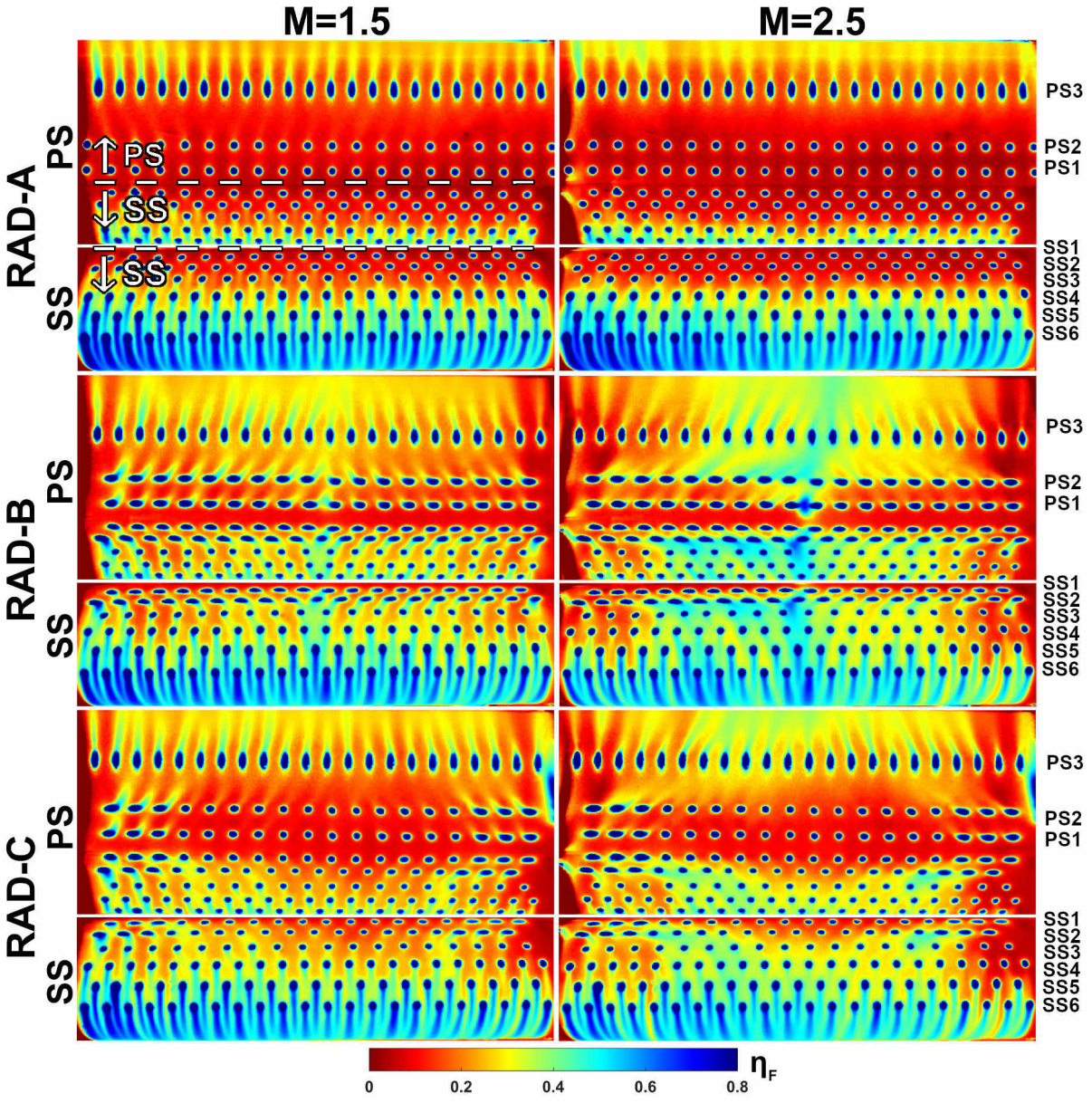


Figure 6.9: Film effectiveness for models RAD-A,B,C at $M = 1.5$ and 2.5. $J_D = 9$.

$M = 1.5$ is much lower than at higher blowing ratios, suggesting that the PS1 and SS1 jets substantially reverse instead of crossing over the stagnation line. This supports the hypothesis that the lift-off is underestimated by RANS CFD, which predicted little flow reversal even at $M = 1.5$. The reasons for greater jet reversal in the radially inner half of the leading edge include the hole geometry differences, the slight mainstream momentum excess near the inner endwall contraction, and the spanwise recovery of static feed pressure inside the leading edge coolant passage (an effect which has been measured in section 7.3).

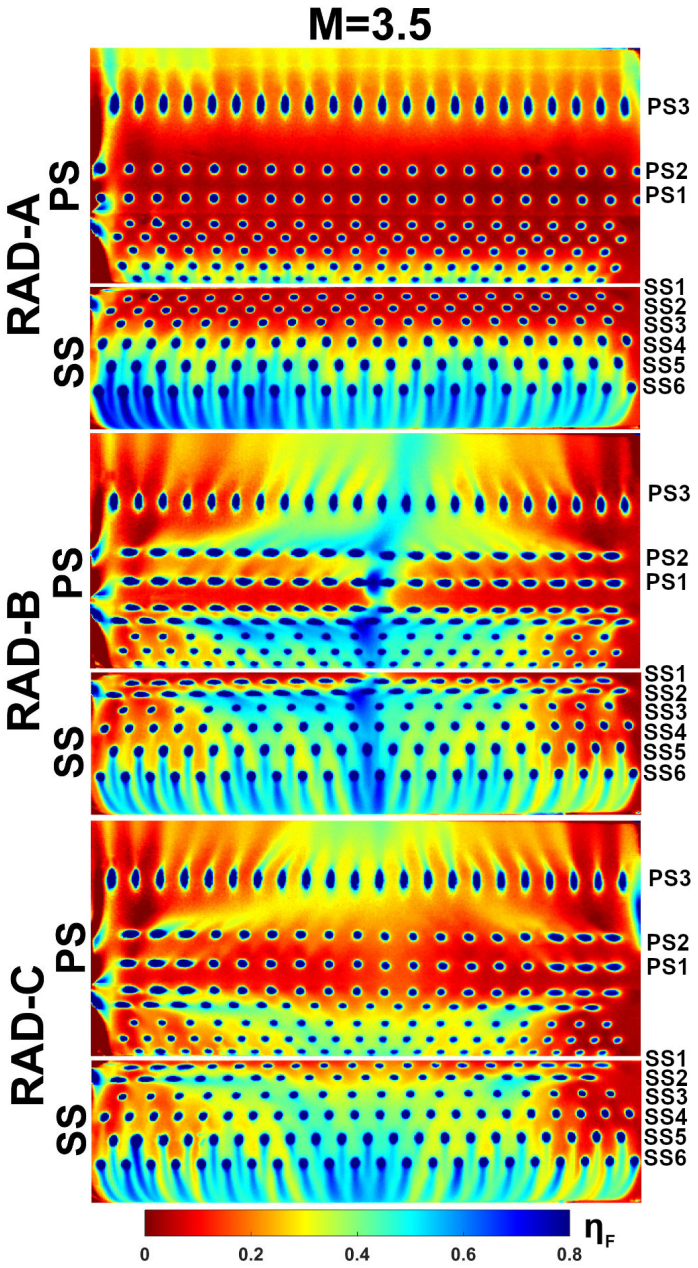


Figure 6.10: Film effectiveness for models RAD-A,B,C at $M = 3.5$. $J_D = 9$.

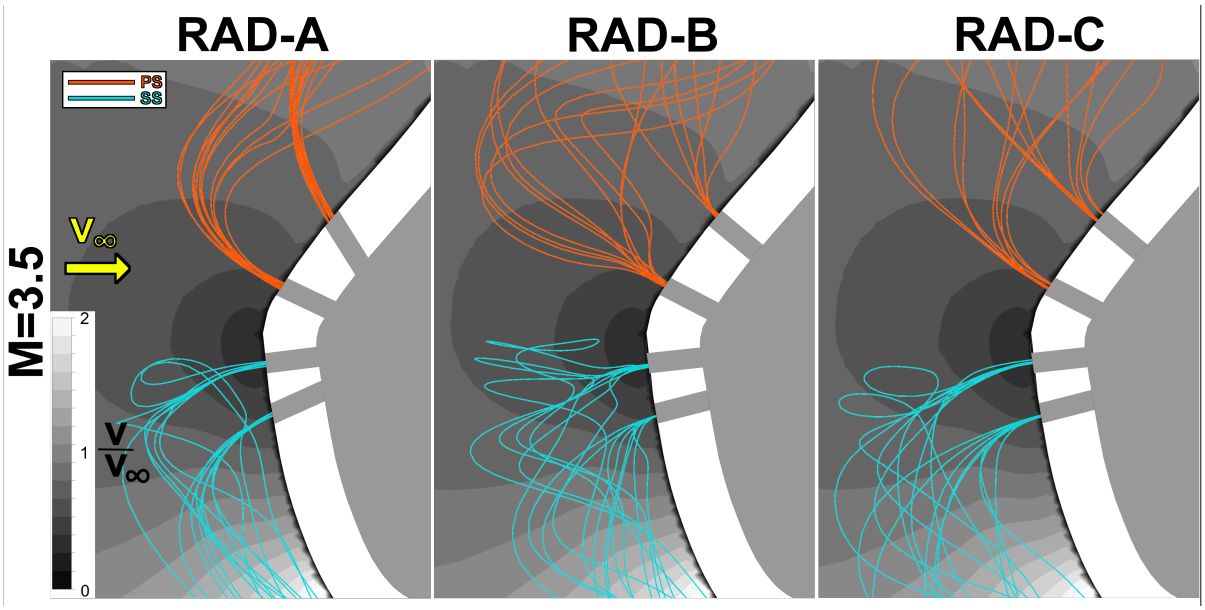


Figure 6.11: Streamlines of coolant from the radial holes of models RAD-A,B,C, at three blowing ratios $M = 1.5, 2.5, 3.5$, according to steady RANS CFD simulations. The mainstream flow velocity magnitude is shown as a grey-scale contour.

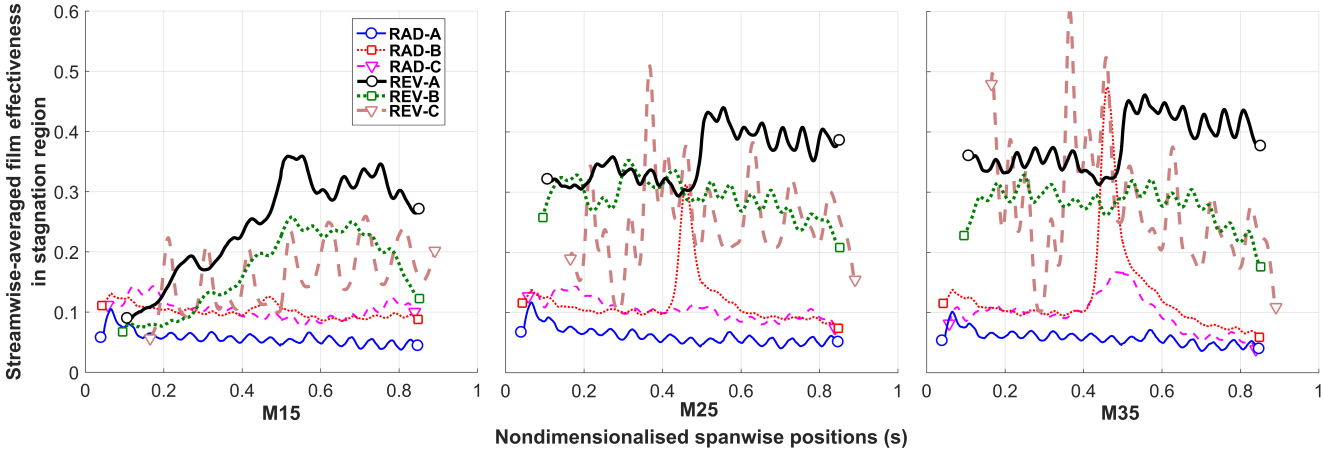


Figure 6.12: Film effectiveness along the geometric stagnation line of models RAD-A,B,C and REV-A,B,C at three blowing ratios $M = 1.5, 2.5, 3.5$. $J_D = 9$.

The REV-A2 fans clearly offer the best performance in cooling this traditionally troublesome region between the two most upstream hole rows, achieving film effectiveness of around 0.4 where radial geometries usually achieve around 0.1. The REV-A1 cylinders slightly outperform their compound-angled REV-B counterparts, which in turn outperform the still more highly compound-angled REV-C cylinders (except where the opposed holes within each row cause very high effectiveness where their jets collide). This is in part due to the longer trajectory of these jets before they cross over the stagnation line, which increases the amount of coolant extracted from each jet by the mainstream on the

original side from which the jet issues forth. Another possible mechanism for reduction in the amount of coolant reaching and crossing the stagnation line is increased collision of jets crossing from opposite sides. This could explain the slightly lower stagnation line effectiveness of REV-B2 (1D stagger) compared to REV-B1 (no stagger). The stagnation line performance of all of the reverse-blowing designs increases with blowing ratio. By contrast, the radial designs are insensitive to blowing ratio except near the midspan (due to the increased collision momentum of the directly opposed jets). Aside from these narrow midspan peaks, the radial designs universally underperform all of the reverse-blowing designs. RAD-A is consistently the worst since its lack of any truly radial holes minimises the amount of coolant which is transported to the region between the PS1 and SS1 rows.

6.4.4 Lateral and Area Averages

Figure 6.13 shows laterally averaged effectiveness results for all six Rohacell leading edge models. While the reverse-blowing models each feature distinct spanwise halves, the symmetry of the radial models about the midspan is conducive to investigation of the effects of the single-end coolant feed on the laterally averaged effectiveness of the two halves. The results indicate negligible differences between the two spanwise halves of RAD-A due to the single-end coolant feed, but significant effectiveness advantages for RAD-C1 and especially RAD-B1, whose radial cooling holes are closely aligned with the bulk coolant passage flow. The excess effectiveness peaks just downstream of the radial hole rows before gradually decaying, and is more significant at higher blowing ratios. This spanwise effectiveness advantage is due to the formation of larger flow separations from the acute solid angles of film cooling hole inlets when the coolant passage flow makes a reflex turn into the holes, rather than an acute one. These larger separations act as an increased effective blockage, reducing the mass flow rate at the affected holes. Figure 6.14 presents RANS CFD results which capture this effect for model RAD-B. The contours indicate the flow velocity magnitude in a plane through the centre of row PS1, with flow separations visibly larger for the holes more distant from the coolant passage inlet. The predicted mass flow rates through these holes are therefore lower than those through the holes closer

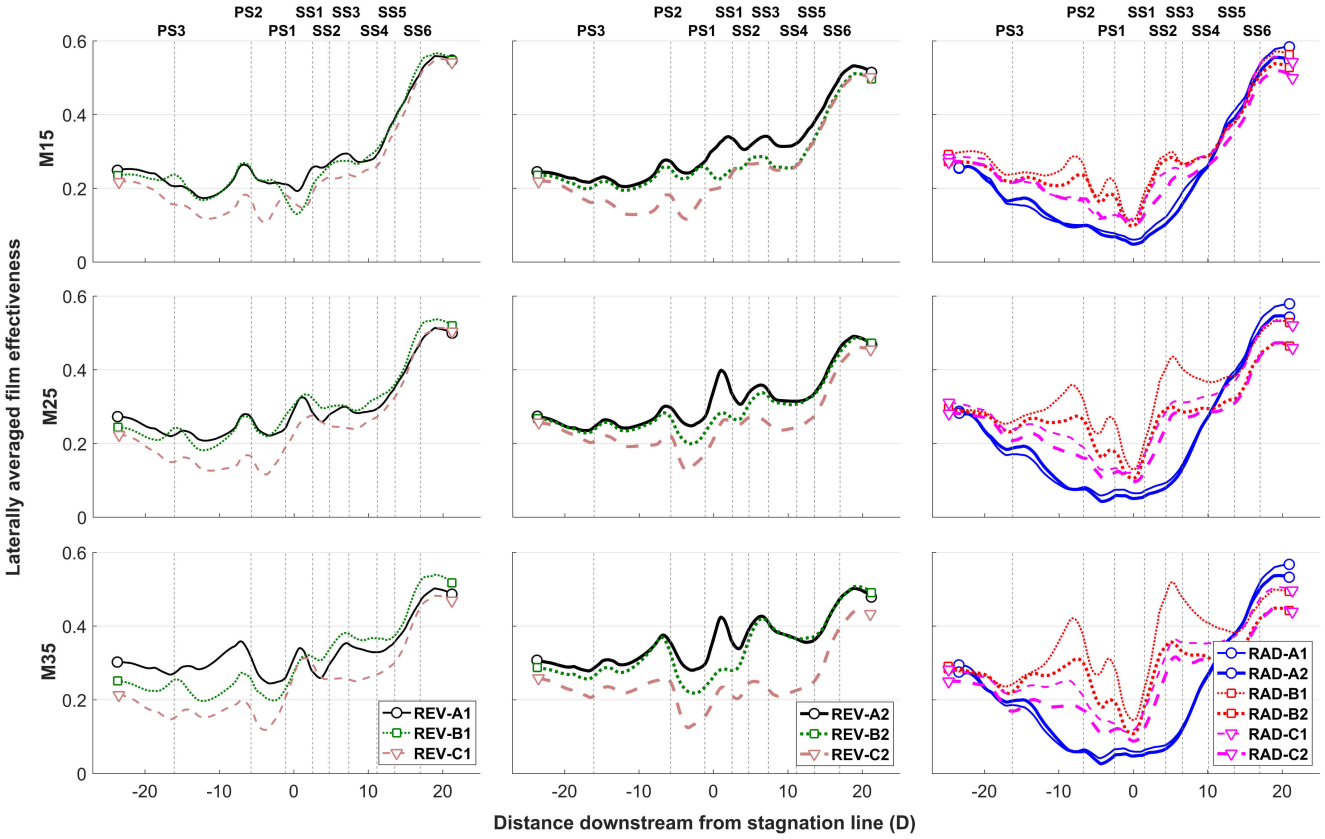


Figure 6.13: Laterally averaged film effectiveness for models RAD-A,B,C and REV-A,B,C at three blowing ratios $M = 1.5$, 2.5, 3.5. $J_D = 9$.

to the passage inlet, and the lower exit momentum of their jets is evident in the asymmetry of the velocity contour where the jets penetrate into the mainstream.

Given that the reverse-blowing models feature a single row of opposed-blowing, radial cooling holes on each side and essentially spanwise-uniform PS1 and SS1 hole inclinations, a small effectiveness advantage would be expected on the radially inner halves of these test pieces (REV-A1,B1,C1). Despite this, REV-A2 (fan holes) exhibits equal or higher laterally averaged film effectiveness on both the PS and SS for all blowing ratios, suggesting that the reverse-blown coolant from fan holes remains closer to the aerofoil surface during its passage downstream. In addition to significantly outperforming RAD-B (the most successful radial model) between the PS1 and SS1 hole rows, both of the REV-A designs also have comparable or (for $M = 3.5$) slightly higher laterally averaged effectiveness on the late pressure side, and comparable performance on the suction side (intermediate to the two RAD-B spanwise halves). Only just downstream of its low

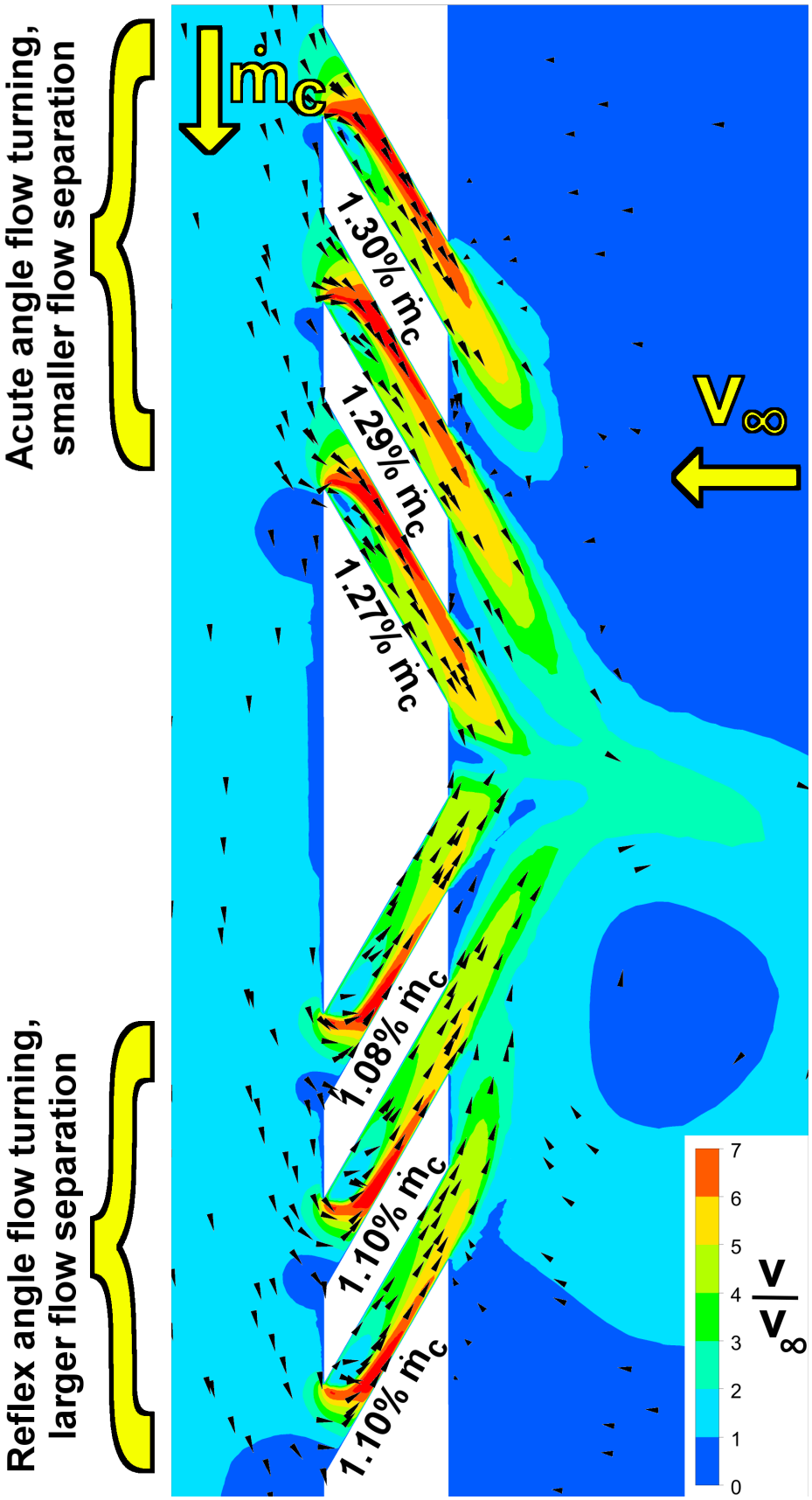


Figure 6.14: RANS CFD predictions of velocity in a plane through the PS1 hole row of leading edge model RAD-B, showing the increased flow separations and reduced mass flow rates in holes inclined against the coolant passage bulk flow. $M = 3.5$.

surface angle radial showerhead does RAD-B briefly outperform REV-A to a significant extent. This further suggests that the REV-A reverse-blown coolant remains at a similar average distance to the surface during its passage downstream as the coolant from low surface angle radial PS1 and SS1 holes.

REV-B competes closely with REV-A in terms of downstream performance (except on the suction side for $M = 3.5$), but with substantially poorer performance between and nearby the PS1 and SS1 rows. Compared to REV-B2, REV-B1 offers better stagnation line and suction side performance at the expense of pressure side performance. This is likely the result of increased PS1-SS1 jet collisions for the REV-B1 (no stagger) geometry, in which the PS1 jets dominate, crossing the stagnation line and causing significant SS1 coolant reversal. A similar suction side bias also occurs for REV-C1 over REV-C2, implying improved cross-over performance of dominant PS jets when the opposed, compound-angled holes are more closely spaced, reducing their interactions with suction side jets. RAD-C offers similar performance to REV-C. Owing to their higher surface angles, the midspan radial jets are detached, reducing the showerhead effectiveness relative to RAD-B (except between PS1 and SS1). This shows the significance of the film cooling penalty introduced by endwall-restricted radial cooling hole surface angles. As quantified in section 5.5.3, this penalty can be partially offset in the midspan showerhead region by the effect of the dilution ports. Since the showerhead holes of RAD-A are nearly orthogonal to the surface, the lift-off is even more significant, and this design suffers the worst performance of the six. Far downstream (after PS3 and SS4) the laterally averaged effectiveness is essentially independent of the PS2-SS2 showerhead design.

Figure 6.15 shows area averages of the film effectiveness on the pressure and suction sides of each spanwise half of each leading edge model. A stagnation region area average from a thin strip between the PS1 and SS1 holes is also shown. The reverse-blowing fan holes of REV-A2 produce by far the best stagnation region average at all blowing ratios, followed by the corresponding cylinders of REV-A1 (except at $M = 1.5$ when the cylinder jets

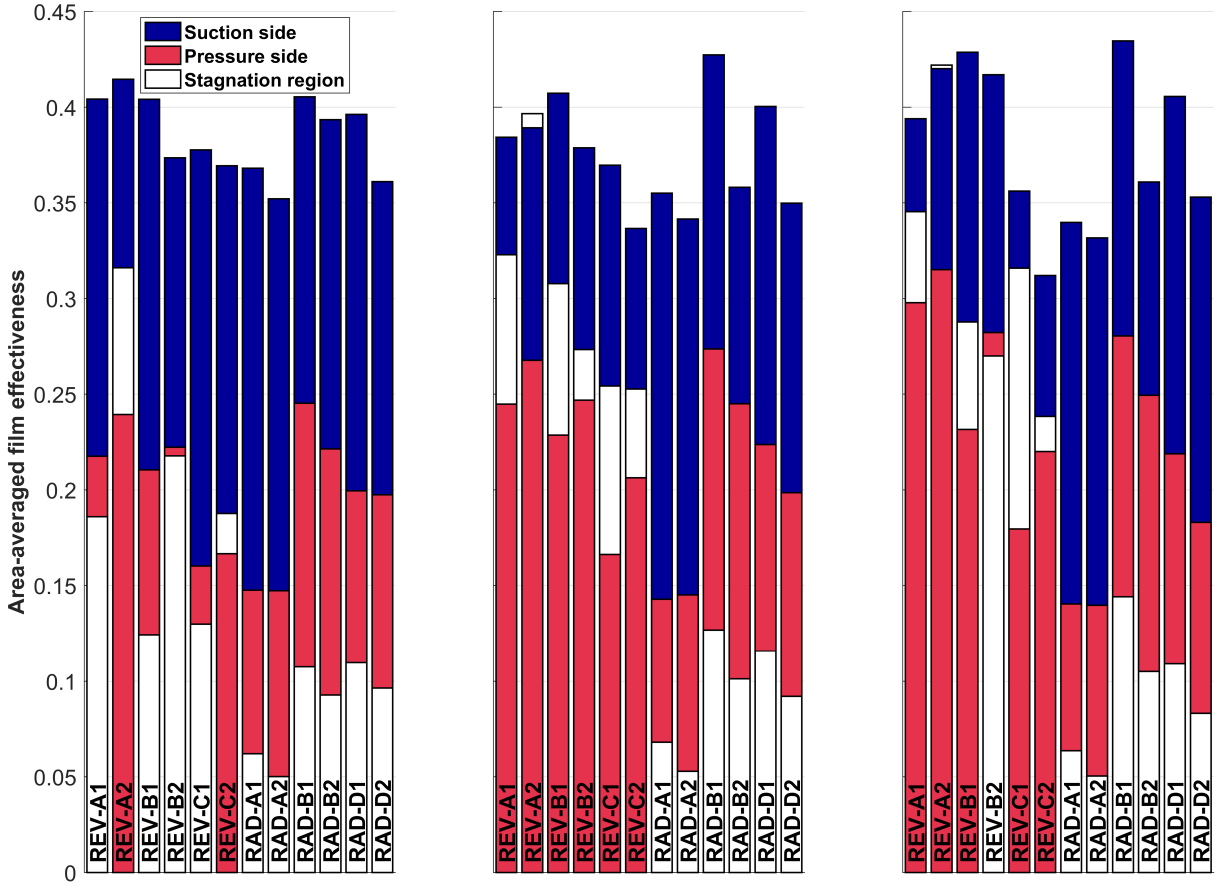


Figure 6.15: Area-averaged film effectiveness for models RAD-A,B,C and REV-A,B,C at three blowing ratios $M = 1.5$, 2.5, 3.5. $J_D = 9$.

experiences significant reversal). REV-A2 also achieves similar or better performance on the pressure side than the best radial geometry, RAD-B1, and just slightly lower suction side performance (around 0.01 effectiveness). REV-B outperforms REV-C in all aspects except REV-C1 stagnation region cooling at the highest blowing ratio. The area averages for RAD-B1/B2 and RAD-C1/C2 emphasise the performance differences between radial holes which are aligned with the coolant passage flow and those which are not, an effect which is less relevant to reverse-blowing designs with no or fewer radial holes. RAD-A performs poorly in all aspects because of the significant PS2-SS2 coolant lift-off.

6.5 Coolant-Mainstream Mixing Analyses

When mainstream flow passes through a film-cooled turbine stage, the majority does not interact with the stator or rotor film coolant, but instead remains at a relatively great

distance from the aerofoils as it is turned through the stage by the potential flow field which they establish. In this section, the fraction of mainstream flow which mixes with NGV leading edge film coolant is estimated on the basis of the film effectiveness measurements of previous sections. The purpose of this is to lend understanding of the extent of interaction between leading edge films and the mainstream flow. Consider a rectangular cross section streamtube which connects the two endwalls a short distance upstream of an NGV's geometric stagnation line. A third edge is situated on the streamsurface of the time-averaged mainstream flow which intersects the stagnation line of the NGV. Opposite to this, the final edge lies some narrow width W_{ST} away, towards either the PS or SS. This streamtube extends downstream around that side of the NGV and upstream into the combustor simulator. This streamtube concept is illustrated in Figure 6.16. If the NGV pitch is P_{NGV} and the simulator has two NGV passages and a mass flow rate approaching the cascade of $\dot{m}_\infty$, then the mass flow rate through the streamtube is given by Equation 6.1.

$$\dot{m}_{ST} = \frac{W_{ST}}{2P_{NGV}}\dot{m}_\infty \tag{6.1}$$

The vane surface adiabatic wall temperature is assumed to be close to the mass-averaged temperature of the local coolant and mainstream gases, as per Equation 6.2. This quantity is also available from rearrangement of the definition of effectiveness (Equation 6.3). Equating these two expressions and rearranging results in a simple expression for the ratio of local coolant ($\dot{m}_{c,L}$) to local mainstream gas ($\dot{m}_{ST}$) in terms of the effectiveness only (Equation 6.4).

$$T_{aw} = \frac{\dot{m}_{c,L}}{\dot{m}_{c,L} + \dot{m}_{ST}}T_c + \frac{\dot{m}_{ST}}{\dot{m}_{c,L} + \dot{m}_{ST}}T_\infty \tag{6.2}$$

$$T_{aw} = T_\infty - \eta(T_\infty - T_c) \tag{6.3}$$

$$\frac{\dot{m}_{c,L}}{\dot{m}_{ST}} = \frac{\eta}{1-\eta} \tag{6.4}$$

The relevant coolant mass flow rate $\dot{m}_{c,L}(x)$ depends on how many hole rows lie upstream of a given film-cooled surface streamwise location, x. It is assumed that only film holes upstream of a given location can contribute to the film effectiveness there. The exception

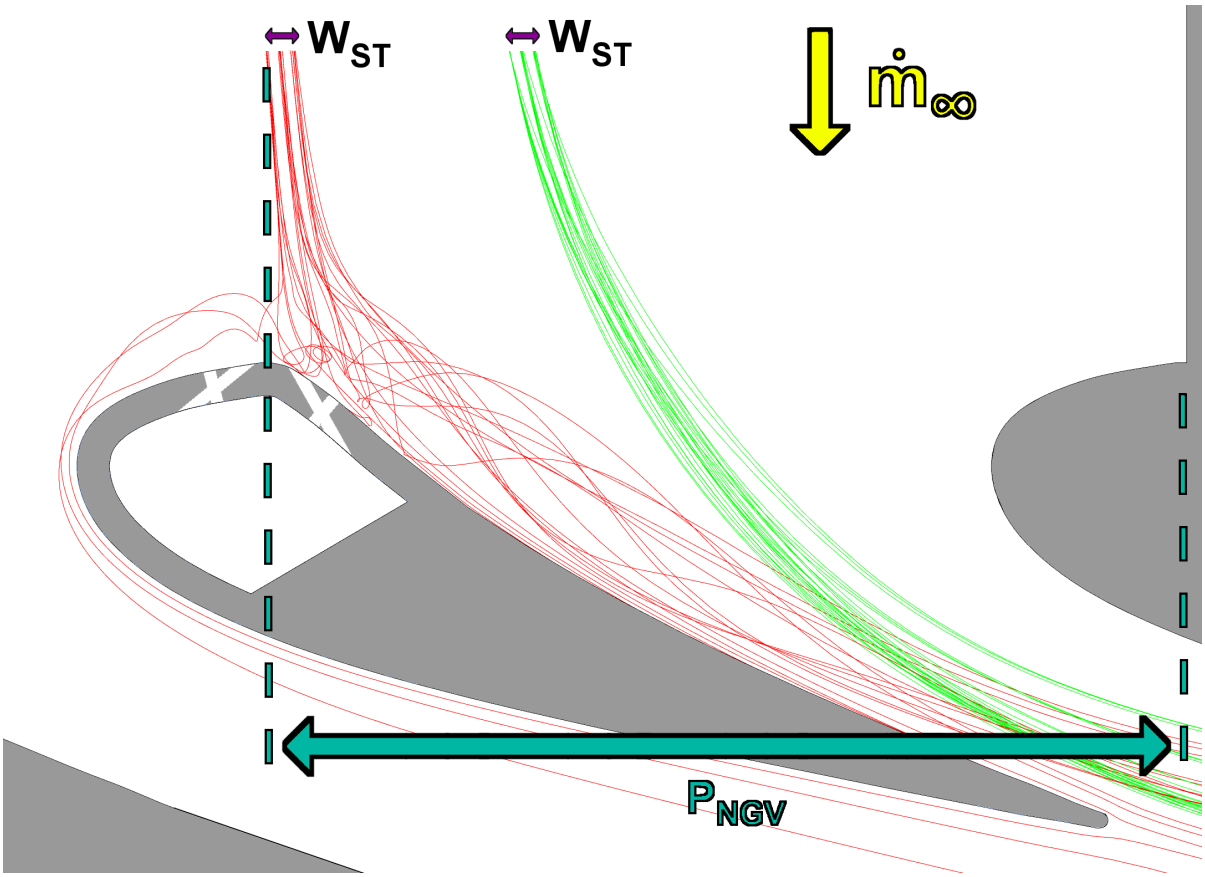


Figure 6.16: A thin streamtube beginning upstream of the NGV pressure side stagnation region (red) interacting with coolant from reverse-blowing model REV-A and a streamtube of equal initial width which passes through the cascade at a distance from the NGVs (green).

is between the PS1 and SS1 rows, where it has been shown that due to the low local mainstream flow velocities, these rows are capable of generating significant film effectiveness in this region, especially for reverse blowing designs. By substituting for $\dot{m}_{ST}$ using Equation 6.1, the mainstream streamtube mass flow rate is replaced by its implied width and the overall mainstream mass flow rate per NGV pitch, $\frac{1}{2}\dot{m}_{\infty}$. Rearranging again, an expression is obtained for the estimated width of the streamtube which is involved with film coolant mixing, as a proportion of the NGV pitch (Equation 6.5). Since the streamtube extends the entire span of the NGV, the film effectiveness used is the laterally averaged effectiveness, $\bar{\eta}(x)$.

$$\frac{W_{ST}(x)}{P_{NGV}} = \frac{2\dot{m}_{c,L}(x)}{\dot{m}_{\infty}} \frac{1-\bar{\eta}(x)}{\bar{\eta}(x)} \tag{6.5}$$

6.5.1 Known Coolant Mass Flow Rate

In order to estimate the width of the mainstream streamtube which is involved with film coolant mixing, several further assumptions are made regarding the amount of coolant involved in mixing at each streamwise surface location, $\dot{m}_{c,L}(x)$:

1. All of the nine film cooling hole rows emit the same mass flow rate of coolant i.e. $\dot{m}_{c,row} = \frac{1}{9}\dot{m}_c$, where $\dot{m}_c$ is the overall leading edge coolant mass flow rate.

2. The amount of coolant crossing over from one side to the other is equal to that crossing the opposite way.

3. All of the emitted coolant is relevant to the determination of the film effectiveness i.e. no coolant escapes beyond the mainstream streamtube.

Under these assumptions, $\dot{m}_{c,L}(x)$ is given by the discontinuous, piecewise function in Equation 6.6. The location of a hole row is considered as the streamwise location of the centres of its hole exits. The effective coolant mass flow rate between the PS1 and SS1 hole rows is as estimated in section 6.5.2.

$$\dot{m}_{c,L}(x) = \begin{cases} \frac{3}{9}\dot{m}_c & x < PS3 \\ \frac{2}{9}\dot{m}_c & PS3 \leq x < PS2 \\ \frac{1}{9}\dot{m}_c & PS2 \leq x < PS1 \\ \text{Eq. 6.4 prediction} & PS1 \leq x < SS1 \\ \frac{1}{9}\dot{m}_c & SS1 \leq x < SS2 \\ \frac{2}{9}\dot{m}_c & SS2 \leq x < SS3 \\ ... & \\ \frac{6}{9}\dot{m}_c & x \geq SS6 \end{cases} \tag{6.6}$$

The least sensible of the assumptions used is number 3, since a great deal of coolant in fact lifts off and contributes little to the effectiveness. Referring to Equation 6.5, this

overestimation of the relevant coolant mass flow rate implies a proportional overestimation of the relevant mainstream streamtube width. The data presented in Figure 6.17 are therefore expected to represent upper limits on the width of the locally relevant mainstream streamtube.

According to Equation 6.5, the leading edge models with greater predicted mainstream streamtube widths (i.e. more mainstream mass flow mixing with coolant) are those with poorer film effectiveness. Physically, this is because greater coolant lift-off from the surface permits a greater amount of mainstream gas to penetrate near to the cooled surface. The model performs poorly for the showerhead of RAD-A, owing to the asymptotic nature of Equation 6.5 for the near-zero effectiveness in this region. Otherwise, sensible, upper limit estimates are yielded of the fraction of mainstream flow which actually interacts with leading edge coolant. The upstream width of the mainstream streamtube which mixes with the leading edge film coolant tends to increase from around $1\% - 2\%$ near the geometric stagnation line up to around 15% downstream. This increase downstream is due to the gradual diffusion of coolant away from the cooled surface and farther into the mainstream (or equivalently, the mixing of mainstream fluid into the coolant film). This is greater for higher blowing ratios since the additional initial momentum of the coolant jets carries them farther from the surface. The streamtube thickness for the far-SS tends to be slightly lower than for the far-PS because the higher speed mainstream flow reduces the local blowing ratios at each row, and hence the jet lift-off and the amount of mainstream flow reaching the surface.

6.5.2 Known Mainstream Mass Flow Rate

Since there can be no film cooling holes upstream of the geometric stagnation line and there are often none directly on it, there is relatively little film cooling effect nearby it. It is therefore of interest to estimate, for various designs, the proportion of the PS1 and SS1 coolant which produces useful film cooling between these two rows by assuming that the only mainstream flow reaching this area originates from a streamtube whose width

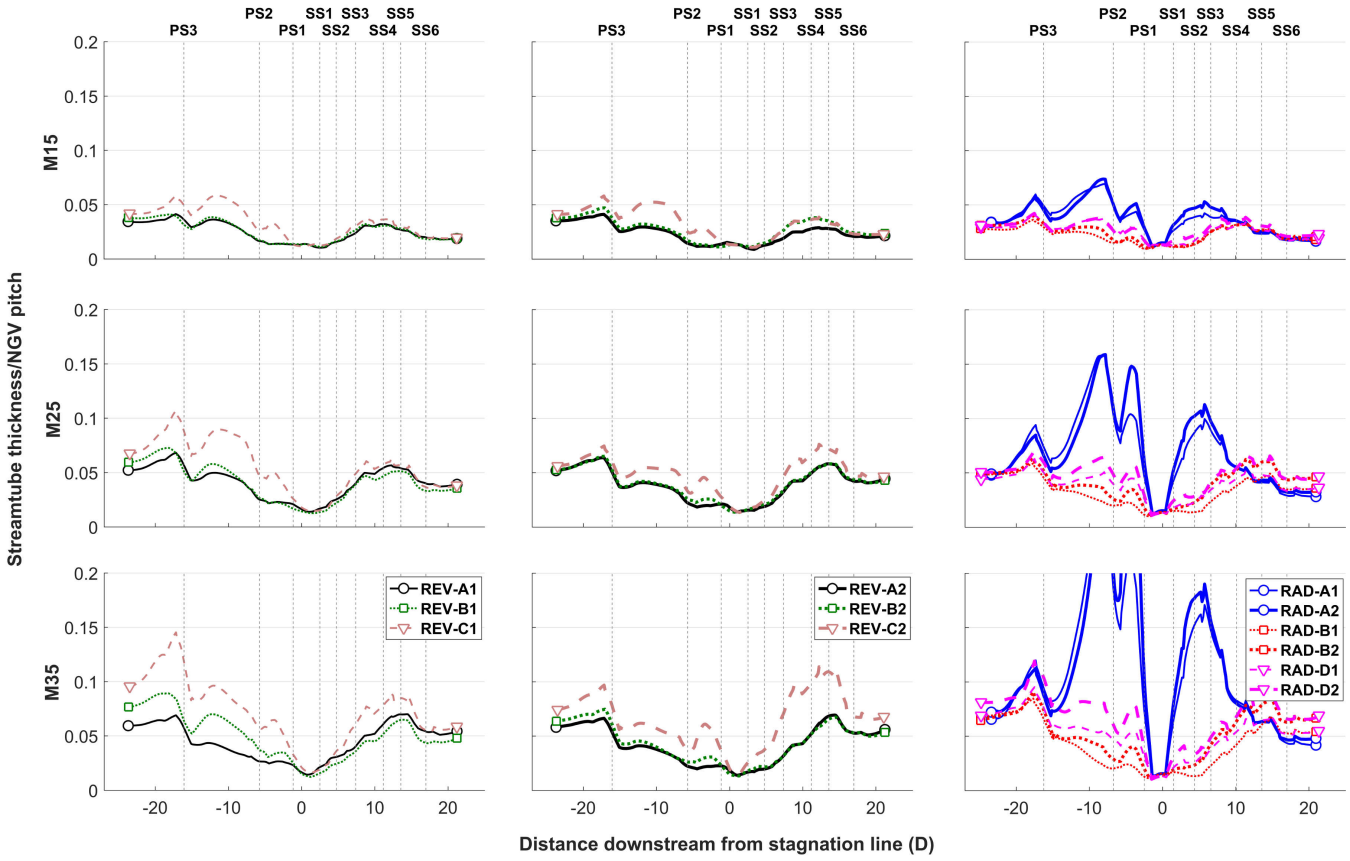


Figure 6.17: Normalised, estimated streamtube width of mainstream gas participating in coolant mixing at various positions downstream of the geometric stagnation line. All six leading edge models. $M = 1.5, 2.5, 3.5$. $J_D = 9$.

(approaching the leading edge, i.e. after the endwall contraction) is the same as the circumferential width of an average effectiveness region between PS1 and SS1. Flow outside of this narrow streamtube is expected to be diverted to either side of the NGV without ever passing through the region immediately in front of the PS1-SS1 gap, which includes the geometric stagnation line. The width of the average effectiveness region (an example of which is shown in Figure 5.8) fixes the streamtube mass flow rate according to Equation 6.1. Substitution of this quantity into Equation 6.4 yields the estimated mass flow rate of coolant producing useful cooling between PS1 and SS1. The results for all leading edge models and blowing ratios with $J_D = 9$ are presented in Figure 6.18 as a fraction of the combined PS1 and SS1 mass flow rates, which is estimated as $\frac{2}{9}\dot{m}_c$.

The results correspond well with the stagnation line film effectiveness results. This is expected because the film effectiveness is implicitly a measure of the same thing, since

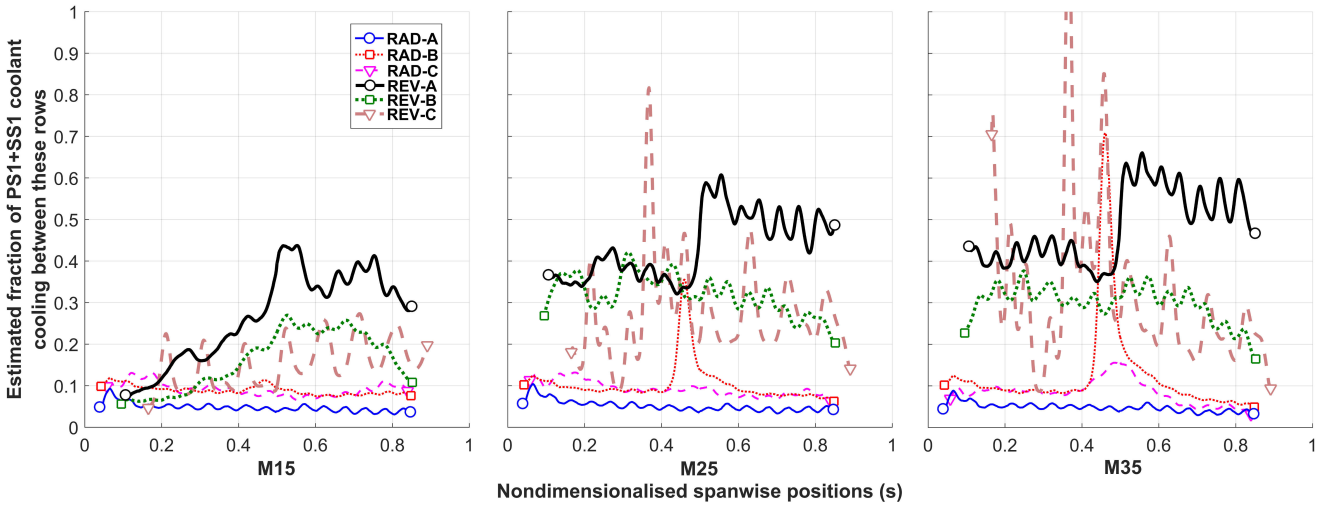


Figure 6.18: Estimated fraction of PS1 and SS1 hole row coolant effectively cooling between these two rows. All six leading edge models. $M = 1.5, 2.5, 3.5$. $J_D = 9$.

the adiabatic wall temperature is essentially the mass-averaged temperature of the mainstream and any present coolant. The streamwise, reverse-blowing holes of REV-A produce the highest predicted fraction of usefully employed coolant, especially with fans (up to around 60%). As would be expected, all of the models whose PS1 and SS1 holes direct coolant towards the stagnation line deliver more coolant there than do models whose equivalent holes are radial, and the surface-orthogonal holes of RAD-A deliver the least (only around 5%). In the model used to calculate these results, it is assumed that the streamtube relevant to coolant mixing near the region from which effectiveness data is taken has the same width (equal to the width of the effectiveness region) near to the vane as it does farther upstream. In fact, the deceleration of the mainstream as it approaches the leading edge implies that the streamtube should be somewhat thinner upstream, and hence that the mass flow rate of PS1 and SS1 coolant being utilised is overestimated. However, the absence of significant discontinuities in Figure 6.17 where the results of this model have been used (except for the case of RAD-A where the stagnation line film effectiveness is very close to zero) supports its use despite the underlying simplification.

6.6 Conclusions

Three different leading edge film cooling designs were tested in which coolant is blown in reverse (against the mainstream flow) from the PS1 and SS1 hole rows in a criss-cross pattern which allows the jets to cross over the stagnation line. The film effectiveness results both near the stagnation line and farther downstream were compared to the corresponding results for conventional radial showerhead designs, and it was found that the novel concept could be highly beneficial to engine film coolant efficiency if implemented.

- Reverse-blowing films which cross the aerofoil stagnation line exhibit much higher film effectiveness at the geometric stagnation line (up to approximately 0.4) than do traditional radial showerhead designs (up to approximately 0.1).
- The best-performing cross-over design's averaged downstream performance is almost identical to that of the best-performing radial design, and a more even film is produced by the cross-over holes since they do not contribute to coolant migration in the direction of the radial blowing.
- The cross-over design offers the opportunity to eliminate radial holes at the showerhead midspan, which might otherwise need to be drilled at poorly performing high surface angles due to the machining limitations imposed by the NGV endwalls.

Comparisons between the film effectiveness data for the various reverse-blowing models suggested some preliminary design rules for optimising film effectiveness performance with the novel concept.

- Complete flow reversal (with reverse-blown coolant staying on its side of origin) was observed at the lowest investigated blowing ratio.
- Hole pitch and stagger variations in models REV-B and REV-C demonstrate the interdependence of successful coolant cross-over on geometry and blowing ratio; these affect the nature of collisions between jets as they attempt to traverse the stagnation line.
- The attempts of these models to reduce lift-off in the stagnation region via compound angling and in-row hole intersections appear to be slightly deleterious rather than helpful across the blowing ratio range investigated.

- Hole intersections have a very small effect on the film effectiveness.
- Hole shaping is by far the most effective means of improving the performance, especially near the stagnation line. This is because the reduced exit velocities of diffusing holes keep the coolant closer to the aerofoil surface.
- Thus the best performing geometry was REV-A with its reverse-blowing holes which lacked compound angling, and in particular those which were fan-shaped. Its lack of compound angling and its even stagger have the advantage of minimising collisions between coolant from opposing aerofoil sides at any given blowing ratio, and thus less required geometric tuning.
- Successful coolant cross-over is evidenced experimentally by effectiveness increases between and behind PS1 and SS1 holes, where coolant could not be arriving from any other source. When this occurs, films also build up behind PS2 and SS2.

Additionally, it was found that RANS CFD underpredicts the jet dispersion and lift-off of the reverse-blown jets. The optimisation of geometrical parameters such as streamwise position, surface angle, fan angle, and pitch of the reverse-blowing hole rows presents a possible avenue for future investigations. Moreover, the thermal stresses within these models have not been studied or compared to those of more conventional geometries. It is likely that further design optimisation would be needed to minimise these given the streamwise angling of the reverse-blowing rows and the resulting reduced distances (or intersections) between these holes and those of adjacent rows.

Finally, temperature mass-averaging arguments were used to generate estimates of the proportion of the mainstream which interacts with NGV leading edge film coolant. These range from 1-2% near the geometric stagnation line to 5-10% behind the PS3 hole row and 2-6% behind the SS6 hole row. Similarly, the proportion of PS1 and SS1 combined coolant flow reaching the stagnation line was estimated as a minimum of 5% for radial holes to a maximum of 60% for diffusing cross-over holes.

Chapter 7

Pressure Margin Enhancement with a Coolant Passage Insert

In this chapter, an NGV leading edge coolant passage geometric modification is proposed which is shown to be capable of reducing the risk of ingestion of hot mainstream gases into the film cooling holes. This is achieved by increasing the pressure margins by which the coolant static feed pressure exceeds the vane external pressures to which the coolant holes exhaust. These pressure margins are lowest for cooling holes near the stagnation region, and their improvement would potentially allow engine performance gains via reduced combustor pressure loss requirements. Design rules for the geometric modifications are suggested which lead to significant improvements in the ingestion risk region, without causing ingestion risks elsewhere. An analytical model of combined converging, diverging and prismatic coolant channels is validated by experimental data to be capable of accurately predicting coolant pressure margins. This work furthers a concept conceived of and initially investigated by Cresci [78], and was published in a paper for an international conference [132].

7.1 Introduction and Motivation

Steady or transient ingestion of hot mainstream gas into NGV leading edge film cooling holes has the potential to cause localised heating leading ultimately to NGV failure. For a given hole geometry, the likelihood of an ingestion event depends upon the amount by which the hole inlet static pressure exceeds the hole outlet static pressure, known as the

pressure margin. The NGV coolant feed passage must therefore be designed with respect to its internal pressure distribution such that the pressure margin at all hole inlets is sufficient to prevent ingestion events. The maximum coolant feed total pressure available is that of the air bled from between the final compressor stage and the combustor inlet. Conventionally, several suction side hole rows and pressure side hole rows are fed from a single supply passage, despite the fact that hole exit static pressure for the final suction side row is considerably lower than for hole exits nearer to the leading edge stagnation line, due to the acceleration of the mainstream flow around the NGV. This means that the suction side holes typically operate with an excessive pressure margin in order that the holes farther upstream may maintain a merely sufficient margin, which usually requires an increase in the pressure loss across the combustor, at the expense of engine efficiency.

This chapter describes a solution permitting reduced combustor pressure losses while maintaining the same minimum pressure margins, by geometrically partitioning the NGV leading edge feed passage such that the excess pressure margin typical of the suction side holes is partially redistributed to the at-risk stagnation region holes. As illustrated in Figures 7.1 and 7.2, this is achieved by creating a sub-passage feeding only the stagnation region holes which due to its large cross-sectional area decelerates the local flow and causes a greater recovery of the coolant dynamic pressure, increasing the pressure margin for these holes. For a fixed original passage geometry, such a partition implies an acceleration of the coolant in the sub-passage feeding the suction side hole rows, reducing their ordinarily excessive pressure margin. The proposed means of this partition is that of an 'insert' attached to the inside of the aerofoil leading edge coolant passage, though casting in a single part may also be feasible. In addition to the potential to reduce combustor pressure losses, the additional pressure margin control provided by such an insert could permit reshaping of an aerofoil external profile, where this may otherwise have been compromised by the need to contour the coolant passage while maintaining allowable metal thickness. Slowing coolant flow with an insert will reduce the local internal heat transfer, though this could potentially be offset by increased turbulation on the coolant passage

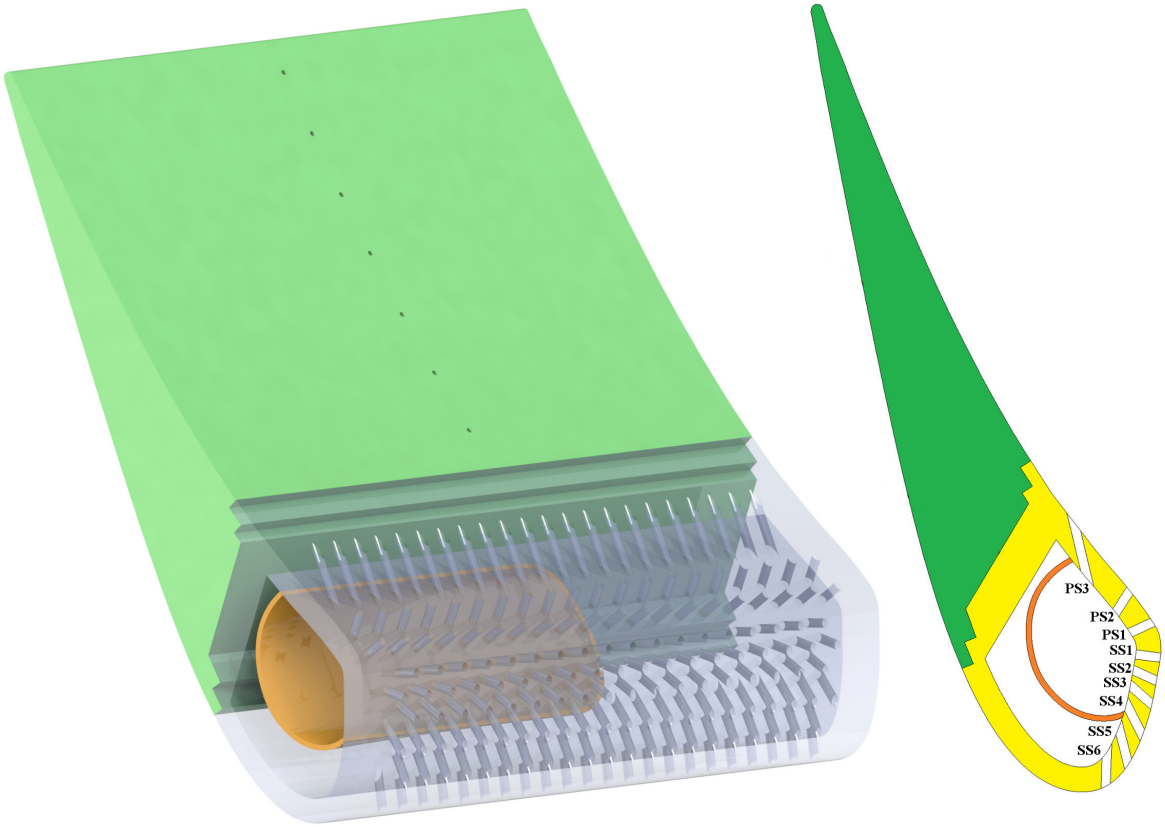


Figure 7.1: Illustration of the placement of the pressure margin inserts studied herein, all of which cover the PS3 to SS4 hole rows, inclusive.

wall (itself introducing additional coolant pressure losses). Alternatively, the loss of internal heat pickup might already be more than offset by the improved film behaviour. As a separate piece to the main NGV, the insert could be affixed using the same techniques as existing baffle plates which are used in current engines to control coolant mass flow rates within double-end fed NGVs. Its aerodynamic presence may slightly change the vane internal stresses, possibly requiring some structural geometry changes to the vane itself.

Cresci originally proposed the insert concept [78], but investigated only a single, short (30% of the NGV span) insert which covered the inlets of the four most upstream hole rows (PS2-SS2) of a leading edge similar to the model RAD-A described in section 5.1.1. The pressure margins were measured to more than double inside the insert for the highest coolant mass flow rates. Besides this, there appears to be no previous academic litera-

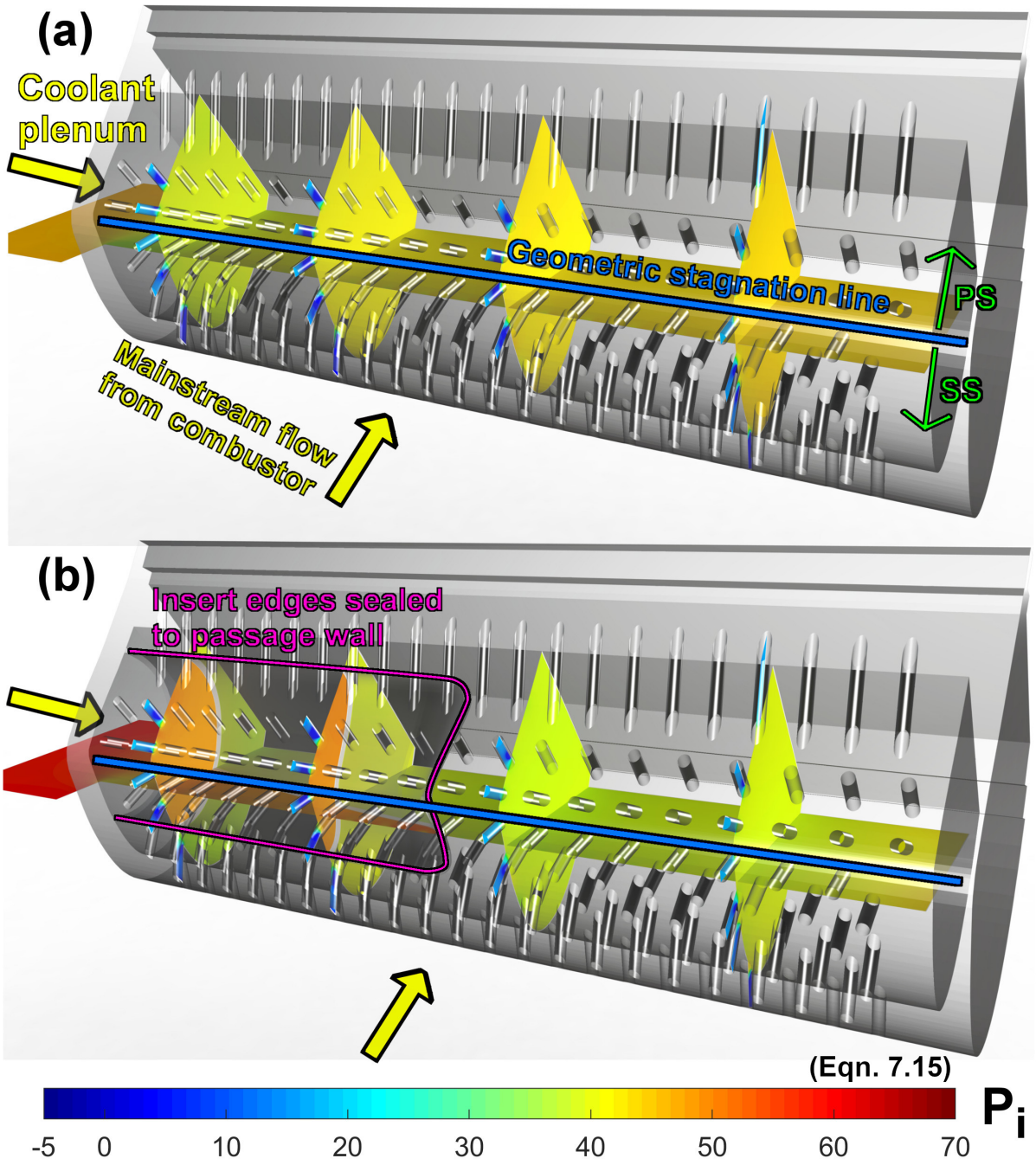


Figure 7.2: NGV leading edge (a) without and (b) with a half-span insert, with internal pressure contours from RANS CFD ($\%m_{NGV} = 9.9$). A rise of static pressure inside the insert is evident. Pressures relative to the indicated stagnation line ($P_i = 0$).

ture directly concerned with the measurement or control of aerofoil film coolant pressure margins, though there are several studies on the effects of coolant supply conditions on exiting jet physics (e.g. Walters and Leylek, Gritsch et al., and Thole et al. [28, 32, 133]) and ample studies of the pressure loss characteristics of conventional aerofoil internal cooling schemes (impingement jets, rib turbulators, and pin-fins). Domaschke et al. [134]

reviewed the prior literature of rib-turbulated cooling in triangular cross section passages, which are taken to resemble the cooling passages in aerofoil leading edges. There is a recent trend in aerofoil internal cooling research to combine and integrate the various existing technologies [135]. A promising example is the impingement of coolant into wall cavities bridged by pin-fin arrays. In these 'double-wall' configurations, there is little additional pressure loss concomitant with the extra heat transfer surface area provided by the pin-fins [136]. The complex internal flow field, combined with the use of low blowing ratio, high hole density film cooling, mimics the operation and performance of a porous material undergoing transpiration cooling [137]. The insert concept of this study is investigated in a purely film-cooled geometry, though it has potential to be integrated with double-wall cooling designs, which could be permitted more aggressive impingement pressure losses as a result.

7.2 Pressure Margin Insert Theory and Preliminary Design

7.2.1 Experimental Approach

The two 3D-printed, leading edge pressure test pieces described in section 3.2.1 feature the same film cooling hole arrangement as the Rohacell test piece RAD-A, and are used to measure coolant passage internal pressures for seven different inserts at span fractions from the inlet of $s = 0.15$, $s = 0.30$, and $s = 0.75$, as well as the external pressure distribution at $s = 0.50$. In combination, these measurements permit calculation of the span- and row-dependent pressure margins, for the range of tested inserts and at four different leading edge coolant mass flow rates. Following Cresci [78], this flow rate is expressed as a percentage of overall throat flow, according to Equation 7.1:

$$\%\dot{m}_{NGV} = \frac{\dot{m}_c}{\dot{m}_c + \frac{\dot{m}_\infty}{2}} \times 100 \tag{7.1}$$

where $\dot{m}_c$ is the leading edge film coolant mass flow rate and $\frac{\dot{m}_\infty}{2}$ is half of the combined combustor simulator inlet, dilution port, and endwall coolant mass flow rate, in accordance

with the fact that only one of the two total NGVs in the Oxford CTI rig cascade is cooled. For these experiments, the dilution port momentum flux ratios are $J_D = 9$ and the outer and inner endwall momentum flux ratios are $J_E = 7$ and 11, respectively. The percentages calculated in this study are not engine representative because of the absence of downstream pressure side film cooling holes and slots. True engine matching in this respect would also require testing of geometry with a more engine-realistic coolant flow path with varying coolant passage area and curvature, and potentially a variety of internal cooling features. The primary purpose of varying $\%\dot{m}_{NGV}$ in this study is to examine its influence on the inserts' flow attributes.

7.2.2 External Pressure Distribution

Calculation of the pressure margin for different cooling hole rows requires knowledge of the aerofoil external pressure distribution. The measured distributions for each of five coolant flow rates, including a no-coolant case, are shown in Figure 7.3. These pressures are relative to the maximum measured tapping pressure (near the geometric stagnation line) and normalised by the throat dynamic pressure $(\frac{1}{2}\rho v^2)_{throat}$:

$$C_p = \frac{p_{s,e} - p_{s,e,max}}{(\frac{1}{2}\rho v^2)_\infty} \tag{7.2}$$

The dynamic pressure is calculated in two different ways: by excluding the NGV coolant mass flow rate (empty circles) and by including it (filled circles). The addition of film coolant reduces the suction side and downstream pressure side surface static pressures because the effective blockage of the coolant films accelerates the mainstream flow compared to the uncooled case. Greater mass flow rates of coolant increase the blockage, exacerbating the effect, which is strongest on the suction side due to the larger amount of film cooling holes and the greater amount of mainstream flow. The trend appears to reverse when normalising by $(\frac{1}{2}\rho v^2)_{throat}$ including NGV coolant, which increases with the NGV coolant mass flow rate. For all cases, the suction surface pressure distribution is discontinuous around the joint between the leading edge and main vane pieces of the NGV

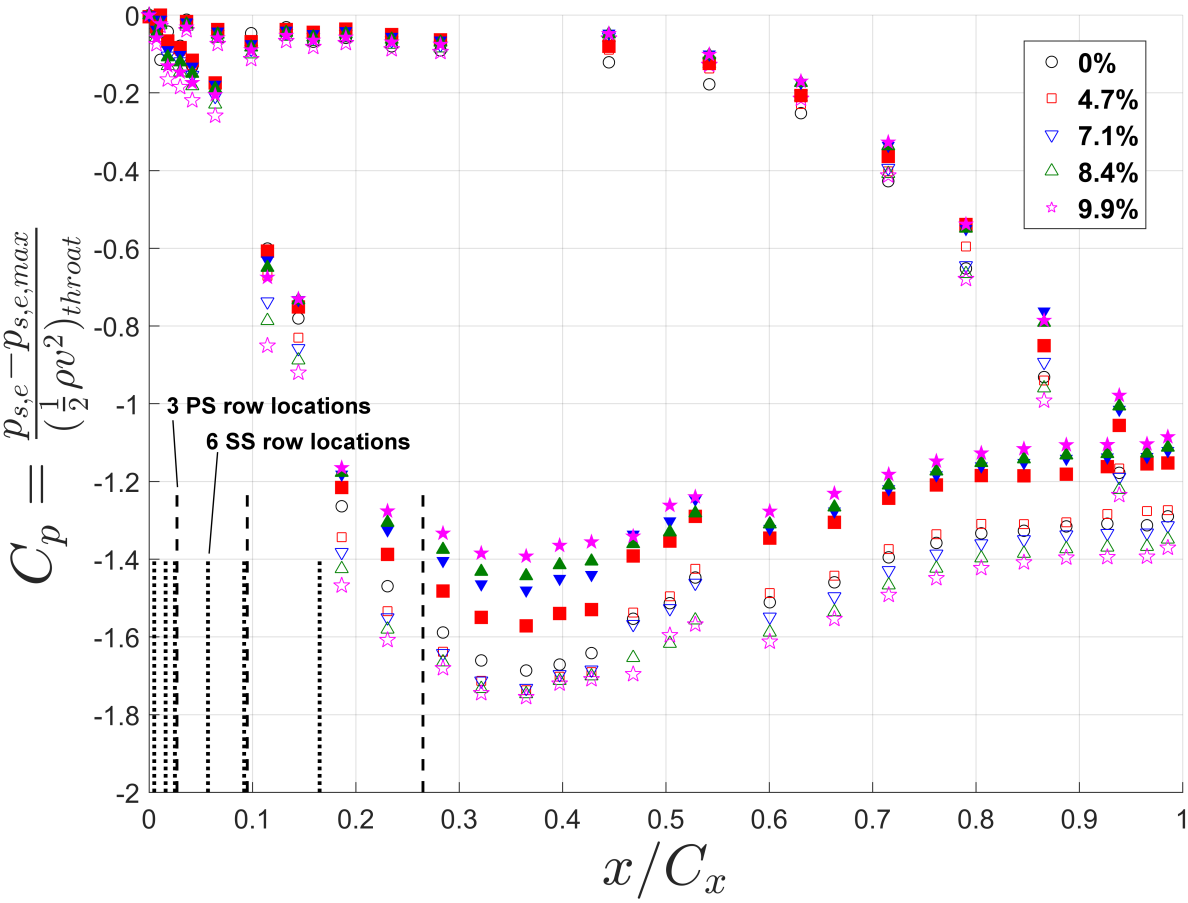


Figure 7.3: Experimental pressures on NGV exterior, with no insert present. Filled/empty circles are normalised by $(\frac{1}{2}\rho v^2)_{throat}$ including/excluding the NGV coolant mass flow rate.

at approximately $\frac{x}{C_x} = 0.55$. This is due to a separation of the suction surface boundary layer, which, unlike the pressure side boundary layer, is subject to an adverse pressure gradient around this joint. The separation region is of lower pressure than the mainstream flow, causing a rapid reattachment of the flow and continuation of the pressure recovery for the remainder of the suction side. For all experiments, a thin strip of packaging tape was sealed over the gap, though little improvement was yielded. As also measured previously by Cresci [78], a separate 3D-printed leading edge with external pressure tappings at $s = 0.75$ showed that the pressure distribution has little spanwise variation far from the endwalls. It is likely that the pressure margins very close to the endwalls are slightly lower due to the enhanced momentum of the endwall film coolant, which would need to be taken into account for engine design purposes. Identical experiments with pressure margin inserts in place generated essentially identical vane external pressure results.

Preliminary design decisions were made with reference to the experimental pressure margin results for the case of the baseline NGV geometry with no insert. Four coolant mass flow rates were investigated, and the pressure margins for individual hole rows were calculated separately at the three different spanwise positions where internal coolant pressure measurements were available. The external pressures were interpolated to the cooling hole row external breakouts in order to calculate pressure margins separately for each row. Since the external pressures are similar for all of the rows except the final two on the suction side, it was found that the three pressure side rows and first four suction side rows operated at a similar margin, while the margins of the final two suction side rows were significantly higher. Therefore, the pressure margin inserts in this study were designed to cover all but these two hole rows (SS5 and SS6). There is a small recovery of static pressure due to the progressive effusion of coolant through the cooling holes, which causes the velocity of the remaining coolant to reduce as it travels along the coolant passage. However, this effect was very small compared to the variation of static pressure externally to the aerofoil, suggesting that for a single-end fed leading edge, spanwise pressure margin variations are relatively small and the insert should extend all the way into the passage (i.e. unity insert length as a fraction of span, $H = 1$). This would also likely be the case for the same coolant passage under engine conditions, since the recoverable coolant dynamic pressure is smaller than the rig case relative to the respective estimated mainstream NGV dynamic pressures. However, to investigate the device's feasibility for double-end fed NGVs as well, shorter inserts were also tested ($H = 0.3$ and $H = 0.5$).

7.2.3 Inviscid Analysis for Insert Cross Section Design

The following inviscid analysis shows that a sufficiently broad insert can increase its internal static pressure, thus increasing the pressure margin of enclosed holes. The fundamental mechanism is to slow the coolant, increasing the local recovery of dynamic pressure. Consider an inviscid and incompressible analysis (constant coolant total pressure, p_{0c}, and density, ρ_c) in which a prismatic coolant passage of constant cross-sectional area A_T and internal length L feeds N cooling holes from a single end. Let s represent the fractional

spanwise distance from the inlet ($0 \leq s \leq 1$). If the coolant mass flow rate at the inlet is $\dot{m}_T$ and the coolant is assumed to be expelled evenly along the span, then the passage mass flow rate and bulk velocity at a position s can be approximated by Equations 7.3 and 7.4, respectively.

$$\dot{m}_c(s) \approx (1-s)\dot{m}_T \tag{7.3}$$

$$v_c(s) \approx (1-s)\frac{\dot{m}_T}{\rho_c A_T} \tag{7.4}$$

Rearrangement of the definition of total pressure yields Equation 7.5, into which can be substituted Equation 7.4, which then yields Equation 7.6 for the static pressure in the coolant passage, $p_{sc,passage}$, as a function of spanwise position.

$$p_{sc,passage}(s) = p_{0c} - \frac{1}{2}\rho_c[v_c(s)]^2 \tag{7.5}$$

$$p_{sc,passage}(s) = p_{0c} - \frac{1}{2\rho_c}(1-s)^2(\frac{\dot{m}_T}{A_T})^2 \tag{7.6}$$

Consider also the two adjacent channels of nondimensionalised length $0 < H < 1$ formed by an insert of the same length H, and resembling those of Figure 7.2(b). If n is the number of holes covered by the insert (i.e. whose inlets are within the converging channel) then the mass flow rate within the converging channel can be approximated by Equation 7.7.

$$\dot{m}_c(s) \approx (1-\frac{L}{H}s)\dot{m}_T\frac{n}{N} \tag{7.7}$$

If the channel's spanwise-varying cross-sectional area is $A(s)$ then the velocity $v_{c,conv}(s)$ and static pressure $p_{sc,conv}(s)$ in this channel can be expressed as Equations 7.8 and 7.9, respectively.

$$\dot{v}_{c,conv}(s) = (1-\frac{L}{H}s)\frac{\dot{m}_T}{\rho_c A(s)}\frac{n}{N} \tag{7.8}$$

$$p_{sc,conv}(s) = p_{0c} - \frac{1}{2\rho_c}(1-\frac{L}{H}s)^2(\dot{m}_T)^2(\frac{n}{NA(s)})^2 \tag{7.9}$$

Employing Equations 7.6 and 7.9, the condition for $p_{sc,conv}(s) > p_{sc,passage}(s)$ simplifies to Inequality 7.10.

$$\frac{A(s)}{A_T} > \frac{n(1-\frac{L}{H}s)}{N(1-s)} \tag{7.10}$$

At the inlet ($s = 0$), the static pressure within the insert converging channel increases above the prismatic passage static pressure when the proportion of the total passage inlet area occupied by the insert's cross section exceeds the proportion of included cooling holes. To determine a profile of minimum allowable cross-sectional area, $A_{min}(s)$, the above analysis can be repeated with the inclusion of a desired minimum pressure margin, the amount by which the static pressure inside the insert exceeds the maximum external NGV static pressure, $p_{se,max}$.

$$PM_{design} = p_{sc} - p_{se,max} \tag{7.11}$$

Since the external pressure around the aerofoil varies, the pressure margins between covered hole rows will be different even if the static pressure inside the insert is uniform, but all will be greater than PM_{design}. Using Inequality 7.12 (the condition that the coolant static pressure exceed $p_{se,max}$ by PM_{design}) and Equation 7.8 for the coolant passage velocity, Inequality 7.13 is obtained, which can be simplified to find $A_{min}(s)$.

$$p_{0c} - \frac{1}{2}\rho_c[u_c(s)]^2 \geq p_{se,max} + PM_{design} \tag{7.12}$$

$$p_{0c} - \frac{1}{2}\rho_c[(1-\frac{L}{H}s)\frac{\dot{m}_T}{\rho_c A(s)}\frac{n}{N}]^2 \geq p_{se,max} + PM_{design} \tag{7.13}$$

$$A_{min}(s) = \frac{(1-\frac{L}{H}s)\dot{m}_T\frac{n}{N}}{\sqrt{2\rho_c[p_{0c} - (p_{se,max} + PM_{design})]}} \tag{7.14}$$

To obtain the $A(s)$ profiles of the inserts used in this study, the chosen PM_{design} was approximately three NGV mainstream inlet dynamic pressures as measured in the CTI rig, since this was estimated as representative of the equivalent pressure margin in a modern civil jet engine. The other parameters in Equation 7.14 were measurable from rig tests on the film-cooled NGV model with no insert attached and at four coolant mass

flow rates $\%\dot{m}_{NGV} = 4.7$, 7.1, 8.4, 9.9. Three insert lengths were tested, the shorter two of which with three different inlet areas each, resulting in seven insert designs (three with $H = 0.3$, three with $H = 0.5$, one with $H = 1$). Table 7.1 summarises the geometric details of the tested designs. As dictated by Equation 7.14, the inserts are designed so that their cross-sectional areas descend from their inlet values to zero in an approximately linear fashion.

Table 7.1: Lengths and inlet areas of the seven tested inserts.

Insert	**A**	**B**	**C**	**D**	**E**	**F**	**G**
H	0.3	0.3	0.3	0.5	0.5	0.5	1
$A(0)/A_T$	0.22	0.33	0.41	0.34	0.53	0.60	0.89

7.3 Internal Pressure and Pressure Margin Results

Since the amount of film coolant injected subtly influences the upstream flow rates (combustor inlet, endwalls, and dilution ports), the pressure results are normalised by the NGV mainstream inlet dynamic pressure calculated on a run-by-run basis. Two copies of each pressure margin insert design were 3D-printed. To test each design, the edges of one copy were sealed with flowable silcone to the inside of the coolant passage of each of the two pressure tapping leading edge models described in section 3.2.1. Occasionally, the coolant passage tappings were obstructed by the inserts or by excess silicone, creating anomalous data points, and these were removed from the data as necessary.

7.3.1 Internal Pressures with Overly Broad or Narrow Inserts

The measured internal pressures are expressed relative to the maximum measured external static pressure and normalised by the mainstream inlet dynamic pressure:

$$P_i = \frac{p_{s,c} - p_{s,e,max}}{(\frac{1}{2}\rho v^2)_\infty} \tag{7.15}$$

and are shown in Figure 7.4. $\frac{x}{C_x}$ describes positions around the cross section of the coolant passage inner surface (PS negative, SS positive, $x = 0$ is the vane's geometric stagnation line, and C_x is the vane's axial chord length). The internal pressure tends to increase with coolant mass flow rate because higher velocity coolant recovers more dynamic pressure as it slows. Considering the experimental data with no insert, a spanwise increase in static pressure due to progressive effusion of coolant is only just apparent for $\%\dot{m}_{NGV} = 9.9$.

The tested $H = 0.30$ inserts illustrate the need to design inserts for low diffusion rate in the diverging channel. The tappings lie just downstream of the inner ends of these inserts (many were prone to blockage by adhesive, causing the irregular pressures just downstream of insert A). Those just downstream of the portion of inner surface covered by insert B experience the same uniform pressure as those farther around the passage surface. By contrast, the pressures measured just behind insert C are substantially lower than those farther around the passage surface, and indeed much lower than with no insert. This is because insert C has the widest inlet area of the three candidates and hence the greatest diffusion rate in the diverging channel, causing a flow separation and low pressure region near its end. The pressure inside insert A is slightly less than in the absence of an insert, indicating that the converging passage is too narrow and accelerates the flow. The effective cross-sectional area will always be less than the ideal inviscid one, because of boundary layers within the converging passage. The restriction of mass flow into the converging channel explains why insert A exhibits the highest static pressures at $s = 0.30$; the associated increase in mass flow rate to the diverging channel increases the recoverable dynamic pressure. Compared to no insert, inserts B and C succeed in significantly increasing the pressures within the inserts, while reducing the pressures outside at $s = 0.15$. Coolant pressures at $s = 0.75$ are only very slightly reduced by the three $H = 0.30$ inserts. The $H = 0.50$ inserts make this reduction significant, especially for larger inlet areas, because slowing the coolant flow at more holes in the converging channel must increase mass flow rate per hole in the diverging channel. This trend is continued by the $H = 1$ insert G for holes within the diverging passage. At $s = 0.15$,

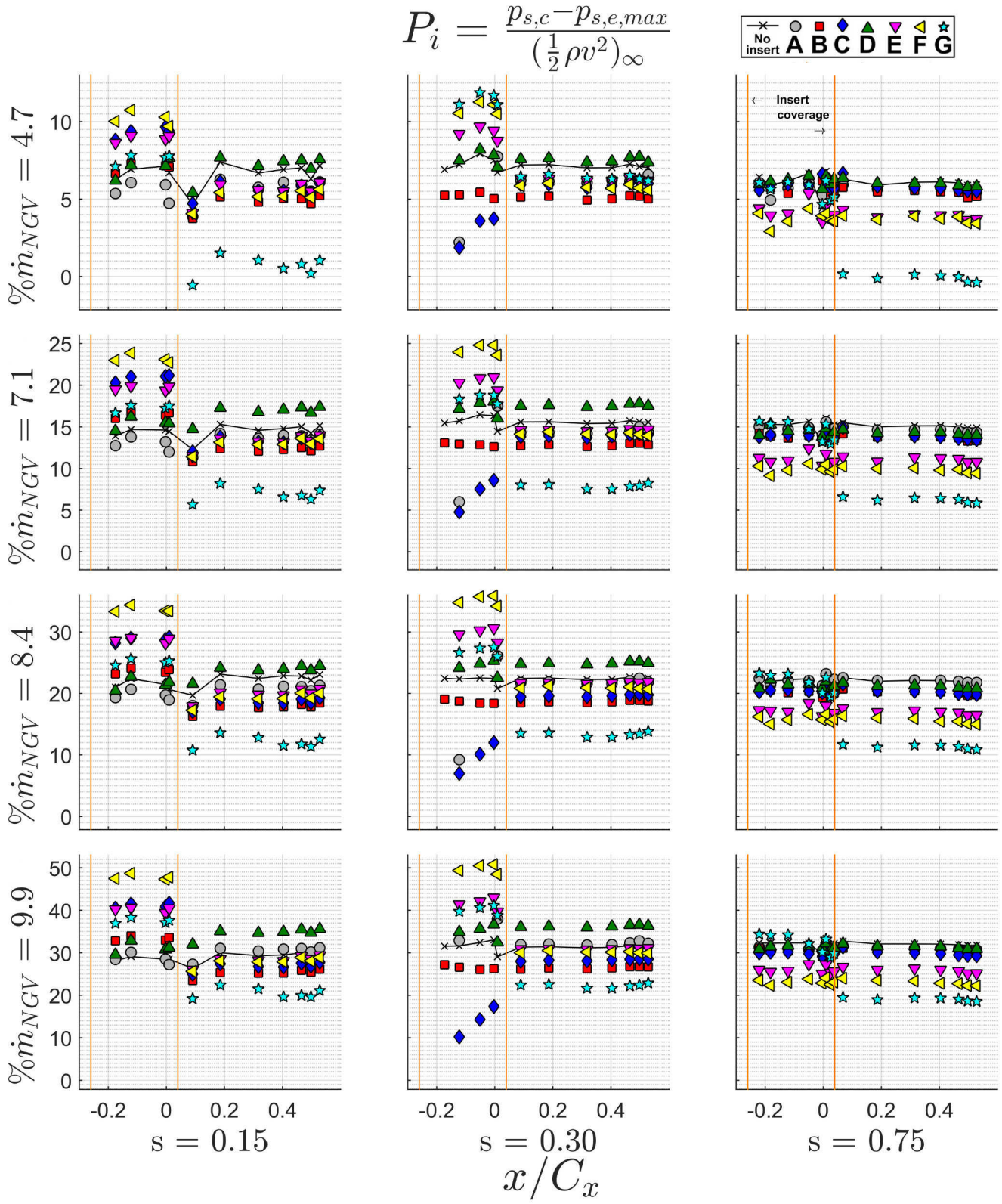


Figure 7.4: Experimentally measured static pressures inside the NGV coolant passage for seven pressure margin inserts. $\frac{x}{C_x} < 0$ and $\frac{x}{C_x} > 0$ are the coolant passage wall regions internal to the NGV pressure and suction sides, respectively. Note the vertical axis scale variations.

insert D increases coolant pressure outside of the insert, and effects little change inside it. At $s = 0.30$, it yields an equal but small static pressure gain both inside and out. These changes are not useful; it is preferable to realise a significant gain within the inserts, at the expense of the static pressures outside them (at the inlets of low ingestion risk holes).

7.3.2 Internal Pressures with Successfully Designed Inserts

Both inserts E and F produce greatly increased static pressures inside, with only slight reductions outside at $s = 0.15$ and $s = 0.30$ compared to the no-insert pressures. The trade-off between them is that the even higher pressures within F cause lower static pressures outside at $s = 0.75$. The choice between them in a double-end feed arrangement would therefore depend upon the relative static pressure requirements at the ingestion risk film cooling holes and any (internal or film) cooling features fed from the channels outside of the inserts. As mentioned previously, a full-span insert such as G may be required for application of the concept in a single-end feed NGV leading edge. This device also succeeds in increasing its internal static pressures at $s = 0.15$ and $s = 0.30$. The static pressure results for $s = 0.75$ are increased inside the insert, but appear to decrease towards the stagnation region ($\frac{x}{C_x} = 0$). This indicates a leak where the insert is not fully sealed by the silicone adhesive, which proved difficult to apply at locations deep within the passage. If the two channels were properly isolated in this region, the pressure within the insert would further increase, while the pressure outside it would further decrease. Moreover, only a single $H = 1$ profile has been tested. Therefore, the results show that the insert concept is viable for both single- and double-end fed NGVs.

7.3.3 Pressure Margins

The internal and external pressure data at each of the three measurement spanwise positions can be interpolated to estimate the static pressures at the centres of each hole inlet ($p_{s,i}$) and exit ($p_{s,e}$), respectively. The difference between these pressures is normalised

by the mainstream cascade approach dynamic pressure to give the hole pressure margin:

$$PM = \frac{p_{s,i} - p_{s,e}}{(\frac{1}{2}\rho v^2)_\infty} \tag{7.16}$$

Figure 7.5 shows the normalised pressure margins implied by this process, across all hole rows. The external pressure distribution causes SS5 and SS6 margins to be much higher than others; to facilitate comparison of insert performance for all rows, the hole pressure margin results for each row are normalised once more by the highest margin achieved in that row by any insert. For insert A, the margins of covered holes decrease at $s = 0.15$, in accordance with the decreased internal pressures noted previously. Inserts B and C increase these margins at the expense of the SS5 and SS6 margins. The effect is more significant at higher coolant mass flow rates, for which insert C almost equalises the margins of all rows. These $H = 0.3$ inserts slightly reduce the downstream margins at $s = 0.30$ and $s = 0.75$, except for the separation region behind insert C, which suffers significantly reduced margins (note the change of vertical axis scale for $s = 0.30$). Insert D is too narrow to produce a significant effect. Inserts E and F significantly improve the hole margins within them for all coolant mass flow rates, and at high mass flow rates F essentially equalises the margins at all rows. Both tend to reduce the pressure margins at $s = 0.75$, though this is only significant for high coolant mass flow rate. Insert G increases the at-risk row margins for all coolant mass flow rates and spanwise positions. At-risk margins appear unaffected at $s = 0.75$, but this is a relic of the leakage from this region of the diverging channel due to poor sealing.

Figure 7.6 captures the main insert effects in a simplified format by considering only the cooling hole row with the greatest exit static pressure (and hence lowest and most critical pressure margins), row SS1. The nondimensionalised pressure margins across this row are shown for all seven inserts plus the datum case of no insert. While experimental data are only available at $s = 0.15$, 0.30, and 0.75, it is clear that the half-span inserts E and F vastly improve pressure margin near the inlet, while full-span insert G somewhat improves margin for the entire span.

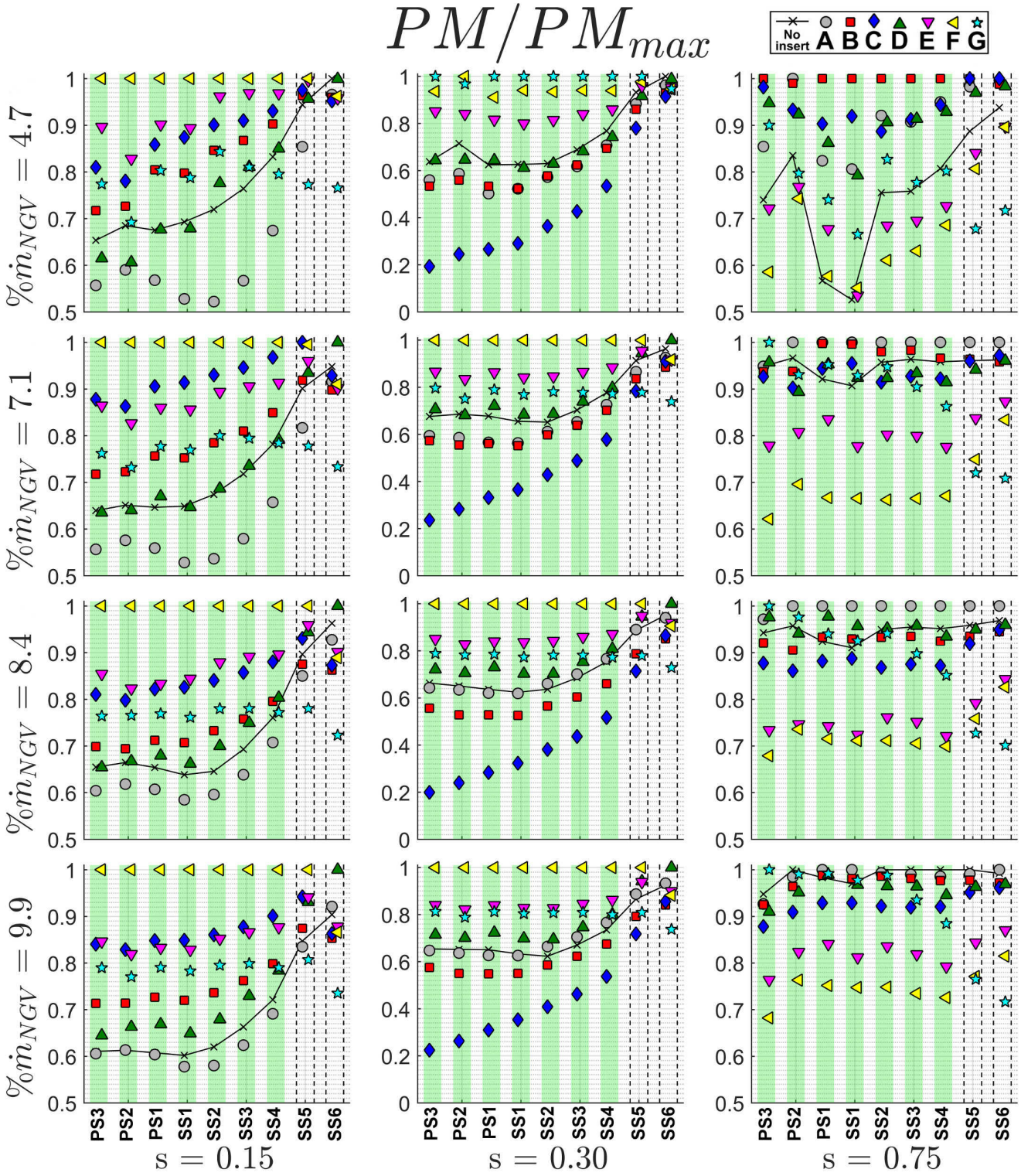


Figure 7.5: Pressure margins across film cooling hole rows for seven pressure margin inserts. Note the change of vertical axis scale for $s = 0.30$ results. Covered hole rows are shaded.

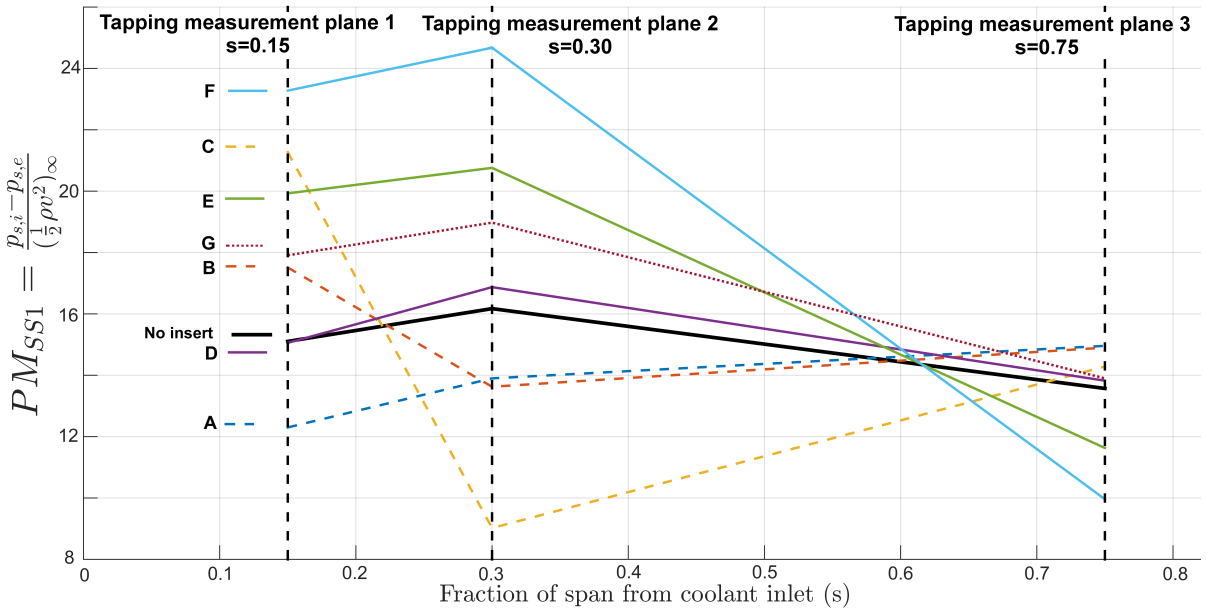


Figure 7.6: Measured SS1 hole row pressure margins for $\%\dot{m}_{NGV} = 7.1$, all seven tested inserts.

7.3.4 Uncertainty Analysis

The uncertainties in the derived flow quantities listed in Table 7.2 are calculated with those propagated by orifice meter, pressure tapping, pitot tube, and thermocouple measurements. $\%\dot{m}_{NGV}$ values are highly sensitive to adjustment of the relevant butterfly valve, with a maximum variation from the stated target quantities across all runs of 0.09 (which is added to the uncertainty based on orifice plate calculations). Small variations in cascade approach mass flow rates are accounted for since all vane pressure data are normalised by simultaneously recorded NGV mainstream dynamic pressures. Calculation of the nondimensionalised hole pressure margins requires interpolation of the tapping data to the centres of the hole inlets and exits. The hole exit pressure uncertainty is largest for SS5 and SS6, as they reside in the region of greatest pressure gradient on the NGV exterior. This additional uncertainty in PM is estimated as 0.1, based on the maximum residual of a linear fit through the pressure data points in this region. The normalised internal pressures, P_i, are not subject to this additional uncertainty as they represent the pressures measured directly at tappings. The main contributor to uncertainty in both PM and P_i is the cumulative mass flow rate uncertainty in the estimation of the normalising dynamic pressures. Their largest percentage uncertainties apply only to low NGV coolant mass flow rate cases for which some internal pressures approach external pressures.

Table 7.2: Estimated maximum uncertainties for the derived insert performance flow quantities.

Quantity	Symbol	Range	Maximum uncertainty
NGV coolant percentage of throat flow	$\%\dot{m}_{NGV}$	4.7 - 9.9	0.26 (2.6 - 5.5%)
Vane internal pressure	P_i	-0.56 - 50.8	0.18 (0.3 - 32.1%)
Dimensionless hole pressure margin	PM	2.5 - 61.7	0.28 (0.5 - 11.2%)

7.4 Viscous Modelling for Prediction of Coolant Pressure Margin

The coolant passage internal pressures generated by ANSYS Fluent RANS CFD (e.g. Figure 7.2) were significantly overestimated, independently of mesh density (4.5 million, 11.4 million, and 55.0 million elements) and turbulence model ($k-\epsilon$ and $k-\omega$). This is attributed to the overly large flow separations (i.e. underestimated discharge coefficient, $C_d = \frac{(\rho v A)_{actual}}{(\rho v A)_{ideal}}$) predicted within each cooling hole. The reduced effective flow area due to larger separations means that an unrealistically high driving pressure is needed in order to produce the mass flow rates equivalent to experiments. For long cooling holes (length-to-diameter ratios greater than two) such as those of this study, such C_d underestimation is ubiquitous with RANS. The effect has been observed in comparisons to experimental C_d data, even when individual holes are simulated with a variety of aerofoil film cooling inlet and outlet conditions and various turbulence models and mesh fidelities (e.g. by Gupta et al. [138]). In the absence of easily obtainable, reliable CFD results, the following enhanced analytical method may complement or replace limited resolution experimental data. The method resembles the analysis presented in section 7.2.3, but accounts for coolant channel total pressure losses with pipe flow Darcy friction factors, f, in converging sections and diffuser pressure loss coefficients, K_L, in diverging sections. The analysis makes use of the ratio of static-to-total pressure $Q(s)$ defined in Equation 7.17 and derived from the definition of total pressure and the relation $p_{0c} \approx \rho_c R T_0$, which is a good approximation for incompressible flow. It also makes use of the Darcy-Weisbach equation for $F(s)$, the

fraction of inlet dynamic pressure lost for a circular pipe of length ds. R is the specific gas constant for air and $f(s)$ is estimated according to Serghides [139], making it in fact a function of Reynolds number, hydraulic diameter D_H (ultimately functions of s), and surface roughness (assumed constant).

$$Q(s) = \frac{p_{sc}(s)}{p_{0c}(s)} = 1 - \left[\frac{\dot{m}_c(s)}{\rho_c A(s)}\right]^2 \times \frac{1}{2RT_0(s)} \tag{7.17}$$

$$F(s) = \frac{f(s)ds}{D_H(s)} \tag{7.18}$$

The analysis begins by expressing the channel static pressure as a function of $Q(s)$ and the cumulative total pressure loss $p_{0,lost}(s)$, according to Equation 7.19.

$$p_{sc}(s) = Q(s) \times p_{0c}(s) = Q(s) \times [p_{0c}(s=0) - p_{0,lost}(s)] \tag{7.19}$$

A converging channel is treated as a series of pipes of infinitesimal length dz, yielding the viscous form of Equation 7.9, Equation 7.20, which applies also to prismatic sections. z is a dummy variable.

$$p_{sc,conv}(s) = Q(s) \times [p_{0c}(s=0) - \int_0^s (F(z) \times \frac{1}{2}\rho_c[v_c(z)]^2)dz] \tag{7.20}$$

The static pressure in a diverging channel $p_{sc,div}(s)$ is determined more simply, by assuming a linear $p_{0,lost}(s)$ amounting at the channel's exit to K_L times the dynamic pressure at its inlet. In practice, total pressure loss can be calculated at specific spanwise intervals which divide the channels into short, successive sections of diffuser or pipe. This avoids the need to solve exactly the integral in Equation 7.20. Connected channels can be treated consecutively. For comparisons to the experiments of this study, inlet total pressures were estimated from static pressure measurements within inserts at $s = 0.15$, the channel velocities, and pipe flow losses. Area distributions $A(s)$ of the channels and spanwise reductions of channel mass flow rate ($\dot{m}_c(s)$) were approximated as linear. The results are insensitive to surface roughness values around the estimated 0.1 mm value used. The K_L values were estimated as 1.0 for insert F and 0.5 for the lower diffusion

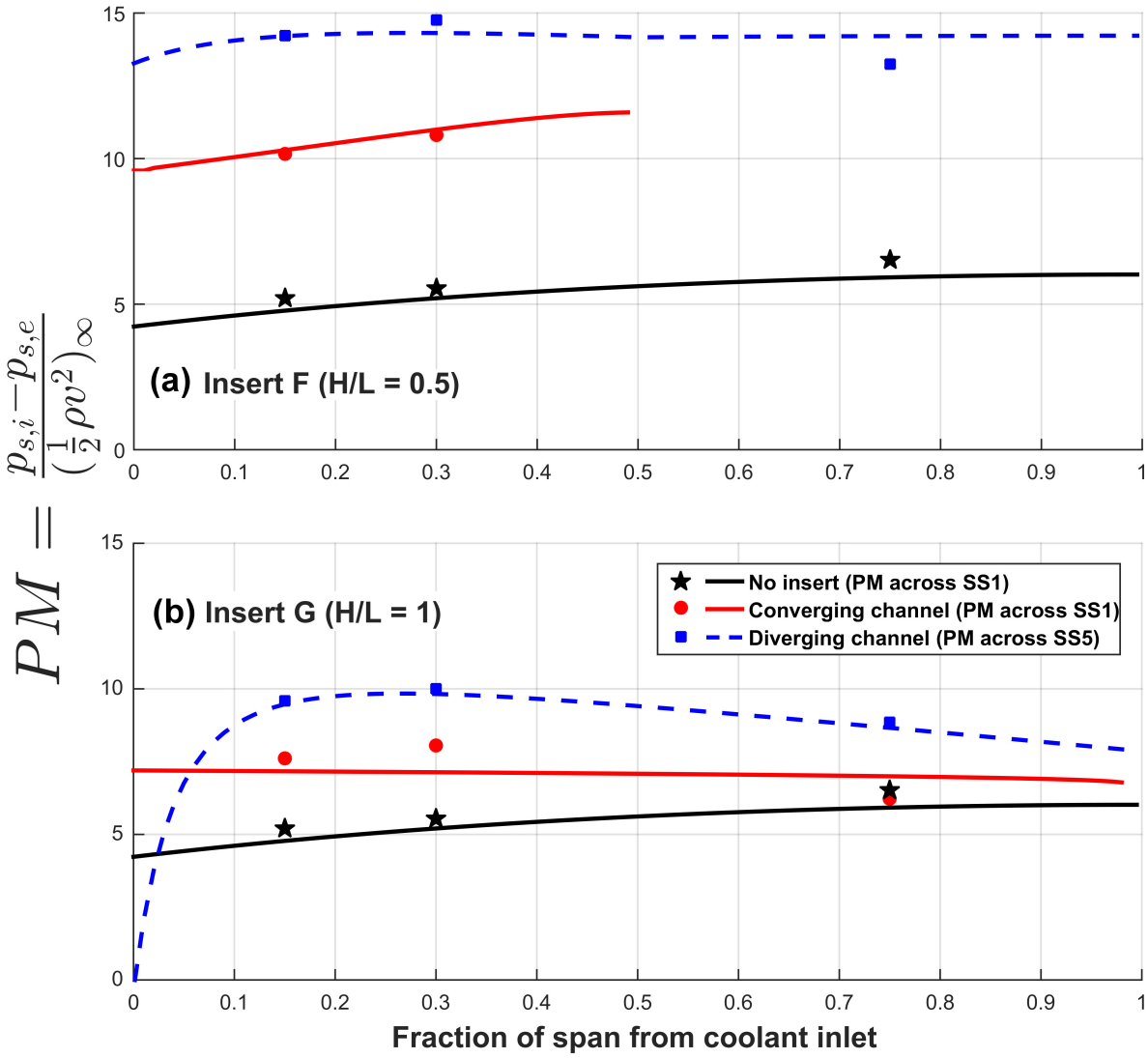


Figure 7.7: Viscous model hole pressure margin predictions for inserts F and G. $\%\dot{m}_{NGV} = 4.7$.

rate insert G. Little basis currently exists for more accurate prediction of performance of irregularly shaped diffusers with flow extraction due to film cooling holes. The pressure margin for a cooling hole row with spanwise constant exit static pressure $p_{se,row}$ is $PM_{row}(s) = p_{sc}(s) - p_{se,row}$. Despite these simplifications, accurate and useful hole pressure margin predictions were made, as shown in Figure 7.7. SS1 and SS5 are typically the lowest margin hole rows inside and outside of the inserts, respectively. The near-inlet pressure margin in the diverging channel is revealed to be significantly reduced by the overly broad insert G. This suggests that for a full-span insert, special care must be taken near the coolant inlet to balance the coolant pressures inside and outside of the insert.

7.5 Conclusions

The large scale of the Oxford CTI rig film-cooled NGV cascade has been exploited to experimentally measure at very high resolutions the internal coolant and external surface pressures at a range of coolant mass flow rates. The addition of film coolant slightly reduces the suction side and downstream pressure side surface static pressures because the effective blockage of the coolant films accelerates the mainstream flow compared to the uncooled case.

Stagnation region holes are at considerably greater risk of hot gas ingestion than rows far around the suction side. Seven coolant passage inserts were tested with the goal of reducing the ingestion risk by increasing the margins by which the static pressure at the entrances of at-risk holes exceeds the static pressures at their exits. This is achieved by slowing the coolant flow to these holes by enclosing them within a converging channel with cross-sectional areas which are large relative to the number of holes supplied by the channel. The pressure margins for the unaltered prismatic leading edge coolant passage are compared to those in the presence of the inserts, in order to evaluate the efficacy of the concept and to identify design rules. The rules identified are that in the diverging channel formed outside of an insert, the rate of diffusion must not be so large as to produce separations, and that broader inserts increase the pressure margins for cooling holes inside the inserts, and decrease them for those which are outside. Higher coolant flow rates exacerbate the latter effects, resulting in more complete equalisation of the margins of holes within the inserts and outside. Therefore, the insert concept can improve pressure margins, while potentially also controlling blowing ratios and/or internal cooling feature feed conditions, for single- and double-end fed aerofoils. The data were used to validate an analytical method for predicting the pressure margin performance of combined converging, diverging and prismatic cooling passages.

Chapter 8

Conclusions and Recommendations

The present work has disclosed a wide variety of novel research pertaining to aerofoil leading edge film cooling. In this final chapter, more thorough summaries are given of each of the six principal achievements mentioned in section 1.3, as well as recommendations for future research on these topics.

8.1 A Spatially Resolved Infrared Camera Calibration in the Presence of NGV Endwall Film Cooling (Section 4.6)

- Infrared camera output was compared to thermocouple temperature readings at a dense grid of locations across an NGV cascade leading edge, in order to measure the full-surface infrared radiation reflections under different combustor coolant flow rate conditions.
- Dilution ports had a negligible effect on the reflected radiation because the jets penetrate away from the combustor walls.
- Endwall film coolant significantly reduces its local surface temperatures and thus the thermal emissions of the endwall.
- The reduced thermal emissions of a cooled endwall reduces the amount of radiation reflected from the nearby vane surface to the camera.

- Due to this reflection non-uniformity, using only a single vane surface calibration thermocouple in an experimental apparatus such as the CTI rig can lead to severe effectiveness errors of up to 0.05.

- The reflections from surfaces of interest could be reduced (and hence the requirement for a spatial calibration in the presence of nearby cooling features potentially eliminated) by several means:

    1. Further increasing the emissivity of the surfaces of interest (with superior paints), thus reducing their reflectivity.

    2. Reducing the emissivity of the other surfaces (cooled and uncooled) e.g. by coating them with low emissivity paints or materials, thus reducing the magnitudes of the extraneous radiation at its source.

    3. Reducing the coolant-mainstream temperature difference to increase temperature uniformity in the surroundings (though this may have adverse effects on other aspects of the experiment).

8.2 A Novel Method for Measuring Film Cooling Effectiveness and Heat Transfer Coefficients in a Single Test (Section 4.7)

- Film effectiveness and HTC from a single, heated film cooling experiment.

- Film effectiveness is determined at steady-state, then used in conjunction with the measured mainstream temperature transient to determine the pixel-wise, transient, hot gas driving temperatures.

- These are applied as transient boundary conditions to pixel-wise finite element simulations of the test piece, for which guesses of the HTC are iteratively improved until the predicted transient phase surface temperature history matches that of the experiment.

- Unlike conventional analytical techniques, there is no need to assume that the test piece thickness is essentially semi-infinite or initially uniform in temperature, increasing experimental accuracy and flexibility.

- The technique could be applied nearer to film cooling holes and to more sophisticated geometries by use of fully 3D finite element simulations.

8.3 A Novel Method for Measuring NGV Leading Edge Film Effectiveness in the Presence of Non-uniform Temperature Profiles (Section 5.2)

- Dilution ports produce inhomogeneous profiles of both temperature (affects the amount of surface cooling required) and turbulence (affects the performance of the coolant jets) at the NGV inlet.

- Measurements of film effectiveness dependence on the flow field effects of combustor dilution ports or other upstream disturbances are conflated with changes in the temperature profile.

- By separately measuring the dilution port temperature profiles as manifested on the leading edge in the absence of film cooling, the leading edge effectiveness independent of the temperature profiles can be estimated.

- Lower film effectiveness uncertainties could be achieved by several means:

    1. Lower uncertainty flow temperature measurements (e.g. improved thermocouples or substitutes).

    2. Lower uncertainty mass flow rate measurements (e.g. more upstream pitot tubes and automatic mass flow rate controllers for coolant supplies).

    3. Lower uncertainty infrared surface temperature measurements (e.g. improved calibration thermocouples, reduced extraneous reflections, higher speed and resolution cryocooled infrared cameras).

8.4 Quantification of the Enhancement by Dilution Port Turbulence of the Film Effectiveness Produced by Lifted-off Leading Edge Coolant Jets (Section 5.5)

- The above method was applied to measurements of NGV radial showerhead geometries in the presence of multiple upstream dilution port momentum flux ratios.
- Low surface angle radial holes tend to produce attached coolant jets, while higher surface angle radial holes experience significant lift-off.
- Where jets are attached, the film effectiveness they produce in their immediate trajectories is diminished by additional dilution port turbulence since the mainstream removes more coolant from the jet, however this coolant tends to still contribute to effectiveness downstream from where it was extracted.
- Where jets are lifted-off, additional turbulence returns some of the coolant to the surface, especially for intermediate surface angle radial holes with jet trajectories closer to the surface.
- Relative to a no-dilution case, the dilution port turbulence can increase the effectiveness contribution of such jets by up to 0.2 in the leading edge midspan region, where higher surface angle radial holes are common due to machining limitations.
- Thus combustor dilution ports ought to be designed not only in terms of the temperature profiles they produce at the NGV inlet, but also in terms of the flow effects they produce on the leading edge film coolant jets.

8.5 Quantification of the Film Effectiveness Advantages of Leading Edge Films Which Blow Across the Geometric Stagnation Line in Criss-cross Patterns (Section 6.4)

- Leading edge films which blow across the stagnation line from both sides in criss-cross patterns can generate much higher effectiveness there (up to approximately 0.4) than do traditional radial showerhead designs (up to approximately 0.1).

- The best tested cross-over design's averaged downstream performance is almost identical to that of the optimised (low surface angle) radial design, but a more even film is produced by the cross-over holes since they do not contribute to coolant migration in the direction of the radial blowing.

- Cross-over designs offer the opportunity to eliminate radial holes at the showerhead midspan, which might otherwise need to be drilled at low-performing, high surface angles due to machining limitations imposed by the presence of NGV endwalls.

- The improved overall film effectiveness performance of the cross-over designs compared to traditional showerheads means that the concept could potentially be highly beneficial to engine film coolant efficiency and thus engine specific fuel consumption.

- Temperature mass-averaging arguments were used to generate estimates of the proportion of the mainstream which interacts with NGV leading edge film coolant: from 1-2% near the stagnation line to 10% behind the leading edge hole rows.

- Similarly, the proportion of the coolant from the two hole rows straddling the stagnation line that actually reaches the stagnation line was estimated as a minimum of 5% (radial holes) to a maximum of 60% (fan-shaped cross-over holes).

8.6 Quantification of the Improvements to Minimum Hole Pressure Margin Due to a Novel Geometric Modification to Leading Edge Coolant Supply Passages (Section 7.3)

- The addition of film coolant slightly reduces NGV external surface static pressures because the effective blockage of the coolant films accelerates the mainstream flow compared to an uncooled case.

- Inserts which divide the leading edge coolant passage into two channels can improve the pressure margins of holes at risk of hot gas ingestion (fed by the created converging channel) at the expense of those operating with surplus pressure margins (late suction side, fed by the created diverging channel).

- They can achieve near-equalisation of the hole row pressure margins in both single- and double-end fed aerofoils (permitting reduced combustor pressure losses leading to reduced specific fuel consumption) and can potentially also be used for controlling blowing ratios and/or internal cooling feature feed conditions.

- The converging channel must have a profile of cross-sectional area which is disproportionately large for the number of cooling holes fed by it, since this slows the coolant, thus increasing the holes' static feed pressures.

- If the insert is too broad, the flow in the outer channel may separate, creating regions of dangerously low coolant feed pressure.

8.7 Scope for Further Research

The novel geometry concepts discussed in chapters 6 and 7 each show great promise for engine applications despite their developmental infancy, and there are clear areas for further research in both cases. The concept of reverse-blowing holes whose coolant jets cross the geometric stagnation line has been shown to be capable of yielding significant effectiveness

benefits compared to conventional radial designs, however the optimal designs remain unclear. There is a substantial design space regarding hole positioning, angling, shape, and intersections which remains to be explored in order to optimise the performance of this concept. While streamwise-blowing holes performed best among the geometries in this study, this may have been due to the particular hole breakout positions or hole angles used, and angled fan-shaped holes are also yet to be studied in this application. It also remains to consider the thermal stress implications of each such design given the high local vane surface curvature and the inter-row hole intersections which can be produced.

A novel viscous analytical model was developed for predicting the leading edge film coolant pressure margin due to a coolant insert, sufficient for accurate pressure margin predictions under certain conditions. However, the development of computationally efficient CFD methods capable of accurately predicting feed pressures and flow separations would be still more useful in permitting cheaper and more rapid design of the inserts for a given application. In the present experiments, a great number of tappings at each spanwise location reduced uncertainties in the local coolant pressure measurements and helped to identify the possibility of diverging channel flow separations, however test pieces with pressure tappings at a greater number of spanwise locations could produce more data for validating predictive models.

Appendix A

Operating Procedures for the Oxford Combustor-Turbine Interactions Rig

The steps for operating the Oxford CTI rig can be divided into a setup stage in which no air flows and an experiment stage in which the two fans are powered on and aerothermal data are collected.

A.1 Setup

1. Seal or unseal the dilution ports and endwall film cooling as appropriate to the experiment.
2. Insert Rohacell test piece (for leading edge surface temperature measurements) or resin test piece (for pressure measurements) as appropriate to the experiment and reseal the access wall. If necessary, an infrared calibration experiment may be conducted either before or after the main infrared experiment.
3. Power on the mainstream and coolant mass flow rate pressure transducer box (and additional transducer boxes if performing a pressure test piece experiment).
4. Power on the main PC, which controls the LabVIEW data acquisition software and the pressure side infrared camera. For infrared experiments, also turn on the secondary PC which controls the suction side camera, and ensure that the cameras are powered on and connected to the PCs.
5. Power on the data acquisition system, which digitises both pressure transducer and thermocouple signals for the main PC.
6. Open two LabVIEW interfaces: one time-averages over several seconds to record mass flow rate information, and the other records a temperature transient from all of the thermocouples and triggers both cameras to record simultaneously.
7. Record the ambient temperature and pressure and input them into the mass flow rate LabVIEW interface.

8. Calibrate the mass flow rate pressure transducers by running the mass flow rate interface once (without the fans running) to find the zero pressure differential transducer voltages. Input these manually from the readouts back into the appropriate input boxes of the interface.
9. Run experiments as below.
10. Power off the aforementioned items.

A.2 Experiment

1. For a heated experiment, turn on the 'Drake' power supply system and unisolate the CTI rig's heater mesh. The very high current of the heater mesh makes its operation the most hazardous part of the experiment, and prior training is required.
2. Power on the suction (mainstream) and blower (coolant) fans. Adjust the suction fan to the desired speed (the blower fan is fixed-speed).
3. Alternately adjust the butterfly valves and run the mass flow rate LabVIEW interface until the measured dimensionless coolant mass flow rates (J_E, J_D, M) are all as intended for the present experiment. If a heated experiment is to be performed, they should be set slightly lower as per section 3.5.
4. (a) For a pressure test piece experiment, the heater mesh is not required. A third LabVIEW interface for collecting the additional transducer box data is run, and the experiment is completed.
   (b) For a surface temperature test piece experiment, the temperature transient/infrared camera LabVIEW interface is activated.
5. Promptly turn on the heater mesh (ideally within a few seconds so that the 60 second duration temperature data recording captures a sufficiently long transient).
6. While the temperature data are being collected, run the mass flow rate LabVIEW interface again to measure the actual dimensionless mass flow rates achieved during the hot experiment.
7. When the temperature capture finishes, promptly turn off the heater mesh. This saves power and extends the life of the heater mesh.
8. The mass flow rates can be adjusted again to a different setting if required. If the test piece or other experimental conditions need to be changed, the fans must be powered off.
9. When all experiments are complete, turn off the fans, isolate the heater mesh and, turn off the 'Drake' power supply.
10. Export the captured infrared camera data to a format readable by the post-processing scripts. The LabVIEW interfaces automatically save mass flow rate and thermocouple data to files specified before they are activated.

Appendix B

Heat Transfer Coefficient Uncertainty Contributions

The following images represent the HTC uncertainty contributions of the underlying uncertain measurements for the technique described in section 4.7. Those underlying measurements are the material thermal diffusivity (α), the time error (Δt), the film effectiveness (η), the surface temperature (T_s), the coolant temperature (T_c), and the mass-averaged mainstream temperature (T_∞). The uncertainty due to the internal HTC boundary condition is negligible by comparison.

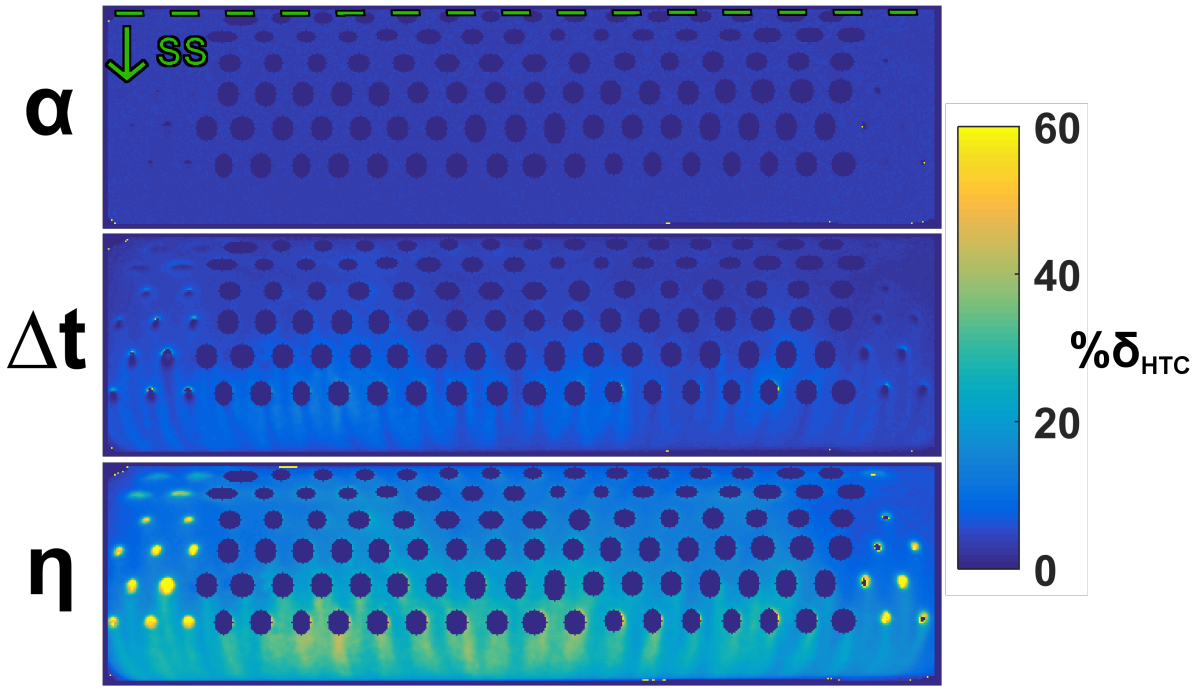


Figure B.1: Suction side HTC uncertainty contributions of the material thermal diffusivity (α), the time error (Δt), and the film effectiveness (η).

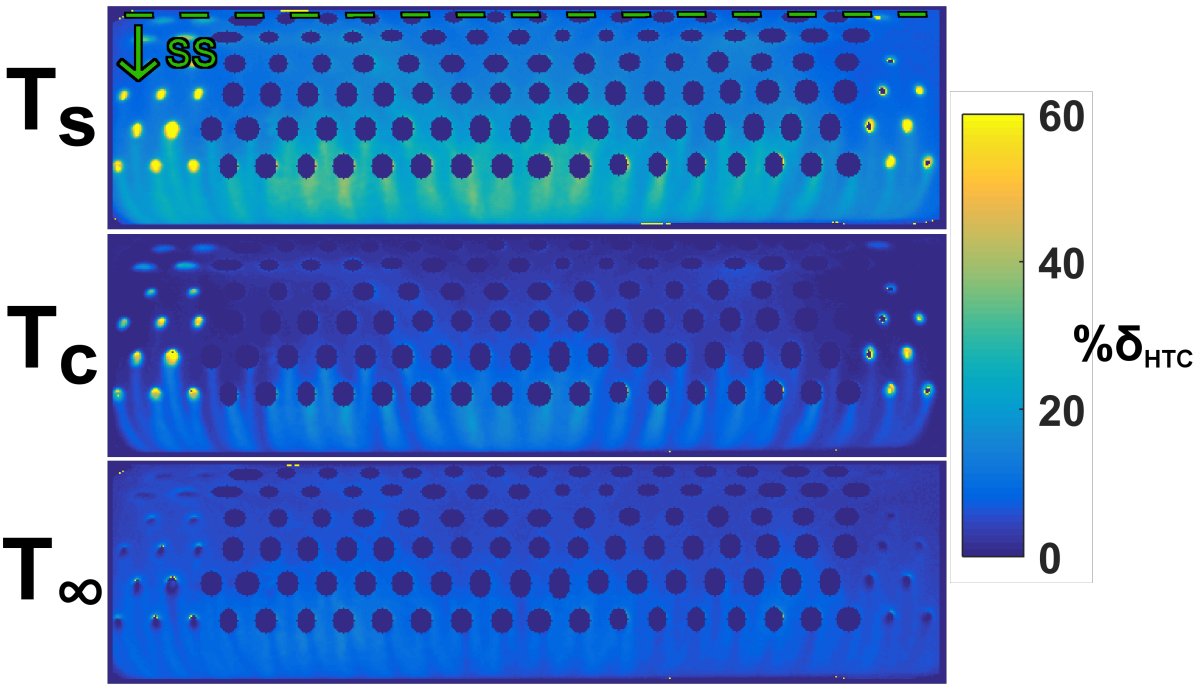


Figure B.2: Suction side HTC uncertainty contributions of the surface temperature (T_s), the coolant temperature (T_c), and the mass-averaged mainstream temperature (T_∞).

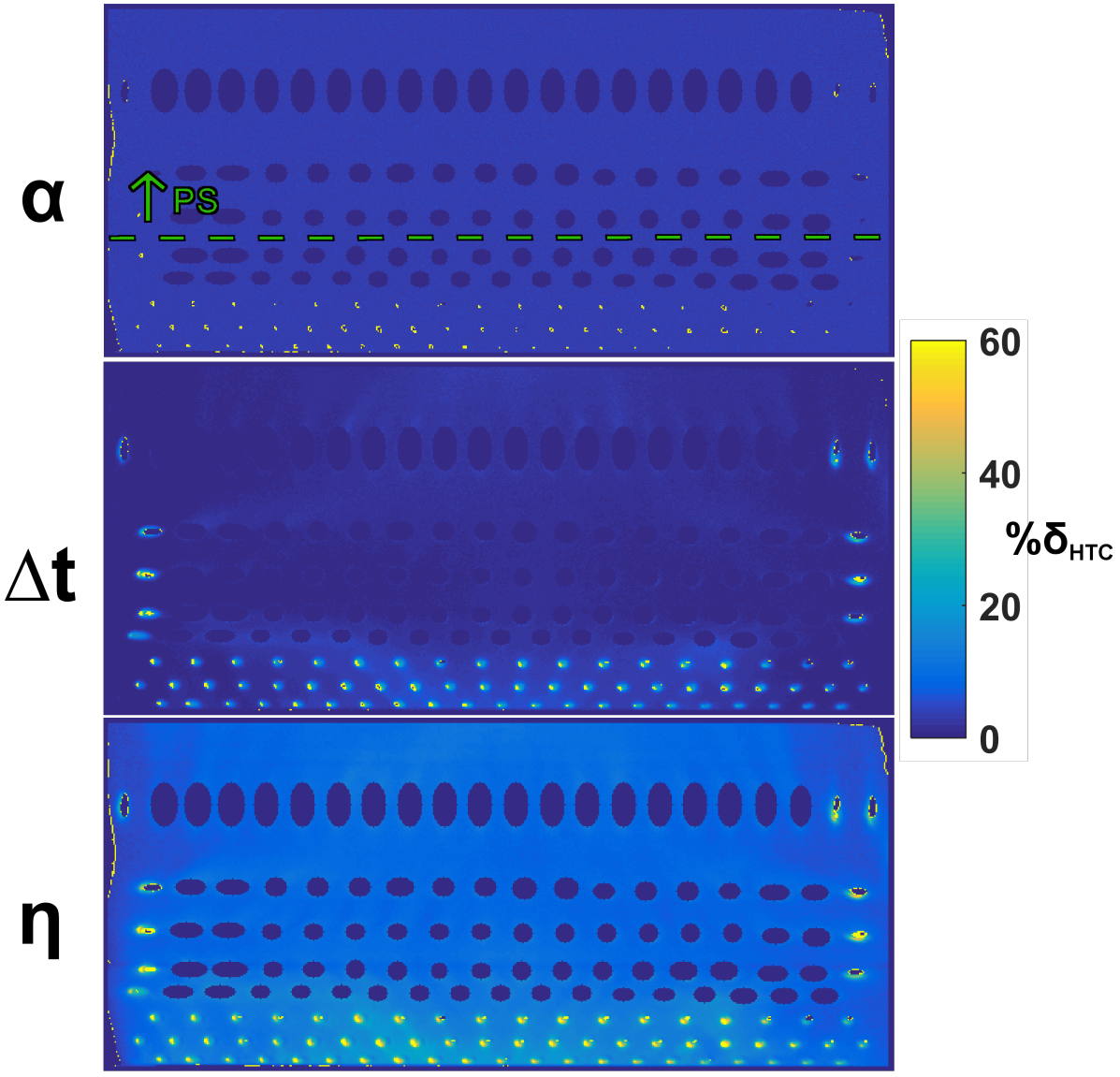


Figure B.3: Pressure side HTC uncertainty contributions of the material thermal diffusivity (α), the time error (Δt), and the film effectiveness (η).

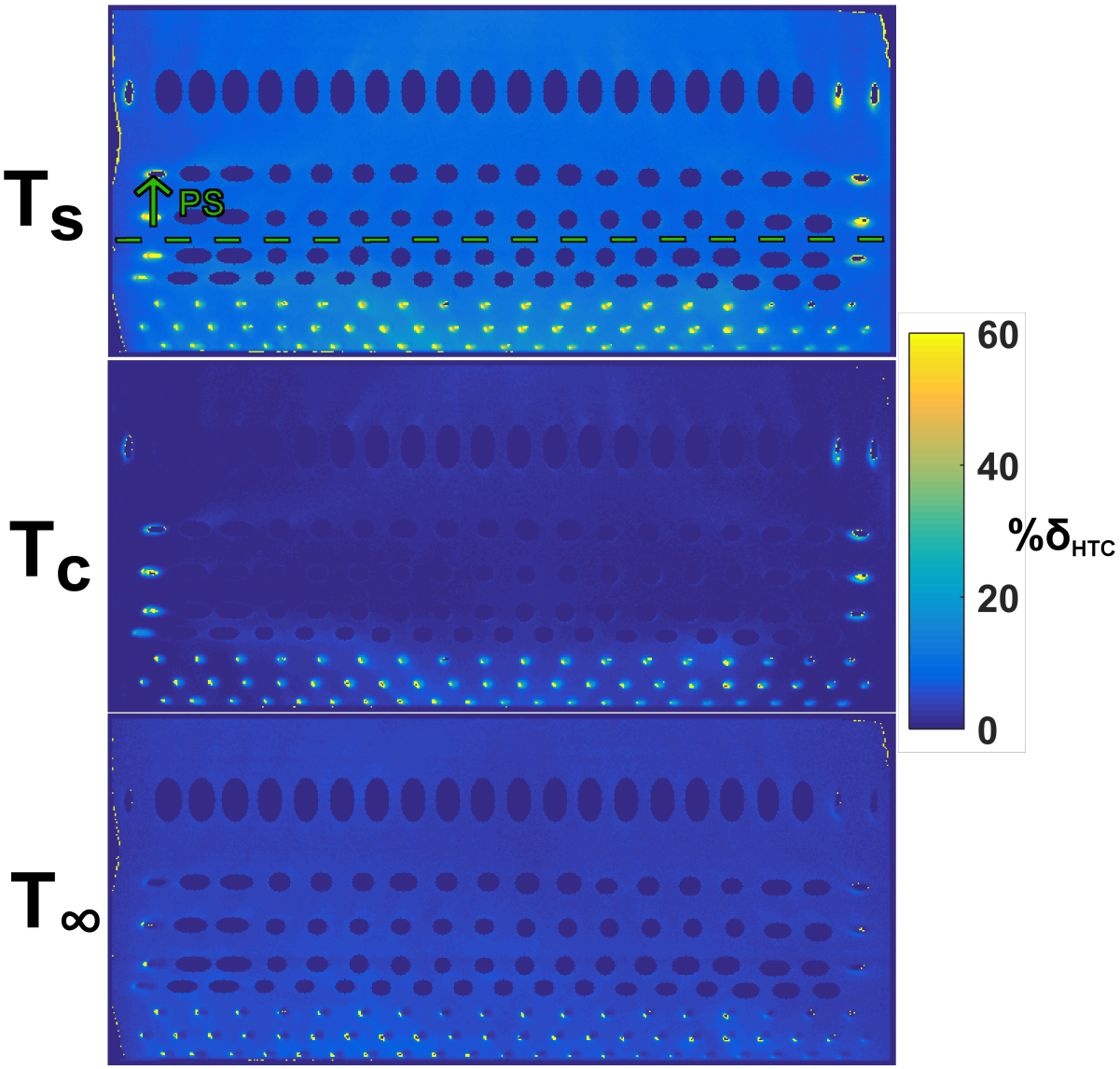


Figure B.4: Pressure side HTC uncertainty contributions of the surface temperature (T_s), the coolant temperature (T_c), and the mass-averaged mainstream temperature (T_∞).

References

[1] G. Elert. The Physics Hypertextbook, 2019.

[2] Airlines for America. The Air Travel Value Proposition: Safer, Cheaper, Greener, Quieter - and Fast, 2018.

[3] European Commission. Annual Analyses of the EU Air Transport Market 2016. Technical Report March, 2017.

[4] International Air Transport Association. Aviation Benefits Beyond Borders. Technical report, 2017.

[5] The Boeing Company. Boeing 737 Performance Summary, 2010.

[6] Bombardier Inc. Bombardier C Series Environmental Product Declaration, 2017.

[7] Intergovernmental Panel on Climate Change. Aviation and the Global Atmosphere. Technical report, 1999.

[8] International Council on Clean Transportation. Transatlantic Airline Fuel Efficiency Ranking, 2014. Technical Report November, 2015.

[9] International Energy Agency. Renewables 2017: Analysis and Forecasts to 2022. Technical report, 2017.

[10] G. W. Meetham. *The Development of Gas Turbine Materials*. Applied Science Publishers, 1981.

[11] M. Zivic, A. Galovic, and Z. Virag. Detailed Analysis of the Effect of the Turbine and Compressor Isentropic Efficiency on the Thermal and Exergy Efficiency of a Brayton Cycle. *Thermal Science*, 18(3):843–852, 2014.

[12] J. C. Han. Fundamental Gas Turbine Heat Transfer. *J. Thermal Science and Engineering Applications*, 5(2), 2013.

[13] F. T. Jane. *Jane's Fighting Aircraft of World War II*. Random House Value Publications, 1994.

[14] C. B. Meher-homji and E. Prisell. Developments of Dr . Hans Von Ohain — from the HeS 1 to the HeS 011. In *Proc. International Gas Turbine and Aeroengine Congress and Exhibition*, Indianapolis, IN, 1999.

[15] D. G. Bogard and K. A. Thole. Gas Turbine Film Cooling. *J. Propulsion and Power*, 22(2):249–270, 2006.

[16] R. A. Miller. Thermal Barrier Coatings for Aircraft Engines: History and Directions. *J. Thermal Spray Tech.*, 6(1):35–42, 1997.

[17] T. J. Carter. Common Failure in Gas Turbine Blades. *Eng. Failure Analysis*, 12:237–247, 2005.

[18] Australian Transport Safety Bureau. Australian Transport Safety Bureau Report: In-Flight Uncontained Engine Failure Airbus A380-842, VH-OQA, 2013.

[19] U.S. Department of Energy. *National Energy Technology Laboratory Gas Turbine Handbook*. 2006.

[20] B. Sen, D. L. Schmidt, and D. G. Bogard. Film Cooling With Compound Angle Holes: Heat Transfer. *J. Turbomach.*, 118:800–806, 1994.

[21] B.D. Mouzon, J.E. Albert, E.J. Terrell, and D.G. Bogard. Net Heat Flux Reduction and Overall Effectiveness for a Turbine Blade Leading Edge. In *Proc. ASME Turbo Expo*, Reno, NV, 2005.

[22] K. A. Thole, A. K. Sinha, D. G. Bogard, and M. E. Crawford. Mean Temperature Measurements of Jets with a Crossflow for Gas Turbine Film Cooling Application. In *Proc. Third International Symposium on Transport Phenomena and Dynamics of Rotating Machinery*, pages 69–85, Honolulu, HW, 1992.

[23] U Drost and A. Bölcs. Investigation of Detailed Film Cooling Effectiveness and Heat Transfer Distributions on a Gas Turbine Airfoil. *J. Turbomach.*, 121(2):233–242, 1999.

[24] J.R. Pietrzyk, D. G. Bogard, and M. . Crawford. Effects of Density Ratio on the Hydrodynamics of Film Cooling. *J. Turbomach.*, 112(3):437–443, 1990.

[25] K. Takeishi, S. Aoki, and T. Sato. Film Cooling on a Gas Turbine Rotor Blade. In *Proc. ASME Turbo Expo*, Orlando, FL, 1991.

[26] J. Ahn, M. T. Schobeiri, J. C. Han, and H. K. Moon. Film Cooling Effectiveness on the Leading Edge Region of a Rotating Turbine Blade with Two Rows of Film Cooling Holes Using Pressure Sensitive Paint. *J. Heat Transfer*, 128:879–888, 2006.

[27] J. H. Leylek and R. D. Zerkle. Discrete-jet Film Cooling: A Comparison of Computational Results with Experiments. In *Proc. International Gas Turbine and Aeroengine Congress and Exhibition*, Cincinnati, OH, 1993.

[28] D. K. Walters and J. H. Leylek. A Detailed Analysis of Film Cooling Physics Part 1: Streamwise Injection with Cylindrical Holes. In *Proc. ASME Turbo Expo*, Orlando, FL, 1997.

[29] R. J. Goldstein and P. Jin. Film Cooling Downstream of a Row of Discrete Holes With Compound Angle. *J. Turbomach.*, 123:222, 2001.

[30] I. Cresci, P. T. Ireland, M. Bacic, I. Tibbott, and A Rawlinson. Realistic Velocity, Turbulence and Temperature Profiles at the Combustor-Turbine Interaction Plane in a Rig. In *Proc. International Gas Turbine Congress*, Tokyo, Japan, 2015.

[31] R. J. Goldstein, E. R. G. Eckert, and F. Burggraf. Effects of Hole Geometry and Density on Three-Dimensional Film Cooling. *J. Heat and Mass Transfer*, 17(5):595–607, 1974.

[32] M. Gritsch, A. Schulz, and S. Wittig. Adiabatic Wall Effectiveness Measurements of Film-cooling Holes with Expanded Exits. *J. Turbomach.*, 120(3):549–556, 1997.

[33] D. Schmidt, B. Sen, and D. Bogard. Film Cooling with Compound Angle Holes: Adiabatic Effectiveness. *J. Turbomach.*, 118:807–813, 1996.

[34] B. Sen, D. Schmidt, and D. Bogard. Film Cooling with Compound Angle Holes: Heat Transfer. *J. Turbomach.*, 118:800–806, 1996.

[35] J. Dittmar, A. Schulz, and S. Wittig. Assessment of Various Film Cooling Configurations Including Shaped and Compound Angle Holes Based on Large Scale Experiments. *J. Turbomach.*, 125:57–64, 2003.

[36] T. H. Wong, P. T. Ireland, and K. P. Self. Film Cooling Effectiveness Downstream of Trailing Edge Slots Including Cutback Surface Protuberances. *International J. Turbomach. Propulsion and Power*, 1(1), 2016.

[37] N. Gurram, P. T. Ireland, T. H. Wong, and K. P. Self. Study of Film Cooling in the Trailing Edge Region of a Turbine Rotor Blade In High Speed Flow Using Pressure Sensitive Paint. In *Proc. ASME Turbo Expo*, Seoul, South Korea, 2016.

[38] J. E. Sargison. *Development of a Novel Film Cooling Hole Geometry.* PhD thesis, The University of Oxford, 2001.

[39] S. K. Waye and D. G. Bogard. High-Resolution Film Cooling Effectiveness Measurements of Axial Holes Embedded in a Transverse Trench With Various Trench Configurations. *J. Turbomach.*, 129(2):294–302, 2006.

[40] Y. Okita and M. Nishiura. Film Effectiveness Performance of an Arrowhead-Shaped Film-Cooling Hole Geometry. *J. Turbomach.*, 129(2):331–339, 2006.

[41] H. Nasir, S. Acharya, and S. Ekkad. Film Cooling From a Single Row of Cylindrical Angled Holes with Triangular Tabs Having Different Orientations. In *Proc. ASME Turbo Expo*, New Orleans, LA, 2001.

[42] X. Li. Numerical Simulation of Fluid Flow and Heat Transfer of Film Cooling with Backward Injection. In *Proc. 14th International Heat Transfer Conference*, Washington, DC, 2010.

[43] J. D. Heidmann. A Novel Antivortex Turbine Film-Cooling Hole Concept. *J. Turbomach.*, 130(3), 2008.

[44] K. Kusterer, D. Bohn, T. Sugimoto, and R. Tanaka. Double-Jet Ejection of Cooling Air for Improved Film Cooling. *J. Turbomach.*, 129(4), 2007.

[45] D. A. Fletcher. *Internal Cooling of Turbine Blades: The Matrix Cooling Method.* PhD thesis, The University of Oxford, 1997.

[46] S. R. Nowlin, D. R. H. Gillespie, P. T. Ireland, E. Romero, and M. Mitchell. An Experimental and Computational Parametric Investigation of Flow Conditions in Intersecting Circular Passages. In *Proc. ASME Turbo Expo*, pages 849–859, Montreal, Canada, 2007.

[47] J. M. Cutbirth and D. G. Bogard. Thermal Field and Flow Visualization Within the Stagnation Region of a Film Cooled Turbine Vane. *J. Turbomach.*, 124:200–206, 2002.

[48] W. J. Mick and R. E. Mayle. Stagnation Film Cooling and Heat Transfer Including Its Effect Within the Hole Pattern. *J. Turbomach.*, 110:66–72, 1988.

[49] A. B. Mehendale and J. C. Han. Influence of High Mainstream Turbulence on Leading Edge Film Cooling Heat Transfer. *J. Turbomach.*, 116:730–737, 1992.

[50] S. Ito, R. Goldstein, and E. Eckert. Film Cooling of a Gas Turbine Blade. *J. Eng. Power*, 100:476–481, 1978.

[51] F E Ames. The Influence of Large-Scale High-Intensity Turbulence on Vane Heat Transfer. *J. Turbomach.*, 119(1):23–30, 1997.

[52] G. J. Van Fossen, R. J. Simoneau, and C. Y. Ching. Influence of Turbulence Parameters, Reynolds Number, Body Shape on Stagnation-Region Heat Transfer. *J. Heat Transfer*, 117(3):597–603, 1995.

[53] G. Jumper, W. Elrod, and R. Rivir. Film Cooling Effectiveness in High Turbulence Flows. *J. Turbomach.*, 113:479–483, 1991.

[54] D. L. Schmidt and D. G. Bogard. Effects of Free-Stream Turbulence and Surface Roughness on Film Cooling. In *Proc. International Gas Turbine and Aeroengine Congress and Exhibition*, Birmingham, UK, 1996.

[55] C. Saumweber, A. Schulz, and S. Wittig. Free-Stream Turbulence Effects on Film Cooling with Shaped Holes. *J. Turbomach.*, 125:65–73, 2003.

[56] A. Hoffs, U. Drost, and A. Bölcs. Heat Transfer Measurements on a Turbine Airfoil at Various Reynolds Numbers and Turbulence Intensities Including Effects of Surface Roughness. In *Proc. International Gas Turbine and Aeroengine Congress and Exhibition*, Birmingham, UK, 1996.

[57] J. E. Wammack, J. Crosby, D. Fletcher, J. P. Bons, and T. H. Fletcher. Evolution of Surface Deposits on a High-Pressure Turbine Blade - Part I - Physical Characteristics. *J. Turbomach.*, 130(2), 2008.

[58] C. M. Cha, P. T. Ireland, P. A. Denman, and V. Savarianandam. Turbulence Levels Are High at the Combustor-Turbine Interface. In *Proc. ASME Turbo Expo*, Copenhagen, Denmark, 2012.

[59] M. Thomas, B. Kirollos, D. Jackson, and T. Povey. Experimental and CFD Studies of NGV Endwall Cooling. In *Proc. ASME Turbo Expo*, San Antonio, TX, 2013.

[60] J. D. Ferguson, D. K. Walters, and J. H. Leylek. Performance of Turbulence Models and Near-wall Treatments in Discrete Jet Film Cooling Simulations. In *International Gas Turbine and Aeroengine Congress and Exhibition*, Stockholm, Sweden, 1998.

[61] P. He, M. Salcudean, and I. S. Gartshore. Computations of Film Cooling for the Leading Edge Region of a Turbine Blade Model. In *Proc. International Gas Turbine and Aeroengine Congress and Exhibition*, Houston, TX, 1995.

[62] M. Salcudean, I. Gartshore, K. Zhang, and I. McLean. An Experimental Study of Film Cooling Effectiveness Near the Leading Edge of a Turbine Blade. *J. Turbomach.*, 116:71–79, 1994.

[63] A. Rozati and D. K. Tafti. Large Eddy Simulation of Leading Edge Film Cooling—Part II: Heat Transfer and Effect of Blowing Ratio. *J. Turbomach.*, 130(4), 2007.

[64] S. S. Sreedharan and D. K. Tafti. Effect of Blowing Ratio on Syngas Flyash Particle Deposition on a Three-Row Leading Edge Film Cooling Geometry Using Large Eddy Simulations. In *Proc. ASME Turbo Expo*, Orlando, FL, 2009.

[65] E. Sakai, T. Takahashi, K. I. Funazaki, H. B. Salleh, and K. Watanabe. Numerical Study on Flat Plate and Leading Edge Film Cooling. In *Proc. ASME Turbo Expo*, pages 491–503, Orlando, FL, 2009.

[66] M. Shur, P.R. Spalart, M. Strelets, and A. Travin. Detached-eddy Simulation of an Airfoil at High Angle of Attack. *Engineering Turbulence Modelling and Experiments*, 4:669–678, 1999.

[67] S. Voigt, B. Noll, and M. Aigner. Aerodynamic Comparison and Validation of RANS, URANS and SAS Simulations of Flat Plate Film Cooling. Glasgow, UK, 2010.

[68] F. Muldoon and S. Acharya. DNS Study of Pulsed Film Cooling for Enhanced Cooling Effectiveness. *International J. Heat and Mass Transfer*, 52, 2009.

[69] D Chandran and B Prasad. Conjugate heat transfer study of combined impingement and showerhead film cooling near NGV leading edge. *Int. J. Rot. Mach.*, 2015.

[70] D. R. Zimmerman. Laser Anemometer Measurements at the Exit of a T63-C20 Combustor. Technical report, NASA Lewis Research Center, 1979.

[71] A. F. Bicen, D. Tse, and J. H. Whitelaw. Flow and Combustion Characteristics of an Annular Combustor. *Combust. Flame*, 72:175–192, 1988.

[72] R. W. Moss and M. L. G. Oldfield. Measurements of hot combustor turbulence spectra. In *Proc. ASME Turbo Expo*, Orlando, FL, 1991.

[73] K. A. Thole, D. G. Bogard, and J. L. Whan-Tong. Generating High Freestream Turbulence Levels. *Experiments in Fluids*, 17(6):375–380, 1994.

[74] C. M. Cha, S. Hong, P. T. Ireland, P. Denman, and V. Savarianandam. Experimental and Numerical Investigation of Combustor-Turbine Interaction Using an Isothermal, Nonreacting Tracer. *J. Eng. Gas Turbines Power*, 134, 2012.

[75] M. D. Barringer, K. A. Thole, and M. D. Polanka. Experimental Evaluation of an Inlet Profile Generator for High Pressure Turbine Tests. *J. Turbomach.*, 129:382–393, 2007.

[76] M. D. Barringer, O. T. Richard, J. P. Walter, S. M. Stitzel, and K. A. Thole. Flow Field Simulations of a Gas Turbine Combustor. *J. Turbomach*, 124(3):508–516, 2002.

[77] I. Cresci, P. T. Ireland, M. Bacic, I. Tibbott, and A. Rawlinson. Velocity and Turbulence Intensity Profiles Downstream of a Long Reach Endwall Double Row of Film Cooling Holes in a Gas Turbine Combustor Representative Environment. In *Proc. ASME Turbo Expo*, Montreal, Canada, 2015.

[78] I Cresci. *High Pressure Nozzle Guide Vane Cooling System Flow Characteristics*. PhD thesis, The University of Oxford, 2016.

[79] Association Française de Normalisation. NF EN ISO 5167-2, 2003.

[80] C. H. Sieverding. The Influence of Trailing Edge Ejection on the Base Pressure in Transonic Turbine Cascades. In *Proc. International Gas Turbine Conference and Exhibit*, London, UK, 1982.

[81] A. J. White, J. B. Young, and P. T. Walters. Experimental Validation of Condensing Flow Theory for a Stationary Cascade of Steam Turbine Blades. *Phil. Trans. R. Soc. A*, 354:59–88, 1996.

[82] S. Luque, V. Kanjirakkad, I. Aslanidou, R. Lubbock, B. Rosic, and S. Uchida. A New Experimental Facility to Investigate Combustor-Turbine Interactions in Gas Turbines with Multiple Can Combustors. *J. Eng. Gas Turb. Power*, 137, 2015.

[83] M. Thomas. *Optimization of Endwall Film-Cooling in Axial Turbines*. PhD thesis, The University of Oxford, 2014.

[84] Emkay Plastics Ltd. Rohacell IG-F Polymethacrylimide Foam data sheet, 2016.

[85] Evonik Industries AG. Rohacell IG/IG-F Properties Online, 2019.

[86] H. Hoheisel, R. Kiock, H. J. Lichtfuss, and L. Fottner. Influence of Free-Stream Turbulence and Blade Pressure Gradient on Boundary Layer and Loss Behavior of Turbine Cascades. *J. Turbomach.*, 109(2), 1987.

[87] Klinger Ltd. Klinger Industrial Sealing Division Product Catalogue, 2012.

[88] K. Thulukkanam. *Heat Exchanger Design Handbook*. CRC Press, Boca Raton, FL, 2nd edition, 2013.

[89] R. C. Juvinal and K. Marshek. *Fundamentals of Machine Component Design*. John Wiley and Sons, Hoboken, NJ, 2nd edition, 1991.

[90] Evonik Industries AG. Private communication, 2018.

[91] A.M. Howatson, P. G. Lund, and J. D. Todd. *Engineering Tables and Data*. Oxford University, UK, 2009.

[92] N. E. Holgate, P. T. Ireland, and E. Romero. The Effects of Combustor Cooling Features on Nozzle Guide Vane Film Cooling Experiments. In *Proc. ASME Turbo Expo*, Oslo, Norway, 2018.

[93] Nicholas E Holgate, Peter T Ireland, and Eduardo Romero. The Effects of Combustor Cooling Features on Nozzle Guide Vane Film Cooling Experiments. *J. Turbomach.*, 141(1), 2019.

[94] Nicholas E Holgate, Peter T Ireland, and Eduardo Romero. An Experimental-numerical Method for Transient Infrared Measurement of Film Cooling Effectiveness and Heat Transfer Coefficient in a Single Test. *The Aeronautical J.*, 2019.

[95] Paul Bonnett. *Applications of Liquid Crystals in Aerodynamics Testing*. PhD thesis, The University of Oxford, 1989.

[96] P. T. Ireland and T. V. Jones. Liquid Crystal Measurements of Heat Transfer and Surface Shear Stress. *Meas. Sci. Technol.*, 11:969–986, 2000.

[97] C. Lempereur, R. Andral, and J. Y. Prudhomme. Surface Temperature Measurement on Engine Components by Means of Irreversible Thermal Coatings. *Measurement Science and Technology*, 19(10), 2008.

[98] J. C. Han and A. P. Rallabandi. Turbine Blade Film Cooling Using PSP Technique. *Frontiers in Heat and Mass Transfer*, 1(1), 2010.

[99] Alexander Murray, Peter Ireland, Tsun Wong, Shaun Tang, and Anton Rawlinson. High Resolution Experimental and Computational Methods for Modelling Multiple Row Effusion Cooling Performance. *International J. Turbomach., Propulsion and Power*, 3(1):4, 2018.

[100] FLIR Systems Inc. FLIR Company History (at http://www.flir.co.uk).

[101] FLIR Systems Inc. Uncooled Detectors for Thermal Imaging Cameras (at http://www.flir.co.uk), 2015.

[102] FLIR Systems Inc. The Ultimate Infrared Handbook for R & D Professionals. Technical report, Wilsonville, OR, 2012.

[103] FLIR Systems Inc. Cooled vs Uncooled Thermal Imaging (at http://www.flir.co.uk), 2015.

[104] R. Siegel and J. R. Howell. *Thermal Radiation Heat Transfer*. Taylor and Francis Group, 4th edition, 2002.

[105] J. R. Mahan. *Radiation Heat Transfer: A Statistical Approach*. Wiley-IEEE, 3 edition, 2002.

[106] B. Kirollos and T. Povey. Laboratory Infra-Red Thermal Assessment of Laser-Sintered High-Pressure Nozzle Guide Vanes to De-Risk Engine Design Programmes. *J. Turbomach.*, 139(4):12, 2017.

[107] M. Vollmer and K. P. Mollmann. *Infrared Thermal Imaging: Fundamentals, Research and Applications*. John Wiley & Sons, 1st edition, 2010.

[108] Edmund Optics. Germanium windows datasheet, 2018.

[109] RS Components Ltd. RS Pro Heat Sink Compound (Stock No: 554-311).

[110] D. E. Metzger and D. E. Larson. Use of Melting Point Surface Coatings for Local Convection Heat Transfer Measurements in Rectangular Channel Flows with 90-deg Turns. *J. Heat Transfer*, 108:48–54, 1986.

[111] R. P. Vedula and D. E. Metzger. A Method for the Simultaneous Determination of Local Effectiveness and Heat Transfer Distributions in Three Temperature Convection Situations. In *Proc. International Gas Turbine and Aeroengine Congress and Exhibition*, Orlando, FL, 1991.

[112] H. Du, J. C. Han, and S. V. Ekkad. Effect of Unsteady Wake on Detailed Heat Transfer Coefficient and Film Effectiveness Distributions for a Gas Turbine Blade. *J. Turbomach.*, 120(4):808–817, 1998.

[113] Andrew C. Chambers, David R. H. Gillespie, Peter T. Ireland, and Geoffrey M. Dailey. A Novel Transient Liquid Crystal Technique to Determine Heat Transfer Coefficient Distributions and Adiabatic Wall Temperature in a Three-Temperature Problem. *J. Turbomach.*, 125(3):538, 2003.

[114] D. N. Licu, M. J. Findlay, I. S. Gartshore, and M. Salcudean. Transient Heat Transfer Measurements Using a Single Wide-Band Liquid Crystal Test. *J. Turbomach*, 122:546–552, 2000.

[115] M. K. Chyu and Y. C. Hsing. Use of a Thermographic Phosphor Fluorescence Imaging System for Simultaneous Measurement of Film Cooling Effectiveness and Heat Transfer Coefficient. In *Proc. International Gas Turbine and Aeroengine Congress and Exhibition*, 1996.

[116] S. V. Ekkad, S. Ou, and R. B. Rivir. Thermography Method for Simultaneous Film Cooling Effectiveness and Heat Transfer Coefficient Measurements From a Single Test. *J. Turbomach.*, 126(4):597–603, 2004.

[117] S. P. Chen, M. K. Chyu, and T. I. P. Shih. Effects of Upstream Ramp on the Performance of Film Cooling. *International J. Thermal Sciences*, 50(6):1085–1094, 2011.

[118] S. A. Hayes, A. C. Nix, C. M. Nestor, D. T. Billups, and S. M. Haught. Experimental Investigation of the Influence of Freestream Turbulence on an Anti-vortex Film Cooling Hole. *Experimental Thermal and Fluid Science*, 81:314–326, 2017.

[119] R. L. Burden and J. D. Faires. *Numerical Analysis*. Cengage Learning, 9 edition, 2011.

[120] F. Coletti, M. Scialanga, and T. Arts. Experimental Investigation of Conjugate Heat Transfer in a Rib-Roughened Trailing Edge Channel with Crossing-Jets. *J. Turbomach.*, 134(4), 2012.

[121] J. C. Ryley, M. Mcgilvray, and D. R. H. Gillespie. Calculation of Heat Transfer Coefficient Distribution on 3D Geometries From Transient Liquid Crystal Experiments. In *Proc. ASME Turbo Expo*, Düsseldorf, Germany, 2014.

[122] N. E. Holgate, P. T. Ireland, and K. P. Self. High Resolution Film Cooling Effectiveness Measurements for Nozzle Guide Vane Leading Edges. In *Proc. ASME Turbo Expo*, Charlotte, NC, 2017.

[123] Robert J. Moffat. Describing the Uncertainties in Experimental Results. *Experimental Thermal and Fluid Science*, 1(1):3–17, 1988.

[124] I. Cresci, P. T. Ireland, M. Bacic, I. Tibbott, and A. Rawlinson. Realistic Velocity and Turbulence Intensity Profiles at the Combustor-Turbine Interaction Plane in a Nozzle Guide Vane Test Facility. In *Proc. European Turbomach. Conference*, Madrid, Spain, 2015.

[125] K. Funazaki, H. Kawabata, D. Takahashi, and Y. Okita. Experimental and Numerical Studies on Leading Edge Film Cooling Performance: Effects of Hole Exit Shape and Freestream turbulence. *Proc. ASME Turbo Expo*, 2012.

[126] S. R. Nowlin. *The Use of Intersecting Film Cooling Passages for Nozzle Guide Vane Cooling*. PhD thesis, The University of Oxford, 2009.

[127] S. Shetty, X. Li, and G. Subbuswamy. Numerical Simulation on Gas Turbine Film Cooling of Curved Surface With Backward Injection. In *Proc. ASME Summer Heat Transfer Conference*, Rio Grande, Puerto Rico, 2012.

[128] G. Subbuswamy, X. Li, and K. Gharat. Numerical Simulation of Backward Film Cooling with Fan-Shaped Holes. In *Proc. ASME Heat Transfer Summer Conference*, Minneapolis, MN, 2013.

[129] A. F. Chen, S. J. Li, and J. C. Han. Film Cooling with Forward and Backward Injection for Cylindrical and Fan-shaped Holes Using PSP Measurement Technique. In *Proc. ASME Turbo Expo*, Düsseldorf, Germany, 2014.

[130] S. Park, E. Y. Jung, S. H. Kim, H. S. Sohn, and H. H. Cho. Enhancement of Film Cooling Effectiveness Using Backward Injection Holes. *Int. J. Thermal Sciences*, 110:314–324, 2016.

[131] R. Prenter, M. A. Hossain, L. Agricola, A. Ameri, and J. P. Bons. Experimental Characterization of Reverse-Oriented Film Cooling. In *Proc. ASME Turbo Expo*, Charlotte, NC, 2017.

[132] N. E. Holgate, I. Cresci, P. T. Ireland, and A. Rawlinson. Prediction and Augmentation of Nozzle Guide Vane Film Cooling Hole Pressure Margin. In *Proc. European Turbomach. Conference*, Stockholm, Sweden, 2017.

[133] K. A. Thole, M. Gritsch, A. Schulz, and S. Wittig. Effect of a Crossflow at the Entrance to a Film-cooling Hole. *J. Fluids Engineering, Transactions of the ASME*, 119(3):533–540, 1997.

[134] N. Domaschke, J. von Wolfersdorf, and K. Semmler. Heat Transfer and Pressure Drop Measurements in a Rib Roughened Leading Edge Cooling Channel. In *Proc. ASME Turbo Expo*, pages 337–348, Orlando, FL, 2009.

[135] P. Ligrani. Heat Transfer Augmentation Technologies for Internal Cooling of Turbine Components of Gas Turbine Engines. *International J. Rotating Machinery*, 2013.

[136] T. Bamba, T. Kumagai, . Mimura, T. Yamane, Y. Fukuyama, T. Usui, and T. Yoshida. Leading Edge Cooling Performance of an Integrated Cooling Configuration. In *Proc. ASME Turbo Expo*, Berlin, Germany, 2008.

[137] A. V. Murray, P. T. Ireland, and A. Rawlinson. Integrated conjugate computational approach for evaluating the aerothermal and thermomechanical performance of double-wall effusion systems. In *Proc. ASME Turbo Expo*, Charlotte, NC, 2017.

[138] A. K. Gupta, D. Ramerth, and D. Ramachandran. Validation of CFD Predicted Discharge Coefficients for Thick Plate Orifices with Flow Perpendicular and Inclined to the Orifice Axis. In *Proc. ASME Turbo Expo*, Berlin, Germany, 2008.

[139] T. K. Serghides. Estimate Friction Factor Accurately. *Chemical Engineering J.*, 91(5):63–64, 1984.